Diamond sensors for extreme environments

William Parfitt

Thesis submitted for the degree of

Doctor of Philosophy

London Centre for Nanotechnology

and

Department of Electronic and Electrical Engineering

University College London

March, 2019

I, William Parfitt, confirm that the work presented in this thesis is my own. Where information has been derived from other sources, I confirm that this has been indicated in the work.

Abstract

Diamond is unique in its collection of superlative mechanical, electronic and electrochemical properties. Through the investigations presented in this work these properties are brought to the foreground to demonstrate how previously intractable problems may be solved by the research and development of diamond-based sensors for extreme environments.

One such solution is the use of diamond as an innovative component in robust, solid-state neutron detection. A comprehensive computational Monte Carlo model is built to simulate and optimise the efficiency and energy resolution of diamond neutron detector geometries, taking into account the significant influence of statistical charge carrier generation, trapping and recombination as well as electronic noise. Consequently, a new and promising route to highly efficient diamond neutron detectors is presented. Additionally, machine learning is used to help improve upon the Bethe equation and semi-empirical fitting methods for the calculation of low-energy ionic stopping powers. A regressive decision tree ensemble is shown to be capable of remarkably accurate predictions for any conceivable ion and target combination when compared to existing experimental data.

The concurrent development of diamond water quality sensors is also described, paving the way for multi-functional monitoring of harsh fluids over extended periods of time. Boron-doped diamond layers are grown on polycrystalline intrinsic substrates and processed for characterisation. Electronic measurements, including circular transmission line and temperature-dependent impedance spectroscopy, are

performed to determine key properties of the layers for use in high temperature applications. Finally, these devices are processed to form novel prototypes for sensors in harsh environments. Results are presented for a diamond pH sensor using an ion-sensitive field effect transistor (ISFET) structure, and an amperometric dissolved oxygen (DO) sensor.

Impact statement

The impact of the work presented in this thesis can be summarised as follows:

- **Academic:** High quality CVD (chemical vapour deposition) diamond is a relatively recent electronic material and as such presents fertile ground for advances in new technology. (1) A number of significant conclusions have been derived from a computational study into the optimisation of diamond neutron detectors. These will benefit the large community of researchers reliant on high-performance neutron detectors and the software will be made available online for future use. (2) A new methodology has been developed for determining the stopping power of ions in the low energy regime using machine learning. Not only may this improve calculations in particle detection and other uses of radiation, such as medicine; but it has the potential to inform an entirely different set of approaches to physical problems. (3) The growth and detailed electronic characterisation of boron-doped diamond layers has furthered the existing knowledge base within the diamond community for the better use of diamond in devices. (4) The development and test of a new device structure for lab-on-chip sensors in extreme environments has brought the wide-scale adoption of diamond technology a step closer.

  Highly noteworthy is the successful award of several research grants as a direct result of the work in this thesis – co-contributed by the author, and awarded to the Diamond Electronics Group at UCL. These are: (1) EPSRC IAA Discovery-To-Use (D2U) award for £87,500; (2) Contract for

project entitled "Diamond sensors for harsh environments: A design study for 'BoltSens-Prime"' from BAE Systems Maritime Ltd. for £61,500; (3) Contract for project entitled: "Diamond sensors for harsh environments: BoltSens" from BAE Systems Maritime Ltd. for £842,000.

- **Commercial:** The funding for the PhD studentship responsible for this work was provided by an Industrial Cooperative Awards in Science & Technology (CASE) award from the EPSRC and BAE Systems plc (BAES) for mutually beneficial academic and commercial gain. As a result, the research outcomes of this work will have direct commercial benefit in applications within BAES. In addition, a number of reports have been co-authored and delivered including a comprehensive 145-page strategy report: "Development of a plan for the use of a diamond-based sensor technology in harsh environments", which has led to the research contracts listed above.

- **Intellectual Property:** The patent (PCT/GB2017/050580) "Diamond-based sensor device for use in hostile environments" has been co-authored and filed nationally and internationally as an outcome of this work. The protection of this important IP will allow the future exploitation of the advances made in this thesis in a wide variety of applications.

- **Dissemination:** The work in this thesis has been presented in poster and oral sessions at the following conferences: (1) Hasselt Diamond Workshop - SBDD (2015, 2016, 2017), Hasselt, Belgium (2) New Diamond and Nano Carbons (2016), Xi'an, China (3) European Materials Research Society (E-MRS) Fall Meeting (2018), Warsaw, Poland. At the time of writing, the following journal publications are being prepared for submission: (1) Parfitt, W., Jackman, R. B., Monte-carlo simulations for the optimisation of diamond-based neutron detectors; (2) Parfitt, W., Jackman, R. B., Machine learning for the prediction of stopping powers.

Acknowledgements

I would like to begin by expressing my profound gratitude to Professor Richard Jackman. Not only did he entrust me with this tremendous opportunity, but he has been the source of immeasurable enthusiasm and support throughout my PhD. His research group, the Diamond Electronics Group (DEG), is quite unique in the excellent level of work that it produces whilst being a happy and fulfilling place to spend each day. It is a testament to Richard's extraordinary qualities, and I am fortunate to count myself as part of his team.

The DEG would not be the group it is without its venerable deputy, Dr Joe Welch, who I must thank deeply for being an accessible port of call for anything from the incidental to the impossible. He has also been a true friend throughout. In addition, I could not have reached the far depths of scientific understanding without the brilliant and untempered mind of Dr Alex Pakpour-Tabrizi – despite his dubious squash performances. Ralph Moors deserves a special mention, not only for being a human Twitter feed of the latest technology gossip, but also for his companionship, particularly when faced with large quantities of food. The list would not be complete without mentioning Terry Kang and Dr Alice Taylor, with whom I have shared several hilarious global adventures; alongside the other wonderful members of the DEG past and present.

Within the London Centre for Nanotechnology, I would like to express my gratitude to the cleanroom staff for their patience and assistance. In particular Rohit Khanna for his expertise with the PCB laser cutter and magical ability to fix priceless bits

of equipment – sometimes merely with his presence. In the wider academic realm I would like to thank Professor Oliver Williams and Dr Soumen Mandal for their help in growing boron-doped diamond, as well as giving me a whistle-stop tour of the pubs in Cardiff. I would additionally like to extend a professional appreciation to Everbeing International Corporation and Lambda Photometrics Ltd. for their kind donation of a very useful probe station.

This thesis would not exist without the crucial funding support of the Engineering and Physical Sciences Research Council (EPSRC) and BAE Systems plc (BAES), both of whom I would like to recognise for awarding me their industrial CASE studentship. The benefit of this award has been considerably greater than a simple research grant, and I am fortunate to have had a very close, productive and stimulating relationship with BAES – one that will extend far beyond this thesis. In particular, I would like to warmly convey my appreciation to Dr Russ Morgan for numerous magnificent anecdotes, along with his formidable technical insight. I would also like to thank Dr David Hankey for the many meetings that we shared to tease the devil out of the detail. These will be fondly remembered as some of the highlights of my PhD.

Finally, I could not have done any of this without the love and support of my family. My mum, Ylva, dad, Richard, and sisters, Emma, Louise and Alice – your encouragement and inspiration (and the fact that you will enjoy these tacky clichés!) mean everything to me. My best friend, Dr Rob Fraser, thanks for showing me how it's done – at least I didn't grow an awful beard whilst writing up. And most importantly, to Georgie, the love of my life. Thank you for putting up with me for all this time. You are my world.

Contents

List of Figures

List of Tables

List of Acronyms

AC	Alternating Current
AES	Auger Electron Spectroscopy
AI	Artificial Intelligence
CAD	Computer Aided Design
CCE	Charge Collection Efficiency
CSDA	Continuous Slowing Down Approximation
CTLM	Circular Transmission Line Model
CVD	Chemical Vapour Deposition
DC	Direct Current
DI	De-ionised
DO	Dissolved Oxygen
FE	Field Emission
FET	Field Effect Transistor
FWHM	Full Width Half Maximum
GE	Glass Electrode

GMC	Graphitic Microchannel
HFCVD	Hot Filament Chemical Vapour Deposition
HOMO	Highest Occupied Molecular Orbital
HPHT	High Pressure High Temperature
ICRU	International Commission on Radiation and Units
IDE	Integrated Development Environment
IPA	Isopropyl Alcohol
IS	Impedance Spectroscopy
ISFET	Ion-sensitive Field Effect Transistor
I-V	Current-Voltage
LCC	Leadless Chip Carrier
LOO-CV	Leave-One-Out Cross Validation
LpO-CV	Leave-p-Out Cross Validation
LOD	Limit Of Detection
LOQ	Limit Of Quantification
LOR	Lift-off Resist
LUMO	Lowest Unoccupied Molecular Orbital
MAE	Mean Absolute Error
MAPE	Mean Absolute Percentage Error
MDI	Mean Decrease in Impurity

MEMS	Micro-electro-mechanical Systems
ML	Machine Learning
MOSFET	Metal-oxide-semiconductor Field Effect Transistor
MW	Microwave
MWPECVD	Microwave Plasma Enhanced Chemical Vapour Deposition
NCD	Nanocrystalline Diamond
PCB	Printed Circuit Board
PCD	Polycrystalline Diamond
PECVD	Plasma Enhanced Chemical Vapour Deposition
PL	Photolithography
PR	Photoresist
PTFE	Polytetrafluoroethylene
PWR	Pressurised Water Reactor
QSPR	Quantitative Structure-Property Relationship
RC	Resistor-capacitor
RF	Radio Frequency
RF	Random Forest
RMSE	Root Mean Square Error
SCD	Single Crystal Diamond
SEM	Scanning Electron Microscope

SHE	Standard Hydrogen Electrode
SIMS	Secondary Ion Mass Spectrometry
SRIM	Stopping and Range of Ions in Matter
TDL	Tunable Laser Diode
TFE	Thermionic Field Emission
TGA	Thermogravimetric Analysis
TLM	Transmission Line Model
TMB	Trimethylborane
TOF	Time Of Flight
UNCD	Ultra Nanocrystalline Diamond
UV	Ultra Violet
XPS	X-ray Photoelectron Spectroscopy

Chapter 1

Introduction

There are many environments on Earth (and beyond) that are inaccessible to humans. This may be because of unbearable temperatures and extreme pressures in these places; they might be associated with large fluxes of ionising radiation and aggressive chemicals; or they may simply be physically isolated, unreachable or constricted. The paradox exists that for many of these inaccessible environments, it is of vital importance to regularly access, measure and characterise the environment. Nuclear reactors, for example, require a detailed knowledge of what is occurring within their complex systems in order to guarantee safety throughout their decades-long lifetime. A lapse in this obligation is a matter of the highest national, if not global, security. Similar challenging circumstances are found in nuclear decommissioning and waste disposal; industrial chemical, water, waste-water or food and beverage processing; subterranean oil, gas and ore mining; monitoring of natural environments – such as rivers, lakes, seas or the deep ocean; and even the exploration of outer space. The upsides are clear, whether they are calculated in financial terms, improved safety, environmental metrics or simply the advancement of human knowledge.

Over many years, technology and operational procedures have been carefully developed to allow us to have specific access to these hostile environments in order to carry out sensing of key parameters. Where remote sensing technology has been

developed it tends to suffer as a consequence of one or more elements of the harsh environment in which it is deployed, usually to the detriment of lifetime and performance. Where operational procedures require a level of human interaction, there exists an additional safety risk to the operator themselves. Despite this level of risk, in many circumstances the solution remains incomplete or inaccurate; restricted to infrequent sampling, secondary measurements, or at best, a system requiring regular maintenance. Where the technology is insufficient or unfeasible, vast costs are associated with system design, commissioning and incident response; as well as the losses absorbed due to inefficient operation of industrial processes. It is here that the field of diamond electronics has the ability to define a completely new category of sensing solutions.

Diamond is synonymous with extreme resilience and longevity – a fact that makes an attractive sentiment as a gemstone but is not understated when considering its physical properties. It is the hardest known natural material and boasts extreme incompressibility and stiffness. It is also resistant to high temperatures, chemical attack, and remains unaffected by radiation over long periods of time. The tetrahedral structure of diamond, formed of hybridised carbon bonds, also imparts many impressive properties that make it suitable for electronics. The main advantage is its semiconducting properties and wide band gap, which permit large electric fields to be applied without breakdown, high carrier mobilities and low carrier recombination rates. Diamond can be doped, most favourably with boron, to create devices that are ideally-suited for extreme sensing. Electrochemistry benefits from diamond having the widest electrochemical window of any material. The work in this thesis explores how key metrics of harsh environments can be monitored remotely over extended periods using diamond electronics, without exposure to many of the downsides of current technologies.

The extraordinary properties of diamond, and their atomistic origins, are examined further in chapter 2. The historical development of laboratory-grown diamond as a scalable and affordable alternative to natural diamond is reviewed, followed

by an evaluation of diamond doping techniques. Chapters 3 and 4 review, specifically, the theoretical background to both neutron detection and aqueous pH and dissolved oxygen sensing, as well as summarising the state-of-the-art in diamond research. Subsequently, chapters 5 and 6 contain a description of the computational and experimental methods used in this thesis. The four results chapters, 7 to 10, are roughly divisible into two separate sensing requirements for harsh environments.

Chapters 7 and 8 endeavour to further the use of diamond as an innovative component in neutron detection, which is a field currently lacking in robust and long-term solid-state solutions. In chapter 7, a comprehensive Monte Carlo model is built to simulate and optimise 'indirect' conversion-layer detectors that rely on high capture cross-section materials (such as ^{10}B) to generate charged products for detection in adjacent diamond layers; and p-n heterojunction diode detectors for the 'direct' conversion and detection of neutrons. Simulations are evaluated, using the model to optimise geometrical and material parameters whilst also taking into account non-idealised effects such as statistical carrier generation, charge trapping, recombination and electronic noise. The model facilitates the extraction of parameters which allow the efficiency to be maximised, providing a promising route towards achieving the latest high-efficiency diamond detectors.

Chapter 8 describes a highly novel method for calculating low-energy ionic stopping powers in materials for which empirical data is incomplete or unavailable, and where the Bethe equation fails to apply. A machine learning algorithm is trained using a database of existing experimental data to predict the stopping power values for any conceivable incident ion, energy and target material. The results are thoroughly evaluated against several error metrics and using a rigorous cross-validation technique. They show exciting potential for the industry-standard parameterised fitting techniques to be matched, and even superseded, using fast, automatic machine learning methods. Complete stopping power curves are generated for diamond and boron carbide with direct application in the simulations described in chapter 7.

Currently there are very limited, or otherwise unsafe, methods to sample fluids

that may be under extreme conditions. Chapters 9 and 10 describe the initial development of a multi-functional diamond water sensor, ultimately capable of measuring a number of key metrics *in-situ*. Chapter 9 presents the growth of thin boron-doped diamond layers on polycrystalline intrinsic substrates using microwave plasma enhanced chemical vapour deposition (MWPECVD). The dopant is introduced through residual growth chamber contamination in order to achieve a controlled impurity concentration that allows high temperature devices to be built. Electronic properties of two optimised samples are characterised using a test pattern of metal electrodes. This pattern allows contact resistance to be calculated using an adapted circular transmission line method. The temperature and frequency-dependent impedance components are measured using impedance spectroscopy, from which activation energies of the layers may be extracted. Chapter 10 builds on these results and describes the fabrication of an ion-sensitive field effect transistor (ISFET) pH sensor and an electrochemical dissolved oxygen sensor. A device design, which will allow the eventual implementation of diamond lab-on-chip technology, is explored in detail; along with the development of a custom calibration setup. The performance of the sensors is evaluated, showing high linear sensitivity across a broad range, low leakage currents and temporal stability.

Chapter 11 summarises the results achieved in this thesis, and describes the ongoing and future work to build on these outcomes. Namely, the further development of a new class of optimised and highly-efficient diamond neutron detectors, based on p-n junction diodes for the separation and collection of ionised charge carriers; as well as the initiation of the commercial development of a multi-functional diamond water sensor for extreme environments.

Chapter 2

Diamond, a very special form of carbon

2.1 Carbon allotropes

Carbon is an impressive element. It is almost impossible to avoid the use of terms such as 'building block' when describing its various atomic combinations – or allotropes – and their importance in nature. Carbon is not alone in being polymorphic, however, it is the vast array of the allotropes that it can form, and their superlative physical and electronic properties that make it extraordinary. These allotropes are typically the products of a vast number of carbon compounds that exist readily in nature and constitute the fundamentals of life on earth – an extraordinary and complex area known as organic chemistry.

A carbon atom consists of 6 protons, with 6 orbital electrons. The most common isotope ^{12}C (98.89% natural abundance) has a nucleus consisting of 6 neutrons, where the second most common isotope ^{13}C (1.11% natural abundance) consists of 7 neutrons; other isotopes exist but are highly unstable and decay predominantly via beta emission. The ground state electron configuration of carbon is therefore written $1s^2\ 2s^2\ 2p^2$.

Name	Configuration	No. hyb. orbitals	Orbital geometry
Un-hybridised	$\uparrow\downarrow$ $\uparrow\downarrow$ $\uparrow$ $\uparrow$ $\uparrow$ $1s^2$ $2s^2$ $2p_x$ $2p_y$ $2p_z$	0	-
sp	$\uparrow\downarrow$ $\uparrow$ $\uparrow$ $\uparrow$ $\uparrow$ $1s^2$ $2sp$ $2sp$ $2p$ $2p$	2	Linear (180°)
sp^2	$\uparrow\downarrow$ $\uparrow$ $\uparrow$ $\uparrow$ $\uparrow$ $1s^2$ $2sp^2$ $2sp^2$ $2sp^2$ $2p$	3	Trigonal planar (120°)
sp^3	$\uparrow\downarrow$ $\uparrow$ $\uparrow$ $\uparrow$ $\uparrow$ $1s^2$ $2sp^3$ $2sp^3$ $2sp^3$ $2sp^3$	4	Tetrahedral (109°)

Table 2.1: The various hybridisation states of carbon.

This configuration implies a full K-shell that does not contribute to any bonding, along with a full 2s orbital and two half-filled 2p orbitals in the L-shell. In this configuration carbon has two valence electrons available, however divalent carbon bonding is rarely found in nature over the much more stable tetravalent bonding that forms common carbon allotropes and compounds. The increase from two to four valence electrons is the result of orbital hybridisation. This occurs when a 2s electron is promoted into the 2p orbital, modifying the electron arrangement in the L-shell and forming hybrid atomic orbitals [1]. These hybrid orbitals take the form of mixed-wavefunction sp^n hybridisation states, where n = 1, 2 or 3, see table 2.1.

These sp^n states are responsible for the large range of carbon allotropes. The sp (diagonal) state forms a sigma (σ) bond consisting of two 2sp orbitals, which have a linear bond angle of 180° due to mutual electron cloud repulsion. Since there are two further 2p valence electrons, these form delocalised pi (π) bonds. Molecules containing such sp bonds are typically unstable linear chain-like polytypes known as carbynes, and acetylene (C_2H_2). The sp^2 (trigonal) hybridised state forms a much stronger bond. In this case the promoted 2s electron forms three $2sp^2$ orbitals, with

one delocalised 2p electron. The three hybridised orbitals are identical and exist in the same plane – with an orientation that forms sigma bonds at 120° angles. The delocalised 2p electron is oriented orthogonal to the bonding plane and allows pi bonding to occur with other atoms. Hence structures may form in which six carbon atoms bond to form sigma-bonded in-plane hexagonal structures. These are the basis of graphite, graphitic structures such as graphene and carbon nanotubes, and aromatic compounds. The delocalised electron is responsible for the weak attraction between graphite planes, as well as the high-mobility electronic conduction observed in graphene.

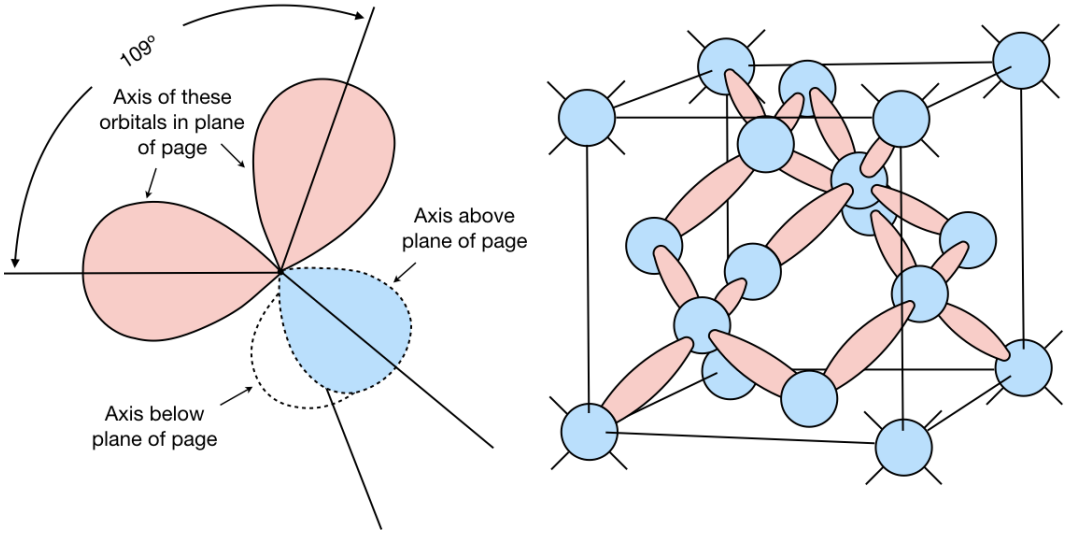

Figure 2.1: Left, tetrahedral hybridisation axes of four sp^3 orbitals; right, diamond crystal (adapted from [1]).

The highest hybrid state (tetragonal) consists of four sp^3 orbitals, with no delocalised p-orbital electrons. The sp^3 electron wavefunctions are asymmetric, and the four orbitals are arranged at equal angles of 109° to form a regular tetrahedral geometry, figure 2.1. These bonds are extremely strong, owing to the fact that four out of the six available electrons are involved in bonding and that the carbon atom is relatively small. As such, a crystal structure consisting of sp^3 bonded carbon maximises mutual nuclear attraction forming an extremely dense ($1.76 \times 10^{23}\,\mathrm{cm}^{-3}$) lattice with an average bond length of 1.54 Å. Figure 2.1 illustrates the crystal lat-

Property	Value
Density	3.52 $g\,cm^{-3}$
Young's Modulus	910 – 1,250 GPa
Vickers hardness	10,000 $kg\,mm^{-2}$
Compression strength	8.68 – 16.53 GPa

Table 2.2: Mechanical properties of diamond (adapted from [1]).

tice for diamond, which possesses extraordinary hardness, incompressibility and stiffness as a result of sp^3 bonding. The unique mechanical properties of diamond are listed in table 2.2. The diamond unit cell is a face-centred-cubic structure with eight carbon atoms arranged tetrahedrally, which can be described by three Miller planes: (100), (110) and (111).

2.2 Diamond synthesis

As described above, carbon can form numerous allotropes depending on its various hybridisation states. Graphite is the energetically more favourable state, although diamond is only 2.87 $kJ\,mol^{-1}$ higher in enthalpy at ambient temperature and pressure – implying that interconversion between the phases may be thermodynamically feasible [2]. However, the large kinetic activation barrier for the conversion from sp^2 to sp^3 demands exceptionally high pressures and temperatures ($>$130 kbar, 3300 K) in order to form stable diamond from graphite at a significant rate, and vice versa for the decomposition of diamond back to graphite. This is evident in the carbon phase diagram, figure 2.2. In nature these specific conditions occur deep within the Earth's crust, causing diamond to crystallise from carbon sources in the rock and be forced rapidly upwards under high pressure by tectonic activity, allowing it to be mined near the surface. These natural diamonds have been cut and traded as gemstones for many centuries, retaining significant financial and sentimental value due to their origin and scarcity. This, along with the extraordinary fundamental proper-

ties and applications of diamond, has motivated great interest in producing diamond synthetically.

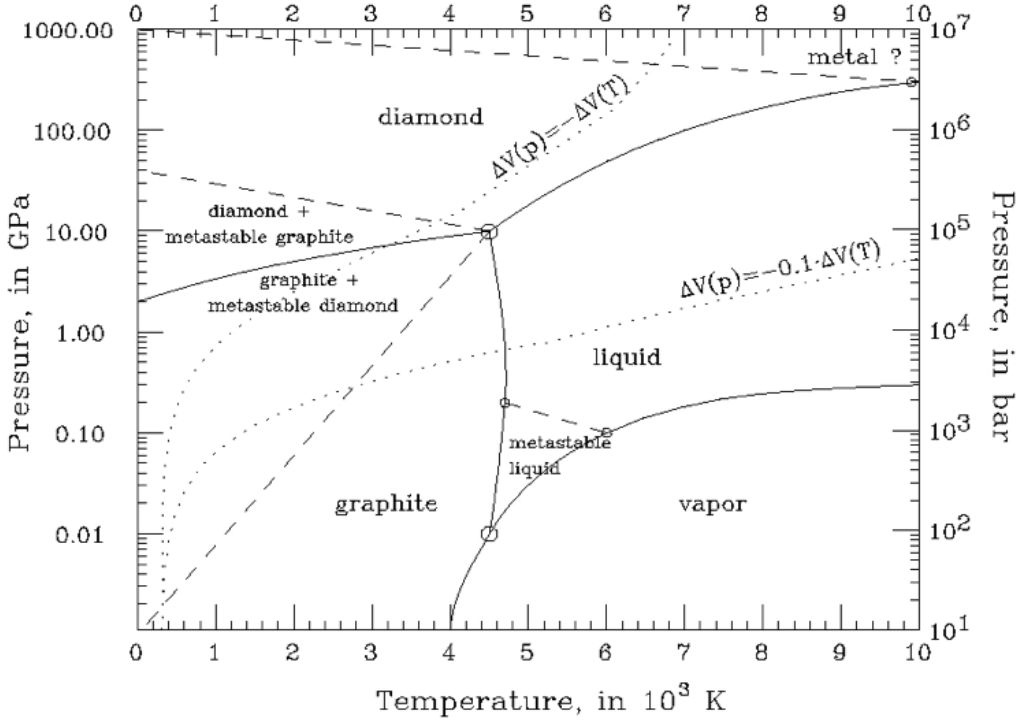

Figure 2.2: The carbon phase diagram [3]. A large kinetic activation barrier for the conversion from sp^2 to sp^3 bonding requires high pressures and temperatures (>130 kbar, 3300 K) to make the transition from graphite to diamond phases at a significant rate.

The most evident method by which diamond might be synthesised is by attempting to replicate the conditions by which natural diamond is formed, namely high pressure high temperature (HPHT) growth. Historically this goal has been pursued since diamond was first proven to be crystalline carbon [4], although it was well over a century until the first successful implementation of HPHT synthesis was achieved. This breakthrough occurred almost concurrently in the early 1950's at General Electric, USA; AESA, Sweden; and at the IHPP in the Soviet Union [5, 6]. The general principle of this HPHT method relies on a solvent-catalyst reaction to provide an alternative lower energy reaction pathway to the large kinetic barrier of direct interconversion. Transition metals (such as iron, cobalt, chromium, nickel, platinum or palladium) are used to dissolve carbon and break the individual atomic

bonds. The metal-solvents then transport the dissolved carbon to the growing surface where diamond is formed under elevated temperature and pressure conditions (55 kbar, 1600 K) using a hydraulic press and electric heating [7].

This method continues to the present day and accounts for the majority of synthetic diamond production annually, however HPHT diamond does still contain a high concentration of lattice impurities such as nitrogen [8] and is therefore unsuitable for many electronic or optical applications of the material. Alternatively, diamond may by synthesised by chemical vapour deposition (CVD) – a technique first reported by William Eversole in 1962 [9] in which diamond was deposited onto a substrate in a metastable low pressure and temperature state from a hydrocarbon gas. This development was followed by intense research efforts, particularly in the Soviet Union, to investigate diamond nucleation and growth mechanisms. Early work depositing onto diamond seed crystals was hampered by low growth rates and the accumulation of unwanted graphite. This ultimately led to a breakthrough in the use of atomic hydrogen to preferentially etch graphitic deposits without affecting the growth of diamond, and was followed by the advancement of electric discharge and hot filament deposition methods that allowed a considerable increase in the concentration of atomic hydrogen [10–12]. In the early 1980's, work at the NIRIM (National Institute for Research in Inorganic Materials) in Tsukuba, Japan resulted in the growth of high quality CVD diamond films at rates of up to 10 $\mu m\,hr^{-1}$ using microwave plasma and hot-filament assisted processes [13–15]. These results marked a watershed moment for CVD diamond research and opened up the field for substantial development of diamond technology to present day.

2.3 Properties of diamond

Diamond can be broadly classified into four types, based upon the nature of the impurities present in the material, table 2.3. Naturally mined diamonds are mostly colourless and contain small clusters of nitrogen impurities within their lattice; far rarer are yellow/brown stones that possess diffuse isolated nitrogen impurities, or

Type	Natural abundance	Impurity/property
Ia	98%	0.1% (1000 ppm) nitrogen in small aggregates Not paramagnetic Pale yellow/colourless
Ib	0.1%	0.05% (500 ppm) nitrogen diffusely distributed Paramagnetic Yellow
IIa	1 - 2%	Very little nitrogen (a few ppm) Colourless
IIb	0.1 %	Very little nitrogen (a few ppm) Contains boron Blue

Table 2.3: Diamond type classification (adapted from [1]).

even small quantities of boron, giving a blue appearance. When considering synthetic diamond, the impurity content is largely controllable, however HPHT synthesis typically produces diamond of the Ib type, whereas CVD is capable of growing high quality IIa diamond that is suitable for sensitive electronic or optical applications.

Further classification of diamond may be made based upon the size and quantity of individual crystal domains within the material. Single crystal diamond (SCD), as the name would suggest, contains only one crystal domain and therefore tends to exhibit the optimal diamond properties. Synthetic techniques can achieve SCD through homoepitaxial growth, usually on an SCD or iridium substrate [16]. Alternatively, several single crystals may coalesce to form a film of polycrystalline diamond (PCD). The properties of PCD are then defined by the size of the individual crystals, 'grain size', and the boundaries between them, 'grain boundaries', which may contain graphitic carbon and degrade the properties of the material. High quality PCD growth is possible, particularly over large areas, and may range from

Property	Value
Thermal conductivity	$21.9\,\mathrm{W\,cm^{-1}\,K^{-1}}$
Thermal expansion coefficient	$1 \times 10^{-6}\,\mathrm{K^{-1}}$ [18]
Hole mobility	$3800\,\mathrm{cm^2\,V^{-1}\,s^{-1}}$ (TOF) $1650\,\mathrm{cm^2\,V^{-1}\,s^{-1}}$ (Hall)
Electron mobility	$4500\,\mathrm{cm^2\,V^{-1}\,s^{-1}}$ (TOF) $660\,\mathrm{cm^2\,V^{-1}\,s^{-1}}$ (Hall)
Band gap	5.47 eV
Breakdown field	10 - 20 $\mathrm{MV\,cm^{-1}}$

Table 2.4: Diamond thermal and electronic properties at room temperature (adapted from [19] unless otherwise referenced). "TOF" – time of flight measurement, "Hall" – Hall effect measurement.

microcrystalline ($>$ 0.1 μm grain size) to nanocrystalline (NCD, 5-100 nm grain size) and even ultrananocrystalline (UNCD, $<$ 5 nm) [17].

Not only does diamond possess superlative mechanical properties, as presented in table 2.2, but the nature of the sp^3 bonding also imparts desirable chemical and electronic properties. The strength and kinetic stability of the bond renders diamond highly chemically inert, radiation hard and resilient to high temperatures; facilitating applications in extreme chemical environments or that require a biocompatible material. Importantly the short lattice constant and tetrahedral bonding creates a dense, non-polar crystal that allows phonons to have a high velocity and long acoustic relaxation time [18]. The effect of this is a very high thermal conductivity, low thermal expansion coefficient and outstanding carrier mobilities [20], [21], table 2.4.

Additionally, the four sp^3 bonds per atom form eight molecular orbitals of which four are higher energy anti-bonding states and four are lower energy bonding states. A large energy difference exists between the bonding and anti-bonding states, giv-

ing diamond a wide band gap of 5.57 eV. This is responsible for the very large breakdown voltage in diamond, useful for high power electronics, and low carrier recombination, useful for low noise sensing and excellent charge collection.

2.4 Doping diamond

The tight carbon bonding and the sp^3 hybridisation state in diamond impart many favourable properties to the material. However, these also deliver fundamental complications when seeking to exploit the extrinsic electronic characteristics of diamond through doping. The meta-stability of diamond limits the temperatures at which it can be heated for vacancy- or interstitial- assisted diffusion doping [22]. This restricts most doping processes to the substitutional inclusion of dopants introduced during growth. The list of atoms, given the short bond length, is therefore limited to dopants with relatively large activation energies. Suitable n-type dopants, such as nitrogen and phosphorus, have activation energies of $\sim$1.7 eV [23] and $\sim$0.46 eV [24], respectively. However, n-type doping in diamond has so far been difficult to achieve. In the case of nitrogen, which is a major impurity in natural diamond, the deep activation energy makes it unfeasible as a conductive electronic material. Some progress has been made to incorporate phosphorus [25–30], which is further complicated due to its large atomic radius and high positive formation energy [31]. However, the properties of these materials are currently not mature enough to make n-type diamond an attractive electronic technology.

Alternatively p-type doping in diamond is, relatively, trivial and widely employed. Boron has an acceptor activation energy of 0.37 eV at low concentrations ([B] $<$ $10^{17}\,\mathrm{cm}^{-3}$) which effectively converges to zero at concentrations [B] $> 10^{20}\,\mathrm{cm}^{-3}$, making it the dopant of choice for many applications [32]. Diamond with boron impurities occur very rarely in nature. Those that do possess a brilliant blue colour, and hence have extremely high value – such as the Hope diamond, reportedly insured for $250 million. As with intrinsic diamond, commercial efforts have been made to synthesise boron-doped diamond for a very large number of attractive electronic

and electrochemical uses.

2.4.1 p-type boron doping during growth

Boron can be introduced into the lattice in a number of ways during diamond growth in order to impart p-type electronic properties to the material. Nishimura et al. [33] have grown boron-doped layers of varying concentrations onto Al_2O_3 substrates by injection of controlled amounts of diborane gas into the MEPCVD reactor. Despite the relatively shallow activation energy for boron, they show that at low doping concentrations only a very small fraction of the boron acceptors are activated; in fact at [B] = $10^{19}\,cm^{-3}$, only 5% of acceptors are active at room temperature. They observe that as [B] is increased beyond this level, full activation can be achieved with the formation of an impurity band that allows conduction between neighbouring acceptors – as first proposed by Collins et. al [34]. Near [B] = $10^{21}\,cm^{-3}$ the activation energy approaches zero, and the heavily doped films behave like degenerate semiconductors. A comprehensive study by Borst and Weiss [23] corroborate these findings on multiple boron layers grown epitaxially on single crystal Ib and IIb diamond substrates using solid B_2O_3 powder and boron wire sources. By examining the conductivity of the samples as a function of temperature they demonstrate two main conduction regimes. At high temperatures valence band conduction is observed, in which the movement of free holes in the valence band is the significant carrier transport mechanism. At room temperature and below, they propose a dominant hopping conduction process – in which carriers can tunnel between nearest ionised and neutral acceptor sites due to the overlap of the impurity wave functions. For those layers with a high enough boron concentration, [B] $\sim 10^{20}\,cm^{-3}$ and above, this overlap is such that it allows them to pass the metal-insulator transition at room temperature and behave metallically.

Lagrange et al. [32] further this work and look to characterise the compensating effect of nitrogen impurities in the diamond, which may act as donors to reduce the hole concentration in the valence band and increase scattering. They observe the

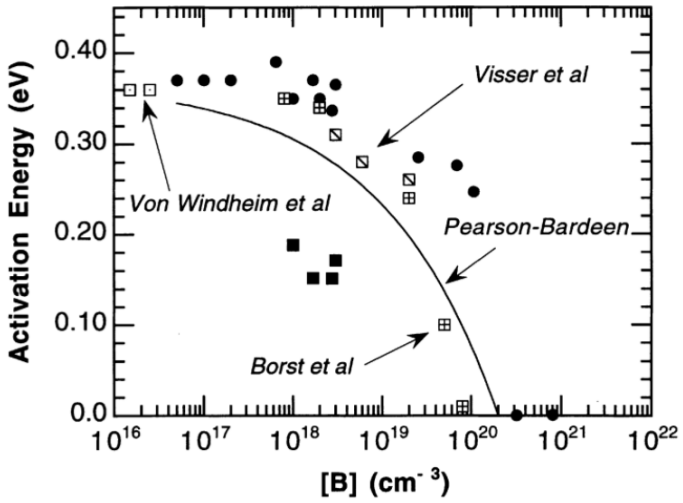

Figure 2.3: A summary of the activation energies as published by various authors as a function of boron concentration; activation energy decreases as boron concentration is increased, from 0.37 eV at low doping concentrations to 0 eV for very heavily doped material [32].

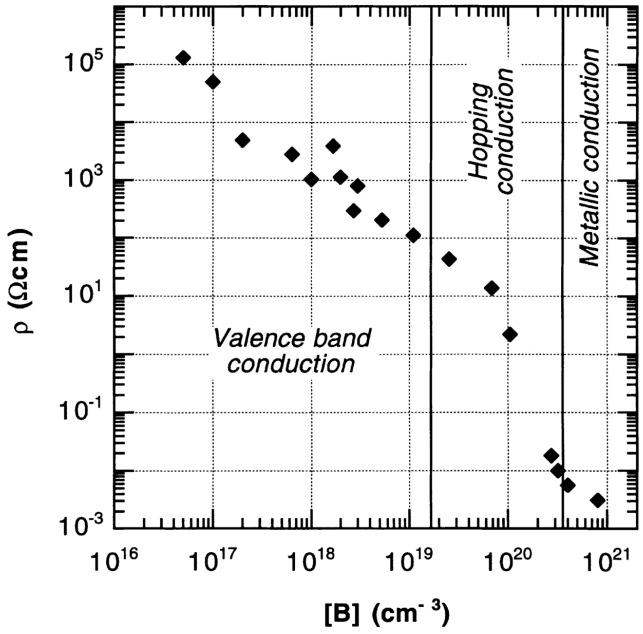

Figure 2.4: The room temperature resistivity as a function of boron concentration; at room temperature the dominant conduction mechanism is in the valence band for low concentrations with a correspondingly high resistivity, followed by a transition to nearest-neighbour hopping at higher concentrations, becoming metallic around [B] = $10^{20}\,\mathrm{cm}^{-3}$ [32].

change in film conductivity with temperature and fit theoretical expressions for a compensated semiconductor in the ionisation regime. It is shown that for low doping levels ([B] $\sim 10^{16}\,\mathrm{cm}^{-3}$), the diamond displays compensated low-conductivity valence band conduction above room temperature (300 – 1000 K), with a compensation ratio $K \equiv N_D/N_A$ (donor concentration: acceptor concentration) greater than 10%. As the dopant concentration is increased, the compensation ratio decreases ($K \sim 2\%$ at [B] = $10^{18}\,\mathrm{cm}^{-3}$) and the higher conductivity hopping conduction regime emerges, to the point where [B] $> 10^{20}\,\mathrm{cm}^{-3}$ the film is metallic at room temperature and hopping conduction dominates even at higher temperatures. Mortet et al. [35] similarly observe no hopping conduction for low [B] samples, at temperatures as low as 150 K; with the transition temperature from hopping to valence band conduction regimes increasing with heavier doping concentrations, as comprehensively studied by Werner et al. [36].

Increased doping to metallic levels is inextricably associated with a corresponding decrease in mobility, figure 2.5. At high [B] the hole mobility is severely reduced as a result of both increased scattering from acceptor impurities, as well as the low-mobility nature of the hopping conduction regime [35]. Highly compensated materials are also subject to lower mobility due to scattering from the greater donor impurity contribution [23], and polycrystalline diamond may additionally suffer transport losses at grain boundaries – although this is an effect which may be more important in lower [B] films [33], [36]. Consequently, Hall effect measurements on highly-doped samples ([B] $\sim 10^{20}\,\mathrm{cm}^{-3}$) show significantly reduced mobilities, as low as $0.28\,\mathrm{cm}^2\,\mathrm{V}^{-1}\,\mathrm{s}^{-1}$ but currently around $830\,\mathrm{cm}^2\,\mathrm{V}^{-1}\,\mathrm{s}^{-1}$ [135].

Low-doped layers ([B] $\sim 10^{16}$ - $10^{17}\,\mathrm{cm}^{-3}$) on the other hand may exhibit Hall mobilities near to or exceeding those measured for natural diamond ($1650\,\mathrm{cm}^2\,\mathrm{V}^{-1}\,\mathrm{s}^{-1}$) by exploiting recent advances in growth processes. Okushi [38] achieves a mobility of $1840\,\mathrm{cm}^2\,\mathrm{V}^{-1}\,\mathrm{s}^{-1}$ using a trimethylborane (TMB) source gas to grow 1.5 - 3 μm diamond films of [B] $\sim 10^{17}\,\mathrm{cm}^{-3}$. It is suggested that the incorporation of impurities, including the deliberate inclusion of boron, is related to a high growth rate and

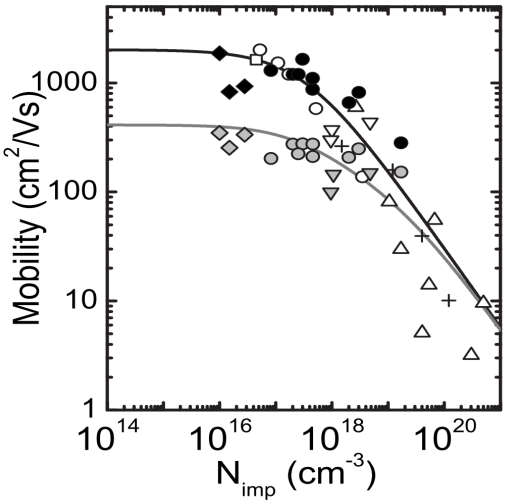

Figure 2.5: A summary of Hall mobility as a function of the number of impurities (sum of donor and acceptor atoms) as published by various authors. Grey markers and line are measured at 500 K, all others at 300 K [37].

hence a large methane concentration [35, 39]. Similarly Teraji et al. [40] show that by using a large CH_4:CH_4+H_2 ratio of 4%, the efficiency of boron incorporation into the diamond lattice is enhanced. They suggest that this is further improved by increasing the plasma power density through the use of a high 4 kW microwave power, at a temperature and pressure of 1000 °C and 120 Torr, respectively. They observe hole concentrations and resistivities superior by an order-of-magnitude to previous work. Volpe et al. [37] additionally show that the presence of oxygen in the gas phase during diamond growth may decrease the boron content of the film, but subsequently achieve a high mobility of $1870\,\mathrm{cm^2\,V^{-1}\,s^{-1}}$, despite very high donor compensation. For low doped samples mobility is seen to fall as $\mu \sim T^{-3.5}$ at higher temperatures due to greater acoustic and optical phonon scattering [35,41], although this may be somewhat suppressed by using a high microwave power density [40].

Author (Year)	[B] [cm^{-3}]	μ_p [$cm^2 V^{-1} s^{-1}$]	[p] [cm^{-3}]	K [%]	E_A [eV]
Nishimura et al. (1991) [33]	7×10^{19}	~ 0.60	3×10^{18}	-	~ 0.14
	2×10^{20}	0.28	$\sim 3 \times 10^{20}$	-	~ 0.05
Borst and Weiss (1996) [23]	7×10^{17}	255	$\sim 3 \times 10^{16}$	37	0.37
	3×10^{20}	~ 3.2	$\sim 2 \times 10^{20}$	-	~ 0.00
Lagrange et al. (1998) [32]	$\sim 10^{16}$	-	-	~ 10	0.37
	$\sim 10^{18}$	-	-	~ 2	~ 0.18
Okushi (2001) [38]	$\sim 10^{17}$	1840	2×10^{14}	0.4	-
Teraji et al. (2006) [40]	6×10^{16} †	1620	3×10^{16}	1.1	0.36
	1×10^{20} †	830	3×10^{18}	1.3	0.29
Mortet et al. (2008) [35]	-	2016	5.2×10^{13}	-	0.32
	-	1529	1.1×10^{14}	-	0.34
	-	138	3.5×10^{15}	-	0.21
Volpe et al. (2009) [37]	1×10^{16}	1870	-	31	-

Table 2.5: A summary of the electronic properties of various CVD boron-doped diamond layers; hole mobility μ_p, hole concentration [p], compensation fraction K, activation energy E_A – all as derived by Hall effect measurements. Boron acceptor concentration [B] as estimated by SIMS, († estimated by Hall measurements).

Table 2.5 summarises the efforts to improve the hole mobility in CVD grown boron-doped diamond layers at the extremes of doping concentration; with all values derived from Hall effect measurements made at room temperature, 290 - 300 K.

2.4.2 p-type hydrogen surface conductivity

P-type conductivity may also be induced without the use of atomic doping in the diamond lattice. This p-type behaviour is a highly conductive phenomenon observed with a hydrogen surface termination, as first reported by Landstrass and Ravi in 1989 [42]. The occurrence can be described by the surface transfer doping model, in which an electron is transferred from the diamond semiconductor to a 'dopant' on the surface [43]. The charge transfer occurs as a result of a misalignment of the Fermi levels at the interface; when the diamond surface is brought into contact with an electrolytic adsorbate this potential difference drives electrons from the diamond valence band to the empty electronic acceptor levels of the adsorbate species. The surface adsorbates attain a negative charge, and the diamond compensates by accumulating holes in the valence band. Since diamond is highly resistant to corrosion, it does not experience oxidative dissolution and an equilibrium is reached whereby there exists a subsurface conductive hole channel [44]. This effect is only observed on hydrogenated diamond and disappears when the surface is dehydrogenated or oxidised, since redox couples in the adsorbed atmospheric water layer provide the necessary surface acceptor levels to facilitate transfer doping with the hydrogen surface. However, it does not present itself as a reliable and consistent means of doping diamond for many electronic applications, due to the delicate stability of the C-H bond and adsorbate layer which does not generally persist for long-term use.

2.5 Metal contacts on diamond

In addition to the growth of high mobility doped films, the second fundamental component to the fabrication of successful diamond devices is the metallisation of the surface to form electronic contacts. Ideally, these contacts need to adhere strongly

to the semiconductor surface and be resilient to high temperatures; they need to be compatible with existing processing techniques and allow robust connection with wire-bonds; and most importantly – depending on the nature of the device – they need to have a low contact resistance and exhibit either ohmic or rectifying electronic properties. However, making good electronic contact to semiconductors is a challenging problem and the subject of prolonged debate within the wider scientific community. The challenge is only amplified when making contacts to a material such as diamond, which falls foul of its extraordinary band gap to form large potential barriers at the interface with metals. Not only this, but diamond can also have a high surface state density that effectively pins the Fermi level away from the band edges. In spite of these difficulties there exists a wealth of well-documented techniques for making high-quality electronic contacts to diamond and, consequently, when evaluating the quality of these contacts it is useful to define a figure of merit known as the specific contact resistance, ρ_C [$\Omega\,\mathrm{cm}^2$].

The behaviour of the metal-diamond interface, and hence the magnitude of the specific contact resistance on diamond, is affected by many factors [45]. It is widely known that the presence of hydrogen at the diamond surface induces an alternative low-resistance conduction path due to a transfer-doping phenomenon [42]. Grot et al. [46] show that this termination effectively makes the measured contact resistance independent of boron doping concentration. Low-resistance ohmic conduction is observed with Au contacts deposited on both intrinsic, and boron-doped layers, which have been exposed to hydrogen plasma. Similar experiments with Al contacts demonstrate rectifying behaviour, suggesting that the nature of the metal-diamond interface is influenced by the electronegativity of the metal contacting the hydrogenated surface. Kawaguchi et al. [47] propose that ohmic properties and a lower contact resistance can be expected for highly electronegative metals such as Au and Pt; whereas metals with low electronegativity such as Al and Ti form resistive rectifying contacts. These results are corroborated by Mori et al. [48], who go on to show that the ohmic properties are invariably lost upon oxidation of the surface to remove the hydrogen termination. With an oxidised surface, the contacts

become rectifying regardless of the metal electronegativity, and the Schottky barrier height at the interface is independent of metal work function. They suggest that the pinning of the Fermi level due to the high surface state density induced by oxidation is likely responsible. As such, it is evident that the surface termination of the diamond is a key consideration when making metal contacts to diamond. The role of hydrogen termination is reviewed extensively by Kawarada [49], however due to the notoriously poor stability of the hydrogen surface, oxidisation is typically required for the manufacture of resilient and reliable devices.

It is therefore desirable to achieve ohmicity and a low specific contact resistance by depositing metals that are capable of forming carbides when subjected to a thermal anneal. This is a widely studied phenomenon [47, 50–59], in which annealing is observed to decrease the contact resistance by several orders of magnitude when compared to the as-deposited metals. Additionally, the I-V properties of the contacts show a distinct transition from rectifying to ohmic behaviour. Carbide forming metals commonly used include Ti [18,25,28,30,31] but other transition metals such as Cd, Cr, Pd, Co, V and Ta exhibit similar characteristics [51, 54, 55]. Often these are deposited with overlayers of Au or Au/Pt to improve mechanical resilience, allow wire bond contacting and to reduce diffusion into the contact. Temperatures between 400 - 500 °C [53–57] are shown to be required for carbide formation. For lower annealing temperatures, treatment durations greater than 60 min produce better contact resistances [53], although at temperatures up to 950 °C [51, 59] as little as 5 - 8 min is sufficient, with possible degradation of the contact observed for longer durations [51, 57]. Annealing can be carried out in an inert Ar atmosphere [50] or under vacuum to avoid modifying the surface.

The formation of the carbide phase has been analysed extensively by the use of x-ray diffraction (XRD) [47, 50], x-ray photoelectron spectroscopy (XPS) [57], and auger electron spectroscopy (AES) [51] surface techniques, as well as cross-sectional transmission electron microscopy (XTEM) [47, 54] for microstructural analysis. Tachibana et al. [57, 58] suggest that the carbide formation causes an in-

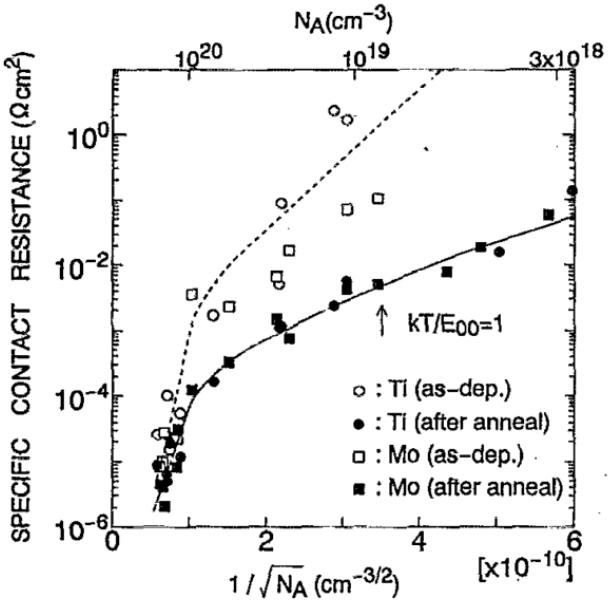

Figure 2.6: Specific contact resistance (ρ_C) as a function of boron acceptor concentration (N_A). It can be observed that ρ_C is several orders of magnitude greater at low doping levels. Annealing at 500 °C is shown to reduce the contact resistance (black points) [53].

crease in the crystal defect density at the metal-diamond interface, which either reduces the effective Schottky barrier height or decreases the size of the space charge region, explaining the ohmic properties after annealing. Yokoba et al. [54, 55] propose a different model: they observe a reduction in the Schottky barrier height from approximately 1.3 eV to 0.5 eV as a result of annealing Ti, Mo, Cr, Pd and Co contacts on boron-doped diamond. They suggest that the carbide formation destroys the atomic bonds near the metal interface, creating a metallic graphite layer. The transition from metastable sp^3 to stable sp^2 bonding during annealing pins the barrier height at the diamond-graphite interface and allows the carriers to tunnel through the space charge region.

In general semiconductor theory [60] the current density flowing between a metal and semiconductor is a mathematical function of three quantities. The first is the Schottky barrier height. As the studies discussed above have shown, when the diamond surface is oxidised the Fermi level is pinned and the height of the Schottky

barrier, approximately 1.1 to 1.3 eV, becomes independent of the metal work function. Upon annealing, the effective barrier height can be reduced to about 0.5 eV by the formation of a carbide if a suitable transition metal is chosen. The current flow through this reduced barrier is then determined by two further components – the doping concentration and the temperature, which in combination determine the dominant charge transport mechanisms between the metal and semiconductor, and hence the specific contact resistance. At low doping concentrations, the space charge region is large but a small number of charge carriers have sufficient thermal energy to pass over the potential barrier maximum. This process is known as thermionic emission (TE) and the contact resistance is exponentially dependent on the temperature $\rho_C \propto \exp^{1/T}$. At higher doping concentrations the depletion region is narrowed such that carrier transport is dominated by quantum tunnelling. This mechanism, known as field emission (FE), is essentially independent of temperature but varies with acceptor concentration (N_A) as $\rho_C \propto \exp^{1/\sqrt{N_A}}$. For doping concentrations between these two extremes, the tunnelling process may be thermally assisted – termed thermionic-field emission (TFE).

These transport regimes have been well demonstrated in silicon, such as by Carver et al. [61]. In diamond, Nakanishi et al. [53] measure the specific contact resistance for layers between [B] = 3×10^{18} - $3 \times 10^{20}\,\mathrm{cm}^{-3}$, figure 2.6. They observe contact resistances as low as $\rho_C \sim 10^{-6}\,\Omega\mathrm{cm}^2$ for heavily boron doped layers, corresponding to the FE regime. The measured resistances increase by several orders of magnitude for lower boron concentrations ($\rho_C \sim 10^{-2}\,\Omega\mathrm{cm}^2$ for [B] = $3 \times 10^{18}\,\mathrm{cm}^{-3}$), which they suggest is the result of TFE. This is supported by Yokoba et al. [54] who show contact resistance is strongly temperature-dependent for low doped samples.

Chapter 3

Diamond neutron detectors

3.1 Motivation

It may be surprising to discover that the global market for neutron detectors is expected to reach $1 billion in the next four years [62]. The demand for neutron detectors is not immediately obvious, but it spans several applications that are of global importance and require devices that offer excellent performance [63]. One of the largest consumers of neutron detection hardware is the nuclear power industry. Neutron flux is directly proportional to reactor power, meaning that it is a key benchmark in both civil nuclear power generators, as well as those used in military applications such as on naval vessels. The secondary requirement in these scenarios, as well as others where a high neutron flux is encountered, is to ensure the radiation safety of personnel. The detection of neutrons is also vital to the control of nuclear weapons and illegal materials, and is employed extensively under national security measures. In addition to this, there are numerous scientific research needs within medical radiotherapy, nuclear fusion, materials characterisation, particle physics and cosmic ray detection.

Conceptually, if the 'ideal' neutron detector could be developed for these applications it would have a broad range of desirable properties. If required, it should be sensitive to very energetic neutrons, such as the 'fast neutrons' directly produced

by nuclear fission – with energies greater than 1 MeV. Alternatively at the other end of the spectrum it should also be sensitive to the slower, 'thermal' neutrons arising from interactions in a moderating medium, with energies around 0.025 eV – approximately in thermal equilibrium with their surroundings ($E = kT$). The detector should be able to detect the entire neutron flux incident upon its active area and convert this into a meaningful count rate. The ratio of incident to detected neutrons can be termed its 'total efficiency', and the shape and size of the active area stipulate a limiting geometric efficiency component to the overall performance of the detector. The ability to convert the neutron flux into a meaningful count rate is synonymous with the ability to discriminate between the energy pulses produced by neutrons and those produced by unwanted background radiation. Such background radiation most commonly presents itself in the form of a high gamma flux – particularly in the vicinity of nuclear reactors – and as such the ideal neutron detector would need to be 'blind' to gamma radiation. Further, the detector should be built entirely of non-fissile materials to avoid an additional background component from secondary reactions within the detector volume itself.

Practically the ideal detector needs to be compact and robust to fit its application. Detection mechanisms that rely on gas ionisation or scintillation are unfeasible in many typical operational environments [64] [†] – which, in effect, limits the operating principle of an ideal detector to the solid-state using semiconductor devices. The act of detection using semiconductors invariably involves the transduction of particle energy into charge carriers that can then be measured by sensitive amplification and pulse-counting electronics. In the electronic regime, therefore, the ideal detector must avoid signal noise produced by leakage currents and charge trapping. Speed is also crucial in that the charge carriers produced must have sufficient mobility to be separated and collected, and to be counted as a single pulse instance. A downside to conventional semiconductor electronics is an inherent vulnerability to challenging environments, in which a high neutron flux is often accompanied by other highly

[†]There is also a pressing shortage of ^{3}He for use in gas proportional detectors that is driving uptake of solid state solutions [65, 66].

Property	Description
Sensitive	Sensitive to desired neutron energy (or energy range)
Efficient	High capture and geometric efficiency
Discriminative	Gamma blind
	Free of fissile materials
	Low electronic noise
	Fast response time
Robust	Radiation hard
	Resilient to high temperatures
	Compact

Table 3.1: The properties of an ideal neutron detector.

ionising radiation and extreme temperatures. The ideal neutron detector therefore demands resilience to high temperatures, hardness to radiation to avoid degradation of the detector and a prolonged lifetime in these environments.

It is here that diamond presents itself as a material of considerable interest. Not only does it facilitate solid state detection, but it also has a high breakdown voltage, so may be exposed to large external potentials and results in low electronic noise. The ionisation energy of diamond is approximately 13.1 eV [67] meaning that it has a low charge yield. However, the relatively high mobilities of the charge carriers facilitates large charge collection efficiencies, a rapid response time and excellent particle discrimination [68]. Alongside its electronic properties, the physical properties of diamond lend themselves extremely well to the challenging application-specific operation requirements. The stability of the sp^3 bond in diamond means that it is both radiation-hard and temperature resilient. These metrics align closely with many of the properties of an ideal neutron detector listed in table 3.1, leading to a concerted research effort over many years devoted to advancing the development of solid-state diamond neutron detectors.

3.2 Detection mechanisms

As a general principle neutron detectors must function as efficient energy transducers. Detection of neutrons directly is not practical as their inherent particle properties – charge, mass, momentum, electric and magnetic dipole or spin – either fall far below the threshold of present measurement capabilities or do not cause quantifiable interactions at all [69]. Further, the mean lifetime of an unstable neutron is too long (approximately 885 sec) to provide useful detection through decay products [70]. Instead detection must occur by exploiting primary, secondary, or even higher-order neutron interaction products.

Since neutrons are charge neutral, electromagnetic interactions with atoms are non-existent and therefore do not provide a detectable primary interaction, such as through atomic ionisation. Instead primary neutron events are the result of strong-force interactions with atomic nuclei, which can be broadly classified into scattering events and absorption events. The former involves a neutron-nuclear interaction where the net result is the emission of a single neutron – either scattering elastically, whereby the total kinetic energy of the system (neutron and nucleus) is unchanged but the neutron may lose some energy to the nucleus causing it to recoil; or inelastically in which the total kinetic energy of the system is changed and the nucleus is left in an excited state. Absorption events involve the capture of the incoming neutron by the target nucleus to form a typically unstable compound nucleus, which may then decay by multiple pathways to produce products such as gamma rays, alpha particles or protons, neutral or charged fission fragments, or more neutrons [71]. These strong interactions are summarised in table 3.2.

It is useful to define a quantity known as the interaction cross-section, expressed in units of barns (1 barn = 10^{-24} cm^{-2}), which describes the probability of a given interaction between an incident neutron and nucleus; or analogously the effective area presented by the target nucleus to the neutron. This is dependent on multiple factors including the neutron energy, the type of target nucleus, the reaction type and the temperature of the target material. The strong dependence of interaction cross-

Interaction	Cross-section	Reaction Type	Reactive Particles
Scattering	σ_s	Elastic	(n,n)
		Inelastic	(n,n')
Absorption	σ_a	Radiative capture	(n,γ)
		Charged capture	(n,p),(n,α), etc.
		Neutron multiplication	(n,xn)
		Fission	(n,f)

Table 3.2: Strong-force neutron interactions with atomic nuclei. These may be classified into scattering events where the net result is a single neutron (with or without kinetic energy transfer), or absorption events resulting in an unstable nucleus which typically decays into other products.

section on neutron energy is shown for (a) ^{239}Pu, figure 3.1; (b) ^{1}H, figure 3.2; and (c) isotopes ^{11}B and ^{10}B, figure 3.3. It is possible to distinguish three distinct regimes. In the low energy region, encompassing the energies of thermal neutrons, the interaction cross-section decreases as velocity of the neutron increases, obeying the approximate reciprocal relationship $\sigma \propto 1/v$. For heavier target nuclei, such as ^{239}Pu, there is a distinct 'resonance region' for medium energy neutrons in which significant peaks in cross-section occur at energies where the neutron energy corresponds to a discrete quantum state in the target nucleus. Beyond this, in the 'fast neutron region' the cross-section drops off significantly and the interaction probability is very low.

For the majority of nuclides, the total cross-section is dominated by absorption and inelastic scattering effects. Elastic scattering is greatly sensitive to atomic mass and the average energy loss in a collision is proportional to,

$$\frac{2E_nA}{(A+1)^2} \tag{3.1}$$

where E_n is the kinetic energy of the neutron and A is the atomic mass of the target. Hence for heavy nuclides the energy loss is insignificant, but for very light nuclei –

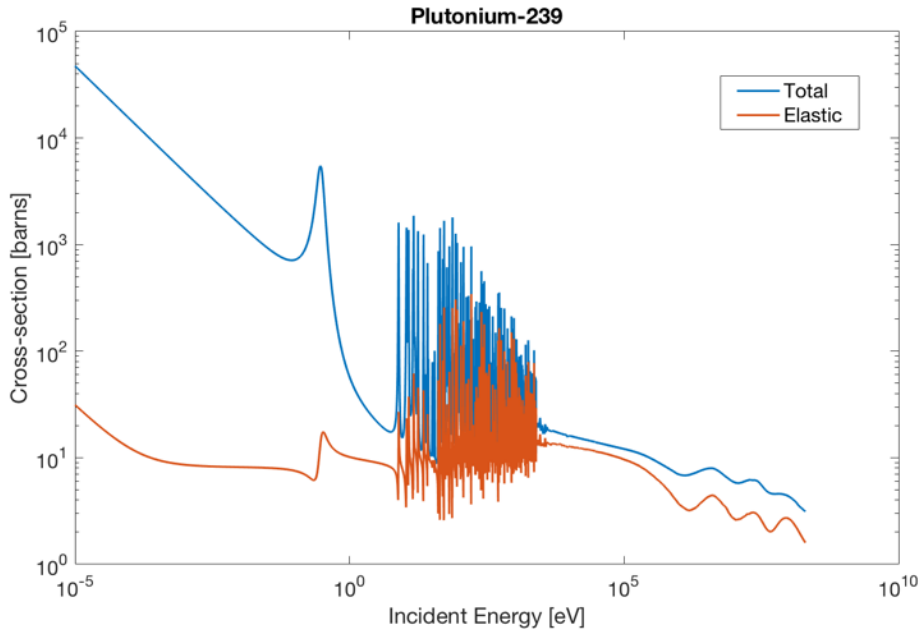

Figure 3.1: The total (blue), and elastic (red) interaction cross-sections for ^{239}Pu plotted as a function of incident neutron energy. Data: Janis 4.0, IRDFF-1.05 [72].

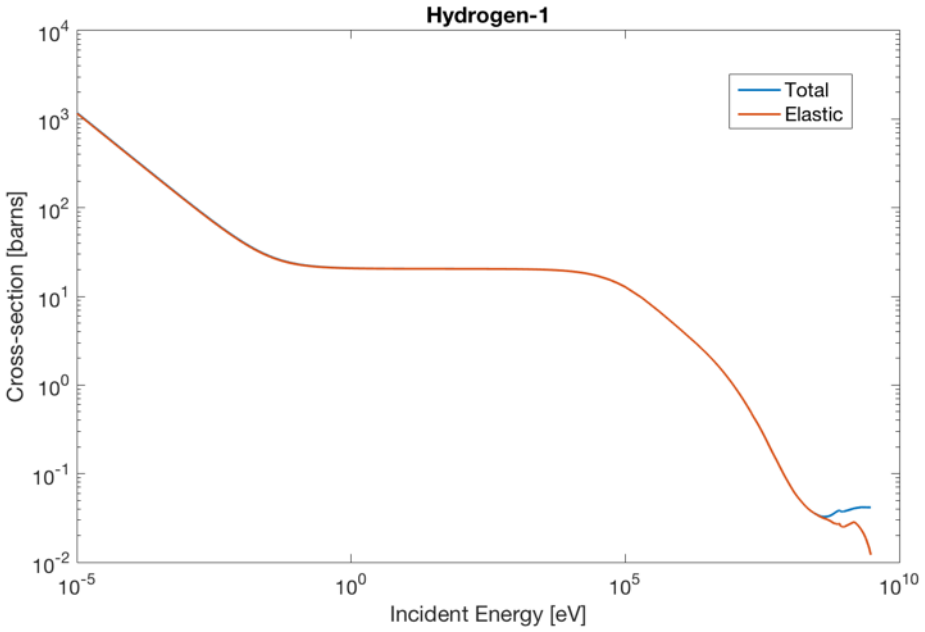

Figure 3.2: The total (blue), and elastic (red) interaction cross-sections for ^{1}H plotted as a function of incident neutron energy. Data: Janis 4.0, JENDL:HE-2007 [72].

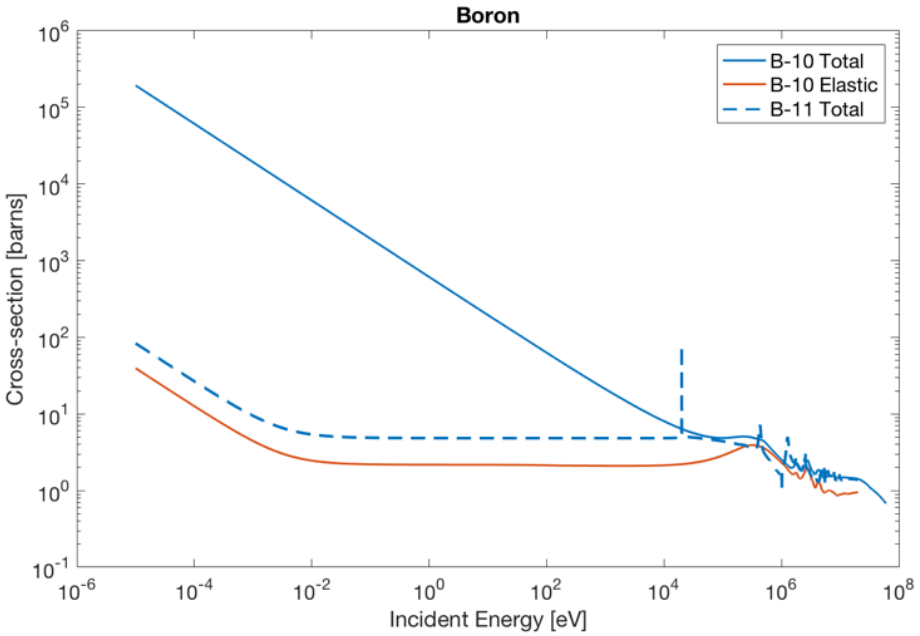

Figure 3.3: The total (blue), and elastic (red), interaction cross-sections for ^{10}B; and total (blue dotted) cross-section for ^{11}B plotted as a function of incident neutron energy. Data: Janis 4.0, JEFF-3.2 [72].

almost exclusively hydrogen isotopes and helium – elastic scattering is a dominant process and can be responsible for the majority of neutron interactions. The elastic scattering data in figures 3.1 to 3.3 highlights this relationship, whereby the inelastic and absorption cross-section components are several orders of magnitude larger than the elastic cross-section for ^{239}Pu and ^{10}B, but negligible in the case of ^{1}H.

This energy relationship has important consequences for neutron detection when considering neutron-nuclide interaction events. If one is to exploit elastic scattering for detection, attaining a useful interaction rate demands the use of a light material such as hydrogen with a (relatively) large elastic scattering cross-section. Elastic scattering interactions do not produce any reaction products but do impart energy to the recoiling nucleus. The amount of energy transferred is greater for higher energy neutrons, especially when collisions are head-on; and if the induced recoil is sufficient, can cause ionisation of the surrounding material. There are a number of detectors that function by this means, which in particular allows for the detection

of fast neutrons where they may otherwise be difficult to detect as a consequence of their poor cross-sections in heavy targets. The additional, significant, upshot of the large fast-neutron scattering cross-section in light target materials is that it allows for the slowing, or moderation, of these neutrons to lower energies through their energy loss in nuclear collisions. Slowing a fast 2 MeV neutron to thermal energies takes approximately 27 collisions in hydrogen as opposed to many thousands in heavier materials [71]. Moderation is not only crucial for maintaining a chain fission reaction in nuclear power generation, but also provides an alternative pathway for the detection of fast neutrons. That is – the thermalisation of fast neutrons in a moderator increases their absorbative cross-section to allow secondary detection by other, more efficient, mechanisms.

3.3 Neutron detection in the solid-state

By elimination, the above considerations lead to the search for viable detection routes by exploiting thermal neutron absorption processes. The most advantageous of the primary absorption products are charged particles that allow detection by secondary ionising energy loss (IEL) reactions. The charged particles may include fast electrons, protons, alpha particles or heavy ions of moderate energy as described in table 3.2, which interact with a medium to generate electron-hole pairs that can be separated by an electric field and collected as a measurable current. Suitable candidate materials for this purpose must therefore have a number of properties. Crucially, to maximise the rate of interaction they must possess a large neutron absorption cross-section in the thermal energy range. The absorption event must also produce useful charged products with an energy and ionising range that allow sufficient charge carrier generation. A number of materials that have particularly large neutron cross-sections are presented in table 3.3.

Boron is a common candidate material, used often for its neutron absorptive properties in reactor control rods, as boron carbide, or in cooling water, as boric acid. In its natural state boron is composed of approximately 19.8% ^{10}B, 80.2% ^{11}B. Fig-

Target Isotope	σ_a (for $n_{thermal}$)	**Reaction Products** (most probable)
^{3}He	5,350	^{1}H, ^{3}H
^{6}Li	925	^{3}H, ^{4}He
^{10}B	3,830	^{7}Li, ^{4}He
^{113}Cd	20,820	γ
^{157}Gd	250,000	γ, β
^{235}U	585	Fission, various

Table 3.3: Typical neutron absorption materials and their reaction products

ure 3.3 highlights the sizeable disparity in cross-section between the two isotopes; where ^{11}B is several orders of magnitude less neutron sensitive. As such, boron can be enriched to obtain near purity in ^{10}B and consequently a very high absorption cross-section. Upon capture of an incident thermal neutron one of the following reactions occurs,

$$^{10}_{5}\mathrm{B} + ^{1}_{0}\mathrm{n} \longrightarrow ^{4}_{2}\mathrm{He}\ (1.47\ \mathrm{MeV}) + ^{7}_{3}\mathrm{Li}\ (0.84\ \mathrm{MeV}) + \gamma\ (0.48\ \mathrm{MeV}) \tag{3.2}$$

$$^{10}_{5}\mathrm{B} + ^{1}_{0}\mathrm{n} \longrightarrow ^{4}_{2}\mathrm{He}\ (1.78\ \mathrm{MeV}) + ^{7}_{3}\mathrm{Li}\ (1.02\ \mathrm{MeV}) \tag{3.3}$$

with a probability of 94% and 6%, respectively. Similarly, lithium may be enriched to enhance neutron capture by ^{6}Li and undergoes the following reaction,

$$^{6}_{3}\mathrm{Li} + ^{1}_{0}\mathrm{n} \longrightarrow ^{3}_{1}\mathrm{H}\ (2.73\ \mathrm{MeV}) + ^{4}_{2}\mathrm{He}\ (2.07\ \mathrm{MeV}) \tag{3.4}$$

At these energies, the emitted charged particles can generate sufficient ionisation for detection, given a suitable collection device structure. Many current and widely deployed detectors rely on these primary neutron reactions for detection.

Solid-state electronics, as in many areas of modern technology, offers compact and reliable solutions that make an attractive choice for neutron detection [73]. Interac-

tions such as those that occur for ^{10}B or ^{6}Li can be exploited by the ready availability of semiconductor devices that are capable of generating and separating charge carriers. Assuming, briefly, that the reaction products of these interactions produce sufficient electron-hole pair generation in a device, there are a number of ways in which these charge carriers can be efficiently collected. Most solid state devices rely on a heterostructure geometry, whereby the charges may be separated using an applied electric field across a resistive dielectric; or separated by an internal electric field produced by a p-n or Schottky junction, figure 3.4.

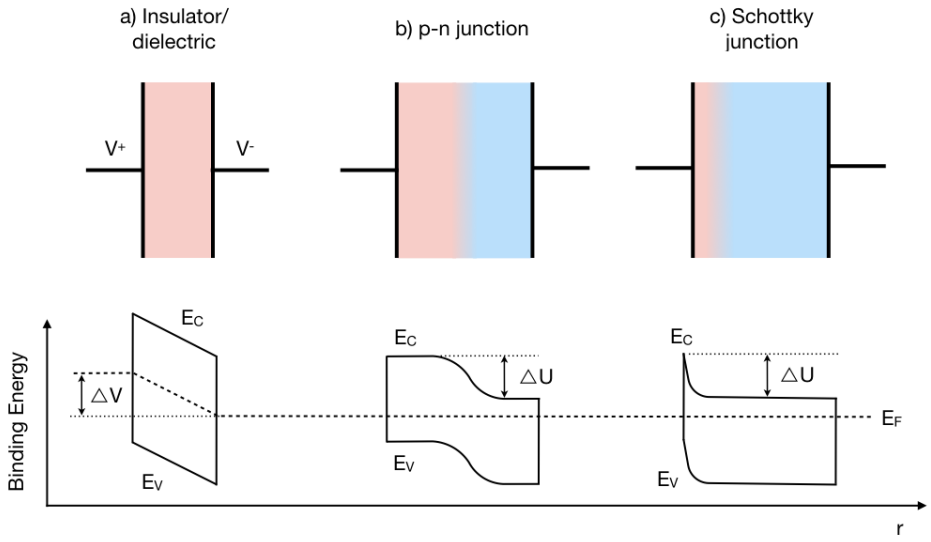

Figure 3.4: Various heterostructure geometries for charge separation (a) resistive material with an external electric field applied by metal electrodes; (b) p–n junction and (c) Schottky junction using an internal electric field generated by the space charge region. E_F is the Fermi level, and E_C and E_V are the conduction and valence band edges, respectively (adapted from [69]).

The simplest mode of neutron detection using these structures is through the 'indirect conversion' device. This involves placing a neutron-sensitive 'conversion layer', such as one containing predominantly ^{10}B, adjacent to the heterostructure. A number of charged primary reaction products are emitted into the semiconductor volume generating charge carriers by IEL interactions, which are then separated by the internal or an applied external electric field and collected at the metal electrodes. The isotropic emission of the charged reaction products contributes to the major

shortcoming of this approach, in that a significant fraction of interactive particles are lost without depositing any energy in the charge collection volume. Those that do enter, will have suffered IEL in the conversion layer that cannot be counted and will deposit less energy to be collected. The total efficiency of indirect conversion devices is consequently impacted.

To avoid this an additional element of complexity can be introduced to the detection scheme. That is, to select materials that have a high neutron absorption cross-section, produce suitable primary interaction products with sufficient energy, *and* have electronic properties to allow an efficient solid-state charge collection device to be designed. These are known as 'direct conversion' detectors, and facilitate high detection efficiencies through neutron absorption, conversion, charge generation and separation occurring in the same layer. The evident disadvantage to these devices is the scarcity in number, scientific understanding and processing techniques for such materials.

3.4 Diamond neutron detectors

In addition to its near-ideal detector properties, the advancement in CVD growth of high quality thin-films has allowed diamond to emerge as a promising solid-state solution for the detection of neutrons; as well as the detection of UV and extreme UV [74–80], X-rays and gamma rays [81–92], alpha particles [93–111], and numerous applications in wider particle physics [112–121].

Fast neutrons can be detected directly in intrinsic diamond by the charged capture reaction ${}^{12}_{6}\mathrm{C}(n,\alpha){}^{9}_{4}\mathrm{Be}$. In practise, neutron energies of the order of 1 - 2 MeV undergo mostly elastic scattering in the diamond layer. The energy imparted to the recoiling carbon nucleus is typically one twelfth of the incident neutron energy, therefore the number of electron-hole pairs generated at an ionisation energy of 13.6 eV is far too small for present counting methods [122]. However at larger neutron energies of up to 14 MeV, this reaction can be detected [123–128]. Schmid et

al. [129] show that a signal can be measured in thin intrinsic SCD membranes 0.5 mm thick, where a 100 V bias is applied across ohmic contacts. Peaks of energy resolution as fine as 2.9% are attributed to a combination of elastic and inelastic neutron scattering, along with ionisation caused by the charged capture products themselves. Diamond fast neutron detectors have been used to monitor fusion plasmas, for example at ITER [130, 131], JET [132–135], or OMEGA [136], where the priorities are 'time of flight' (TOF) and spectroscopic measurements. In these applications they may also be pixellated to achieve spatial resolution [132, 133]. Rebai et al. [137] use uranium foil in conjunction with the diamond to increase the conversion of fast neutrons through further charged capture reactions. Others leverage the extreme properties of diamond to operate at temperatures up to 300 °C [138], for applications such as oil well logging [139].

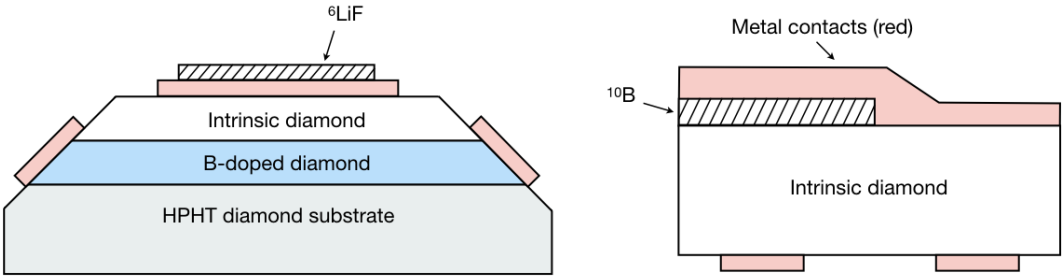

Figure 3.5: Diamond conversion-layer type detector – left, with a lithium fluoride converter layer (adapted from [140]); right, with a boron converter layer (adapted from [122]).

On the other hand, it is usually more pertinent to monitor lower energy thermal neutrons. Using diamond, indirect conversion devices for the detection of these neutron energies can be realised by the use of lithium- or boron- containing conversion layers that undergo ${}^{6}_{3}\mathrm{Li}(n,\alpha){}^{3}_{1}\mathrm{H}$ and ${}^{10}_{5}\mathrm{B}(n,\alpha){}^{7}_{3}\mathrm{Li}$ reactions, respectively. (Inevitably, these detectors also function to a certain extent as fast neutron detectors by the ${}^{12}_{6}\mathrm{C}(n,\alpha){}^{9}_{4}\mathrm{Be}$ reaction directly in the diamond). Almaviva et al. [140] present a device consisting of a boron doped diamond layer electrode, a 25 µm thick intrinsic detection volume and a 100 nm Al upper contact, figure 3.5, left. A 95% ^{6}Li enriched LiF conversion layer is deposited on the detector, which is then biased at

5 V μm^{-1} under thermal neutron irradiation. Similar studies have also been conducted using LiF layers [141–144]; indeed, this type of device has been tested at JET [145, 146]. Some detector geometries use a 'sandwiched' dual-detector configuration [143, 147, 148] in order to capture a greater solid angle of charged products. Mer et al. [122] deposit an enriched ^{10}B conversion layer onto an intrinsic diamond membrane with Au top and bottom contacts, figure 3.5, right. Intrinsic diamond acts as an effective charge generation and separation layer for the resulting conversion products and produces energy resolutions as low as 0.4%. Conversion layer thicknesses are considered to be optimal within the range of a few μm, where the anticipated increase in interaction cross section gained by using a thicker layer is strongly offset by the lower probability of the conversion products leaving the conversion region. Work by Weiss et al. [149] at the neutron time of flight (nTOF) facility at CERN use a polycrystalline diamond detector and an enriched boron carbide (B_4C) converter material separated by a 1 mm air gap. An efficiency of only 3% is reported, which they suggest may be improved through the use of a thinner, high quality single crystal material, along with an evacuated gap between the converter and detector. However fundamental limitations on efficiency still exist due to the loss in the conversion layer itself and more recent studies have failed to improve on this value [150].

Chapter 4

Diamond water quality sensors

4.1 Motivation

Monitoring the quality of water is crucial for a vast range of applications. In regional and national water distribution systems there are concerns about contamination of drinking water by cross-connection with non-potable water, leaking pipes or microbial growth. Additionally, this vital infrastructure is particularly vulnerable to malicious attack due to the nature of the piping systems and lack of surveillance [151]. Equally, the monitoring of rivers, lakes and seawater is vital from an environmental standpoint, with a desire to control pollutant levels and observe factors such as algal blooms in natural habitats.

Fluid environments are also ubiquitous across modern industry [152–154] and require frequent and accurate monitoring to take place. This might be to ensure the safety and effectiveness of solutions in chemical processing; quality control in food and beverage manufacture; meeting legal standards at waste-water treatment plants; improving the environmental footprint of mining and metals manufacturing; reduce unplanned downtime at oil refineries; or to aid exploration in upstream oil and gas.

Significantly, water is also used in nuclear reactors; where the majority of nuclear power generation uses ‘pressurised water reactor’ (PWR) technology. This involves

pumping high-pressure water in a primary circuit through the core of the reactor to extract heat energy from the nuclear fission reaction. The water flows to a steam generator where a secondary cooling circuit generates steam to spin a turbine and generate electricity. It is clear that knowing the exact condition of the water in the primary and secondary circuits is key to the optimal performance and safety of the nuclear facility.

The applications are countless and the definition of water quality may differ in each case, however, there are several key metrics that are commonly monitored. These include, but are not limited to:

- *temperature*
- *conductivity* - a measure of the total ionic concentration of the water (including salinity)
- *pH* - a measure of how acidic/basic the solution is
- *dissolved oxygen (DO) content* - an indicator of gaseous diffusion or aeration, as well as the presence of (or conditions for) bacterial and living organisms
- *turbidity* - a measure of the concentration of suspended solid particulates; this might be further extended to include particle size and compositional analysis
- *total organic carbon (TOC)* - the quantity of carbon attributable to bacterial growth and metabolic activities of living organisms
- *chemical content* - the presence of unwanted contaminating chemicals, such as chlorine
- *radioactivity* - a measure of radiation-emitting (α, β, γ) substances, such as actinide metals

A substantial market for *in-situ* water sensing solutions exists [155–157] – totalling several billions of pounds in each relevant sector. The technologies aimed at solv-

ing these problems are wide-ranging and strive to meet the demanding needs of consumers: high sensitivity and accuracy, broad measurement range, fast response time, convenient and robust form factors, and long life expectancy.

However in reality these devices fail to meet at least one, if not several, of these requirements. Many suffer from poor stability, slow response times or need additional reagents to be added to the solution. Some are practically cumbersome, break easily or need frequent replacement or maintenance. Overwhelmingly, many of these sensors are limited in their ability to operate in the harshest environments, which, by definition, many of the metrics listed above constitute.

Several applications operate at the very extremes of possible environmental conditions – the cooling water in a nuclear reactor, for example, may be over 300 °C and at pressures of $\sim$ 170 bar, not to mention the substantial background radiation flux. Some industries therefore are unable to monitor at all; or, if possible, default to making 'offline' measurements whereby samples are extracted and tested in an external laboratory. This process tends to be time-consuming for the specialist operator; requires expensive and cumbersome laboratory equipment (or access to a specialist facility); provides low sampling frequency; and exposes the operator and environment outside the closed system to the risk of dangerous contamination.

There is consequently a very pressing need for *in-situ* sensing solutions that are capable of operating in these difficult conditions. It may be foreseen that diamond is the ideal material to meet this need, given its ability to be used in effective electronic devices that can survive under extreme temperature and pressure; not to mention its large electrochemical window and corrosion resistance. Hence, work on developing resilient diamond-based sensors for these environments will be presented in chapters 9 and 10 of this thesis, with research focus on making sensors for pH and dissolved oxygen (DO).

4.2 pH sensing

4.2.1 Potentiometric sensing and the glass electrode (GE)

The pH of a solution is given by,

$$pH = -\log[H^+] \tag{4.1}$$

where $[H^+]$ is the molar concentration of protons in aqueous solution. The greater the concentration of hydronium (H_3O^+) ions, the more acidic the solution is and the lower the value of pH; the more hydroxide (OH^-) ions in solution, the higher the pH. A solution that contains an equal concentration of hydronium and hydroxide ions has a pH 7 and is considered neutral. Since its discovery by Cremer in 1906 [158], the glass-membrane electrode remains the most well-known, and commonly used, example of a 'pH meter'. Like most ion sensors the glass electrode (GE) is a potentiometric sensor, meaning that the electrical potential, $\Delta\phi$, at a solid-liquid interface is measured as a function of the ion concentration, in this case H^+ [159]. This potential may be calculated by the Nernst equation,

$$\Delta\phi = \frac{RT}{F} \ln\left(\frac{a_{i1}}{a_{i2}}\right) \tag{4.2}$$

where R is the gas constant, T is the absolute temperature in [K] and F is the Faraday constant; $a_i = f_i c_i$ is the activity, or 'effective concentration', of an ion with concentration c_i and activity coefficient f_i. In diluted electrolytes the activity and concentration are equivalent, such that $f_i = 1$. The Nernst equation describes the fact that if the activity of the ion of interest is kept constant on one side of the interface, the electrode potential is a logarithmic function of the ion activity on the other side.

A 'reference' electrode of constant potential may therefore be created, whereby a silver wire, coated in insoluble silver chloride (Ag/AgCl) is immersed within a known and constant concentration of KCl solution. Using equation (4.2) the poten-

tial resulting from this electrochemical couple may be calculated and, in the absence of any interfering reactions, should always remain stable and defined.

A GE takes this concept a step further; essentially using two reference electrodes to measure the pH of a solution. One electrode is modified such that it consists of a pH-sensitive glass composition (such as silicate, SiO_2) in the shape of a bulb, fused to the end of a glass tube containing the KCl solution (at a constant pH) and Ag/AgCl wire. When submerged into the solution to be measured, any difference in $[H^+]$ across the glass membrane will cause a surface potential to form. The second electrode functions as a regular reference and electrically contacts the solution by a non- pH-sensitive glass barrier, known as a 'frit'. The potential between the two electrodes is measured, allowing the pH of the solution to be determined. In practise these two electrodes are usually combined into a single sensor, figure 4.1.

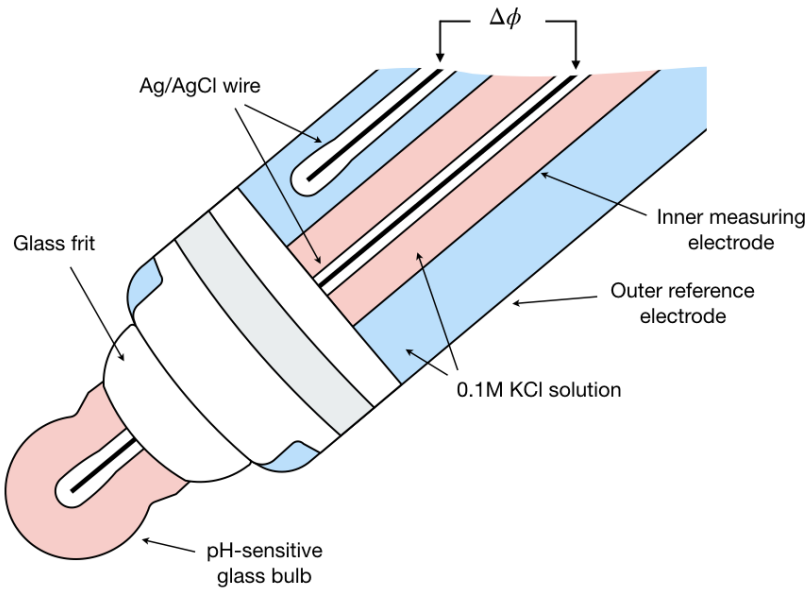

Figure 4.1: A schematic of a combined glass electrode and reference electrode for pH sensing. Both the inner and outer electrodes consist of an Ag/AgCl wire immersed in a fixed concentration of KCl. The inner measuring electrode has a pH-sensitive glass bulb that experiences a surface potential in solution, which may be measured against the outer reference electrode to determine the pH.

These GE sensors are highly popular for laboratory work as a result of their reliability, as well as their fast and accurate results. However for more demanding scenar-

ios they present considerable drawbacks as a consequence of their fragility, relative bulkiness and need to be calibrated frequently [159]. These requirements have fostered the development of other pH measurement techniques such as optical methods, which are based upon reagents that undergo an absorption- or fluorescence-based interaction [160]; or conductimetric sensors, which use pH sensitive conductive polymers such as polyaniline (PANI) deposited over interdigitated electrode contacts [161].

Research continues in these areas although they currently suffer from poor accuracy, low resilience and the need for added reagents makes them impractical in many environments [162]. Alternatively, a more successful approach first established by Bergveld in 1970 [163], has been to measure pH using solid-state materials based upon modifying conventional field effect transistors for ion sensitivity. These devices have occupied the field of ion sensor research over the past few decades because of their considerable advantages in small size, low cost, low power, and compatibility with other semiconductor based functional devices [164].

4.2.2 Ion-sensitive field effect transistor (ISFET)

The operation of an ISFET may be most conveniently described [159] by comparison with its purely electronic analogue – the metal oxide semiconductor field effect transistor (MOSFET). For an ISFET device, the metal gate of a MOSFET is replaced by a reference electrode, whilst the solution to be measured makes contact with the bare gate insulator, figure 4.2. The encapsulation of the ISFET device ensures that the source and drain leads are covered, but the gate area remains exposed to the liquid.

For both FETs equation (4.3a) gives the drain-source current I_{DS} in the non-saturated region of operation, where β is given by equation (4.3b) determined by the mobility μ of the carriers in the inversion layer, the gate insulator capacitance

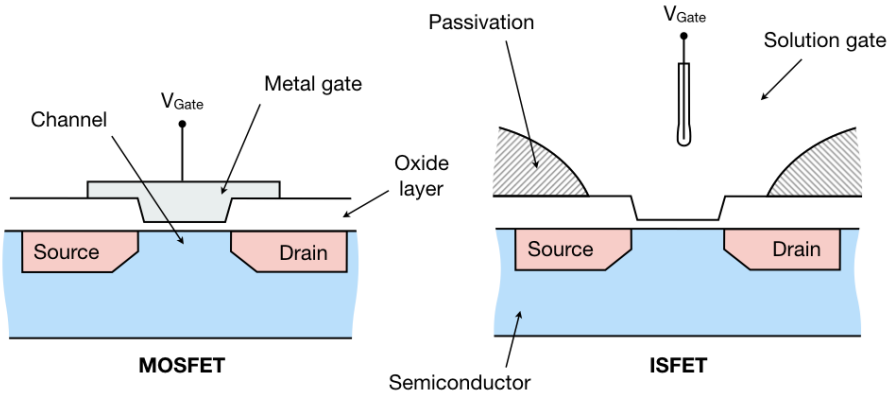

Figure 4.2: The ion-sensitive field effect transistor (ISFET) is analogous to a conventional metal oxide semiconductor field effect transistor (MOSFET), where the metal gate has been replaced with the solution to be measured, contacted by a reference electrode. Source and drain contacts are passivated, leaving the insulated channel exposed.

per unit area C_{ox} and the width to length ratio of the channel W/L.

$$I_{DS} = \beta \left(V_{GS} - V_T - \tfrac{1}{2} V_{DS} \right) V_{DS} \tag{4.3a}$$

$$\beta = \mu C_{ox} \frac{W}{L} \tag{4.3b}$$

The threshold voltage, V_T is given by equation (4.4a), where Q_B is the depletion charge in the semiconductor and ϕ_F is the Fermi potential. The flatband voltage V_{FB} is given by equation (4.4b) where Φ_{SC} is the semiconductor workfunction, Φ_M is the gate metal workfunction, Q_{ss} is the semiconductor surface state density and Q_{ox} is the fixed oxide charge.

$$V_T = V_{FB} - \frac{Q_B}{C_{ox}} + 2\,\phi_F \tag{4.4a}$$

$$V_{FB} = \frac{\Phi_M - \Phi_{SC}}{q} - \frac{Q_{ss} + Q_{ox}}{C_{ox}} \tag{4.4b}$$

It may be observed from equations (4.4a) and (4.4b) that the threshold voltage of a MOSFET is determined by its material properties, namely the workfunctions and charge accumulation. Stable operation of a MOSFET requires a constant V_T which

is achieved by suitable device fabrication, leaving the drain-source current, equation (4.3a) entirely a function of the gate voltage V_{GS}. For an ISFET, V_{GS} is the voltage at the reference electrode (which may be grounded). However the threshold voltage contains terms reflecting the interfaces between the liquid and the gate, and the liquid and the reference electrode, allowing equation (4.4b) to be modified to,

$$V_{FB} = E_{ref} - \Psi_0 + \chi_{sol} - \frac{\Phi_{SC}}{q} - \frac{Q_{ss} + Q_{ox}}{C_{ox}} \tag{4.5}$$

where E_{ref} is the reference electrode potential relative to vacuum, χ_{sol} is the surface dipole potential of the solution and Ψ_0 is the surface potential at the gate. The pH sensitivity of an ISFET derives from the fact that all terms in equation (4.5) are constant apart from Ψ_0, which results from a chemical interaction – usually the dissociation of oxide groups. Achieving the most sensitive device design therefore centres on a detailed understanding of the semiconductor-oxide-electrolyte interface. In the case of a Si/SiO_2 device, for example, the oxide layer contains amphoteric hydroxyl groups which are exposed to the solution. Equilibrium reactions occur whereby these groups may either donate or accept protons from the solution, leaving negatively or positively charged surface groups respectively – known as site-binding, figure 4.3. The pH of the solution, which determines the chemical equilibrium reached, is therefore related to the surface potential Ψ_0 and may be measured as a shift in the threshold voltage by equation (4.4a) (or alternatively, drain-source current equation (4.3a)).

4.2.3 Diamond ISFETs for pH sensing

In the absence of, or indeed the requirement for, a suitable gate oxide or insulating layer, initial efforts to make diamond ISFETs by Denisenko [165] and Kawarada [166] et al. have relied on using hydrogen-induced surface conductivity on bare diamond. Garrido et. al [167] show that purely hydrogenated channels on polycrystalline diamond gated by an Ag/AgCl reference electrode exhibit no pH sensitivity; and ISFET behaviour is obtained only once exposed to mild ozone treatment. This

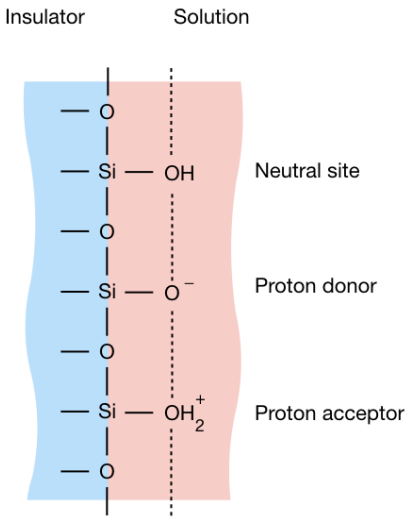

Figure 4.3: The site binding model, as shown for an SiO_2-electrolyte interface. A neutral surface hydroxyl site may bind a proton from the solution, becoming a positive site; or donate a proton, leaving a negative site on the oxide surface. This is known as an amphoteric site.

would suggest that the presence of a certain density of surface hydroxyl ions is key to the sensing mechanism. The authors propose that the oxygen-induced amphoteric surface sites behave like microscopic in-plane chemical gates, acting to laterally modulate the adjacent hydrogen-induced holes – based on observations that surface conductivity is reduced with decreasing pH. Unlike for silicon-based devices, they acknowledge that for diamond it may not be possible to establish a straightforward relationship between the site-binding and surface potential. Interestingly, the Nernst equation (4.2) would suggest a maximum theoretical response of 59.2 mV/pH [168], which is superseded by these devices achieving up to 72 mV/pH, also indicating a possible departure from the conventional ISFET model.

Other subsequent studies [169] have used nanocrystalline diamond (NCD) films grown on p-Si/SiO_2 substrates. They attribute pH sensitivity (38 mV/pH) to site-binding at the oxygen surface of the NCD, although also show some level of sensitivity with a purely hydrogen surface. Similarly, Ahmad et al. [170] use hydrogen-terminated nanodiamonds to coat the gated region of a silicon device in order to

improve reactivity and stability, with some success. Other studies by Sakai et al. [171, 172] have corroborated these results, along with using alternative surface terminations such as amine groups.

Interestingly, Nebel et. al [173–175] have disputed the model proposed by Garrido et al. [167] with single crystal devices that show an increasing surface conductivity with decreasing pH and a response of -56 mV/pH – despite having had no prior surface oxidation treatment. They argue that only a small region close to the source contact controls the channel conductivity, by virtue of the nanometrically thin transfer-doped channel. The chemical potential of the channel, they suggest, may be reduced for higher pH meaning that the diamond Fermi level must move upwards to maintain equilibrium – reducing the surface conductivity. They remark that previous results may have suffered from a pinned surface level due to the presence of grain boundaries in the polycrystalline diamond used.

Dankerl et al. [176] attempt to resolve this difference in theories by evaluating the effect of using a Pt wire instead of an Ag/AgCl reference electrode, as in the case of Nebel et al. [173–175]. They show that this difference in experimental setup may significantly alter the interpretation of the results, including the difference in sign of the pH sensitivity. When using a Pt wire, the pH dependency of the electrode potential itself needs to be accounted for. A decrease in pH results in a lowered position of the Pt electrode potential with respect to the vacuum level; inducing increased surface conductivity as a consequence of the Fermi level being driven further below the valence band maximum. Calculations therefore confirm the notion [166, 167] that purely hydrogenated surfaces, without the presence of hydroxyl groups, show very weak or no pH sensitivity.

Another method by which pH-sensitive channels may be achieved in diamond is by using thin and highly boron doped ([B] $\sim 10^{20}\,\mathrm{cm}^{-3}$) layers. These have the advantage of greatly increased chemical and thermal stability over hydrogen-terminated devices, resulting in longer lifetimes as well as a wider operational range.

Denisenko et al. [177] again pioneer a device consisting of an HPHT diamond substrate with a CVD-grown epitaxial boron-doped layer. Calculations suggest that room temperature operation of these devices require delta-doped profiles ($\sim$ 4 nm thick) in order to achieve full depletion, and hence maximum sensitivity, within the gate potential window of diamond. The delta layer is mesa etched to form a channel and epoxy is used to passivate the source and drain contact areas. The 20 µm x 250 µm channel is left oxidised by means of a wet chemical treatment. FET characteristics show operation within the linear regime, without obtaining saturation. Under exposure to both 0.1M H_2SO_4 (pH 1) and 0.1M KOH (pH 13) solutions, it is demonstrated that the drain-source current may be modulated. Lower pH causes more depletion of the p-type channel and hence a lower current (or lower threshold voltage), with a response of 50 mV/pH.

Edgington et al. [178] show improved FET characteristics, achieving saturation and channel pinch-off within the electrochemical window of diamond. pH sensitivity of 36 mV/pH measured using the delta-doped, plasma oxidised, channels is attributed to site-binding at the high density of amphoteric oxygen moieties. Further attempts to fabricate boron delta-doped ISFET devices have resulted in nano-crystalline diamond channels on silicon [179], oxygen terminated using wet-etch and oxygen plasma to achieve 50% channel modulation with a highly stable pH sensitivity of $\sim$ 50mV/pH. More recently, devices have been successfully fabricated on oxygen [180] and even fluorine-terminated [181] polycrystalline diamond, both with a sensitivity of $\sim$ 30 mV/pH.

Electrochemical pH sensors may also be fabricated using diamond, and are based upon observing a potential change when driving a hydrogen evolution reaction [182–186]. However, these are subject to unwanted reactions by other electrochemically-active species (such as dissolved oxygen, which may be concurrently changing along with pH) requiring careful consideration to achieve accurate results. These will therefore not be presented further.

4.3 Dissolved oxygen (DO) sensing

4.3.1 Amperometric sensing and the Clark electrode

Dissolved oxygen (DO) sensors come in a broad variety of forms, each developed specifically to accommodate the idiosyncrasies of the application – which may extend from determining the oxygen concentration in blood, to that in fuel for combustion. General methods include using optical techniques [187] involving fluorescence quenching; paramagnetic sensing [188]; potentiometric sensing of a Nernstian response akin to that of pH sensors [189]; tunable laser diode (TDL) spectroscopy [190, 191]; and many more [192, 193]. With focus on developing solid-state solutions for sensing in extreme environments the most commonly implemented technique, known as amperometric sensing, will be explored further.

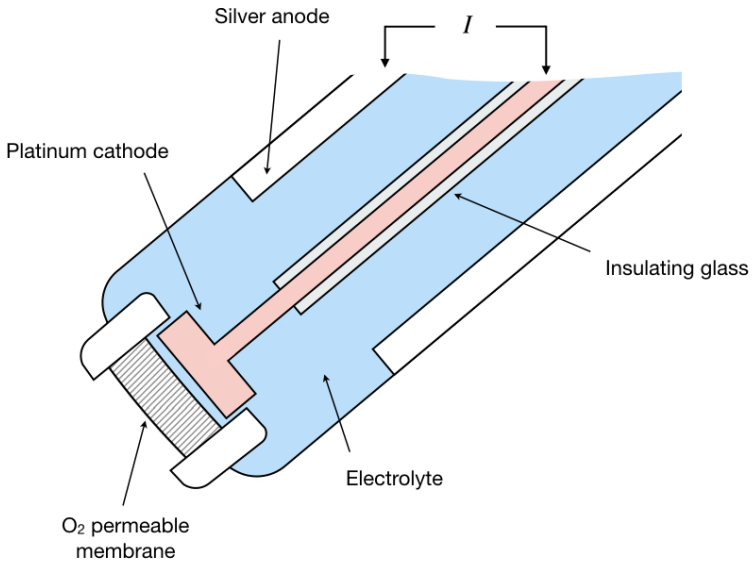

Figure 4.4: A schematic of the Clark electrode for oxygen sensing. A permeable membrane allows oxygen to diffuse to the platinum cathode, where it is reduced. The reduction current I is proportional to the concentration of oxygen in the solution to be measured.

The first practical amperometric oxygen sensor was presented by Clark in 1953 [194], figure 4.4. The Clark electrode is formed by a Pt cathode (working electrode) and Ag anode (counter/reference electrode), electrically connected by an

electrolyte. The solution to be measured is separated from the electrodes by an oxygen permeable membrane, commonly Teflon. Oxygen diffuses in proportion to its partial pressure through the membrane and into the sensor, where it is reduced at the cathode when a potential is applied. The mechanism of oxygen reduction is complex and has been investigated for a large number of electrode materials and various conditions [195–198]. Several reaction pathways have been proposed, where the reduction of oxygen at a Pt electrode is generally considered to occur according to the reaction, equation (4.6a) in acidic, and equation (4.6b) in alkaline solutions.

$$O_2 + 2H_2O + 4e^- \longrightarrow 4OH^- \tag{4.6a}$$

$$O_2 + 4H^+ + 4e^- \longrightarrow 2H_2O \tag{4.6b}$$

The reduction current I is proportional to the oxygen concentration in the solution, C_{O_2}, and may stated by equation (4.7), where n_{app} is the apparent number of electrons transferred during the oxygen reduction reaction, A is the surface area of the working electrode, F is the Faraday constant and D_{O_2} is the diffusion coefficient of oxygen across the membrane.

$$I = 4n_{app}AFD_{O_2}C_{O_2} \tag{4.7}$$

Given this relationship, the oxygen reduction is said to be diffusion-limited as opposed to limited by the kinetics of the reaction at the electrode [199]. This preferred mode of operation ensures a linear dependence of current on dissolved oxygen concentration.

Most modern-day amperometric oxygen sensors operate based upon this simple principle [200], with nominal variations in the geometry and materials that constitute the electrode and membrane with the aim of improving various performance measures or durability of the sensor. Unfortunately, in some practical applications including those consisting of harsh environments, the use of membranes to control the rate of oxygen transport to the electrode are impractical: they are fragile, prone

to blocking, require regular replacement and show reduced permeability with pressure. There is therefore a drive to develop accurate, durable and low maintenance amperometric DO sensors, such as by using electrodes that alleviate the need for a membrane by careful choice of geometry or material – allowing a steady-state diffusion limited current to be obtained [201, 202].

4.3.2 Diamond electrochemical DO sensors

The fundamentals of oxygen sensing using diamond benefit from a long history of research into its use as an electrochemical material [203–205] (these reviews are referenced here amongst an exhaustive number of publications). This has been motivated by the discovery that diamond has an extraordinary potential window – the range of voltage that may be applied (against a standard hydrogen electrode (SHE)) before hydrolysis occurs. Measurements show [206] that for high quality single crystal this window can range between -1.25 V – the onset of hydrogen evolution – to +2.3 V – the onset of oxygen evolution. This wide potential window allows reactants with large positive or negative standard potentials to be investigated without interference from electrolysis. Additionally, diamond is shown to be extremely resistant to corrosion [204], proving to be stable and inert even during cycled hydrogen and oxygen evolution in acidic fluorides; and has a very low background current during voltammetry. As part of this research, the reduction of oxygen at a boron-doped diamond electrode has also been comprehensively studied. In a variety of different solutions [207–210] and using Au nanoparticles to catalytically enhance the reaction [211–213]. Through these studies, diamond presents itself as the ideal working electrode for oxygen sensing in a Clark-type cell, although very little work has been carried out to build a quantitative amperometric oxygen sensor.

A standout example, however, is work by Hutton et al. [214] who describe the development of a Pt nanoparticle-functionalised boron-doped diamond sensor. They laser cut 1 mm diameter disk electrodes, which have a doping concentration of [B] $\sim 5 \times 10^{20}\,\mathrm{cm}^{-3}$. Pt nanoparticles are electrodeposited onto the front face, and

Ti/Au contacts are sputtered and annealed on the rear face to make ohmic electronic contact to the electrode. The disk is mounted into a pulled glass capillary and tinned copper wire is attached to the sensor by silver epoxy paste. The electrochemical measurements are made using an Ag/AgCl reference electrode and Pt counter electrode, where dissolved oxygen concentration is varied in the test solutions by flowing nitrogen and oxygen gas mixtures in various ratios. Cyclic voltammetry measurements show a low background current and wide electrochemical window, as would be expected for diamond. In the oxygenated solution no discernible oxygen reduction peak is seen on the bare boron-doped diamond, however this is revealed at $\sim$ -0.195 V with the addition of Pt nanoparticles, indicating an increased sensitivity and more favourable oxygen reduction reaction. Upon varying the dissolved oxygen concentration, the peak reduction current is seen to correlate linearly. Chronoamperometry measurements confirm the reduction reaction occurring via a four-electron pathway and extended lifetime measurements taken over several days show good stability and reproduciblity.

Chapter 5

Computational methods

5.1 Machine learning

The terms Big Data, Artificial Intelligence and Machine Learning have become much-used buzzwords in recent years – usually associated with the explosion of public interest in doomsday scenarios involving autonomous, often murderous, robots. Whilst we are still a long way off discovering the mechanised fate of the human race [†], the field of machine learning (ML) – using machines to autonomously learn from data, improve their algorithms and make intelligent decisions – has seen a significant upsurge recently. This is primarily due to four key driving forces: faster and more affordable processing hardware; increased connectivity and communication between computers; greater quantities, storage and access to data; and well-funded, extensive research efforts resulting in better and more efficient ML algorithms [218]. Consequently machine learning technology is now present in almost every aspect of modern life, from suggesting a good Netflix movie to watch [219], diagnosing skin cancers in photographs [220], to making instantaneous stock market predictions worth billions of dollars [221].

[†] Although perhaps not as far off as we would like to think. A recent survey [215] of AI experts found that machines capable of matching a human in any intellectual task, 'artificial general intelligence (AGI)', may only be 20-30 years away; with 'artificial superintelligence (ASI)', a machine capable of outperforming a human in any intellectual task [216], being achieved less than 30 years after that. Another study suggests this may occur even sooner [217].

Simply put, machine learning is about extracting knowledge from data [222]. Conventional computer programs rely on a sequence of user-defined instructions to take inputs and compute the desired outputs. These instructions require the user to have a deep understanding of the system to be modelled, and the logic within the resulting program will be narrowly constrained to that specific domain or task. Traditionally such algorithmic approaches have worked extremely well for many applications. For example, a simple program can be written that allows a computer to solve a quadratic equation much better and faster than any human (or simulate a neutron detector – chapter 7). However it is almost impossible to write a conventional program to detect a cancerous mole in a digital image. The problem is that for a human, hard-coding a set of rules that define what a cancerous mole might look like to a computer is extremely difficult. Similarly, writing a sequence of instructions that can accurately model and predict the quirky movie preferences of any person in the world is unthinkable. Hence, what is lacking in knowledge of a system can be made up for in data [223].

Indeed, if it is possible to compile a large number of examples, such as digital images of cancerous and non-cancerous moles, then a computer can 'learn' from these examples to extract its own algorithm for classifying any new or unseen images. The algorithm does not need any prior medical knowledge of skin cancer or its underlying causes, nor does it necessarily derive any new insight into this subject, however it does learn to detect statistical patterns and regularities in the dataset that allow for a very accurate classification of the images without being instructed what to look for.

Machine learning methods can be broadly classified by the type of data passed to the computer during training and the expected outputs of the trained model. 'Supervised learning' occurs when a training sample consists of a set of input variables, known as the 'feature vector', and the corresponding output to be predicted – known as the 'label'. Given a dataset with several samples of feature vectors and labels, the algorithm learns to map the features to the labels, such that new labels can

be predicted for unlabelled data. Other learning approaches include ‘unsupervised learning’, where labels are not provided, and the computer is instead tasked with clustering patterns or trends within the input data; and ‘reinforcement learning’, where the computer seeks to take actions within a defined environment to maximise a notional cumulative ‘reward’. Neither of these methods will be considered any further. In the case of supervised learning, the method may be further separated into the types of labels to be produced. These might be ‘classification’ problems, where the labels belong to a discrete set, for example either cancerous or non-cancerous moles; or ‘regression’ problems, where the labels are continuous values related to the input data, such as stock values.

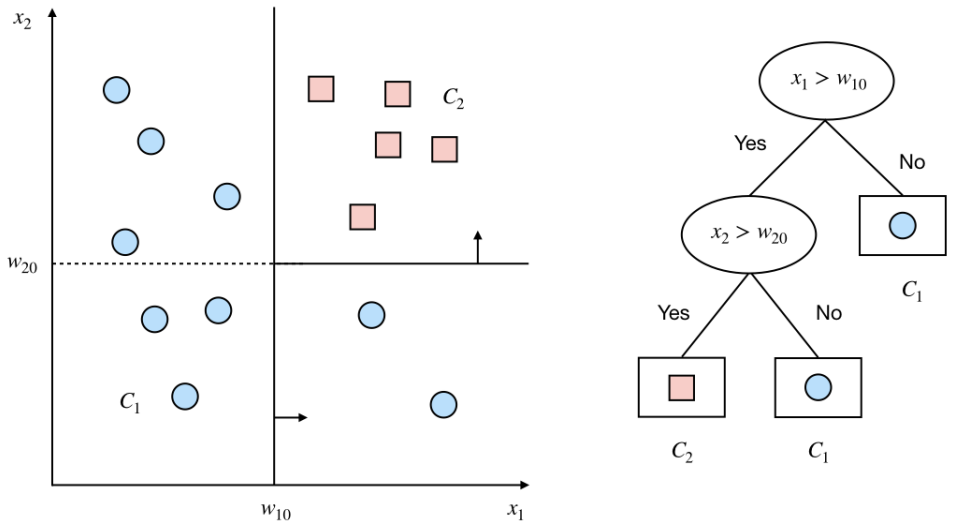

Figure 5.1: An example of a simple decision tree. Ovals represent decision nodes, rectangles represent leaf nodes (adapted from [223]).

The type of problem informs the learning algorithms that are applicable to the problem. One leading supervised learning model widely used for regression and classification problems is a decision tree ensemble, sometimes called a Random Forest (RF). A decision tree is a hierarchical model in which the output labels are determined through a series of recursive splits [223]. Each tree consists of several ‘decision nodes’. At each node m a test function $f_m(x)$ is evaluated, where the discrete outcomes of the test form each of the resulting branches. For a given input

vector, these tests are applied at each node until one of the 'leaf nodes' is reached, at which point this leaf is equivalent to the predicted output of the model, figure 5.1. The test function aims to discriminate in the multi-dimensional input vector space, maximising information gain at each split. A leaf node therefore defines a region of the input vector space where instances all have the same label (for a classification problem) or similar numeric value (for regression problems). Individual decision trees, however, are very prone to overfitting the training data and do not generalise very well. To avoid this problem, multiple decision trees known as a random forest (RF) can be used [224, 225]. RF relies on the principle of 'bootstrap aggregation' in which a random sample (with replacement) of the training data is used to fit each tree in the forest. The output prediction of each individual tree can then be averaged to produce the output of the ensemble overall, reducing susceptibility of the model to noise in the data. RF is further developed such that for each split in a tree, a random subset of the input features are chosen, in order to further de-correlate the trees.

Chapter 6

Experimental methods

6.1 Cleaning of diamond

6.1.1 Degrease

Degreasing is used to remove non-organic residues on diamond samples. The procedure consists of submersion in acetone, then isopropanol (IPA), then de-ionised (DI) water. Each submersion is carried out for 5 min in a low-power ultrasonic bath, after which the sample is dried by N_2 gun.

6.1.2 Piranha clean

A Piranha cleaning solution is made by adding hydrogen peroxide (H_2O_2) to sulphuric acid (H_2SO_4) in a 1:1 ratio. The sample is placed in the solution and left for 20 min, whilst an exothermic reaction occurs (approx. 120 °C). Afterwards the sample is thoroughly rinsed in DI water and dried by N_2 gun. The Piranha etch mixture is used to clean organic residues off diamond samples, and in this work is used immediately prior to photolithography processing to ensure clean adhesion of the photoresist. Piranha etchant is a strong oxidiser and will remove the majority of organic matter, leaving hydroxyl (-OH) groups on the surface.

6.1.3 Oxidising acid clean

An oxidising acid clean is performed to remove adventitious carbon, hydrocarbons and graphitic inclusions from the surface of the diamond. Prior to the treatment a standard degrease is performed. The primary 'cleaning' solution made by adding 20 g ammonium persulphate ($(NH_4)_2S_2O_8$) to 20 ml concentrated sulphuric acid (H_2SO_4) to create a saturated solution at room temperature. The sample is placed into the solution and heated to 100 °C. Once it has been allowed to reach this temperature the heating is increased to a set point of 200 °C and the resulting etch performed for 20 min. White fumes (SO_3) may be noticeable at this temperature, hence the process should be conducted under a fume hood. The solution is then left to cool and the sample is transferred to the secondary 'rinse' solution for 10 min. This solution consists of 10 ml ammonium hydroxide (NH_4OH) added to 10 ml hydrogen peroxide (H_2O_2). Afterwards the sample should be removed, rinsed thoroughly in DI water and dried by N_2 gun.

6.2 Chemical Vapour Deposition (CVD) of diamond

Since the initial work by Eversole [9] at Union Carbide in the 1950s, and the subsequent development of the field in the 1970s - 1980s in the Soviet Union and Japan, CVD diamond growth has become a widely adopted growth technique for commercial applications. The fundamental principle of this method relies on the thermal decomposition of hydrocarbons in the presence of atomic hydrogen. As such many variants emerged through the rapid expansion of the technology, although two processes continue to be the most used today: hot-filament CVD (HFCVD) and microwave-plasma enhanced CVD (MWPECVD) [226].

As first pioneered by Matsumoto et al. in 1982 [13], HFCVD uses a coiled refractory metal wire (typically tungsten or tantalum) to generate atomic hydrogen and carbon radicals in the immediate vicinity of the growth substrate. The filament is heated to approximately 2000 °C, whilst the substrate is kept between 700-1000

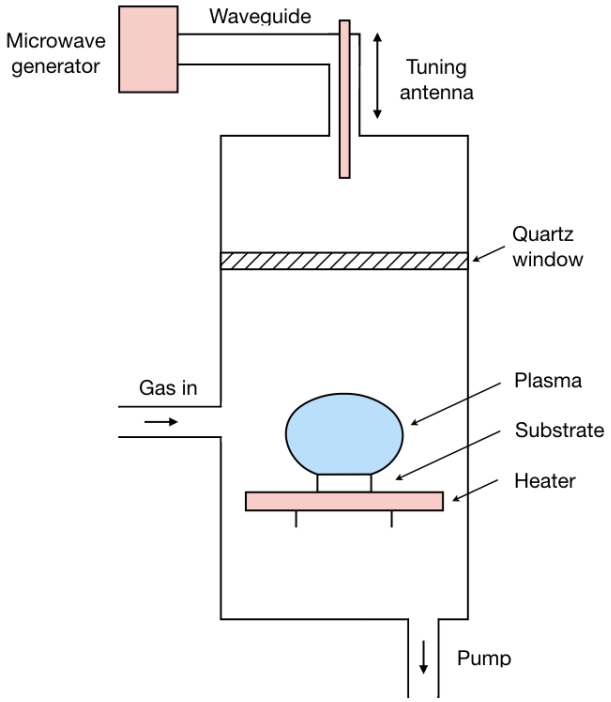

Figure 6.1: A typical ASTeX style MWPECVD reactor; microwave power is directed along a waveguide and transmitted into the chamber through a quartz window generating a plasma of the precursor gases above the heated growth substrate (adapted from [227]).

°C. A process gas of about 1% CH_4:H_2 is injected into the chamber. Alternatives exist on these original process conditions and provide a very simple and scalable approach to diamond growth. However, the major disadvantage inherent with HFCVD is contamination of the film by the filament itself. Efforts to reduce this contamination cause growth rates and purity to suffer, and hence limits the application of HFCVD for electronic and optical applications.

Alternatively MWPECVD offers much higher quality film growth at impressive rates, and with a flexible choice of precursor gases. It is therefore the method of choice for diamond film growth in this thesis, as with many other commercial applications worldwide. MWPECVD was first demonstrated by Kamo et al. in 1983 [14] at NIRIM, Japan. Process gases are introduced into the growth reactor, and microwave power is then directed along a waveguide and transmitted into the

chamber cavity via a quartz window (in the case of an ASTeX-type reactor, figure 6.1). The microwave couples inductively into the chamber and imparts energy to the electrons in the gas, which then transmit this energy to the molecules themselves through collisions. This causes heating and ionisation of the process gases, igniting a plasma of diamond precursors around the growth substrate.

Careful design of the reactor cavity allows one large radial microwave mode to be supported, typically at 2.45 GHz, and the microwave power and process pressure determine the size and energy density of the plasma ball. If the correct combination of surface temperature, pressure and gas composition conditions are used, diamond grows on the substrate in a piece-wise fashion through methyl radicals attaching to the tetrahedral carbon bonds (if a diamond or diamond-seeded substrate are used), figure 6.2. Lower frequency (RF) plasmas are not favourable to diamond growth owing to the higher kinetic energy of the ions which tend to cause etching of the substrate, and the relative instability of the plasmas generated.

Typical modern MWPECVD systems, including the Astex-AX6500 used for the work presented in this thesis, tend to use a standard CH_4:H_2 precursor gas combination. Although other gases such as O_2 or trimethylborane (TMB, $B(CH_3)_3$) may be introduced to affect growth properties or to dope the diamond film. Initially only the non-hydrocarbon gases are flowed via mass flow controllers into the reaction chamber. The chamber is initially under high vacuum ($\sim 10^{-7}$ Torr) and the process pressure is controlled using throttle or butterfly valves with backing pumps. When the substrate reaches the desired temperature (600 – 1000 °C typically), the methane gas is introduced and the microwave power generator, which can range from 1.5 kW to up to 8 kW at 2.45 GHz, is turned on. Growth rates of several $\mu m\,hr^{-1}$ can be achieved under these conditions. The MW power is then shut off after the growth run and samples are left to cool in a hydrogen atmosphere, before venting and removal of the substrate.

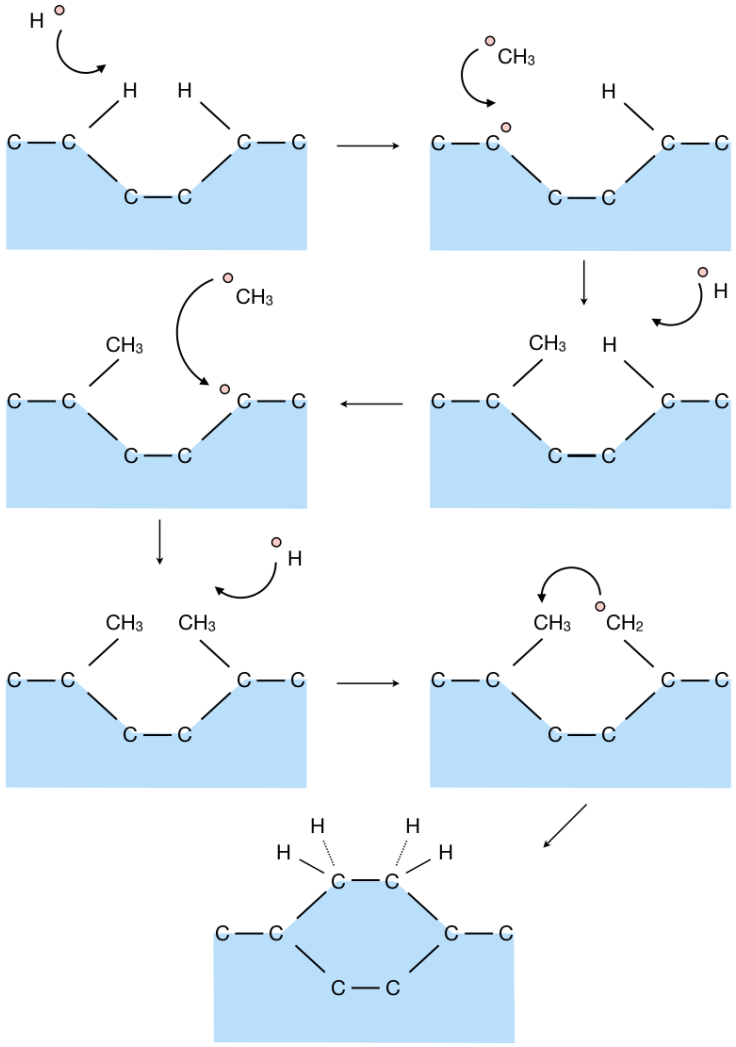

Figure 6.2: A simplified schematic of the step-wise reaction taking place at the diamond surface during growth. Diamond grows on a substrate consisting of diamond or diamond seeds that are nearly fully saturated with hydrogen (H). Atomic H removes (abstracts) a surface H to form H_2, leaving behind a reactive surface site. Occasionally a gas phase methyl (CH_3) radical can collide and react with this site, essentially adding another C to the lattice – which may then also occur at an adjacent site. The process of H abstraction on one of the chemisorbed CH_3 groups creates a radical which can attack the adjacent group to complete the C ring structure as part of the new diamond lattice [227].

6.3 Photolithography

Photolithography (PL) is an industry-standard technique for patterning in microelectronics. PL allows the effective transfer of computer-designed patterns from a mask to a photosensitive polymer photoresist (PR) that has been spin-coated onto the substrate. The patterned PR may then act as a stencil for further processing, and is particularly useful for metal contact patterning, selective etch or selective surface treatment in device fabrication. The specific recipe used for PL depends strongly on the sample substrate and type of PR used and is typically developed and optimised on an individual basis. A general process flow for PL is:

1. Dehydration bake: the substrate may be heated on a hotplate to drive off adsorbed water.

2. Spin coat: the substrate is mounted onto a vacuum chuck and a quantity of solvated PR is dropped onto the centre of the sample. The sample is spun at high rotational speed to evenly coat it with a uniformly thick layer.

3. Softbake: the coated sample is heated on a hotplate to evaporate any remaining solvent in the PR.

4. Exposure: the coated sample is mounted onto a vacuum chuck and aligned with the pattern mask. The mask is usually a quartz or glass slide patterned with chrome to the desired features. The sample and mask are brought into close contact and the PR is exposed to a precise dose of UV light. UV exposure induces a chemical crosslinking in the PR. For 'positive' PR types, any exposed regions are removed during development. The opposite applies for 'negative' PR types.

5. Post-exposure bake: this may be necessary for some resists to complete the crosslinking of the PR or to reduce mechanical stress in the film.

6. Development: the sample is immersed into a developing chemical to remove the non-crosslinked regions of the PR.

7. Hardbake: this may be used to further harden the PR for processing.

6.4 Metallisation

6.4.1 Thermal evaporation

The ability to deposit a thin film of metal onto a substrate is crucial to device fabrication as described in chapter 2. Thermal evaporation enables this through the vaporisation of a source metal, such as gold or chrome, under high vacuum onto a target material or substrate. The source metal is typically heated in molybdenum boats or wire filament form using resistive heating elements. The metal evaporates and travels in a line of sight towards the target, which is suspended above the source, where it condenses into a thin film. Control of the deposition is achieved using shutters above the source, along with the current flow through the heating element to regulate the rate of evaporation. The film thickness is monitored by a quartz crystal microbalance monitor.

6.4.2 Electron beam evaporation

Electron beam evaporation is based upon on a similar principle to thermal evaporation of metals. In this case, a high-energy electron beam is generated by a filament and focused directly onto the source metal using a magnetic field, figure 6.3. Importantly, this avoids contamination of the film with boat or filament material and allows the evaporation of high melting point materials such as titanium or platinum. The source metal is originally in the form of pellets which are melted into a cooled graphite crucible. The target is mounted above the source and rotates in order to achieve a uniform deposition. Evaporation rate can be carefully controlled by the electron beam current to form high-quality thin films suitable for device contacts.

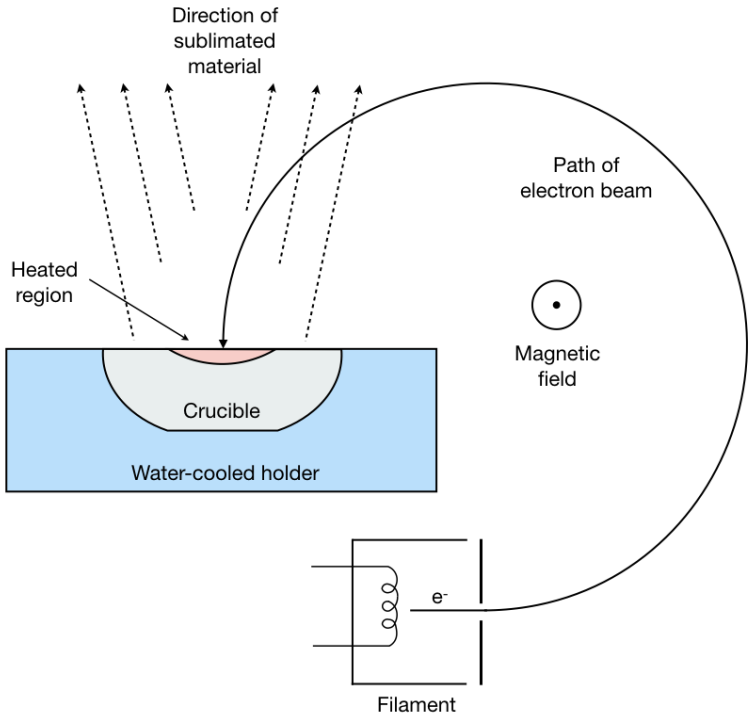

Figure 6.3: Electron beam evaporation (adapted from [228]). A high energy electron beam is focused using a magnetic field such that heats and evaporates a source metal that sits inside a cooled crucible.

6.5 Ozone oxidative treatment

Diamond surfaces, as grown by MWPECVD, tend to possess a hydrogen termination due to the existence of hydrogen radicals in the plasma. They may therefore be treated to ensure termination of dangling bonds with oxygen moieties and to suppress any undesired hydrogen surface conductivity. A dry and non-destructive method for doing this is by ozone oxidative treatment, a UV photochemical process in which the samples are exposed to highly-oxidising ozone which readily dissociates into O_2 and O. The sample is mounted on a ceramic heater in a sealed custom-built chamber. The chamber is flushed with oxygen 5 times prior to processing. The sample is then heated, achieving a continuous oxygen flow before starting the UV ozone generator. A standard process would commonly use a temperature of 200 °C and pressure of 50 mBar. The ozone generator consists of a mercury lamp

that generates UV light at 184.7 nm and 253.7 nm wavelengths to create the oxygen radicals.

6.6 Impedance spectroscopy

Impedance spectroscopy (IS) is a powerful technique used to investigate the electronic properties of materials and their interfaces [229]. It may characterise bound and mobile charge dynamics in the bulk, and at the interface, of many solids and liquids including semiconductors and dielectrics. The most common IS method involves applying a single-frequency AC voltage or current at the electrodes of the material being investigated and measuring the phase shift and amplitude (real and imaginary components) of the resulting current.

A Solartron 1260 Impedance System is used to conduct IS in the following work with the addition of a Solartron 1296A Dielectric Interface – allowing impedance measurements to be taken between 1 - 10^{14} Ω, in the frequency range 10^{-2} - 10^{7} Hz. Impedance spectroscopy is usually performed under vacuum or in a neutral atmosphere such as argon, but may also be studied in air. The measurement depends on a number of factors such as the conductivity, dielectric constant, mobility, charge density, capacitance, grain boundaries and point defects in the material, as well as the properties of the electrodes themselves, and hence can offer deep insight into these parameters and their origins.

In the case of a perfect dielectric material the total impedance Z may be modelled as a basic RC circuit, which, when separated into real and complex components describes a complex semi-circle on a Cole-Cole plot, figure 6.4. This may be described mathematically by equation (6.1), where R_1 and R_2 are ohmic resistances, C is the dielectric capacitance, $\omega = 2\pi f$ the angular frequency and $i = \sqrt{-1}$. The limiting cases of $Z(\omega = 0) = R_1 + R_2$ and $Z(\omega \to \infty) = R_1$ and the condition at the peak of the Cole-Cole semi-circle, $\omega_{max} R_2 C = 1$, allow the values of the capacitance, effective series and parallel resistances of the material to be obtained through

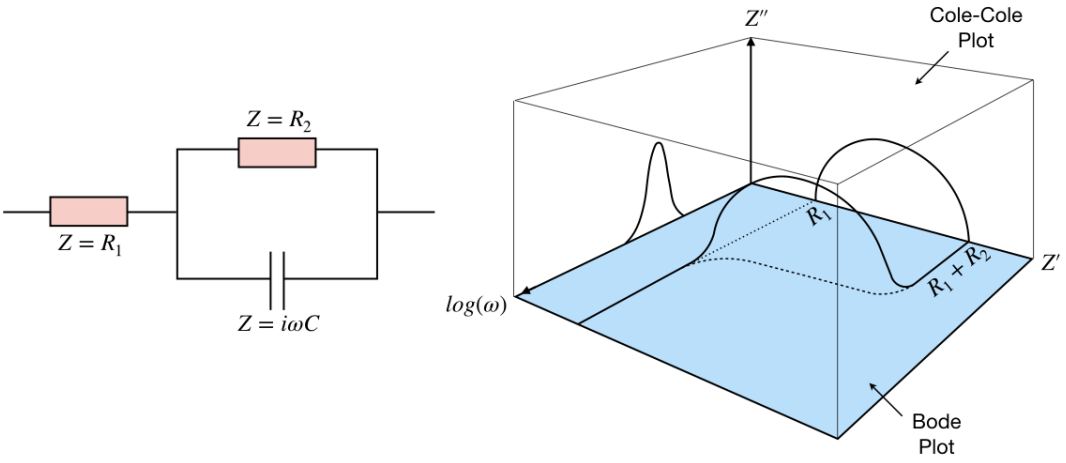

Figure 6.4: Left, RC circuit model for an ideal dielectric material; right, the corresponding impedance spectrum for this circuit showing the complex (Z'') and real (Z') components of the impedance as a function of frequency (ω) (adapted from [230]).

the numerical fitting of circles to the measured data.

$$Z(\omega) = R_1 + \left(\frac{1}{R_2} + i\omega C\right)^{-1} \tag{6.1a}$$

$$= \left(R_1 + \frac{R_2}{1 + (\omega C R_2)^2}\right) - i\left(\frac{\omega C R_2^2}{1 + (\omega C R_2)^2}\right) \tag{6.1b}$$

A material may exhibit multiple conduction paths, which would be measured as a series of overlapping complex circles – each of which may be fitted, and parameters extracted therefrom. In addition to the arcs exhibited by dielectric materials, other impedance features may suggest inductive effects or similar.

$$E_A = \frac{k_B}{q}\frac{\partial \ln Z}{\partial(\frac{1}{T})} \tag{6.2}$$

IS may also be performed within a range of temperatures to extract the temperature dependence of the measured parameters. In particular this allows an Arrhenius plot to be drawn, from which the activation energy E_A to be extracted, equation (6.2), where k_B/q is the Boltzmann constant in units of electronvolts (eV) and T is the

temperature in Kelvin (K). In the case of diamond, the activation energy would commonly correspond to that of any dopants in the material.

6.7 Circular transmission line measurement

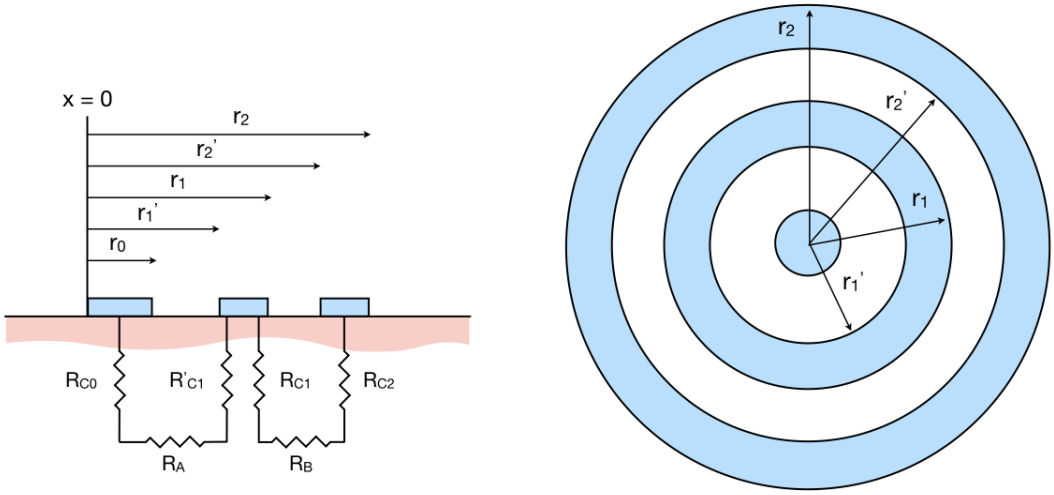

Figure 6.5: Right, the ideal contact pattern for the Circular Transmission Line Model (CTLM); left, cross-sectional schematic of contacts and associated resistances (adapted from [231]).

Measuring the specific contact resistance of an electronic contact to a semiconductor is non-trivial, and may be extracted by use of particular contact test patterns. The Transmission Line Model (TLM) [232] uses the most common of these patterns, in which the total resistance is measured between a series of rectangular contacts at differing separations. The specific contact resistance can then be determined by the gradient of these resistance values plotted as a function of their separation. TLM requires additional processing in the form of etching the contacts onto an isolated mesa of conductive semiconductor, it also makes the assumption that the sheet resistance below the contact is the same as the normal sheet resistance. Hence the Circular Transmission Line Model (CTLM) modification was proposed by Reeves (1980) [231] which obviates the need for a mesa etch, and generally provides a more accurate solution. In this model, the test pattern consists of three concentric ring contacts, figure 6.5, where the resistance is measured between the

inner and middle contact ($R_1 = R_A + R_{C0} + R'_{C1}$) and the outer and middle contact ($R_2 = R_B + R_{C1} + R_{C2}$). The contact end resistance (R_{end}) is also measured by applying a current source to the inner two contacts, whilst measuring the potential drop across the outer two contacts in a three-probe configuration. From these values Reeves derives the relationship,

$$\phi(\alpha) = \chi \tag{6.3}$$

where the components may be described by equations (6.4) and (6.5).

$$\phi(\alpha) = \frac{\ln\left(\frac{r'_2}{r_1}\right)\left[\frac{E(r_0)}{\alpha r_0} + \frac{1}{\alpha r'_1}\frac{A(r_1,r'_1)}{C(r_1,r'_1)}\right] - \ln\left(\frac{r'_1}{r_1}\right)\left[\frac{1}{\alpha r_1}\frac{B(r_1,r'_1)}{C(r_1,r'_1)} + \frac{1}{\alpha r_2}\frac{A(r_2,r'_2)}{C(r_2,r'_2)}\right]}{\frac{A(r_1,r'_1)B(r_1,r'_1)}{C(r_1,r'_1)} + D(r_1,r'_1)} \tag{6.4}$$

$$\chi = \frac{\ln\left(\frac{r'_2}{r_1}\right)R_1 - \ln\left(\frac{r'_1}{r_0}\right)R_2}{R_{end}} \tag{6.5}$$

The functions $A(r,x)$, $B(r,x)$, $C(r,x)$, $D(r,x)$, $E(r)$ are combinations of the modified Bessel functions of the first and second kind; $\alpha = \sqrt{\frac{R_{SK}}{\rho_C}}$, where R_{SK} is the sheet resistance of the semiconductor below the contact and ρ_C is the specific contact resistance.

Equation (6.4) may be plotted numerically as a function of α, using the contact radii, r_0, r'_1, r_1, r'_2, r_2. Equation (6.5) can be calculated using the resistance values obtained experimentally and plotted on the same figure. By obtaining the point of intersection of the functions χ and $\phi(\alpha)$, the value of α at which equation (6.3) is true can be obtained.

$$\rho_C = \left(\ln\left(\frac{r_2'}{r_1}\right) R_1 - \ln\left(\frac{r_1'}{r_0}\right) R_2 \right) r_0^2 \, \theta(\alpha) \tag{6.6}$$

$$\theta(\alpha) = \frac{2\pi}{\left[\dfrac{A(r_1, r_1')B(r_1, r_1')}{C(r_1, r_1')} + D(r_1, r_1') \right] (\alpha r_0)^2 \, \phi(\alpha)} \tag{6.7}$$

One can then derive the specific contact resistance, which gives equation (6.6), where the function $\theta(\alpha)$, equation (6.7), can also be plotted numerically. By finding the solution for α, the value of $\theta(\alpha)$ may be obtained and hence the specific contact resistance calculated. The sheet resistance may also be calculated by derivation of a similar equation.

Chapter 7

Simulations for the optimisation of diamond-based thermal neutron detectors

7.1 Introduction

Substantial effort has been devoted to meet the growing global demand for neutron detectors across a wide range of applications from nuclear power to medical research [63]. Recent advances in solid state detection have been driven by the desire to achieve greater efficiencies, deliver compact and robust form factors, as well as to overcome the considerable shortage of ^{3}He used in gas-filled proportional detectors [65, 66]. Diamond has emerged as the material of choice for the detection of particle radiation due to its high breakdown voltage, large carrier mobilities and radiation hardness. Devices using both ^{6}Li- [140–144] and ^{10}B- [122, 149, 150] enriched conversion layers have been investigated with the aim of harnessing these properties for improved thermal neutron sensing.

However, the efficiencies currently obtainable using these diamond detectors – as well as solid state detectors in general – are low. Indeed, a review by Caruso [69] highlights that "the persisting challenge... for highest total efficiency may be

presently summarised, unfortunately, not in terms of pushing the physics frontier (*vide supra*) but in terms of the maturity of the materials processing technologies, in addition to the advances in heterostructure geometry optimisation and understanding of the electronic and physical properties of the heterostructure materials". That is to say, in order for diamond neutron detectors to fulfil their tall expectations, significant work has to be dedicated to identifying which geometrical and material parameters are important to neutron detection and understanding how they may be optimised to maximise performance. This potentially tireless and costly experimental task may be neatly avoided by the use of computational simulation methods, which already form a cornerstone of particle research with popular packages such as the Geant4 toolkit [233] and MCNP [234]. However, other than for rudimentary interpretation of results [140], there presently has not been any study that seeks to explicitly optimise diamond neutron detectors across a comprehensive range of parameters.

This chapter therefore presents work to address this question. With the intention of achieving the most complete and versatile insight possible, a computational model is developed using a combination of fundamental physical principles and Monte Carlo statistical methods. In line with the theory described in chapter 3, neutron interactions in a ^{10}B conversion medium are accounted for, followed by particle track calculations of the interaction products and their energy loss within the detector. Subsequently, the statistical generation of charge carriers, and their transport to collecting electrodes is modelled, accounting for the effect of imperfect charge collection efficiency due to trapping and recombination effects. Finally, the electronic noise component is also considered. Within this framework a number of key parameters are considered in order to meet the task of detector optimisation, including enrichment fraction, layer thicknesses, mobility-lifetime products, electric field and polarity. In addition, the overarching optimisation question of detector heterojunction configuration is addressed, where indirect conversion layer formats are explored, as well as a novel direct structure based upon a semiconducting boron-

carbide/diamond p-n diode [†]. For adjustments in these parameters, the various efficiency metrics of the detector are simulated along with the output spectra, providing new insight into quantifiable methods to achieve highly efficient diamond-based neutron detectors.

7.2 Experimental methods

7.2.1 Model introduction

A model has been written in Matlab 2016b that allows detectors to be virtually built, tested and optimised. The model is designed such that it is generalisable to practically any conceivable device structure, including multi-layer detectors of both indirect and direct conversion types, and any material.

Simulation results for three different types of planar diamond-based detector are presented in this chapter, figure 7.1. The first is a conversion layer detector with an 'active' (neutron-sensitive) boron carbide layer, layer A, and intrinsic diamond detection volume, layer B, forming an indirect conversion detector. Neutrons are converted into charged products in layer A, these products pass into layer B where they generate charge carriers. An electric field is applied across layer B for the separation and collection of charge carriers. The second is a three-layer 'sandwich' detector, comprising of a boron carbide active layer A and two adjacent intrinsic diamond layers B and B_0. Finally a direct detector is considered. The active layer A is assumed to be a semiconducting n-type boron carbide layer, forming a heterojunction diode with a p-type diamond layer B. Neutrons are absorbed and converted in layer A, and the emitted ions generate charge carriers in both layers that may be separated by the depletion region of the device and any applied bias.

[†]The background theory and a review of literature for this device is presented in appendix A, along with a description of ongoing and future experimental work in this area presented in chapter 11.

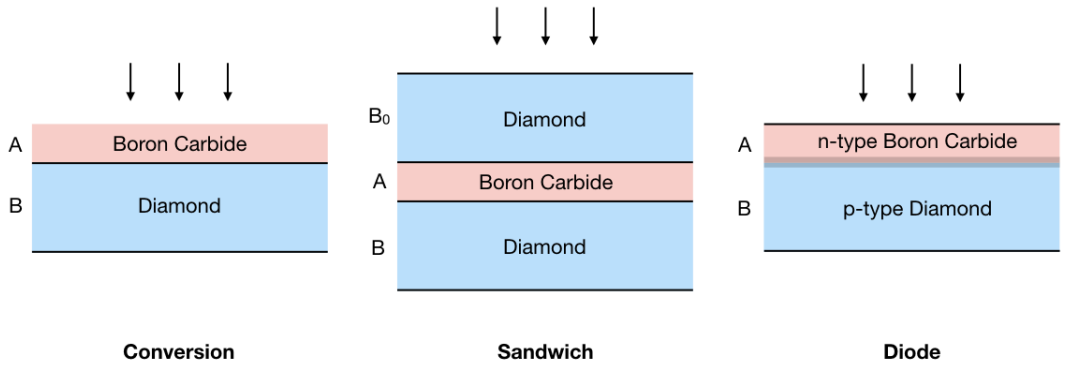

Figure 7.1: Three planar detector geometries are simulated using the model: conversion, sandwich and diode. Red regions indicate the 'active' layers where neutron conversion occurs. Black lines represent charge collection electrodes. Shaded area indicates the diode heterojunction.

7.2.2 Assumptions

The following assumptions are made in the model:

- Any metallisation is assumed to be infinitely thin and does not contribute to the absorption of neutrons or ion energy loss.

- Only the interactions of monoenergetic, thermal neutrons (E = 0.025 eV) are considered. Neutrons are assumed to be emitted uniformly and isotropically from a point source away from the detector. Neutrons are assumed to arrive normal to the detector plane.

- Neutrons only interact through primary nuclear absorption interactions; elastic and inelastic scattering events are assumed to be negligible. This may be justified as scattering cross-sections are several orders of magnitude smaller in materials such as boron.

- Neutron conversion to charged products occurs only in layer A, the 'active' layer. Conversion probability is independent of depth. No neutron conversion occurs in layers B and B_0; although the model is readily extended to include this.

- Gamma ray interaction products are ignored as the absorption cross-section is extremely small.

- Kinetic energy imparted to the reactive nucleus by the neutron is assumed to be zero. Interaction products are emitted in straight, anti-parallel paths, and are not scattered along their paths.

- The continuous slowing down approximation (CSDA) is assumed. That is, the energy of the interaction products is lost at a constant rate along their paths, within the same layer.

- The energy deposited by the interaction products is completely converted into electron-hole pairs. Charge is assumed to be generated at a single point - in agreement with the Hecht model.

- There is a uniform electric field across the device. In the case of a diode detector, the depletion region is assumed to extend across the full thickness of the device.

- The timing resolution of the detector electronics allows discrimination of individual charge pulses.

7.2.3 Model definitions

In its most general form, and consistent with the assumptions above, the model can be described as follows. A neutron source is defined with an emission rate Φ and at a distance D from the detector. The detector geometry is defined in three dimensions, where each layer is directly adjacent to the next and has dimensions X_a, Y_a, Z_a for layer A, etc. Implicitly, the geometric probability of a neutron arriving at the active layer of the detector may be described by equation (7.1).

$$P_{geom} = \frac{X_a\, Y_a}{4\pi D^2} \tag{7.1}$$

Material properties are assigned to each layer. These include parameters such as the chemical formula and isotopic enrichment fractions. In this case the active layer is boron carbide, which has a chemical ratio of R_B boron atoms to R_C carbon atoms. The fraction of boron atoms that are enriched to boron-10 is F_{B10}; which have a thermal neutron capture cross-section of σ_{B10}. The molecular mass of layer A can then be calculated using equation (7.2), using the individual masses m_{B10}, m_{B11} and m_C. Similarly, the density of layer A is calculated by equation (7.3) using the densities ρ_B and ρ_C.

$$m_a = R_B\, F_{B10}\, m_{B10} \;+\; R_B\, (F_{B10} - 1)\, m_{B11} \;+\; R_C\, m_C \tag{7.2}$$

$$\rho_a = \frac{R_B\, \rho_B \;+\; R_C\, \rho_C}{R_B \;+\; R_C} \tag{7.3}$$

As a result the atomic number density of layer A may be calculated, equation (7.4), where N_{Avo} is Avogadro's constant. If it is assumed that all neutron absorption in layer A occurs only by interaction with boron-10, equation (7.4) becomes equation (7.5).

$$N_a = \frac{\rho_a\, N_{Avo}}{m_a} \tag{7.4}$$

$$N_a = R_B\, F_{B10} \left(\frac{\rho_a\, N_{Avo}}{m_a} \right) \tag{7.5}$$

Therefore, the probability of a neutron interaction occurring in layer A, where the interaction cross-section $\sigma_a = \sigma_{B10}$, is described by equation (7.6). In this instance it is valid to assume the universal Beer-Lambert law of attenuation in matter.

$$P_a = 1 - \exp(-\sigma_a\, N_a\, Z_a) \tag{7.6}$$

Equivalent quantities may be calculated for layer B_0 assuming the dominant (but nevertheless very weak) interaction in diamond is with carbon, $\sigma_{b_0} = \sigma_C$. The prob-

ability of neutron transmission through layer B_0 is therefore given by equation (7.7).

$$P_{b_0} = \exp(-\sigma_{b_0} N_{b_0} Z_{b_0}) \tag{7.7}$$

Finally, the rate of neutron interactions within layer A may be written, equation (7.8).

$$Rate = \Phi P_{geom} P_a P_{b_0} \tag{7.8}$$

This prescribes the total number of conversion events that occur per unit time which

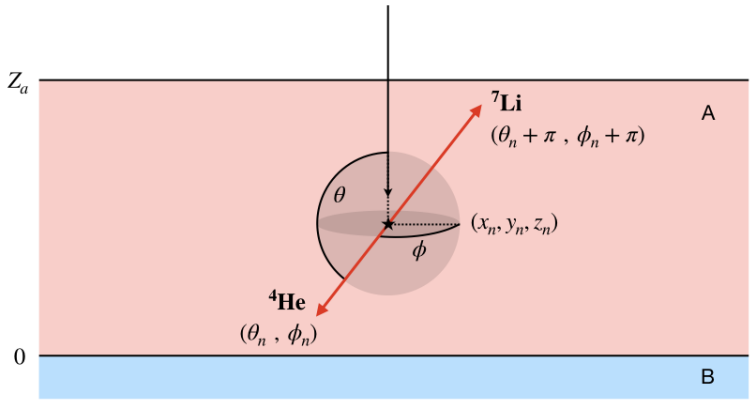

Figure 7.2: A neutron conversion event, n, randomly generated at the origin (x_n, y_n, z_n) in the active layer. ^{4}He and ^{7}Li particles are emitted in anti-parallel with spherical vector (θ_n, ϕ_n).

may occur at any origin coordinate, $(x_n,\ y_n,\ z_n)$ uniformly distributed within the volume of layer A, where $0 < n \leq Rate$. A Monte Carlo pseudo-random number generator assigns a coordinate to each event within the limits,

$$X_a \geq x_n \geq 0$$

$$Y_a \geq y_n \geq 0$$

$$Z_a \geq z_n \geq 0$$

For the charged capture interaction with boron-10, two ions are emitted in anti-parallel with spherical vectors $(\theta_n,\ \phi_n)$ and $(\theta_n^{'},\ \phi_n^{'})$. They are emitted isotropically at random angles within the limits,

$$2\pi \geq \theta_n > 0, \quad \theta_n^{'} = \theta_n + \pi$$
$$2\pi \geq \phi_n > 0, \quad \phi_n^{'} = \phi_n + \pi$$

Each particle in a pair has an associated mass, charge and initial energy, $E_{a,n}^0$. The energy is randomly sampled from a distribution according to the branching fraction of the neutron absorption reaction. An example is shown in figure 7.2. Subsequently, the subscript n will be dropped for clarity and it is assumed that all further mathematical treatment is applied to each particle individually, unless otherwise explicitly stated.

7.2.4 Particle track calculations

Assuming layer A has an infinite volume, the maximum distance that each particle will travel before it has lost all its kinetic energy is given by the range, l_a. This is calculated by the integration of the stopping power function for layer A, $S_a(E) = -dE/dx$, equation (7.9).

$$l_a = \int_0^{E_a^0} \frac{1}{S_a(E)}\, dE \tag{7.9}$$

The stopping power function is calculated by the machine learning model described in chapter 8. Given that layer A in fact has a finite volume, the maximum distance a particle with infinite energy may travel in layer A before reaching a bounding plane, d_a, can be determined geometrically, equation (7.10). The projection of the particle vector onto that bounding plane is given by the equation (7.11). These quantities are illustrated in figure 7.3.

$$d_a = \frac{z^*}{\cos(\theta^*)} \tag{7.10}$$

$$\lambda_a = \sqrt{d_a^2 - z^{*2}} \tag{7.11}$$

$$\theta^* \, , \, z^* = \begin{cases} \theta \, , \, (Z_a - z) & \text{if} \quad \frac{\pi}{2} > \theta \geq 0 \\ \pi - \theta \, , \, z & \text{if} \quad \pi > \theta \geq \frac{\pi}{2} \\ \theta - \pi \, , \, z & \text{if} \quad \frac{3\pi}{2} > \theta \geq \pi \\ 2\pi - \theta \, , \, (Z_a - z) & \text{if} \quad 2\pi > \theta \geq \frac{3\pi}{2} \end{cases} \tag{7.12}$$

By implication, if $d_a \geq l_a$ then the particle comes to a stop before it manages to exit layer A and is fully absorbed. Hence the energy deposited by the particle in layer A is equal to its initial energy, $E_a = E_a^0$. If $d_a < l_a$, then the particle exits layer A and continues its path. In this case, the energy deposited in layer A must be calculated by numerical integration of the stopping power function with respect to distance along its track, equation (7.13). Each iteration of the integration assumes that the particle loses energy ΔE in an incremental distance Δr, such that its new energy is $E^{'}$ at depth $r^{'}$.

$$|\Delta E| = S(E)\Delta r \tag{7.13a}$$

$$E^{'} = E - |\Delta E| \tag{7.13b}$$

$$r^{'} = r + |\Delta r| \tag{7.13c}$$

This may be interpreted as a relaxation of the CSDA, in that a more realistic energy deposition function is assumed where more energy is lost towards the end of the ion path, as opposed to linear energy loss. The next calculation in the particle track is to determine coordinates of intersection with the bounding planes of layer A and whether the particle enters either layer B or B_0, or neither. These coordinates are given by equation (7.14).

$$x^{'} = x + \lambda_a \sin(\phi) \tag{7.14a}$$

$$y^{'} = y + \lambda_a \cos(\phi) \tag{7.14b}$$

If the particle is emitted towards layer B, ie. $3\pi/2 \geq \theta \geq \pi/2$, then the intersection coordinates must fall within the limits, $X_b \geq x^{'} \geq 0$ and $Y_b \geq y^{'} \geq 0$. If not, then it may be assumed that the particle exits layer A and deposits the remainder of its energy outside the detection volume. If it does intersect layer B, then the particle enters layer B with energy $E_b^0 = E_a^0 - E_a$. Similarly, if the particle is emitted towards layer B_0 the converse applies. The above calculations, equations 7.9 to 7.14,

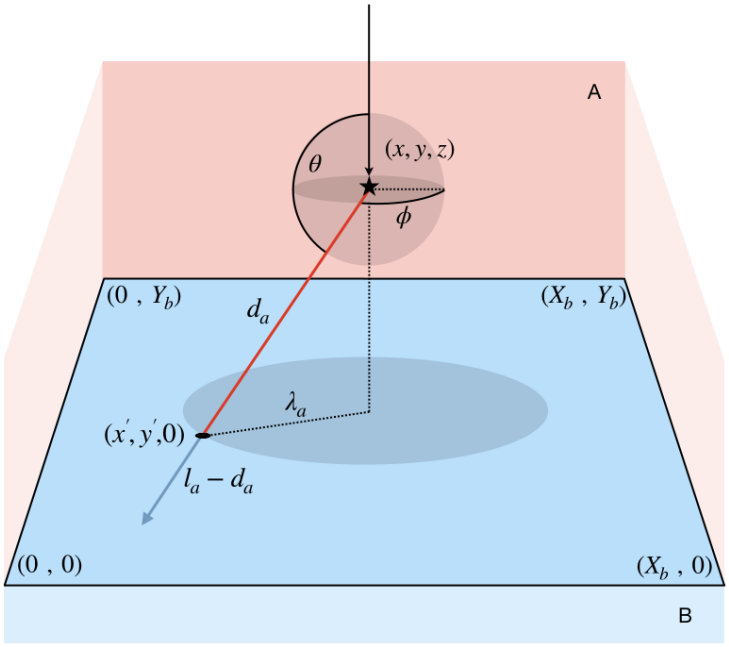

Figure 7.3: A particle traversing layer A with energy E_a^0 has a range d_a, where the maximum distance travelled before intersecting layer B is d_a. The co-ordinates of intersection $(x^{'}, y^{'}, z^{'} = 0)$ can be calculated using the projection onto the plane, λ_a.

are then repeated to determine the range of the particle in layers B and B_0, whether the particle fully absorbed in the layer, and hence how much energy is deposited in layers B and B_0: E_b and E_{b_0}, respectively. In practise this process may be repeated for any number of layers, including several active layers, to construct more complex detector geometries. Particle scattering and charge exchange effects may also be investigated by a treatment similar to that of the particle energy, but are not considered here.

7.2.5 Generation of charge carriers

The energy loss of charged particles in the detector can be transformed into a number of electron-hole pairs created along their tracks. The average charge (in units of electron charge, e) generated is determined by equation (7.15) – where ε is the energy required to form an electron-hole pair.

$$Q = \frac{E}{\varepsilon} \tag{7.15}$$

$$\varepsilon[eV] = 1.76 + 1.84 E_{gap} \tag{7.16}$$

Measurements of ε show a near-linear dependence on material bandgap, E_{gap}, and may be estimated (in units of eV) by the fitting formula, equation (7.16) [235]. For diamond, this would suggest ε = 11.82 eV – however experiments show it is actually closer to ε = 13.1 eV [67], in alignment with others: 13.2 eV [124], 13.9 eV [129], 12.8 eV [236]. The value of 13.1 eV will be used throughout. For boron carbide, assuming a bandgap of E_{gap} = 2.09 eV, the estimated value of ε = 5.61 eV will be used. The production of charge carriers is an intrinsically statistical process. It may be considered that ionising energy loss occurs over a series of discrete steps between the particle's initial energy, and when it is fully absorbed. The probability of a certain number of charge pairs being generated within a fixed distance is governed by Possion statistics and hence the energy loss is unequal along its path. There is consequently a finite statistical limit to the energy resolution of the detector, $(\Delta E/E)_{detector}$. However, the experimentally-observed variance of this resolution is in fact a lot smaller than statistics alone would predict. This was explained by Fano [237] who suggests that the number of charge carriers produced is limited by energy conservation. The corrected variance, scaled by the 'Fano factor' F, as shown in equation (7.17) can be derived [238].

$$\sigma^2_{Fano} = F \frac{E}{\varepsilon} \tag{7.17}$$

The Fano factor in diamond has been experimentally calculated as $F = 0.382$ [67], which is greater than the value of $F = 0.08$ predicted by purely theoretical treatments [235]. It is suggested that this discrepancy may be due to the measurement using alpha particles – which experience large stopping powers in diamond – and a lower value may be determined using X-rays with very low circuit noise [67]. For the purposes of this model the value of $F = 0.382$ will be used for diamond, and in the absence of experimental data, for boron carbide too. Some error will be incurred by this approach although it will be shown that the significance of variations in equation (7.17) is limited.

The Fano resolution may be modelled by a normal distribution with a mean given by equation (7.15) and variance, equation (7.17). Hence, for layer B the charge generated, Q_b, by each particle depositing an energy E_b is given by equation (7.18). Where $\boldsymbol{N}$ is the normal distribution from which Q_b is randomly sampled. Similar quantities are derived for layers A and B_0.

$$Q_b = \boldsymbol{N}\left(\frac{E_b}{\varepsilon_b} \, , \, F_b \frac{E_b}{\varepsilon_b} \right) \tag{7.18}$$

Once the electron-hole pairs are generated, in the presence of an electric field, they immediately begin to drift towards opposite electrodes [239]. However, charge trapping and recombination may prevent these charges from being collected and entering the circuit. The carrier lifetime, τ, characterises the amount of time a charge carrier can 'survive' in a crystal without recombination or trapping. So an initial charge Q_0 will decay exponentially as a function of time, equation (7.19).

$$Q(t) = Q_0 \, \exp\left(-\frac{t}{\tau} \right) \tag{7.19}$$

If an electric field is present, the charge will drift with velocity, $v = \mu\xi$, where μ is the carrier mobility and ξ is the magnitude of the electric field. The time required to travel a distance r is therefore $t = r/\mu\xi$, and the charge remaining after this distance

is given by equation (7.20). The carrier drift distance may be written, $L = \tau\mu\xi$.

$$Q(r) = Q_0 \exp\Big(-\frac{r}{\tau\mu\xi}\Big) \tag{7.20}$$

For a parallel-plate detector with thickness D, the electric field is $\xi = V_{bias}/D$ and the induced signal for a charge travelling distance dr is given by equation (7.21). The total charge is therefore equation (7.22).

$$dQ_S = \frac{1}{D}\, Q(r)\, dr \tag{7.21}$$

$$\begin{aligned} Q_S &= Q_0 \frac{1}{D} \int_0^D \exp\Big(-\frac{r}{L}\Big) dr \\ &= Q_0 \frac{L}{D} \Big(1 - \exp\Big(-\frac{D}{L}\Big)\Big) \end{aligned} \tag{7.22}$$

The drift distance differs for electrons and holes, $L_e = (\mu\tau)_e\, \xi$ and $L_h = (\mu\tau)_h\, \xi$, respectively. Hence the equation (7.22) may be written in full as the Hecht equation (7.23), [240].

$$Q_S = Q_0 \frac{1}{D} \left[L_e \left(1 - \exp\Big(-\frac{D - r_0}{L_e}\Big)\right) + L_h \left(1 - \exp\Big(-\frac{r_0}{L_h}\Big)\right) \right] \tag{7.23}$$

The main assumptions of the Hecht model are that all charge is generated at a single point, r_0 – defined as the distance from the interaction event to the cathode; that detrapping of charges is ignored [241]; and a uniform electric field exist across the detector. The mobility-lifetime product has been determined for single crystal and polycrystalline diamond of various grain sizes [242], and these values will be used to guide experiments utilising the model.

The charge generated in each layer, as calculated using equation (7.18) and its equivalents, is therefore transformed into a collected charge signal based on the

Hecht model. Concurrently, it is assumed that all the charge in each device type is generated at a single point. In the conversion layer detector, r_0 is determined by the z- coordinate at the end of the particle trajectory in layer B, $z_b = d_b\ \cos(\theta)$, where d_b is the total distance travelled in layer B. According to the definitions in figure 7.4, if the cathode is adjacent to layer A – 'forward bias' – then $r_0 = z_b$; or adjacent to layer B – 'reverse bias' – $r_0 = Z_b - z_b$. Using $D = Z_b$, along with the drift distances in diamond $L_{e,b}$ and $L_{h,b}$, and the initial charge $Q_0 = Q_b$, the collected charge signal may be derived by direct use of equation (7.23). Equivalently, for a sandwich detector, the charge signal generated across layer B_0 may be calculated and summed with that of layer B to arrive at the total signal.

The diode detector differs in that it transduces the trajectories of some, or even all, of both particles in a pair within a single volume – as opposed to just the trajectory of one particle. The distance from the cathode may be measured by geometrical consideration, using r_0 as the end point of the particle that has the trajectory ending furthest into the detector. That is, the particle in each pair that is emitted 'downwards', i.e. $3\pi/2 \geq \theta \geq \pi/2$. For forward bias, r_0 may therefore be calculated by equation (7.24a), and for reverse bias by equation (7.24b).

$$r_0 = (Z_a - z_a)\ +\ (d_b + d_a)\cos(\theta) \tag{7.24a}$$

$$r_0 = (Z_b + z_a)\ -\ (d_b + d_a)\cos(\theta) \tag{7.24b}$$

The second difference is that a diode comprises of two different materials which will inevitably have differing carrier drift distances. The transport of charge across a heterojunction is complex, but a simple approximation may be used to accommodate for this. The overall carrier drift distances are calculated by the average of the drift distances for each material, weighted by the distance travelled in each layer. For example, in forward bias, the electron and hole drift distances may be given by equation (7.25a) if the particle trajectory ends in layer B, $r_0 \geq Z_a$, or by equation (7.25b)

if the particle trajectory ends in layer A, $r_0 < Z_a$; where $r_0' = (Z_a + Z_b) - r_0$.

$$L_e = L_{e,b} \qquad L_h = \frac{Z_a\, L_{h,a} + (r_0 - Z_a)\, L_{h,b}}{r_0} \tag{7.25a}$$

$$L_e = \frac{Z_b\, L_{e,b} + (r_0' - Z_b)\, L_{e,a}}{r_0'} \qquad L_h = L_{h,a} \tag{7.25b}$$

Similarly, in reverse bias, these are given by equation (7.26a) if the particle ends in layer B, $r_0' \geq Z_a$, or by equation (7.26b) if the particle ends in layer A, $r_0' < Z_a$. These quantities may then be used in equation (7.23) along with $D = Z_a + Z_b$ and $Q_0 = Q_a + Q_b$ to give the collected charge signals for each polarity. Note that for the special case where $L_{e,a} = L_{e,b}$ and $L_{h,a} = L_{h,b}$, equations (7.25a) to (7.26b) reduce to their default values.

$$L_e = \frac{Z_a\, L_{e,a} + (r_0' - Z_a)\, L_{e,b}}{r_0'} \qquad L_h = L_{h,b} \tag{7.26a}$$

$$L_e = L_{e,a} \qquad L_h = \frac{Z_b\, L_{h,b} + (r_0 - Z_b)\, L_{h,a}}{r_0} \tag{7.26b}$$

A final factor to consider is noise generated by the electronic circuit. There are numerous sources of noise that are unique to each detection setup and contribute to the unwanted broadening of the detector spectra. The complexities of modelling the contributions of these various sources and their relation to the nuances of the detection electronics would fill many volumes and is extensively discussed by Spieler [243]. However, regardless of the intractability of decomposing and evaluating the noise signal, the overall effect of noise needs to be accounted for. Experimentally, the circuit noise may be extracted by use of a precision pulser signal to inject a known charge into the read-out chain. The pulser signal is broadened

by noise and fitted well by a Gaussian function with resolution, $(\Delta E/E)_{noise}$. Therefore, the charge signals calculated for each device may be convoluted with a noise signal representative of a real experimental system. The charge collected is smeared by the normal distribution, equation (7.27), where the nominal value of σ_{noise} = 770 e is used, calculated by taking the average of the noise signals from a number of experiments [121, 124, 129, 244].

$$Q_S = \boldsymbol{N}\Big(Q_S \ , \ \sigma_{noise} \Big) \tag{7.27}$$

Equation (7.27) therefore describes the collected charge pulse for each particle pair, given a particular detector geometry. If it is assumed that the timing resolution of the detector is sufficient to resolve each discrete pulse then a histogram of pulse size may be plotted, representing the detector spectrum.

7.2.6 Detector efficiency

The efficiencies of the detector may be calculated as follows. Firstly, the probability of a neutron hitting the detector surface, known as the geometric efficiency, may be calculated by equation (7.28).

$$\eta_{geom} = \frac{\#n \text{ incident}}{\#n \text{ at source}} \tag{7.28}$$

Thereafter, the conversion efficiency is the probability of that neutron transmitting through layer B_0 (if applicable) and undergoing an interaction event in layer A to form a charged particle pair, equation (7.29).

$$\eta_{conv} = \frac{\#n \text{ converted}}{\#n \text{ incident}} \tag{7.29}$$

The transduction efficiency is the number of conversion events that generate particles which then produce a measurable charge pulse (assuming perfect charge collection), equation (7.30). For example, for a conversion detector this would be the

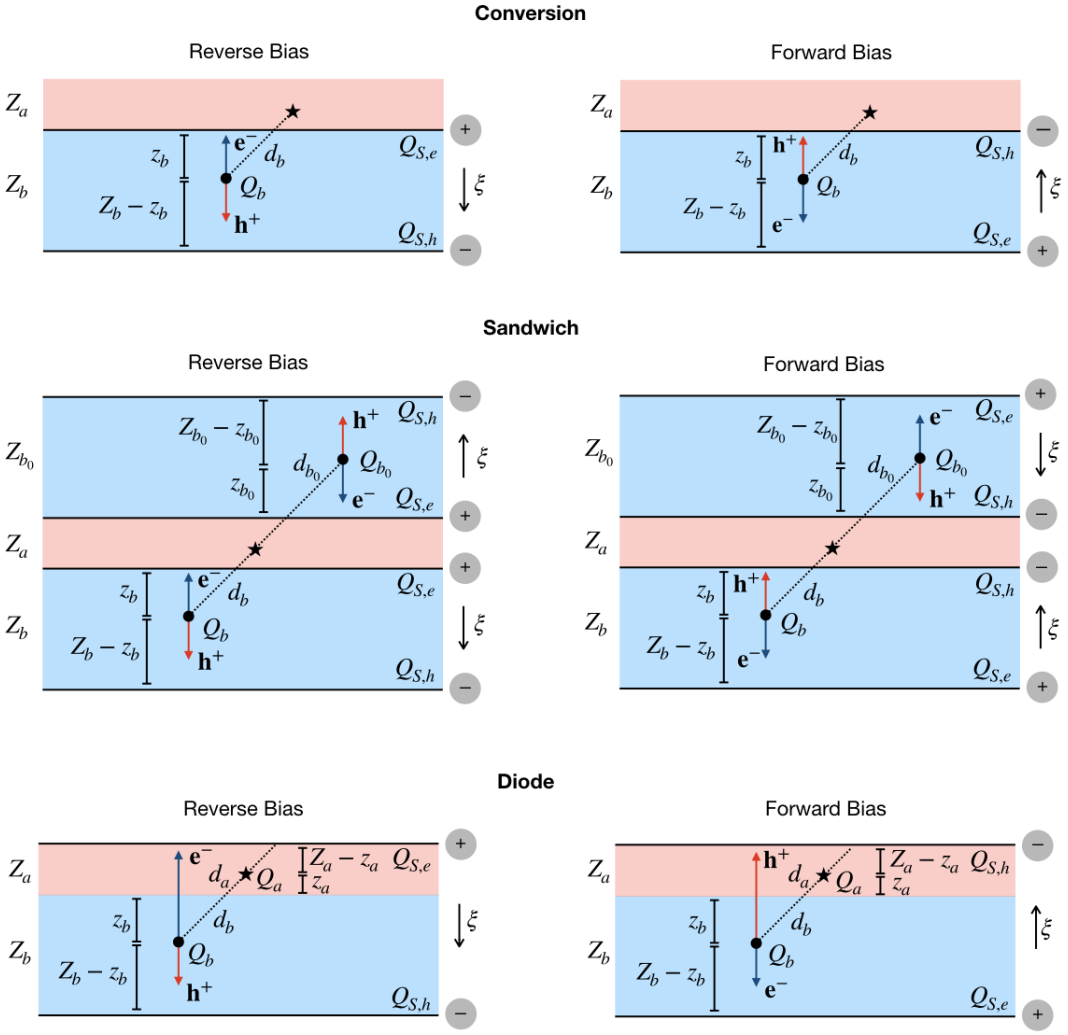

Figure 7.4: Various detector structures and their charge collection distances in both forward and reverse bias.

number of particles that deposit energy in layer B.

$$\eta_{trans} = \frac{\#pulses \text{ transduced}}{\#n \text{ converted}} \tag{7.30}$$

Finally, a discriminatory threshold level may be set in order to filter out any low energy noise or background counts such that only 'real' counts are registered. Hence the threshold efficiency is the number of charge pulses that are greater than the threshold value Q_{th}, 7.31. Set correctly, this is strongly dependent on the 'sharp-

ness' and position of the spectral peaks – and hence is dependent on factors such as charge collection and noise.

$$\eta_{th} = \frac{\#pulses > Q_{th}}{\#pulses \text{ transduced}} \tag{7.31}$$

The total efficiency is therefore the quotient of counted neutrons – ie. counted pulses above the threshold value – to the total number of neutrons produced by the source, equation (7.32).

$$\eta_{total} = \frac{\#pulses > Q_{th}}{\#n \text{ at source}} \tag{7.32}$$

This metric is dominated by the, somewhat arbitrary, solid angle that the detector presents to the neutron source; hence the real performance is better evaluated independent of the geometric efficiency. More commonly quoted is the total efficiency written as the number of counted neutrons to the number of incident neutrons, equation (7.33).

$$\begin{aligned} \eta_{total} &= \frac{\#pulses > Q_{th}}{\#n \text{ incident}} \\ &= \eta_{conv}\ \eta_{trans}\ \eta_{th} \end{aligned} \tag{7.33}$$

Separately, the charge collection efficiency may be calculated, equation (7.34). Q_S is the collected charge and Q_0 is the initial charge generated. For each device type Q_0 is the sum of the initial charges generated in each applicable layer given by equation (7.18) (and its equivalents).

$$\eta_{CC} = \frac{Q_S}{Q_0} \tag{7.34}$$

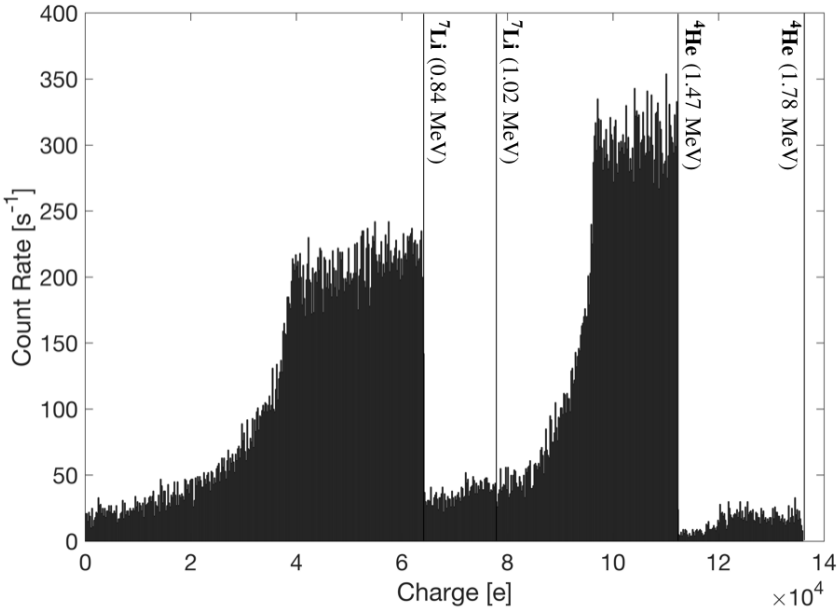

Figure 7.5: Simulated spectrum for an un-optimised conversion layer detector. Charge pulses [e] are plotted (bin width = 200 e) against count rate [s^{-1}]. Peaks are resolved at the ion energies according to the interaction of neutrons with ^{10}B.

7.3 Results

7.3.1 Un-optimised detector

To gauge the effectiveness of subsequent optimisation studies it is useful to consider the results for a control model. This is a simplified model, where the detector structure is reduced to the most simple case of a two layer indirect conversion device, with arbitrary layer thicknesses of $Z_a = 0.5$µm and $Z_b = 50$µm and $X_{a,b}, Y_{a,b} = 5$mm. Layer A is B_4C boron carbide, consisting of the natural 19.8% ^{10}B enrichment, layer B is intrinsic diamond. The control model also does not consider the finite detector resolution due to Fano broadening and noise; recombination and trapping of carriers is also ignored. This allows these contributions to be isolated and evaluated independently. A neutron source with an emission rate $\Phi = 10^{15}\,s^{-1}$ and distance from the detector of $D = 10$ m gives a geometric efficiency of $\eta_{geom} = 1.989 \times 10^{-8}$,

η_{conv}	η_{trans}	η_{th}	$\eta_{\mathbf{total}}$
0.41	91.27	70.63	**0.26**

Table 7.1: The efficiencies of an un-optimised conversion layer detector [%].

and a fluency of approximately $8 \times 10^{11}\ \mathrm{s}^{-1}\,\mathrm{m}^{-2}$.

Figure 7.5 is the simulated spectrum: the magnitude of the charge pulses are plotted along the x-axis in units of electron charge [e] with a binwidth of 200 e, against the count rate on the y-axis. It should be noted that the units of the y-axis are chosen specifically to be independent of experiment duration, which is an arbitrary parameter, and are hence quoted as a count rate [s^{-1}] for the given fluency, as opposed to an absolute count value. Alternatively the y-axis could be interpreted as equivalent to the absolute count value for a one second detection experiment.

The spectrum has a clearly defined shape, with a number of resolvable peaks. These peaks correspond to the four particle energies emitted from the neutron interaction with ^{10}B, equations (3.2) and (3.3): ^{4}He at 1.47 MeV ($\sim$ 112,000e) and 1.78 MeV ($\sim$ 136,000e), along with ^{7}Li at 0.84 MeV ($\sim$ 64,000e) and 1.02 MeV ($\sim$ 78,000e). Two of these peaks are much greater in size due to the relative branching fractions of this reaction. The peaks can be seen to tail dramatically towards low energies, which is a direct consequence of energy loss in the active boron carbide layer A. Because charge pairs can only be collected in the diamond layer B, signals may only be measured from particles that enter this layer. These particles will inevitably lose a portion of their energy travelling through layer A before reaching layer B. The highest charge pulses are therefore observed for interaction events that generate ions very near to the interface between the layers; whereas those that undergo the most straggling are generated further away.

The shape of the spectrum is observed to contain some noise despite being an idealised case. This is a consequence of the random nature of ion generation – embodied in the Monte Carlo modelling technique. If the experiment is run for a longer

duration and accumulated counts are recorded, this noise will represent a smaller proportion of the spectral magnitude, however will never be eliminated entirely.

The overall efficiency of the detector is very low, $\eta_{total} = 0.26\%$, which is largely dominated by a very low conversion efficiency, table 7.1. The conversion efficiency is dependent on two factors: the thickness of the active layer A, and its enrichment fraction. The probability of an interaction occurring will increase if the thickness is increased or the quantity of ^{10}B is enriched, due to the larger effective interaction cross-section presented to the incident neutrons.

The transduction efficiency is relatively high, which means that only a small proportion of interactions produce ions that do not enter layer B. This is primarily due to the thickness of the layer being less than the range of the ions – thicker layers will therefore reduce the transduction efficiency. The threshold efficiency, where the threshold charge is set at 50,000 e, is reduced because of the low energy tailing of the peaks. Sharper energy peaks would increase the threshold efficiency.

7.3.2 Enrichment fraction

The analysis of the control model suggests that initial performance gains may be achieved through increasing enrichment fraction of the active layer. In this case the enrichment of ^{10}B will increase the probability of a neutron conversion event occurring in layer A. Figure 7.6 shows the variation of conversion efficiency η_{conv} with enrichment fraction, F_{B10}. There is a strong dependency on layer thickness, and so the enrichment is presented as a surface plot against the thickness of layer A, Z_a. The distinct effect of increasing enrichment is to increase conversion efficiency – the dotted red lines indicate the natural enrichment level (19.8%) and highly enriched (99%) boron carbide. However, the magnitude of the increase is determined by the thickness. Very thin and very thick layers will see marginal gains, because the effective absorption cross-section of the neutrons is dominated by the depth of the absorbing medium in these cases. However in the region of layer thicknesses of $\sim 1 - 100$ μm, enrichment may improve conversion efficiency by several factors.

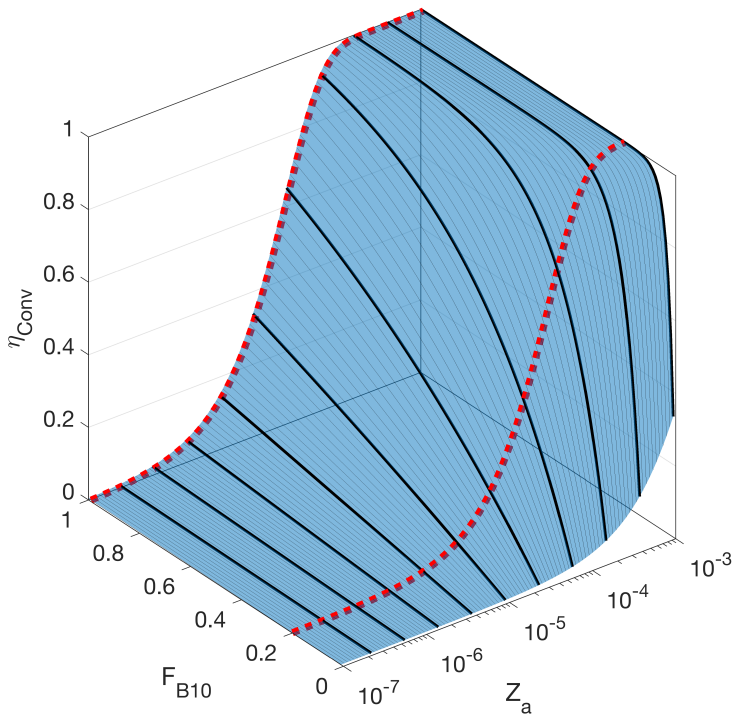

Figure 7.6: The variation of conversion efficiency η_{conv} with ^{10}B enrichment fraction F_{B10} and layer A thickness Z_a. Red dotted lines highlight natural (19.8%) and highly enriched (99%) states.

7.3.3 Detector structure

Performance gains may also be made in using different detector types. That is, altering the design of the detector to improve the measurement of the energetic ions generated upon neutron conversion. The most basic design, as presented in the un-optimised control model, is the conversion layer detector. The spectrum for a 99% enriched device is presented in figure 7.7, where the notable differences are a higher count rate and lower random noise.

The conversion layer detector has an obvious disadvantage, in that it is capable of only detecting ions that are transmitted 'downwards' towards layer B. Half of the ions generated exit 'upwards' and are uncounted. Hence, a direct improvement is to use a structure capable of detecting these uncounted particles – known as a '4π

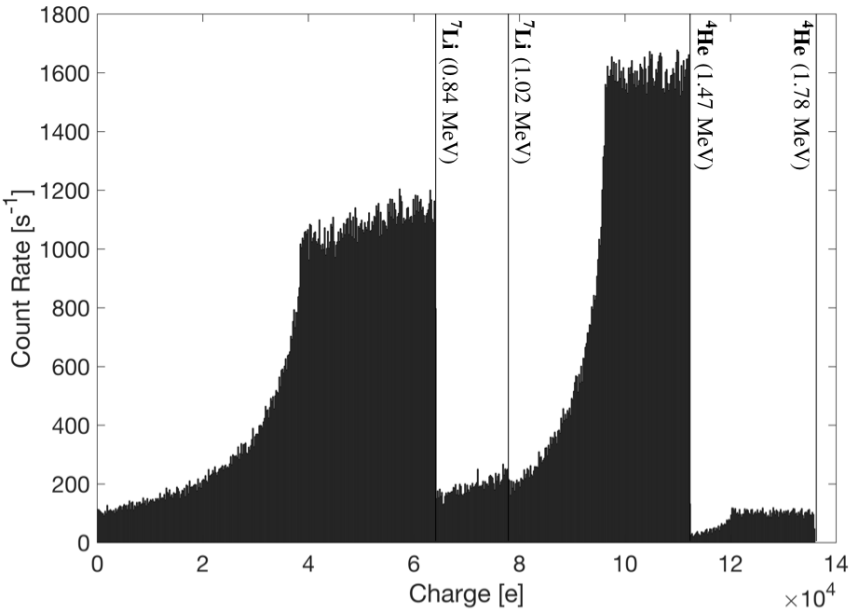

Figure 7.7: Simulated spectrum for an enriched conversion layer detector. Charge pulses [e] are plotted (bin width = 200 e) against count rate [s^{-1}]. Peaks are resolved at the ion energies according to the interaction of neutrons with ^{10}B.

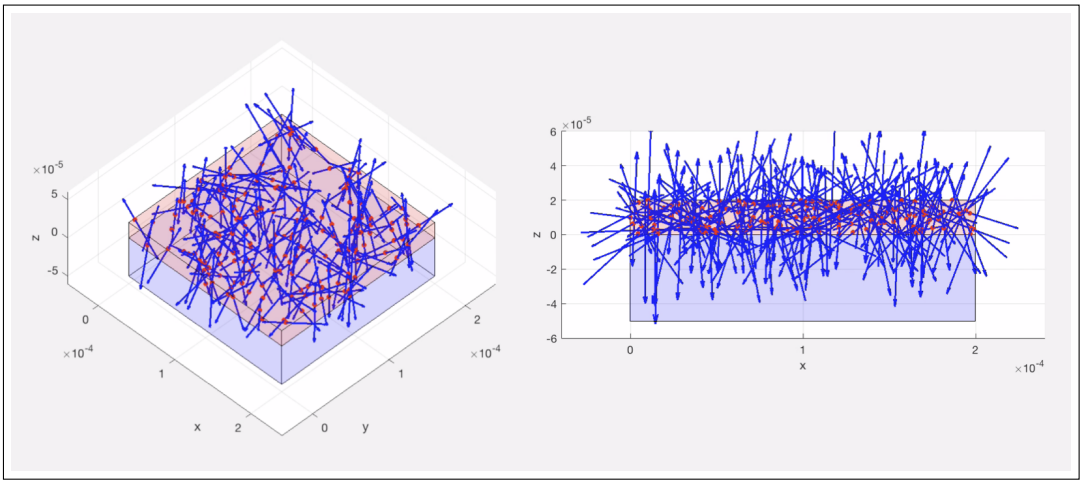

Figure 7.8: A screen-shot of the animation produced by the Matlab model during simulation of a conversion layer detector structure. Red region indicates the active boron carbide layer A, blue region indicates the diamond layer B. Red circles show neutron conversion events, generating particles with tracks shown by blue arrows. For clarity, the animation only illustrates a portion of the device and exaggerates particle tracks. Note: this animation is graphically equivalent to that for a diode device structure.

geometry' for the fact that it is capable of detecting ions over a solid angle of 4π [†]. A three-layer 'sandwich' detector leverages such a geometry, which allows detection of ions in layer B_0 in addition to layer B. The spectrum is shown in figure 7.9.

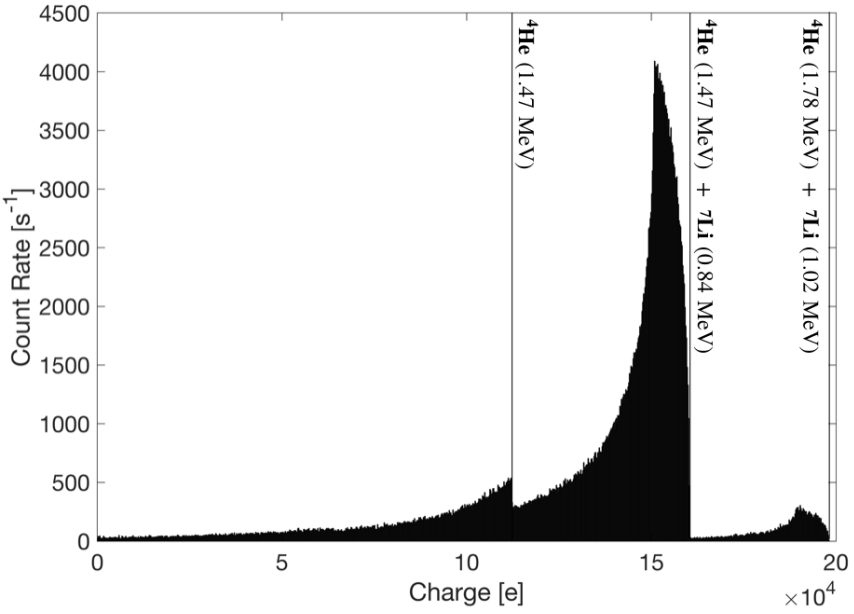

Figure 7.9: Simulated spectrum for an enriched sandwich layer detector. Charge pulses [e] are plotted (bin width = 200 e) against count rate [s^{-1}]. Dominant peaks are resolved at the sums of ion energies according to the interaction of neutrons with ^{10}B.

The sandwich detector differs by the set of dominant peaks that are observed. The highest peak occurs at $\sim 160,000$ e, which is most likely caused by the simultaneous detection of both the ^{4}He and ^{7}Li ions produced by the principal neutron interaction with ^{10}B. The peak occurs at an energy lower than would be expected if the entire sum of the energies was collected ($\sim 176,000$ e), and this is due to a finite proportion of energy being lost in layer A no matter where the particles are generated. The greatest amount of charge is produced by particles that are emitted directly normal to the detector plane, as they travel the least distance in layer A. There is therefore an angular dependence to energy deposited in layers B and B_0,

[†]The structure described here is not a true 4π detector as there will still be some uncounted particles that do not exit layer A, or are emitted laterally away from layers B and B_0.

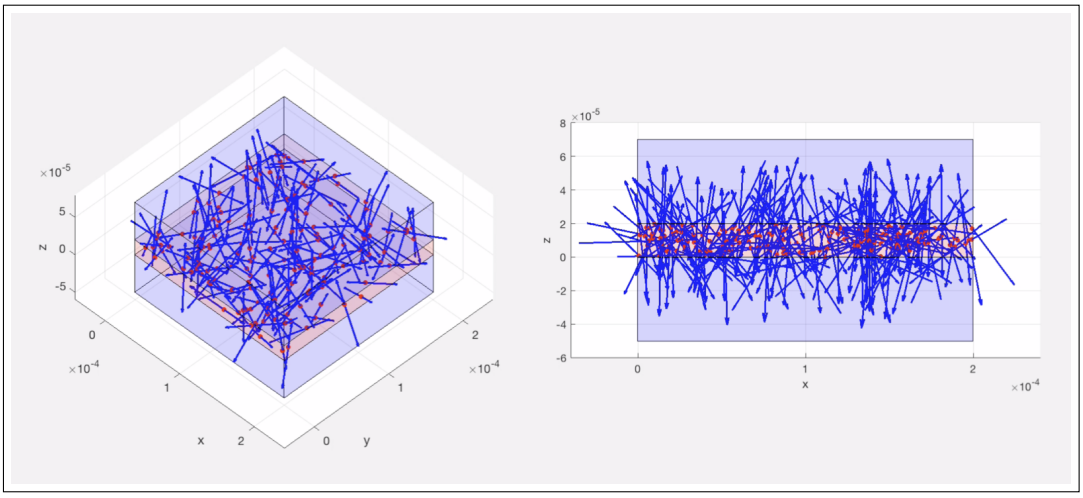

Figure 7.10: A screen-shot of the animation produced by the Matlab model during simulation of a sandwich detector structure. Red region indicates the active boron carbide layer A, blue regions indicate the diamond layers B and B_0. Red circles show neutron conversion events, generating particles with tracks shown by blue arrows. For clarity, the animation only illustrates a portion of the device and exaggerates particle tracks.

where the charge pulse is smaller for greater deviations from the normal, resulting in the high energy tail of the peak maximum. The low energy tail is produced akin to the two-layer conversion detector, by z-dependent energy straggling in layer A. A secondary peak is seen at $\sim 112,000$ e where the ^{4}He ion alone is detected, but the ^{7}Li is absorbed in layer A – similarly, it would be expected that there would be an equivalent peak at $\sim 64,000$ e for the converse scenario, although it is obscured by the tails of the other peaks. A second 'sum-peak' is observed at $\sim 195,000$ e concurrent with ion energies in the smaller proportion of the branching fraction.

The diode detector type is fundamentally different, in that charge carriers are also collected in layer A. The spectrum, irrespective of the electric field in the device (which is not considered in these idealised models), is presented in figure 7.11. As a result of the smaller ε value for boron carbide, equation (7.15), greater charge is generated in layer A than layer B and the spectrum is shifted towards higher bins. Major peaks are seen at $\sim$ 98,000 e (^{7}Li, 0.84 MeV) and $\sim$ 133,000 e (^{4}He, 1.47 MeV) which tail towards high energies and are convoluted with minor peaks at $\sim$

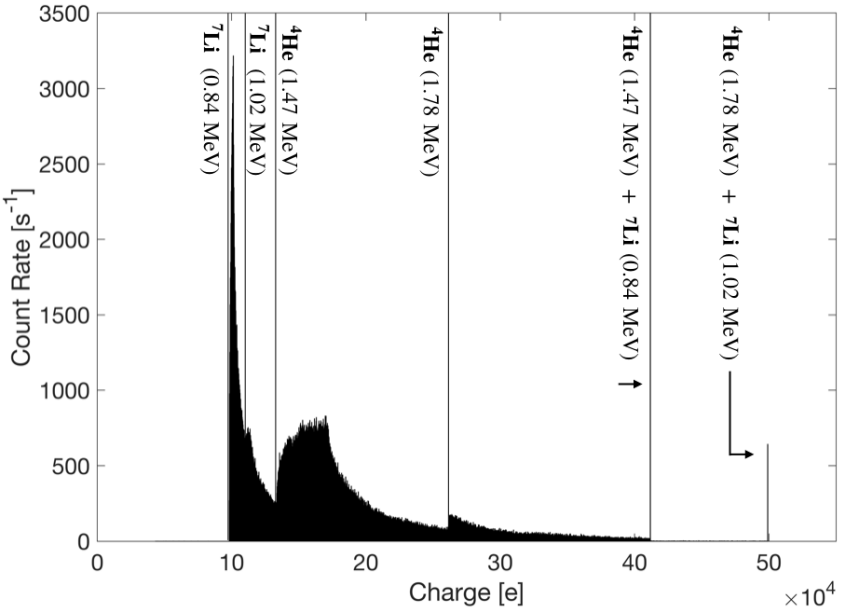

Figure 7.11: Simulated spectrum for an enriched diode detector. Charge pulses [e] are plotted (bin width = 200 e) against count rate [s^{-1}]. Shifted peaks – due to the smaller ε value in layer A – are resolved at the ion energies according to the interaction of neutrons with ^{10}B, as well as two narrow peaks at the sums of these ion energies.

110,000 e and $\sim$ 261,000 e produced by the smaller branching fraction. The high energy tailing is distinctive from the other device types. It is geometrically (almost) impossible for the diode detector to capture any less than the full energy of at least one particle – hence there is a definite low-energy cut-off below each signal peak. For the most part, the detector will capture the full charge of one particle and a fraction from the paired anti-parallel particle. The higher-energy tailing is therefore caused by varying fractions of the secondary particle energy contributing to the charge pulse, dependent on the spatial and angular properties of the particle pair. The distinct upward curve between 133,000 and 170,000 e is most likely caused by an angular dependence similar to that seen for the sandwich detector, although in this case maximum charge is generated when particles are emitted parallel to the detector plane and are absorbed fully in layer A. Additionally, two very sharp sum-peaks are seen for the eventuality that the full energy of both particles in a pair is

Detector Type	η_{conv}	η_{trans}	η_{th}	$\eta_{\mathbf{total}}$
Conversion	2.13	91.10	70.71	**1.37**
Sandwich	2.12	96.64	97.10	**1.99**
Diode	2.13	99.72	99.99	**2.12**

Table 7.2: The efficiencies of various detector types [%].

captured. The larger sum peak is truncated in the figure for clarity as it is contains a count rate of 13,250 s^{-1}.

The properties of each detector type contribute to their respective efficiencies, table 7.2. The efficiency of the conversion detector is seen to be improved by enrichment, with gains made in increased conversion efficiency against the results in table 7.1. Similar conversion efficiencies are observed for the other detector types, as expected, considering the identical layer A compositions in the model. However, differences are noticeable in the transduction efficiency – where the sandwich and diode detectors are geometrically able to collect more charge pulses; and the threshold efficiency – where the sharp, high energy peaks improve the performance of the sandwich detector, and the diode is nearly ideal due to the lack of low-energy tailing.

7.3.4 Active layer thickness

The results in figure 7.6 show a substantial increase in conversion efficiency with increasing active layer thickness, which should translate to an increase in total efficiency. However, the analysis above suggests that a considerable trade-off exists between the increased conversion probability and the consequent decreased number of ions that may be detected. In essence, a thicker layer A leads to fewer particles entering layers B and B_0 – and those that do, having lost a greater fraction of their initial energy. For conversion and sandwich detector types this is detrimental to overall performance, and hence it is useful to extract the global optimum thickness

in order to maximise total efficiency.

It should be noted that for an idealised detector there is no change in performance with an increase in the thicknesses of layers B and B_0. Theoretically, there is no upper bound to these thicknesses, although as will be shown, this changes when non-ideal physical effects are considered. The lower bound is determined by the maximum distances travelled by the charged particles and hence, $Z_b > d_a + d_b$ and $Z_{b_0} > d_a + d_{b_0}$. Hence, only optimisation of Z_a is considered for the case of an ideal detector.

Multiple simulations are carried out as Z_a is varied between 10^{-9} and 10^{-1} m, each time the spectrum is plotted and the efficiency components are calculated. For the conversion layer detector, spectra at Z_a = 0.1 μm, 1 μm and 10 μm are plotted in figure 7.12. For the very thinnest layer, sharp spectral peaks can be resolved because of relatively little energy loss in layer A; as the thickness is increased the peak resolution is gradually lost as the energies are uniformly straggled. However, count rate is seen to increase as more conversion events occur. Figure 7.13 shows how each efficiency changes with thickness. As expected, conversion efficiency (red) increases dramatically with thickness. However, the number of particles detected in layer B, transduction efficiency (blue), suffers at a near- equal rate. Additionally, the loss of spectral resolution and greater low energy tailing causes more counts to fall below the threshold level (50,000 e) (green). The oscillations that can be observed towards the higher thicknesses is a result of the greater importance of statistical fluctuations when fewer detection events occur. The total efficiency (black) is calculated to achieve a single maximum of η_{max} = 2.96% at 2.29 μm.

A similar response is seen for the sandwich detector, figure 7.14. Notably, the sum-peaks are very sharp and dominate at smaller thicknesses. However, with thicker layers the probability of detecting both particles in a pair diminishes substantially and the individual particle peaks dominate. In fact, at Z_a = 10 μm the sandwich detector spectrum resembles that of the conversion layer detector. The efficiency relationship, figure 7.15 is also similar, but benefits from greater transduction ef-

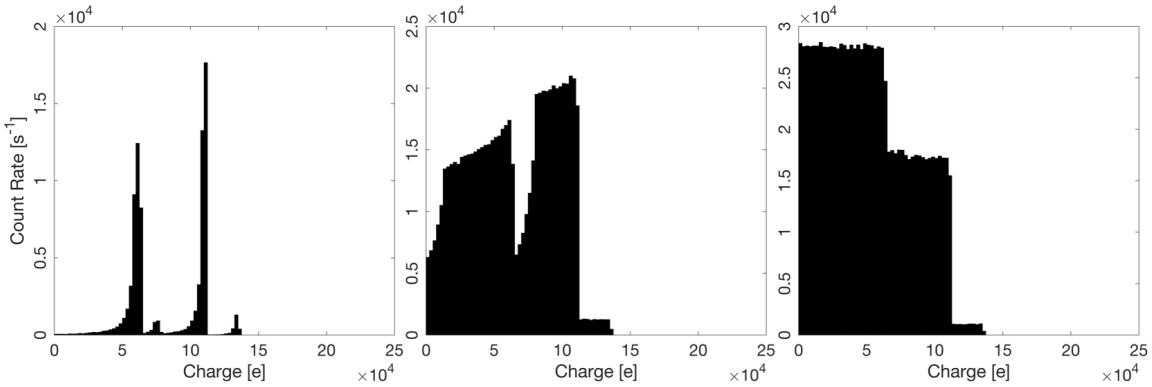

Figure 7.12: Conversion layer detector spectra plotted for active layer thicknesses: $Z_a = 0.1$ µm, 1 µm and 10 µm (left to right); binwidth = 2500e.

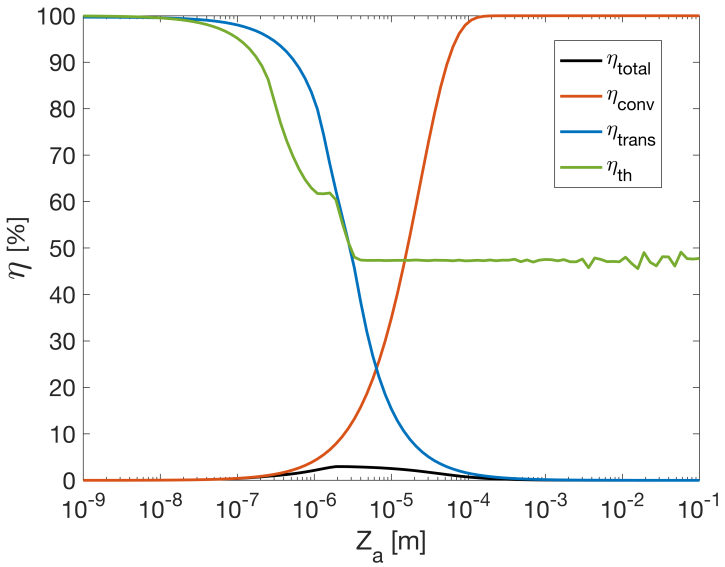

Figure 7.13: The variation of each efficiency component for a conversion layer detector with active layer thickness, Z_a.

ficiency due to the 4π geometry; as well as a larger threshold efficiency at greater thicknesses as a result of the higher energy sum-peaks. Consequently, the maximum efficiency is calculated to be $\eta_{max} = 6.94\%$ at 2.75 µm.

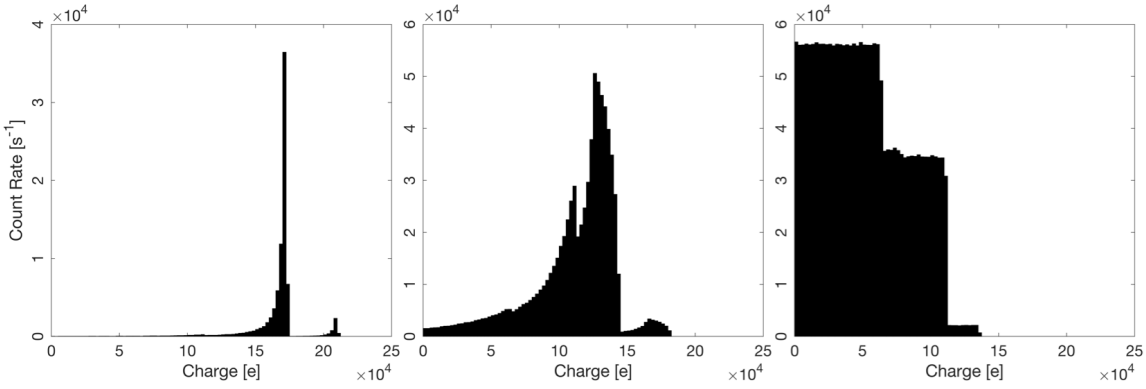

Figure 7.14: Sandwich detector spectra plotted for active layer thicknesses: $Z_a = 0.1$ µm, 1 µm and 10 µm (left to right); binwidth = 2500e.

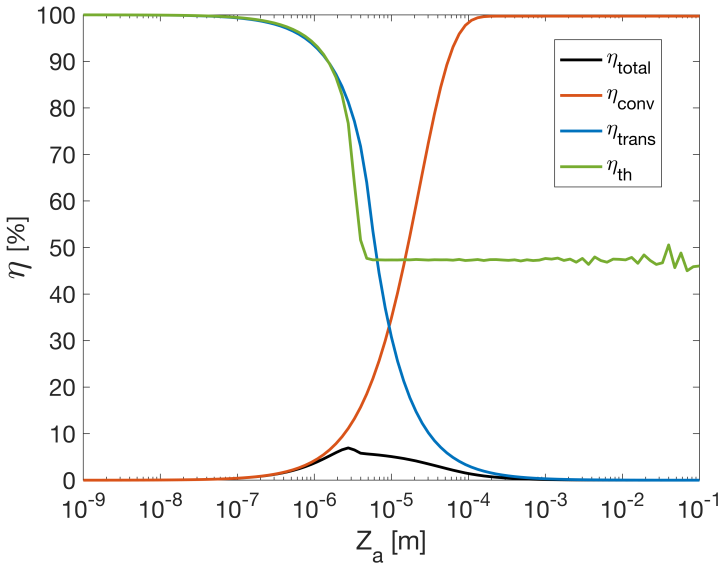

Figure 7.15: The variation of each efficiency component for a sandwich detector with active layer thickness, Z_a.

A very different relationship is observed for the diode detector. The fact that charge is also collected from layer A means that the compromise encountered for standard indirect detectors (eg. conversion and sandwich types) does not apply for direct detectors. As the layer thickness is increased, figure 7.16, the probability of measuring

the full energy of both particles in a pair increases. Hence the individual particle peaks broaden (by a similar mechanism to the detectors above) and diminish in size, but the sharp sum-peaks increase in magnitude and resolution. Taking the upper limit of an infinitely thick diode detector, nearly all ions will be fully absorbed and measured – which means that almost perfect efficiency can be attained, figure 7.17. The highest efficiency, $\eta_{max} = 99.72\%$, is achieved at thicknesses $>398\,\mu m$, where the detector is able to convert all incident neutrons.

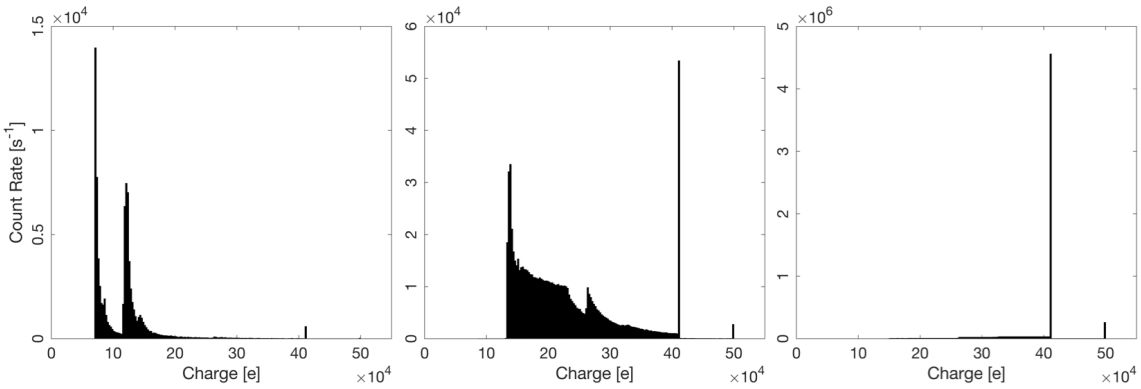

Figure 7.16: Diode detector spectra plotted for active layer thicknesses: $Z_a = 0.1\,\mu m$, $1\,\mu m$ and $10\,\mu m$ (left to right); binwidth = 2500e.

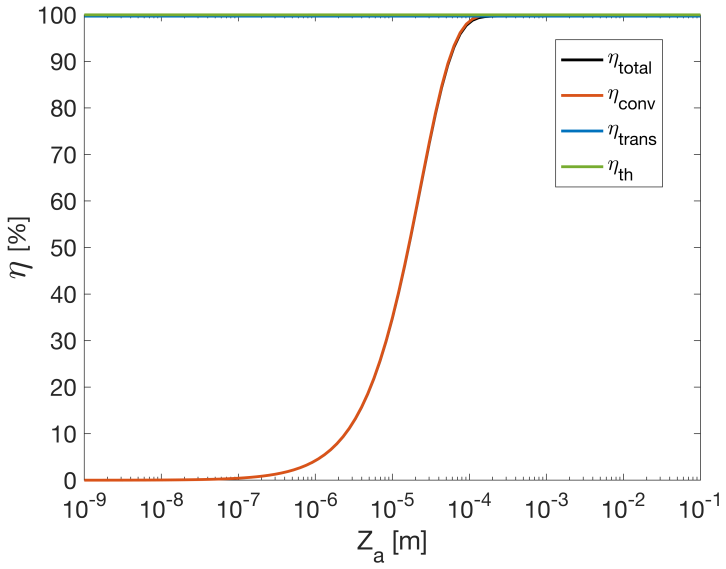

Figure 7.17: The variation of each efficiency component for a diode detector with active layer thickness, Z_a.

The maximum efficiencies for each detector type are summarised in table 7.3. There are two key caveats to these values. The first being that the threshold value is arbitrarily set at 50,000 e, and therefore the maximum efficiencies are likely to change if more or less discriminative detection is required. Secondly, is the fact that these calculations are carried out for an idealised model and so represent the highest theoretical value attainable, disregarding factors such as the statistics of generation and recombination of charge carriers and noise. It is therefore useful to study the effect of these components in further detail.

Detector Type	$\eta_{\mathbf{max}}$ [%]	$Z_a(\eta_{max})$ [µm]
Conversion	**2.96**	2.29
Sandwich	**6.94**	2.75
Diode	**99.72**	>398

Table 7.3: Maximum (ideal) attainable efficiencies for each detector type and the optimum active layer thickness.

7.3.5 Charge collection

The impact of charge collection statistics on the detector performance is complex. The Hecht equation, equation (7.23), gives an expression for the signal generated by a packet of charge deposited in a detector. The quotient of deposited to collected charge, known as the charge collection efficiency (CCE), is consequently dependent on a number of variable factors: the total thickness of the detector, D, and the charge drift distances L_e and L_h – which are themselves a function of the mobility-lifetime products of the semiconductor, $(\mu\tau)_e$ and $(\mu\tau)_h$, and the applied electric field ξ. It can be analytically inferred that a thinner detector, a larger mobility-lifetime product or a greater electric field all serve to increase the resulting signal produced by a deposited charge. However this is not always possible: the detector thickness is bounded by other efficiency factors (as outlined above); the electric field is limited by the breakdown potential of the materials and leakage currents; and the mobility-lifetime product is determined by various inherent properties of

the crystalline semiconductor(s) such as the presence of trapping sites.

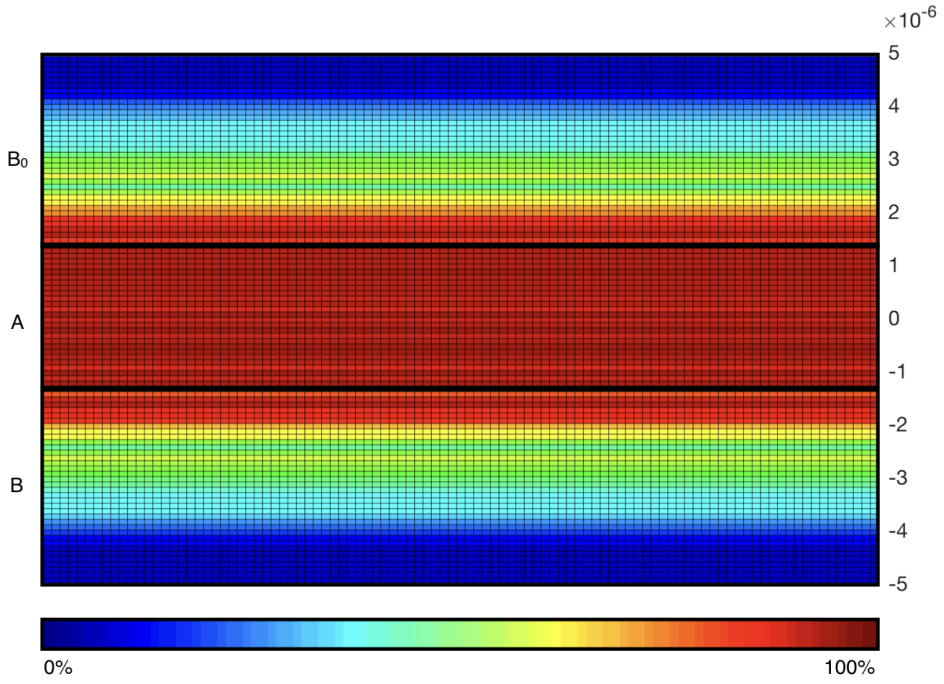

Figure 7.18: Heat map showing the relative (0-100%) distribution of charge within a neutron detector with Z_a = 2.29 µm (relevance of layer B_0 only applicable to sandwich detectors). Red indicates the highest charge deposition, blue indicates the lowest charge deposition. Notably, there is no charge deposited beyond $\sim$ 3 µm outside layer A due to the limited range of the ions.

Additionally, equation (7.23) asserts that the CCE is dependent on the position of the initial charge packet within the detector, r_0. This complicates the situation when there are numerous deposited charge packets – such as in the case of a neutron detector. There exists a spatial distribution of charge, as highlighted in figure 7.18, which consequently leads to a distribution in the CCE. Experimental measurement of the CCE is therefore a measurement on the *distribution* of the CCE as opposed to the measurement of a single value. For the following results the mean CCE, η_{CC}, averaged across all events is taken as an indicator of the overall detector CCE. It is useful to simulate η_{CC} for each detector type against these variables and compare them to typical experimental values.

Figure 7.19 presents η_{CC} plotted against electric field and mobility-lifetime product for a conversion layer detector (the plot is identical for sandwich and diode

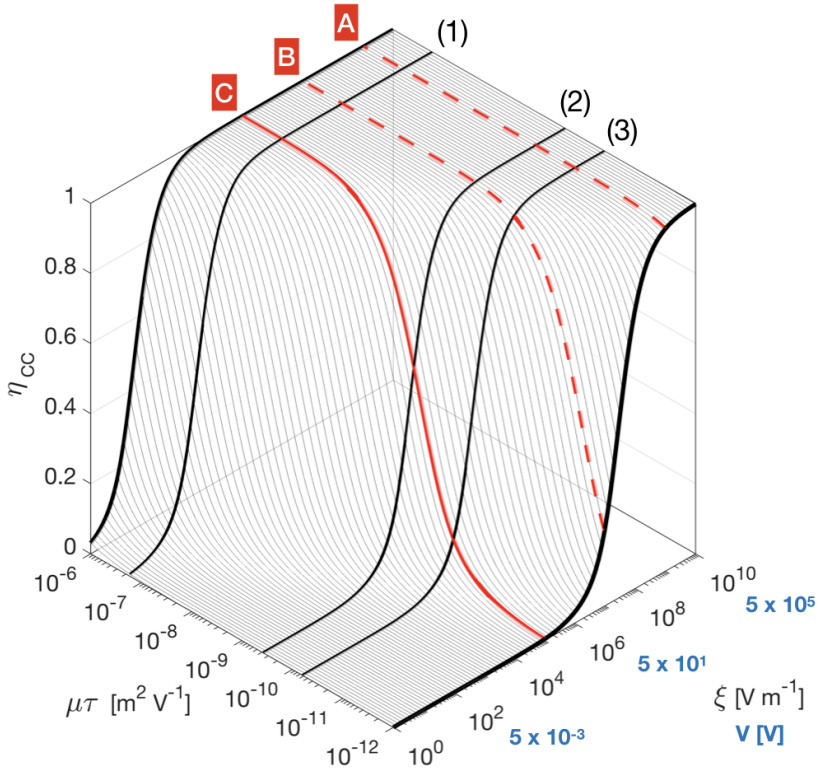

Figure 7.19: The charge collection efficiency (CCE) of a conversion layer detector, η_{CC}, calculated for a range of mobility-lifetime products, $\mu\tau$, for various electric field magnitudes, ξ. Labelled black lines indicate experimentally measured $\mu\tau$ values for diamond [242]. Labelled red lines indicate breakdown fields of: (A) diamond [245] , (B) boron carbide [246]; and (C) a typical experimental value. Voltages are shown in blue, calculated based upon a detector thickness, Z_b = 50 µm.

detectors). The CCE is calculated by simulation of each device at a constant layer thickness. Nominally, the idealised optimum layer A thickness is chosen: Z_a = 2.29 µm, along with Z_b = 50 µm. Simulations are repeated for different values of $\mu\tau$ in the range 10^{-6} to 10^{-12} m^2V^{-1}, as the electric field is swept between ξ = 1 - 10^{10} Vm^{-1}. For the purposes of generating figure 7.19 it is assumed that electrons and holes have the same mobility-lifetime products and are treated equivalently, therefore the direction of bias is unimportant. Similarly, in the case of the diode detector, the mobility-lifetime product of the diamond and boron carbide layers is assumed to be identical and are treated equivalently. In reality these values will differ and the result of this will be explored further below.

A number of electrical potentials are highlighted as red lines. Significantly, the estimated breakdown fields of diamond, $\sim 10^9\,\mathrm{Vm}^{-1}$ [245], and boron carbide $\sim 10^7\,\mathrm{Vm}^{-1}$ [246] – labelled A and B on figure 7.19, respectively. A typical applied field strength of $10^5\,\mathrm{Vm}^{-1}$ is also highlighted, C, to indicate the importance of mobility-lifetime product on CCE. The black lines represent electron mobility-lifetime products that have been experimentally measured for various diamond samples [242]: (1) single crystal diamond, $\mu\tau = 1.7\times10^{-7}\,\mathrm{m}^2\mathrm{V}^{-1}$; (2) polycrystalline diamond of average grain size 110 µm, $\mu\tau = 3.8\times10^{-10}\,\mathrm{m}^2\mathrm{V}^{-1}$; and (3) average grain size 25 µm, $\mu\tau = 0.6\times10^{-10}\,\mathrm{m}^2\mathrm{V}^{-1}$. The correlation of increasing mobility-lifetime product with grain size has been widely documented [247–250]. It follows that the presence of fewer grain boundaries reduces the number of trapping or recombination sites, and hence allows more charge to be collected. These values, (1) to (3) will be used as convenient reference quantities in the following analyses.

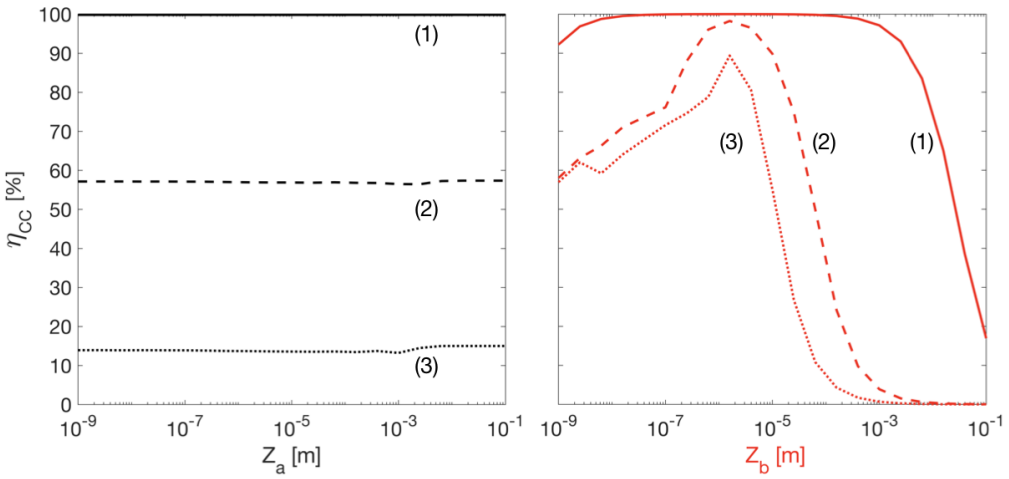

Figure 7.20: The relationship between η_{CC} and detector layer thicknesses for a conversion/sandwich device. Left (black), variation against layer A thickness, Z_a; right (red), against layer B thickness, Z_b. Curves are shown for three different $\mu\tau$ products: (1) $1.7\times10^{-7}\,\mathrm{m}^2\mathrm{V}^{-1}$, (2) $3.8\times10^{-10}\,\mathrm{m}^2\mathrm{V}^{-1}$, (3) $0.6\times10^{-10}\,\mathrm{m}^2\mathrm{V}^{-1}$.

The relationship between layer thicknesses and η_{CC} for a conversion layer (and equivalently for a sandwich detector) is shown in figure 7.20. The model is run for an electric field of $10^5\,\mathrm{Vm}^{-1}$ and $(\mu\tau)_{e,h}$ corresponding to the diamond grain sizes above – labelled (1), (2) and (3). The black lines on the left hand plots show the

change of η_{CC} with Z_a (for a fixed value of Z_b = 50 µm), and on the right, the red lines show the change with Z_b (for a fixed value of Z_a = 2.29 µm). There is no observable dependence on layer A thickness, which is to be expected considering that no charge is collected from this layer in conversion and sandwich detectors. In the case of layer B (and equivalently B_0), the lower values of $\mu\tau$ have a greater dependence on Z_b. For these values η_{CC} is zero for very thick layers, where the charge drift distance is much smaller than the detector thickness and all charge becomes trapped. As the layers become thinner, the CCE increases and peaks in the region $0.2 < Z_a < 10$ µm, although width and height of the peak is strongly dependent on $\mu\tau$. For the very thinnest layers η_{CC} decreases slightly and the trend becomes irregular. This is likely a consequence of the fact that very little or no charge is generated in an infinitesimally thin layer, and therefore the CCE distribution becomes irregular and dominated by random statistical fluctuations. It can be deduced that to maximise η_{CC} the optimal thickness of layers B and B_0 should lie in the peak range, although with better quality (greater $\mu\tau$) semiconductors the limit is less stringent.

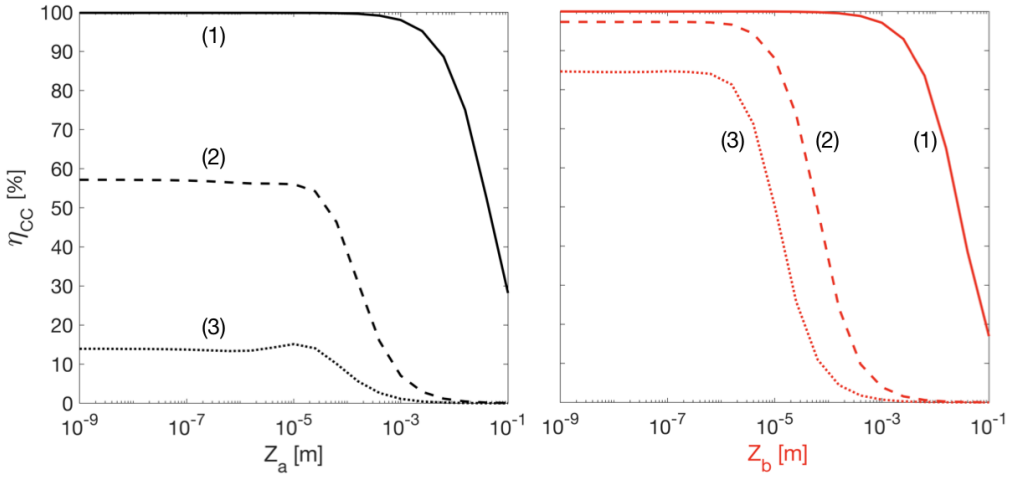

Figure 7.21: The relationship between η_{CC} and detector layer thicknesses for a diode device. Left (black), variation against layer A thickness, Z_a; right (red), against layer B thickness, Z_b. Curves are shown for three different $\mu\tau$ products: (1) 1.7×10^{-7} m^{2}V^{-1}, (2) 3.8×10^{-10} m^{2}V^{-1}, (3) 0.6×10^{-10} m^{2}V^{-1}.

Similarly, figure 7.21 shows the dependence of η_{CC} on the diode layer thicknesses. As for the conversion/sandwich detector, there is an optimal range in which Z_b must lie in order to avoid compromising η_{CC} – particularly for low $\mu\tau$ semiconductors

(albeit the trend is more regular than in figure 7.20 as the total detector thickness does not become incalculably thin as a result of charge collection in layer A). Importantly, there is also a strong dependence on Z_a. The optimisation studies for the idealised diode detector, table 7.3, suggest an unlimited upper bound to Z_a where a maximum efficiency of 99.72% may be reached for layers over 398 µm. Figure 7.21 shows that beyond $Z_a \sim 10$ µm the charge collection efficiency becomes a decisive limiting factor.

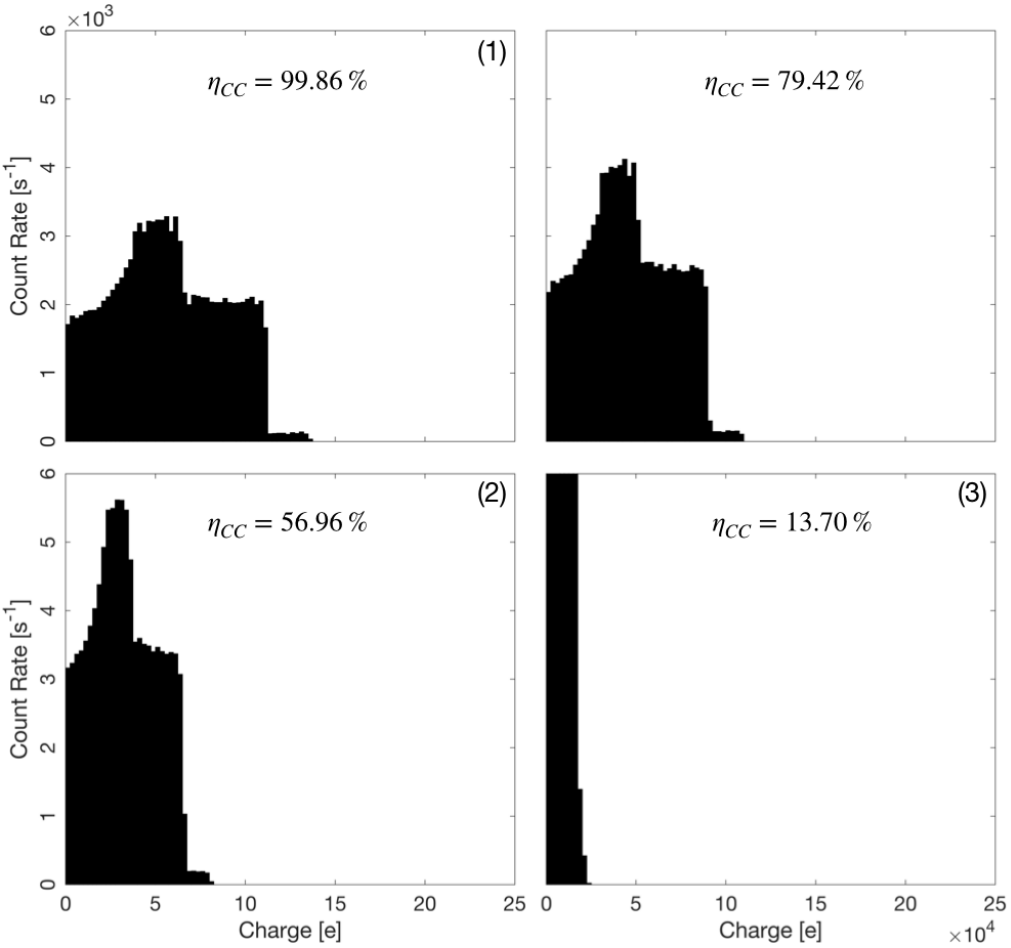

Figure 7.22: The simulated spectrum for a conversion detector with η_{CC} = 99.86%, 95.34%, 56.96% and 13.70% (top left to bottom right). Spectra labelled (1) to (3) correspond to experimental diamond $\mu\tau$ values.

Figures 7.19 to 7.21 establish the relationship between the properties of the detector and the charge collection efficiency. However, it is equally important to subsequently determine the relationship between the CCE and the resulting detector per-

formance. Figure 7.22 shows the simulated spectrum for a conversion layer detector at four different values of η_{CC}; including three corresponding to the experimental diamond $\mu\tau$ products (1)–(3). All spectra are plotted on the same axis scales to show the relative changes. For high CCE values (>95%) there is very little change in the spectrum, however below this the spectrum shifts substantially towards lower charge counts. This is to be expected given the fact that increased trapping reduces the size of the measured charge pulse. For very poor CCE, the shape of the spectrum is entirely lost and comprises of a large number of very low charge counts.

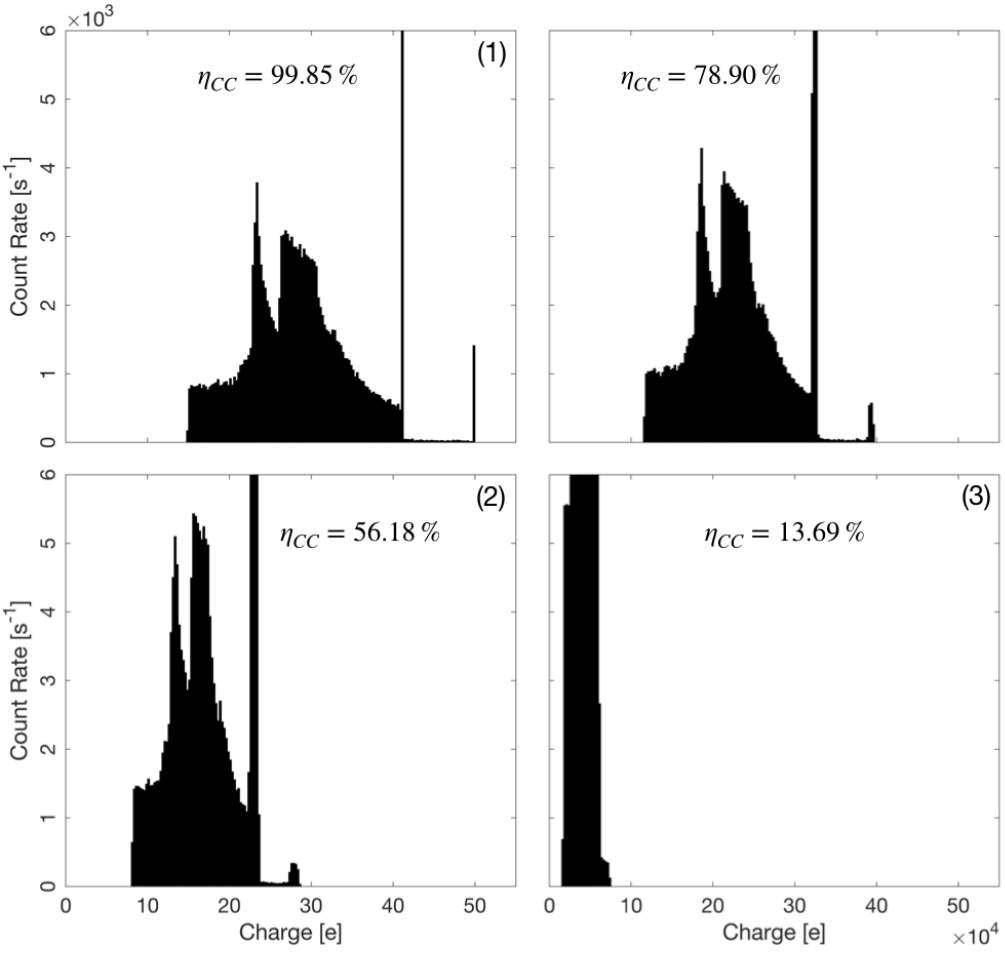

Figure 7.23: The simulated spectrum for a diode detector with η_{CC} = 99.85%, 78.90%, 56.18% and 13.69% (top left to bottom right). Spectra labelled (1) to (3) correspond to experimental diamond $\mu\tau$ values.

Less intuitive is the fact that the peaks are also seen to broaden – clearly illustrated in figure 7.23 for the case of the diode detector where the sharp, high energy

sum-peaks broaden significantly. This occurs as a direct result of the geometric distribution of energy loss, and hence CCE, in neutron detectors. Each charge pulse is shifted towards a lower charge value by a different amount, resulting in a spread about the mean shift. A drop in peak height is also seen due to the counts being divided between more bins (note that the top of the highest sum peak is cropped in figure 7.23). For decreasing values of CCE the spectrum shifts further and the peaks distort, akin to the conversion detector.

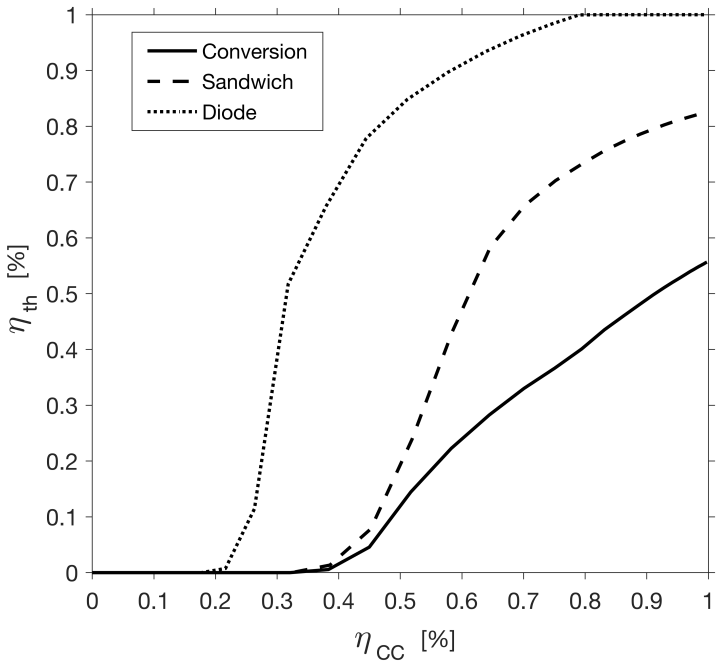

Figure 7.24: The threshold efficiency, η_{th}, of each device type, plotted against the CCE, η_{CC}. For all devices Z_a = 2.29 µm, Z_b (and Z_{b_0}) = 50 µm. η_{CC} is calculated for all values of $\mu\tau$ and ξ.

The spectral shift caused by imperfect CCE consequently means that fewer events are counted above the discrimination threshold (50,000 e) and a reduction in total detector efficiency should be expected. Indeed, figure 7.24 shows the relationship between η_{CC} and η_{th} for each detector type, calculated at Z_a = 2.29 µm and Z_b = 50 µm for the full range of $\mu\tau$ and ξ values. It can be seen that the threshold efficiency η_{th} decreases from its 'ideal' value as η_{CC} gets worse. Large drops in efficiency are observed for the detectors (most prominently the diode) as the major

peaks broaden and are shifted below the threshold limit. It is therefore clear that the CCE is not only crucial to achieving high spectral resolution, but also a detector with high counting efficiency.

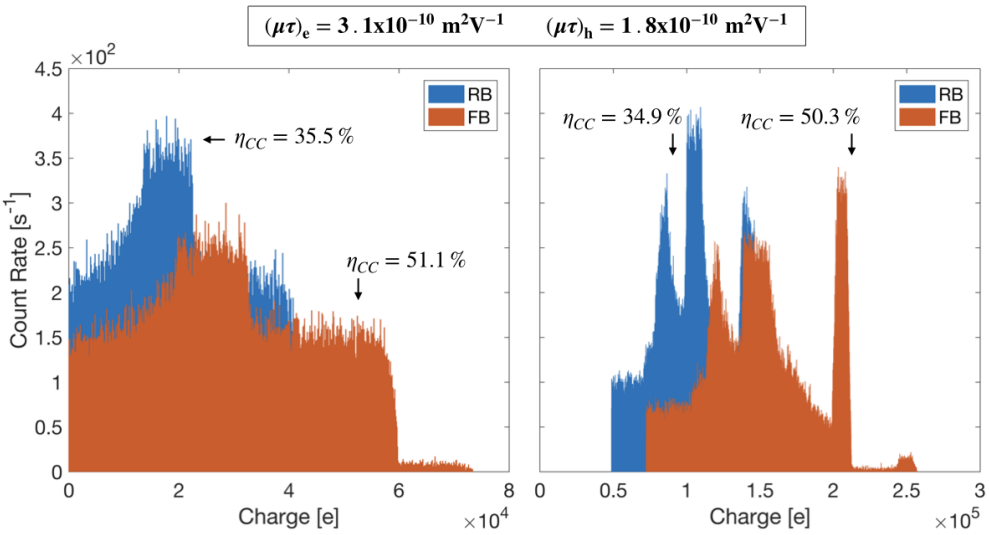

Figure 7.25: Simulated spectra for $(\mu\tau)_e > (\mu\tau)_h$. Forward bias achieves a higher η_{CC} and less distorted signal. Left: conversion layer detector, right: diode detector.

Finally, the spectra should be examined for the case where electrons and holes have different mobility-lifetime products. The above spectra are produced for the special case where $\mu\tau_e = \mu\tau_h$, and therefore it does not matter whether the signal is collected in forward or reverse bias – as the magnitude will be the same either way. However, in reality there is always a discrepancy in carrier mobilities, particularly in diamond where the hole mobility is generally limited. This introduces a preferential bias to the detector, and hence also differing spectra. Figure 7.25 shows the simulated spectra for the case that the electron mobility, $(\mu\tau)_e = 3.1 \times 10^{-10}\,\text{m}^2\text{V}^{-1}$, is greater than the hole mobility, $(\mu\tau)_h = 1.8 \times 10^{-10}\,\text{m}^2\text{V}^{-1}$. For the detector geometries considered in this work, the charge is inevitably generated much closer to one electrode than the other, figure 7.18. Hence, the induced signal will be almost exclusively due to the drift of either electrons or holes. In forward bias, where the majority of charge is generated near the cathode, the signal is primarily due to the electron current [251]. In reverse bias, the majority of the signal is due to holes. Lower hole mobility therefore leads to a shifted spectrum and smaller collection ef-

ficiency in reverse bias as seen in figure 7.25. For diamond, where the hole mobility may be limited, the preferred conversion detector polarity should be forward biased.

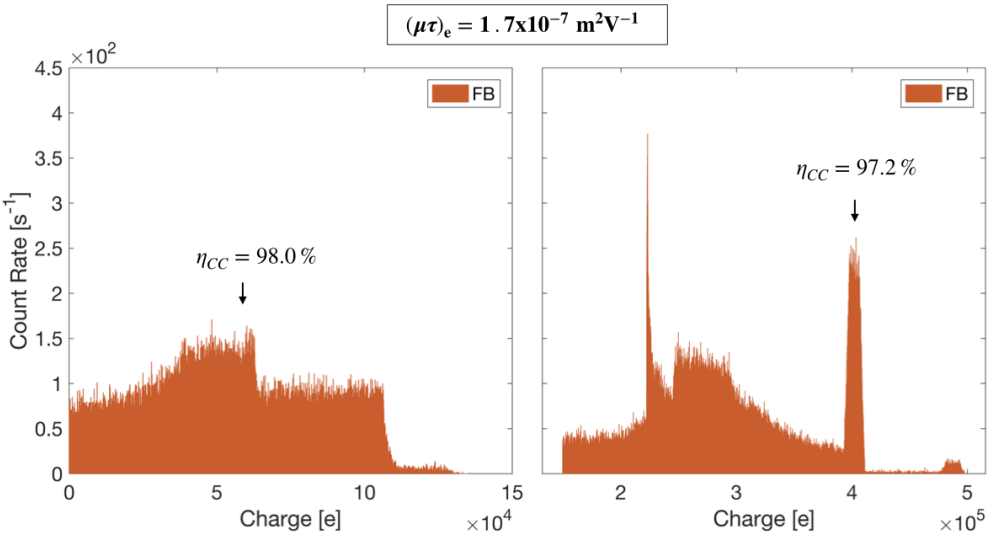

Figure 7.26: Simulated spectra for single carrier collection. Measurements are taken such that only electrons are collected. Left: conversion layer detector, right: diode detector.

Because the signal current is dominated by the contribution of a single carrier, in practise it is common to ground one electrode and to measure the charge from the other. The bias with respect to ground therefore determines the carrier that is collected. In the case that the current is collected at the anode, only the electron current will be measured. The spectrum in this instance is shown in figure 7.26 for $(\mu\tau)_e$ = 1.7×10^{-7} m^{2}V$^-$1. Notably, despite the high electron mobility-lifetime product, the spectrum is broadened slightly and the collection efficiency is reduced due to loss of the hole signal.

7.3.6 Spectral resolution

As investigated above, the trapping of charge leads to a broadening of the spectral peaks. However, this is not the only factor that causes a loss of resolution in a non-ideal detector. Electronic noise, and the statistics of charge carrier production, both also contribute to approximately Gaussian blurring of the signals. By isolating each effect individually and running the model, the magnitude and spectral change

of each physical component may be established. Figure 7.27 highlights the results of this experiment on the major sum-peak of the diode detector. The 'ideal' spectrum (shown in black) is extremely sharp and consists of a single charge bin at $Q = 4.117 \times 10^5$ e. This peak is centred with respect to the x-axis for clarity; the magnitude of the peaks is scaled such that they all have the same height and the y-axis is ignored. When the statistical charge generation is included in the model (green), the pulse is broadened by the normal distribution with a standard deviation, σ_{Fano}, given by equation (7.17). A Gaussian curve is fitted to the spectrum showing that this accounts for an increase in the FWHM of the peak by $\Delta Q = 935$ e and consequently a spectral resolution of, $R = \Delta Q/Q = 0.227\%$.

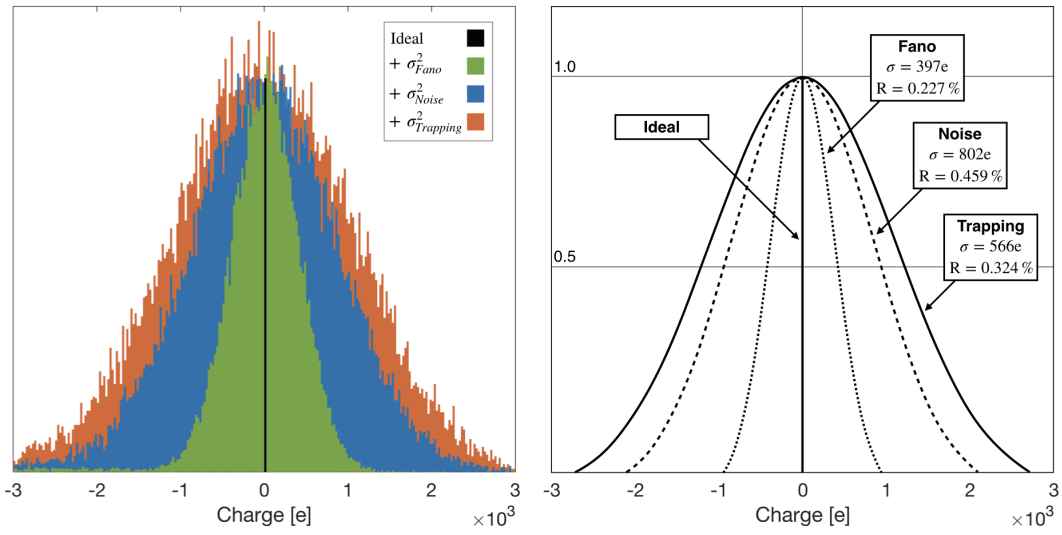

Figure 7.27: The effect of spectral broadening on the major diode sum-peak. Left figure: The 'ideal' peak at 411,700 e is shown in black, and centered to 0 e for comparison. Broadening due to statistical charge generation, scaled by the Fano factor, is shown in green. Electronic noise is shown in blue. The broadening due to charge trapping is shown in red, calculated for a CCE of 92.17%. Right figure: the broadened peaks are fitted by Gaussian distributions to extract their respective standard deviation, σ and resolution, R.

Additionally, when typical experimental noise is then factored into the model – with $\sigma_{Noise} \sim 770$ e – the signal is further broadened. Fitting another Gaussian curve, and assuming that the errors add in quadrature, gives a component increase to the FWHM of 1889 e and 0.459% resolution. Finally, the effect of trapping is included in the simulation, shown in figure 7.27 for $\eta_{CC} = 92.17\%$. Even for a

Source	ΔQ [e]	σ_Q [e]	R [%]
Fano	935	397	0.227
Noise	1889	802	0.459
Trapping	1333	566	0.324
Total	**2494**	**1059**	**0.606**

Table 7.4: The full-width half maximum (FWHM), ΔQ, standard deviation σ and resolution R for each individual source of spectral broadening, along with the total calculated value.

small reduction in CCE, a significant amount of resolution is lost. Characteristic of trapping, the peak is offset by 0.73% and is therefore shifted to align with the other peaks. A normal fit through the spectrum gives a FWHM of 1333 e and resolution of 0.324%.

Assuming that all these components add in quadrature, equation (7.35), the total broadening due to their combined effect is a FWHM of 2494 e, σ = 1059 e, and R = 0.606%. The values for the fitted distributions is shown in table 7.4.

$$\sigma = \sqrt{\sigma_{Fano}^2 + \sigma_{Noise}^2 + \sigma_{Trapping}^2} \tag{7.35}$$

7.3.7 Active layer thickness (non-ideal)

The simulations carried out for the ideal model, above, are repeated with the inclusion of non-ideal physical effects, namely: incomplete charge collection due to trapping, statistical charge generation, and noise. The thickness of layer A, Z_a is varied as the resulting efficiencies are calculated. Figure 7.28 shows the variation of each efficiency component against Z_a, with a fixed $Z_b = 50$ µm, for the conversion layer detector at the reference $\mu\tau$ values (1), (2). The deviations from the ideal model relate to electronic and signal effects, so no change in the conversion or

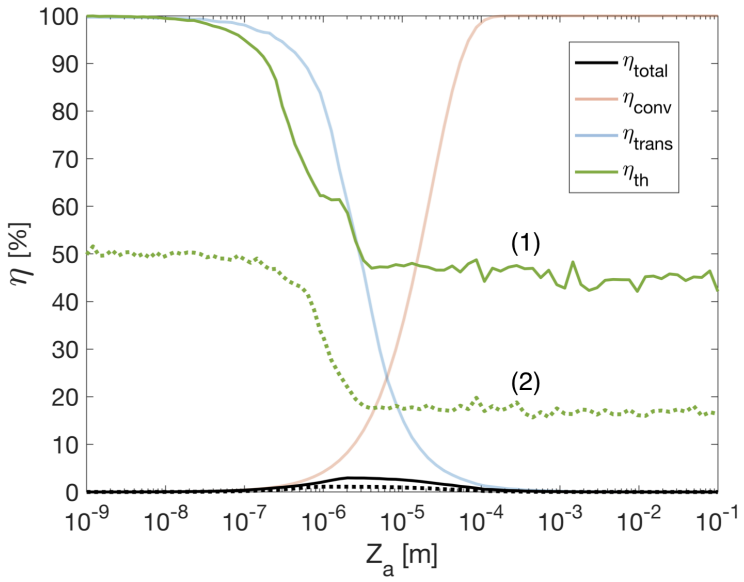

Figure 7.28: The variation of each efficiency component for a conversion detector with active layer thickness, Z_a. Threshold efficiency is calculated for diamond (layer B) $\mu\tau$ values (1) $1.7 \times 10^{-7}\,\mathrm{m^2V^{-1}}$ and (2) $3.8 \times 10^{-10}\,\mathrm{m^2V^{-1}}$.

transduction efficiencies should be expected – these are shown in the background of figure 7.28. The important change is in the threshold efficiency, which has been shown to be related to the spectral shift caused by imperfect CCE, figure 7.24, and any broadening effects that move counts below the threshold charge. For high $\mu\tau$ the relationship is nearly identical to that for the ideal scenario and the optimal values are very similar to those in table 7.3. However below this, the efficiency suffers greatly. For $\mu\tau$ (2), the threshold efficiency is limited to approximately 50% even for the thinnest layers. This is the effect of low CCE and broadening, causing the spectrum to be partially shifted below the detection threshold. As the thickness of the active layer is increased, low energy tailing shifts more of the spectrum below the threshold charge and the efficiency decreases accordingly. The maximum efficiency is reduced to 1.1% at a thickness of 1.9µm. At the lowest $\mu\tau$ (3), the CCE is so poor that the entire spectrum is shifted below the threshold and $\eta_{th} = 0$ for all values of Z_a – it is therefore not plotted.

Similar to the conversion layer detector, the sandwich detector resembles the ideal

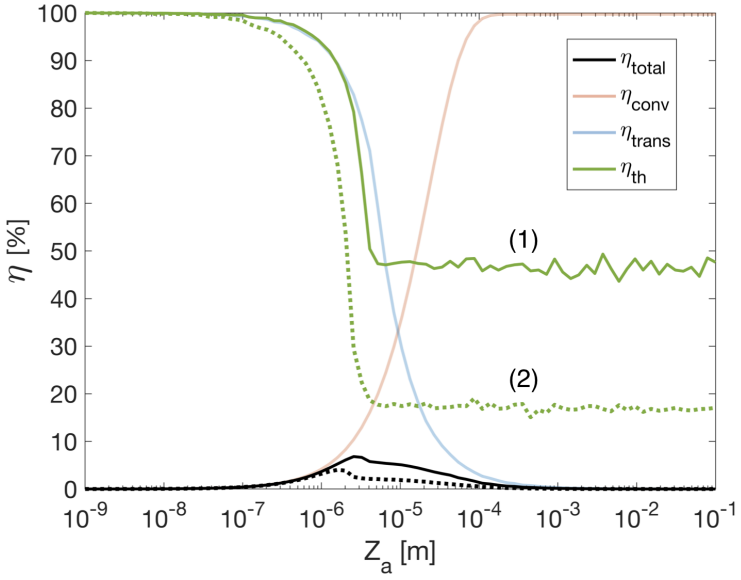

Figure 7.29: The variation of each efficiency component for a sandwich detector with active layer thickness, Z_a. Threshold efficiency is calculated for diamond (layer B) $\mu\tau$ values (1) 1.7×10^{-7} m^{2}V^{-1} and (2) 3.8×10^{-10} m^{2}V^{-1}.

case when the mobility-lifetime product is relatively high, figure 7.29. At $\mu\tau$ (2), the thinnest Z_a are still capable of achieving 100% threshold efficiency. This is because, despite losing charge to trapping, the spectrum consists of the very sharp higher energy sum-peaks that remain above the threshold. Increasing the active layer thickness tails the spectrum towards lower energies and the threshold efficiency drops dramatically. More so than the ideal case because the spectrum is shifted towards the threshold limit to begin with. The maximum efficiency is only 4.0% at 1.6µm in this instance.

For the diode detector the situation is more intricate, because unlike the other detector types the CCE in layer A is also important. This means that as Z_a is increased, the performance of the device will be increasingly limited by trapping in layer A. Figure 7.30 shows the various detector efficiencies as the thickness of layer A is increased, using the same $\mu\tau$ reference values as before and assuming that they are the same in both layers A and B. Figure 7.31 displays screen-shots from an animation produced by the model, showing the change in spectrum as Z_a is changed, for $\mu\tau$ (2). As with the other detector types, high mobility-lifetime products give

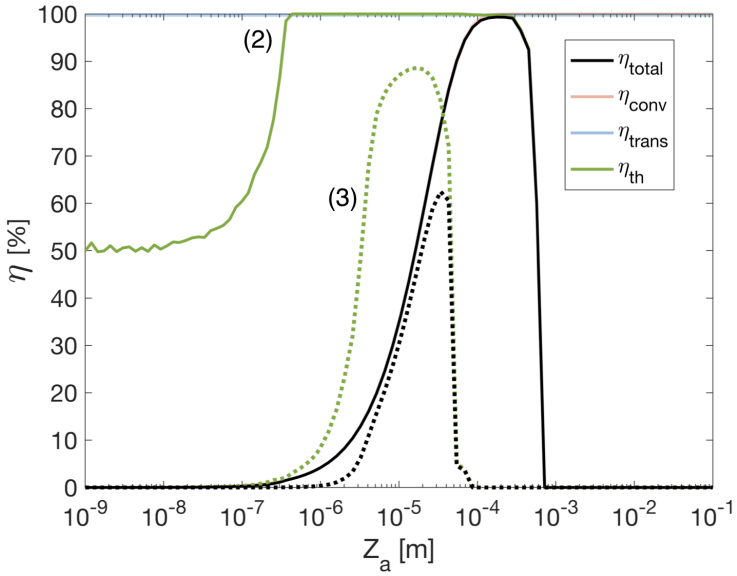

Figure 7.30: The variation of each efficiency component for a diode detector with active layer thickness, Z_a. Threshold efficiency is calculated for equivalent diamond (layer B) and boron carbide (layer A) $\mu\tau$ values (2) $3.8 \times 10^{-10}\,\mathrm{m^2V^{-1}}$ and (3) $0.6 \times 10^{-10}\,\mathrm{m^2V^{-1}}$.

responses very similar to the ideal case. Consequently $\mu\tau$ (1) is not plotted for clarity. For the lower $\mu\tau$ values, and when Z_a is very thin, the threshold efficiency is initially dominated by the limited charge collection in layer B. At these thicknesses, the spectrum is comprised of four peaks from the individual particle energies. These peaks are shifted to lower charge magnitudes due to trapping in the diamond layer and therefore, depending on the CCE, a portion of the counts sit below the threshold limit. As Z_a increases, and more of the ion energies are captured, these peaks broaden, shift towards higher charge bins and form high-energy tails. The sum-peaks become increasingly dominant. The majority of counts therefore lie above the threshold charge and the threshold efficiency reaches a maximum.

Beyond this maximum, the trapping in the boron carbide layer becomes significant such that the spectrum is shifted back down in charge magnitude. At a certain thickness, the entirety of the spectrum passes under the 50,000 e threshold boundary such that the total efficiency of the device becomes zero. The maximum thickness that can be obtained without compromise, and hence the maximum efficiency obtain-

able, can be seen to be strongly dependent on the CCE in both layers. Despite its relatively low magnitude, $\mu\tau$ (2) reaches a maximum efficiency of 99.3% at 158µm, whilst $\mu\tau$ (3) achieves a maximum efficiency of 62.5% at 34µm.

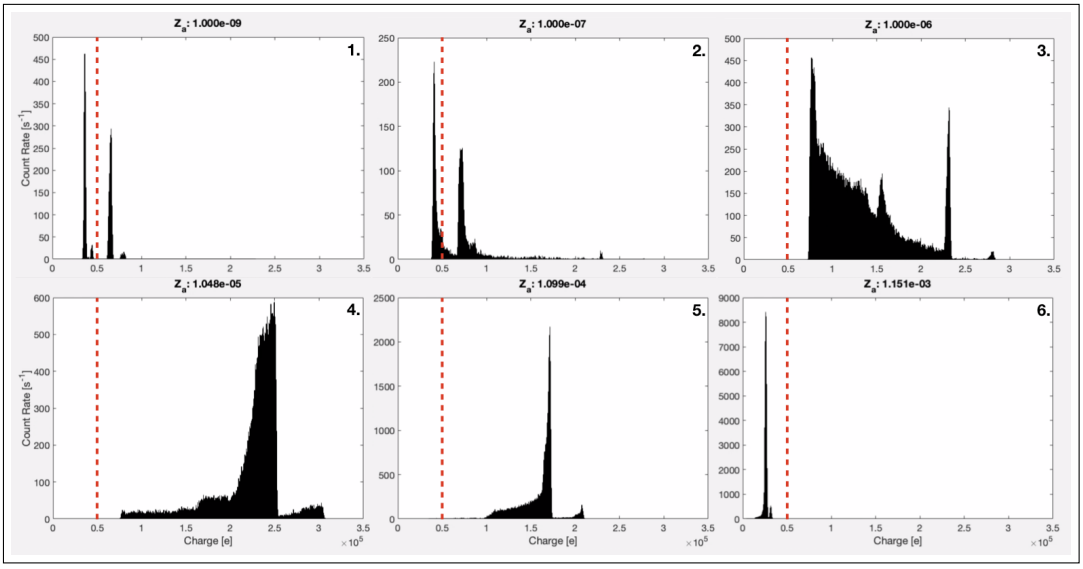

Figure 7.31: A screen-shot of the animation produced by the Matlab model during simulation of the diode detector spectrum, for various layer A thicknesses, Z_a. The spectrum is seen to change as the thickness is increased from left to right, top to bottom. Maximum threshold efficiency is obtained when the spectrum lies beyond the red dotted line (50,000 e).

It is clear that the maximum efficiency obtainable for each detector is intimately related to the mobility-lifetime product of the materials used. The relationship between maximum efficiency and diamond (layer B) $\mu\tau$ is shown in figure 7.32 for both conversion layer and sandwich detectors. This is derived by running a looped optimisation calculation over all Z_a thicknesses for several $\mu\tau$ values, where the apex of the η_{total} curve is determined each time. Diamond layers with $\mu\tau > 10^{-7}\,\mathrm{m^2V^{-1}}$ achieve the highest possible values, whereas below $10^{-9}\,\mathrm{m^2V^{-1}}$ the efficiency drops off substantially.

The equivalent study for the diode detector, figure 7.33 considers the efficiencies obtainable when the $\mu\tau$ is varied in both layer A, boron carbide, and layer B, diamond. Given the previous analysis, it is evident that the diamond CCE is the dominant factor when $Z_b > Z_a$, and boron carbide when $Z_a > Z_b$. However due to

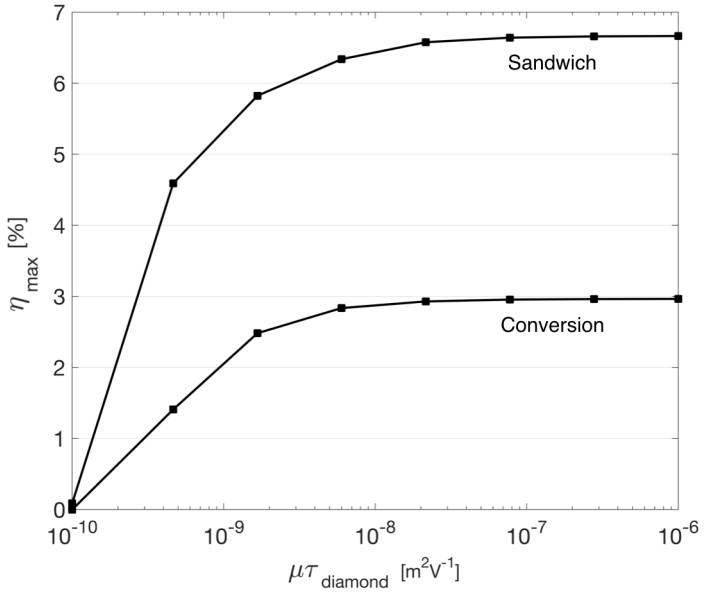

Figure 7.32: The maximum efficiency obtainable, considering full detector optimisation, for a conversion layer and sandwich device, as a function of diamond (layer B) $\mu\tau$.

the additional dependency of total efficiency on conversion rate, the point of inflexion is not trivial. Interestingly, as long as $\mu\tau > 10^{-9}\,\mathrm{m^2V^{-1}}$ in at least one of the layers, a very high efficiency should still be obtained. This result can be interpreted by the fact that a high diamond CCE causes the collected charges to be large enough for the spectrum to remain above the threshold, even at the moderate boron carbide thicknesses required for sufficient conversion.

Conversely, a high boron carbide CCE means that the upper limit on layer A thickness is relaxed, allowing 100% conversion to take place, even if large amounts of charge are lost due to trapping in diamond.

In the case that the mobility-lifetime products of both materials is poor, the efficiency drops off very quickly for boron carbide $\mu\tau < 10^{-10}\,\mathrm{m^2V^{-1}}$. This is because layer A needs to be so thin in order to maintain an un-trapped signal above the threshold, that the neutron conversion rate is almost zero. For diamond, the maximum efficiency falls more gradually beyond $\mu\tau = 10^{-9}\,\mathrm{m^2V^{-1}}$ as the peak threshold efficiency is squeezed to larger layer A thicknesses.

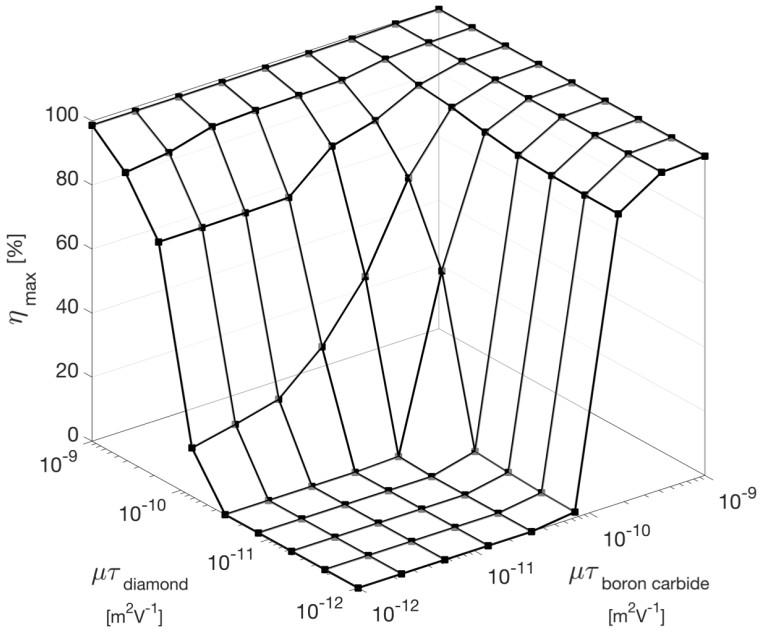

Figure 7.33: The maximum efficiency obtainable, considering full detector optimisation, for a diode detector, as a function of diamond (layer B) and boron carbide (layer A) $\mu\tau$.

7.4 Discussion

7.4.1 Idealised model

The results of a purpose-built Monte Carlo model have been presented above. The objective of the model is to provide new insights into improving the efficiencies of solid state neutron detectors using diamond.

Initially, an idealised model is used. This ignores physical effects of statistical charge generation, carrier trapping and electronic noise. Each optimisation parameter is considered in isolation, and following this method of analysis an idealised 'control' model is presented for the purposes of comparison. This control model represents the most basic solid-state detector design – a conversion layer detector – with arbitrarily selected structural and material parameters. The predicted spectral output of this detector is similar to that produced by other simulations, such as Monte Carlo analysis in more sophisticated packages like GEANT4 [252]. This

indicates primarily that the purpose-built model is functioning correctly.

The first efficiency increase is seen to come from enrichment of the active neutron-converting layer. By enrichment of the ^{10}B isotope in the boron carbide conversion layer, the efficiency of conversion may be increased substantially. The effect of enrichment fraction is, however, strongly dependent on the thickness of the active layer – where layers in the region of $\sim$ 1 to 100 μm benefit from the greatest improvement. Enrichment does not adversely affect other performance metrics of the detector and hence maximum enrichment ($\sim$ 99%) is key to the highest efficiency detectors.

The second performance improvement may be derived from modification of the detector structure. Direct extension of the conversion layer structure to a 'sandwich' detector offers charge capture over nearly twice the solid angle of the former. Not only are more particles captured within the sensitive diamond regions, but greater portions of the anti-parallel particle tracks are 'swept-out'. This results in larger energy pulses, including dominant peaks at the summed energies of both the ^{4}He and ^{7}Li, which may be counted well above the threshold boundary. This detector structure is consequently seen to improve both the transduction and the threshold efficiencies, resulting in a 45% uplift in total efficiency over the standard conversion layer detector.

An even greater performance improvement may be realised by using a 'direct' conversion structure. This leverages the ability to use materials that can both convert neutrons, as well as transport charge – allowing the capture of energy deposited in the active layer, too. Recent experimental studies [253–256] propose a diode device structure for this purpose. Similar to the sandwich detector, greater portions of the particle tracks may be captured increasing both the transduction and threshold efficiencies in concert. In the case of the diode detector spectrum, particularly sharp sum-peaks and distinct high-energy tails means that the threshold efficiency is essentially 100%. The diode detector improves on the conversion detector by 55%.

Finally, the optimisation of the ideal models is completed by iterative simulations across a continuum of layer thicknesses, with the intention of increasing the probability of neutron conversion against commensurate losses in transduction and threshold efficiencies. In the ideal scenario, the thickness of the non-neutron sensitive layers B and B_0 has no bearing on the total efficiency and is therefore not considered. Instead the crucial influence of active layer A thickness on efficiency and spectral output is determined. Both conversion and sandwich detectors lose considerable transduction and threshold efficiency as the thickness of layer A is increased. A compromise is seen between converting more neutrons overall, and increasing the energy deposited – and hence detected – outside layer A.

Alongside this, spectral resolution suffers as a result of greater geometrical straggling of the conversion products. Maximum efficiencies of 2.96% (at 2.29 μm) and 6.29% (at 2.75 μm) are attainable in conversion and sandwich detectors, respectively, as predicted by the ideal model. It should be noted that these values are strongly limited by the charge threshold that is selected – 50,000 e in this instance. In practise greater maximum efficiencies may be realised if the low energy background level allows a lower threshold to be set.

Similar analysis of the diode detector suggests an unlimited increase to the thickness of layer A that may be used without compromise. As such, a maximum efficiency of nearly 100% can theoretically be achieved at thicknesses of approximately 400 μm. Thicker layers see greater amounts of the anti-parallel ion paths being captured and an increasing prominence of the sum peaks.

The X and Y dimensions of the detectors do not need to be optimised given the symmetry of the planar geometries considered. Hence, the initial use of the model presents a complete optimisation of the structure of ideal detectors. It is straightforward to adapt the model to further geometries, both planar and non-planar – and for the modification of other parameters.

7.4.2 Inclusion of physical effects

The second phase of analysis comprises of simulating a selection of physical effects that are by no means exhaustive, but are considered to be fundamental to the performance of neutron detectors. The intention is to allow more realistic estimates of optimal parameters and maximum attainable efficiencies, within the limits and assumptions of the model. The most significant effect is that of charge collection, determined by the electron and hole transport properties of the detector materials.

Although not explicitly linked to the total efficiency of the detector, the charge collection efficiency (CCE) is shown to have a significant impact. The Hecht model of CCE is used in this instance, and modified for the particular structures considered. There are two parts to the analysis of charge collection: the analytical derivation of the relationship between material properties and the CCE; and the simulated implicit impact of CCE on the detector performance, both in terms of resolution and total counting efficiency.

For all detector types, the CCE is shown to be determined by the applied detector bias, and the mobility-lifetime products of the materials that are involved in charge transport. Typical predicted CCE values are calculated for various material values, and may be linked specifically to the quality and crystallinity of diamond [242]. Analogously this applies to boron carbide also, although for the purposes of these results, the $\mu\tau$ products are assumed to be the same.

Significantly, the relationship between layer thickness and CCE is derived. It is shown that, unlike in the ideal case, the thickness of layers B and B_0 are important for maintaining a high CCE. For diamond with high $\mu\tau$ products, such as single crystal diamond, thicknesses up to 1 mm may be used without significant compromise. Polycrystalline diamond requires layers in the range 0.2 - 10 μm to ensure complete charge collection. Layers as thin as these border on the limit of mechanical impracticability when using diamond neutron detectors in a real-world environment, and hence there exists the incentive to opt for the use of thicker layers of

higher quality diamond instead.

The second useful insight from this analysis is the loss of CCE with increasing active layer A thickness for diode detectors. Not only is the maximum attainable CCE greatly limited by the carrier mobilities in layer A, but there exists an upper limit to the thickness that this layer may reach without reducing the charge signal to zero. This conclusion is in direct conflict with the recommendations of the idealised model that the active layer in a diode detector may be increased without limit. In fact, CCE begins to drop from 158 μm even for the highest $\mu\tau$ products, and ~ 3 μm for poorer ones. Within this analysis lies one of the greatest disadvantages of a diode detector – very high efficiencies may be obtained in theory, but they are strongly dependent on the charge collection properties of the semiconductors that are used.

This notion is underpinned by the fact that the model shows an implicit link between CCE and overall detector efficiency. Low CCE contributes to a broadening and low-energy shift of the output spectrum, which serves to move more counts below the threshold limit. This effect is the same, independent of detector type, although the most dramatic change is visible in the sum peaks of the diode spectrum and has been verified experimentally for boron carbide diode neutron detectors [257]. Loss of threshold efficiency with CCE is quantified for each detector. The diode is shown to be the most resilient to poor CCE: the entire spectrum lies below the threshold limit for CCE lower than $\sim 25\%$ as opposed to $\sim 40\%$ for conversion and sandwich detectors. However it can be concluded that the threshold efficiency, and hence the total detector efficiency, is greatly impacted by the CCE.

It is shown that in the case of an imbalance in electron or hole mobility-lifetime product, that there exists a preferential bias, where a better signal may be attained depending on the polarity. For diamond the implications of this suggest that electron currents should be favoured over the lower-mobility hole signals – such that conversion or sandwich devices using diamond layers should usually be 'forward' biased (that is – the cathode being the electrode adjacent to the conversion layer, as

defined in the schematic figure 7.4). For the diode configuration, advances in doping favours the use of p-type diamond, which would invariably require detection in 'reverse' bias. Lower hole mobilities in diamond would therefore suggest that performance may be worse than if n-type diamond was used.

The spectral energy peaks produced by a thermal neutron detector are not related to the incident particle energy, hence the ability to resolve individual peaks for spectroscopy purposes is not a requirement. However, broadening contributes to loss of counts below the threshold limit; and an analysis of the components of this broadening may aid the interpretation of real neutron detector spectra, as well development of future spectroscopic detectors.

Three main sources of peak broadening are evaluated using the sharp (single-bin) sum-peak of the diode detector as a convenient reference. The statistical treatment of charge generation within the detector using an experimentally-determined Fano value for diamond produces the smallest resolution loss, 0.227%, and its effect is almost unnoticeable on any other part of the spectrum. It should be noted that the Fano factor measured for diamond is much larger than that predicted by theoretical models, and so may include the effect of other Gaussian broadening mechanisms. Trapping broadening is characterised and is shown to contribute a greater amount than the Fano spread alone. The amount of broadening is only characterised for a relatively large CCE and is expected to increase dramatically with lower $\mu\tau$. Additionally, tailing towards low energies and a deviation from Gaussian broadening would be expected, such as predicted by analytically derived expressions [258]. Using the Monte Carlo model for a more detailed study into the relationship of trapping resolution loss in neutron detectors would yield interesting results, and may be compared with other derived forms for relative broadening [259–262]. Finally, noise is considered and is the largest component in the analysis. The overall impact of the broadening sources is a loss of pulse height and increase in pulse width. The most notable is that of the largest diode sum-peak, which suffers a 99.35% decrease in height when physical effects are applied.

The ultimate utility of the model lies in aggregating these physical effects in order to provide a realistic design brief for the optimal neutron detector. The thickness optimisation simulation carried out for the ideal case is repeated with typical physical effects included. The key change is a greater influence of the threshold efficiency, which becomes an instrumental limiting factor for all detector types. For conversion and sandwich detectors, it is shown that the total efficiency is compromised substantially if diamond of $\mu\tau < 10^{-9}\,\mathrm{m^2V^{-1}}$ is used. Given the fact that conversion and sandwich detectors suffer from a very low ideal efficiency anyway, it is imperative that high quality intrinsic single crystal diamond is used for these devices.

In the case of diode detectors an interesting result emerges: the maximum obtainable efficiency of the device remains high ($\sim 100\%$) if the $\mu\tau$ of *one* of the materials in the heterojunction is above $10^{-9}\,\mathrm{m^2V^{-1}}$. In practise a number of factors will limit the ability to reach this efficiency. The first is that semiconducting boron carbide layers, as deposited by current processing methods, are highly amorphous and therefore contain high defect densities [263]. Hence, the mobility-lifetime product is estimated to be in the range $\mu\tau = 10^{-17}$ to $10^{-18}\,\mathrm{m^2V^{-1}}$ [264]. The lower mobilities may also inhibit efficiency by the fact that the longer charge rise time in boron carbide may create pulses that are not recognised by the signal processor. The model would suggest that this low $\mu\tau$ may be overcome by use of high quality diamond, however, the p-type doping required for diode behaviour increases impurity scattering to the detriment of mobility [37]. Given knowledge of the relative mobility-lifetime products, a major advantage of the model is its ability to predict the optimum layer thicknesses capable of maximising efficiency.

7.4.3 Limitations of the model

The model by no means provides a complete description in lieu of a physical experiment. The assumption that the detector is irradiated by mono-energetic, point-source neutrons vastly simplifies any real measurement environment. At the other end of the process, the model fails to account for the particulars of the signal pro-

cessing electronics. The exact parameters used and specifications of the hardware will have a significant impact on how the measured spectrum will appear. However the model does provide a very useful insight into processes that are local to the detector itself, which are relevant to the overall aim of improving neutron detection through detector optimisation.

Within this scheme, the model relies on a number of assumptions that can be justified within certain boundary conditions and degrees of idealisation. Future simulations can likely be improved by relaxing these conditions. The first is the assumption that neutron conversion occurs uniformly throughout the active layer. This is valid when the thickness of the layer is very thin, however conversion events will be increasingly concentrated towards the irradiated face of the detector for thicker layers. It is particularly important for diode detectors, where the conversion efficiency should be as close to 100% as possible and layer thickness is large. More charge will be deposited in the upper region of layer A, which, when considering a finite depletion width at the heterojunction, may cause less charge to be separated and collected. Additionally, ignoring the effect of the metal contacts - which are approximately 0.1 μm in thickness if standard processing is used - will have the effect of over-estimating the efficiency of the detectors. Particularly in sandwich and conversion layer devices where ions will suffer greater straggling.

The use of the Hecht equation for charge collection is also an idealised scenario. In materials where the de-trapping time is significantly shorter than the integration time of the pulse counting electronics, more charge may be collected than would be expected. A Monte Carlo extension of the Hecht approach includes these effects [265] and could be implemented in further iterations of the model. Additionally, the assumption of a uniform electric field does not apply across the space-charge region of the diode detector, and a modified equation may be used to account for this [266]. Finally, the it is assumed that the depletion region extends across the full width of the diode detector. This assumption is valid when the layer thicknesses are thin and the electric field bias is large enough to achieve full depletion, however for thicker

layers the depletion region will occupy a finite width at the heterojunction. This may stipulate a smaller 'effective' detection volume where charge may be generated and separated. Hence an improved optimisation model should include calculations on the depletion width, as well as the effect of the built-in potential, in addition to the other parameters considered.

7.4.4 Comparison to other models

There are a number of other studies that seek to solve a similar problem. Previously, analytical models [252] have been used to functionally approximate the spectral shapes that might be expected from boron carbide/silicon conversion layer and diode detector types. The aim is not to optimise the efficiency, but to allow distinction between detectors that are operating as conversion layer devices, and those that are truly converting neutrons and collecting charge directly. Other work [267] has used Monte Carlo analysis for the same purpose and obtained largely similar results. The model presented above can similarly be used to distinguish between conversion, sandwich and diode detector types, albeit with much greater comprehension owing to the additional complexity factored in. The work presented in [252] also compares against results generated using a well-established Monte Carlo toolkit, known as GEANT4 [268]. It is interesting to note that the predicted spectra appear very similar to the 'ideal' results presented by the model in this work. The advantage being that the model used here allows a much deeper understanding to be obtained through more flexible experimentation options and low-level insight into the mechanics of the model. Some work has been conducted into optimising the active layer thicknesses of various detector types [269], which generally aligns with the highly optimistic conclusions made in the present study for the 'ideal' case. However, although reference is made to the importance of charge collection efficiency of the detector materials, no simulations are carried out to characterise this. Additionally, there is no previous work that relates the extensive investigations carried out in this study to the properties of diamond-based neutron detectors.

7.5 Conclusions

A purpose-built Monte Carlo model for the simulation of diamond-based neutron detectors has been developed. Results are presented in a progressive order, starting with an un-optimised control model and ending with a complete physical simulation, to show the isolated effect of each model parameter as it is included and subsequently optimised for. By simulating the output spectra and efficiency components important qualitative conclusions can be made, alongside significant quantitative calculations for a range of typical values.

As such, it is shown that the ideal maximum efficiencies attainable for conversion and 'sandwich'-layer detectors are 3-6% and 7-14% respectively, depending on the variable noise threshold value. To achieve these optimised efficiencies active layers of respective thicknesses 2.29 μm and 2.75 μm should be used. In contrast a diode detector may reach a theoretical maximum of 100% if active layers greater than 398 μm are used.

The most significant outcome of the work follows, by notably linking the material properties of diamond and boron carbide to their charge collection efficiencies (CCE); and the consequent impact that a variation in CCE has on the detector performance. It is comprehensively shown that imperfect CCE leads to spectral broadening, a shift to lower energy values and reduced total detection efficiency. Alongside this, the total peak broadening is decomposed to exhibit that energy resolution (for example, 0.6%) is the result predominantly of electronic noise (0.46%), followed by charge trapping (0.32% at CCE = 0.92%) and statistical Fano broadening (0.23%). The variation of these values with detector properties can be explicitly modelled, paving the way for potentially improved spectroscopic performance of detectors. Finally, the effect of unequal electron and hole mobilities, and device polarity is explored.

This complete approach arrives at a number of recommendations for achieving highly efficient neutron detectors. Conversion and sandwich detectors must use the

highest possible quality single crystal diamond substrates with $\mu\tau > 10^{-7}\,\mathrm{m^2V^{-1}}$ to fulfil close to ideal performance. Below $10^{-9}\,\mathrm{m^2V^{-1}}$, as would typically be expected for polycrystalline material, the efficiency is curtailed significantly in the region of 1% and 4% (1.9 μm and 1.6 μm optimal boron carbide layer thicknesses), respectively. Even achieving these diminished efficiency values would require mechanically impractical diamond substrates with a thickness in the range 0.1 - 10 μm. Despite this, it is clear that the use of a three-layer sandwich geometry is an improvement on two layer conversion geometries – both due to charge collection over a greater solid angle, as well as higher-energy spectral peak signatures.

On the other hand, diode detectors show the most promising potential for realising the upper bounds of solid state detection efficiency. Taking into account the effects of charge generation, trapping and recombination, gives evidence to the fact that the theoretical maximum of 100% efficient detectors may not be realised. The overriding effect of finite mobility-lifetime products of the constituent semiconductors is to reduce the total efficiency, albeit the relationship is highly complex. This point is elucidated extensively by the interpretation of results generated by the simulations. The extraordinary conclusion is that the maximum obtainable efficiency remains very high as long as *one* of the materials in the p-n junction has $\mu\tau > 10^{-9}\,\mathrm{m^2V^{-1}}$. Where poor quality of both materials in the heterojunction is unavoidable, the greater loss in efficiency will be due to the CCE of the boron carbide active layer. This conclusion needs to be offset against the challenges of processing doped semiconductors with high mobilities, but leads the way to the realisation of very efficient diamond-based neutron detectors based upon p-n junctions. The further experimental development of these devices is presented in chapter 11, with the relevant background in appendix A.

Overall, the model makes a very important advance in the need expressed by Caruso [69] to improve the optimisation of heterostructures, and the concurrent understanding of the physical and electronic properties of their constituent materials.

Chapter 8

Machine learning for the prediction of stopping powers

8.1 Introduction

A crucial component when investigating the performance of a neutron detector is to accurately determine the range of the charged conversion products in each of the detection layers. These ions lose energy as they pass through a material; the energy loss dE of a particle traversing path length dx through a material is known as it's stopping power. The stopping power $S(E)$ of a material with density ρ is defined as,

$$S(E) = -\frac{dE}{dx} \tag{8.1}$$

alternatively the mass stopping power, which removes the dependency on the material density (and will be used hereafter), may be defined as

$$S(E) = -\frac{1}{\rho}\frac{dE}{dx} \tag{8.2}$$

and can be resolved into three components that contribute to energy loss in the medium,

$$S(E) = S_{el}(E) + S_{rad}(E) + S_{nuc}(E) \tag{8.3}$$

$S_{el}(E)$ is the electronic stopping power, due to inelastic collisions with atomic electrons causing ionisation and excitation; $S_{rad}(E)$ is the radiative stopping power, attributed to the emission of Bremsstrahlung radiation; and $S_{nuc}(E)$ is the nuclear stopping power due to elastic electromagnetic collisions with nuclei, in which recoil energy is lost to the atoms [270]. The electronic stopping power is the dominant component for 'light' ions ($Z \leq 10$), such as ^{4}He; although at low kinetic energies, the nuclear contribution also becomes significant. The radiative stopping power is proportional to $(m_e/M)^2$ where m_e and M are the electron and ion rest masses, respectively, and can therefore be considered negligible for particles other than electrons and positrons.

Considering the electronic stopping power alone, an ion loses energy to Coulombic interactions with atomic electrons in the material. To a first approximation, this can be described by the Bethe theory [271], which is derived upon the assumptions of the first-order Born approximation, namely:

- In the case of light particles ($Z \leq 10$): the velocity of the traversing ion must be much greater than the velocities of the atomic electrons. For the innermost K-shell electrons, this is true for $(\alpha Z/\beta) \ll 1$, where $\alpha = 1/137.036$ is the fine structure constant.

- For heavier particles ($Z \geq 10$): the amplitude of the wave scattered by the field of the atomic electron is insignificant compared with the amplitude of the undisturbed incident wave. Therefore demanding that $(\alpha z/\beta) \ll 1$, where z is the charge of the incident particle in units of electron charge.

The mass electronic stopping power can be written [272],

$$S(E)_{el} = \frac{4\pi r_e^2 m_e c^2}{\beta^2} \frac{1}{u} \frac{Z}{A} z^2 L(\beta) \tag{8.4}$$

where,

$$r_e = \frac{e^2}{m_e c^2} \tag{8.5}$$

is the classical electron radius, e is the electron charge, c is the speed of light in a vacuum, u is the unified atomic mass unit and A is the atomic mass number. $\beta = v/c$ is the particle velocity in units of the speed of light.

L is known as the 'stopping number' and can be expressed fully as,

$$L(\beta) = L_0(\beta) + zL_1(\beta) + z^2 L_2(\beta) - \frac{C}{Z} - \frac{\delta}{2} \tag{8.6}$$

which, if the first term is considered alone, forms Bethe's equation for the electronic stopping power,

$$L_0(\beta) = \ln\left(\frac{2m_e c^2 \beta^2}{I(1-\beta^2)}\right) - \beta^2 \tag{8.7}$$

$$S_{Bethe}(E) = \frac{4\pi r_e^2 m_e c^2}{\beta^2} \frac{1}{u} \frac{Z}{A} z^2 \left[\ln\left(\frac{2m_e c^2 \beta^2}{I(1-\beta^2)}\right) - \beta^2\right] \tag{8.8}$$

where I is the mean excitation energy of the material. As the Bethe equation is derived on the basis of the first-order Born approximation, the subsequent terms that constitute the stopping number, L, offer corrections to account for deviations from this approximation. These are the Barkas correction [273, 274], $zL_1(\beta)$, the Bloch correction [275], $z^2 L_2(\beta)$, the shell correction [276], C/Z, and the density effect correction [277, 278], $\delta/2$. These corrections are further outlined in appendix B.

For large particle energies ($E > 2$ MeV, in the case of alpha (^{4}He) particles) the corrections are negligible, and the Bethe equation provides a sufficiently accurate

prediction of stopping power. However, in the low energy regime ($E < 2$ MeV, for ^{4}He) the equation breaks down. Adjustments such as the shell correction become dominant and purely theoretical descriptions are insufficient. Additionally, at low velocities ions travelling through the medium are able to lose or capture electrons from the medium. This creates a charge shroud attributing the particle an effective charge $z^* < z$, which experiences a lesser stopping power. The lower the energy of the particle, the lower the effective charge and hence slower particles are able to travel further than Bethe theory would predict.

There are methods for attempting to describe the stopping power in this regime. A widely accepted approach is to use semi-empirical fitting formulas that provide adequate fits to existing experimental stopping power data for various incident ions and target materials; such as that proposed by Varelas and Biersack [279]. In particular, the principal parameters to this formula are provided by Ziegler [280–282], with other coefficients proposed by Watt [283]. These coefficients are compiled and published by the International Commission on Radiation Units and Measurements (ICRU) [272]. Additionally, Powers [284] publishes some fitting parameters for a limited number of compound targets, although most existing experimental data is provided only for elements restricting the utility of fitting formulas. In this case, compound stopping powers may be approximated as a weighted linear combination of the stopping powers for their atomic constituents – known as the Bragg additivity rule. However this suffers further errors:

- The elemental constituents themselves already contain errors as a result of the parameterised interpolant fits. These errors are compounded as they are propagated further.

- Stopping power is strongly influenced by chemical bonding of the atomic constituents (these errors can be 15% or more).

- Stopping power is influenced by the phase of the material. For example, solids have a tighter binding of the outer-shell electrons and therefore a lesser

stopping power.

- In highly crystalline materials, such as diamond, channelling effects reduce the stopping power for certain angles of incidence.

- These effects are all expected to be inter-related, but the associations are currently not well understood.

The accuracy of the Bragg additivity rule may be increased by applying it to molecular fragments, which already include the chemical bonding [285]. However this adds yet another element of approximation, source of error and increased computation. It is widely acknowledged [272] that improving the accuracy of the Bragg additivity rule by semi-empirical methods is better applied to interpreting existing data than predicting the stopping power of other materials.

The reality is that accurate stopping power data is crucial for applications such as medical radiotherapy, particle research, space technology, nuclear energy generation and wider industry. Inaccuracies may generate large errors in particle range calculations, which are derived by integration of the stopping power with respect to energy (equation (7.9)). Ideally data is required for a vast number of elements, mixtures and compounds; for a large range of incident ionising particles; and across the complete energy spectrum.

As shown above, the present understanding of particle energy loss in matter does not allow for an analytical solution to the stopping power formula at low energies. There is a corresponding incompleteness of experimental data in this regime, and the parameterised approximations currently used to solve these problems are burdened with errors and the inability to generalise well to other ions and target materials. Machine learning (ML) methods are therefore perfectly placed to provide an alternative solution; using the current incomplete experimental datasets to predict unknown values. A novel concept is presented in this chapter whereby an ML algorithm is trained and evaluated with the goal of achieving a complete model – capable of accurately predicting the stopping power values for any feasible inci-

dent ion, energy and target material. Additionally the final algorithm is then used to produce predicted stopping power curves for both diamond and boron carbide – necessary for the simulations of neutron detectors in chapter 7.

8.2 Experimental methods

8.2.1 Objective

The objective of this work is to train and optimise a machine learning model that is capable of predicting mass stopping power values. The model should take inputs for any incident ion: from protons $Z = 1$ and alpha particles $Z = 2$, to heavy ions such as uranium $Z = 92$; for any target material: pure elemental materials, complex crystalline, amorphous or polymeric compounds, and mixtures of varying composition; in any state: solid, liquid or gas. The model should then be able to generate predictions for mass stopping power across a continuous incident ion energy range.

Key to the utility of the model is the ability to make fully 'blind' predictions. That is, for a given ion-target combination the model should never have 'seen' any prior experimental data. The model will be trained on a dataset comprising experimental data for numerous ion-target combinations and use complex learned feature relationships to infer the stopping power function for any new unseen combination. Second to this, the model must be fully generalisable to achieve consistent accuracy across the full range of ion-target combinations. Care must be taken to avoid 'overfitting' of the model to a particular subset of the data. Weaknesses and limits to the model, instances where the model fails to perform well or is biased, should be evaluated.

All cleaning, pre-processing, modelling and evaluation is performed in Python 3.7 using the Spyder IDE as part of the Anaconda 5.3 distribution.

8.2.2 Dataset

The training data is comprised of discrete experimental observations in the form,

$$\text{Ion, Target, Energy} \longrightarrow \text{Measured Stopping Power}$$

Over several decades these measurements have been taken by numerous independent authors and subsequently published in literature. The data is, in general, publicly-available in the form of journal publications and industry reports. Nevertheless, in the first instance, it is presented in a sparse and non-standardised format: hidden in text documents, written in multiple languages, with stopping power values quoted in different units, varying error levels and digit significance. To the immeasurable benefit of this work, alongside a wealth of previous citations, vast amounts of this data has been amassed and documented by Professor Helmut Paul, University of Linz. A unique and free-to-download database is provided by Prof. Paul on the website of the International Atomic Energy Agency, Nuclear Data Services [286]. The data comprises nearly all historical experimental data (most recently updated June 2018), across a full energy range from eV to GeV, for ions in the range $Z = 1$ to $Z = 92$, for approximately one hundred target elements, compounds and mixtures. The data is downloadable in the form of a .zip file. This is organised into sub-folders for each incident ion, which contain the experimental data for each target material. The data is contained across a total of 8,118 files.

However, the data in this form is, to a degree, non-standard and inconsistent – particularly for machine-learning purposes. The folder and file names are inconsistent in labelling format, numbering and capitalisation. The file extensions are unspecified. Some files are in located within incorrect folders. There are some files containing data from individual authors and some summary files for combined data. There exist duplicate data, files and folders. There exist many non-stopping-data containing files such as scripts and database system files. Some files are labelled with a non-obvious text symbol representing the material and some materials have multiple symbols. Additionally some energy data is presented in [keV] and some in

[MeV], and some stopping data is in units of [eV 10^{-15} cm^2 atoms^{-1}] and some in [MeV cm^2 mg^{-1}].

The files are therefore cleaned and prepared, both manually and by writing Python script, in the following process:

- Folders are renamed to be consistent and representative of the ion data that they contain. Folder name: 'ion', eg. He.
- Files are renamed to be consistent and representative of the ion-target data that they contain. File name: 'ion_target.txt', eg. He_Al.
- Files are converted to .txt type.
- Files that are deemed not to contain stopping data are deleted.
- Files that contain data by individual authors are deleted, files that contain summary data are retained.
- Files that contain inconsistent tabular formatting are deleted, files that contain numeric energy values in the first column and numeric stopping data in the second columns are retained.
- Files containing erroneous or incoherent data points are deleted.
- All units are standardised to energy [MeV], and stopping power [MeV cm^2 g^{-1}].
- Data is limited to an energy range from 10^{-3} MeV to 10^2 MeV.

The final dataset structure is of the form 'Folder: ion $\rightarrow$ File: ion_target.txt' in which the files contain two columns: Energy [MeV], Stopping Power [MeV cm^2 g^{-1}]. The process above is considered to be an efficient solution for handling the large and distributed data file, but has the inevitable downside in that a portion of potentially useful training data is lost. This could be extracted and processed to improve the future performance of the model. The 'cleaned' data is as described in table 8.1, with associated terminology to be used here on.

Name	Meaning	Number
Dataset	All cleaned experimental data	1
Ion	Incident particle	32
Target	Material under irradiation by the *Ion*	97
Combination	A unique *Ion-Target* pair	522
Sample	Each observation (row) in the *Dataset*, consisting of a single stopping power value given for a particular energy, *Ion* and *Target*	34,237

Table 8.1: A description of the terminology and quantities within the final 'cleaned' data.

8.2.3 Features

These data files are then further processed to make them suitable for training a machine learning model. This takes the form of feature extraction and pre-processing. Feature extraction involves extending the dataset to contain relevant values, or 'predictors', that may be predictive of the stopping power. By building a supplementary dataset of ion and target material parameters, the following feature vectors are generated: the atomic mass of the incident ion; the atomic number of the incident ion; the relative atomic (or molecular) mass of the target material; the state of the target material 'one hot' encoded as three binary vectors for solid, liquid or gas; the normalised fractional composition of the target material, encoded as a sparse matrix where each column represents an element in the periodic table and the values contained in the columns indicate the relative fractional composition of the target materials (ie. for pure aluminium, the column 'Al' will contain a value of 1.0 – whereas for aluminium oxide, Al_2O_3, the column 'Al' will contain a value of 0.4). Other features generated include the mean ionisation energy of the target material, the mean density of the target material, and a binary vector indicating whether the target material is polymeric or not. The final predictor of the stopping power is the incident ion energy derived from the experimental dataset. Equivalently, the value to be predicted is the experimental stopping power.

8.2.4 Model

The decision tree machine learning model – 'RandomForestRegressor' – is provided as part of the scikit-learn library in Python, version 0.19.1 [287–289]. During training, each decision tree is built from a number of samples of the input training data drawn with replacement, to produce a bootstrapped ensemble. A random subset of the features are used at each split – according to the principle of a random forest. The number of trees in the ensemble and the maximum number of features used when evaluating a split are both hyperparameters to be set. The sizes of the trees are left unrestricted, that is: the minimum number of samples required for a split to occur is set to 2; the trees are fully expanded until all the leaves are 'pure', i.e. they cannot be split any further, regardless of tree depth; and the minimum number of samples required at each terminal leaf node is set to 1. The number of trees used is 100; any increase in this number showed only a marginal improvement in model performance at the expense of a much greater computing time. Training is only performed on a single processing core, although this may be parallelised across multiple cores for speed improvements if required. The predicted output is calculated as the mean of the outputs of each tree in the ensemble. Through training on the features provided in the dataset and obtaining the best splits in each tree, the model becomes optimised to calculate outputs for any set of input features.

Only the random forest model is evaluated in this case. It was found that an MLPRegressor neural network model provided in scikit-learn took an unfeasible number of iterations to converge. Additionally, linear models such as LinearRegressor, Lasso and Ridge regressors were unable to provide satisfactory fits to the dataset, even with the inclusion of higher-degree polynomial features. Significant performance improvements could be gained in future model-optimisation studies. Performance improvements may also be found, inclusive of the random forest model, within a rigorous hyperparameter optimisation study using a methodical gridsearch.

8.2.5 Error metrics

Four error metrics are used to quantify the performance of the model in terms of the predicted values y_{pred} against the true experimental values, y_{true}. The first is the coefficient of determination, R^2,

$$R^2 = 1 - \frac{\sum(y_{true} - y_{pred})^2}{\sum(y_{true} - \bar{y}_{true})^2} \tag{8.9}$$

where the numerator of the fraction describes the size of the residuals (difference between predicted and true values) produced by the model; and the denominator describes the size of the residuals for a null model in which the regression predicts the average value, $\bar{y}_{true}$ [290]. The value of R^2 is a widely used metric to describe the 'goodness of fit' of a regression model to the observed data, in which a perfect model achieves a score of $R^2 = 1$. An arguably better metric for the 'usefulness' of a model is the root-mean-squared-error (RMSE),

$$RMSE = \sqrt{\frac{\sum(y_{true} - y_{pred})^2}{n}} \tag{8.10}$$

where the square root is taken of the sum of squared residuals, divided by the number of samples, n. The value of the RMSE is therefore expressed in the units of the quantity being estimated, in this case the stopping power, and therefore provides a more tangible accuracy metric. The RMSE represents an estimate for the standard deviation of the model (for an unbiased model it is equal to the standard deviation), which scales with the magnitude of the stopping power, and hence smaller values indicate a better model. The fact that the square of the residuals is summed means that it penalises large errors to a much greater extent. To avoid this, in the case where independent large errors are not relatively much worse than the overall errors, the mean-absolute-error (MAE) may be evaluated,

$$MAE = \frac{1}{n}\sum\left|y_{true} - y_{pred}\right| \tag{8.11}$$

which measures the absolute (unbiased) sum of residuals. Finally, the most intuitive – but also fundamentally limited – metric of error is the mean-absolute-percentage-error (MAPE),

$$MAPE = \frac{100}{n} \sum \left| \frac{y_{true} - y_{pred}}{y_{true}} \right| \tag{8.12}$$

in which the percentage deviation of the residuals is calculated. This metric is easily comparable with other work that quotes errors in terms of percentages, such as the ICRU reports [270, 272], however suffers from several drawbacks. The first is that a 'divide-by-zero' error may be encountered if the true value is zero (not an issue in this instance). The most significant, however, is that there is no upper bound on the percentage error for forecasts that are too high. Hence model optimisation based upon the MAPE metric will systematically favour models that make too-low predictions over those that are too high.

8.2.6 Model evaluation

Two extensive evaluations of model performance are sought. First, the ability of the model to fit regressively to the samples in the experimental dataset. The error metrics outlined above are calculated to indicate how well the predicted and experimental values align for each combination, as well as how well the model fits onto the dataset in general. This is achieved by training the model on the full dataset then making equivalent predictions for each sample.

This first evaluation is an assessment of the fundamental 'internal' performance of the model but not indicative of the 'external' predictivity of the model on new data that has not been used in training. Hence the second evaluation is on that of the predictions against 'unseen', new, data. In lieu of acquiring new experimental observations in a laboratory, a more practical (and statistically rigorous) method is to remove, or 'hold-out', a portion of the dataset known as the 'test data'. The model is trained on the remainder of the data, the 'training data', and then asked to make blind predictions on the test set.

The most rigorous method by which this can be implemented, in this instance, is by exhaustive leave-p-out cross-validation (LpO-CV). LpO-CV is a variant on leave-one-out cross-validation (LOO-CV), which involves holding out a single sample, training the model using the rest of the data and then using the model to make a blind prediction on the hold-out sample. The hold-out sample is rotated through the full dataset, with the model retrained each time on the remainder, until all the data has been used both for both training and testing. The total error of the model is given as the mean average of the error metric evaluated for each hold-out sample.

However, LOO-CV would give an unrealistically optimistic evaluation of the model performance since each combination contains several closely spaced samples, allowing the model to perform the simpler task of interpolation to make the prediction. The ultimate utility of the model lies in its ability to predict the full energy range stopping power for combinations with no existing experimental data. Hence LpO cross-validation is performed, whereby all samples for each unique combination are left out in turn. The model is trained on all other combinations and predictions are made on the p samples for the hold-out ion-target combination.

Finally, an evaluation is sought in the ability of the model to interpolate between discrete energy points where there exists no experimental data. This evaluation is essentially the ability of the model to 'curve-fit' to the experimental samples. It is difficult to quantify this performance without using LOO-CV, which would take an inordinate amount of processing time given the 34,237 samples. However, by implication, the upper bound to the ability of the model in this regard is the 'internal' model performance and the lower bound is the 'external' model performance on the LpO cross-validated test data. The evaluation may also be completed by qualitative assessment of the predicted curve shape across a wide range of energies.

8.3 Results

8.3.1 Dataset analysis

A fundamental problem when attempting to build a generalisable machine learning model is biased training data. Training data that under or over-represents certain features or qualities will, in the best case, result in a model that is better at some prediction tasks than others – and in the worst case, produce a model that heavily overfits to the nuances of the data and therefore is unable to generalise at all. It is therefore important to understand the key patterns within the dataset before training such that these biases can be understood or adjusted for. Unfortunately, any database that is made up of real-world observations will contain inherent sampling biases. In the case of the stopping power dataset, experimentalists are incentivised to make measurements of ions and targets that are useful to their specific field, and less so to improve the continuity of the existing knowledge base which may otherwise be scientifically irrelevant. Certain combinations will attract intense study and hence be indulged with many hundreds of observations by many authors. Others will be less so and may only contain a single observation by a lone author. Figure 8.1 is a representation of the distribution of samples within the dataset. The black squares represent a unique ion-target combination, in which the ion has atomic mass A_{Ion} and the target has relative atomic mass A_{Target}. The histograms represent the relative distribution of samples within the dataset for both ions and for targets, where the total area under each histogram is equal to the total number of samples, 34,237.

There is a noticeably greater density of combinations containing low mass ions: data exists for every ion up to $Z = 22$. Above that, the dataset represents only a fraction of the heavier ions up to $Z = 92$. The number of samples is heavily weighted towards the lighter ions, with hydrogen ($Z = 1$) and helium ($Z = 2$) the most commonly observed. The range of target materials favours lower relative atomic masses and lighter incident ions, although the distribution of samples is more continuous. Notably, the largest number of samples are recorded for gold ($A \sim 197$), aluminium

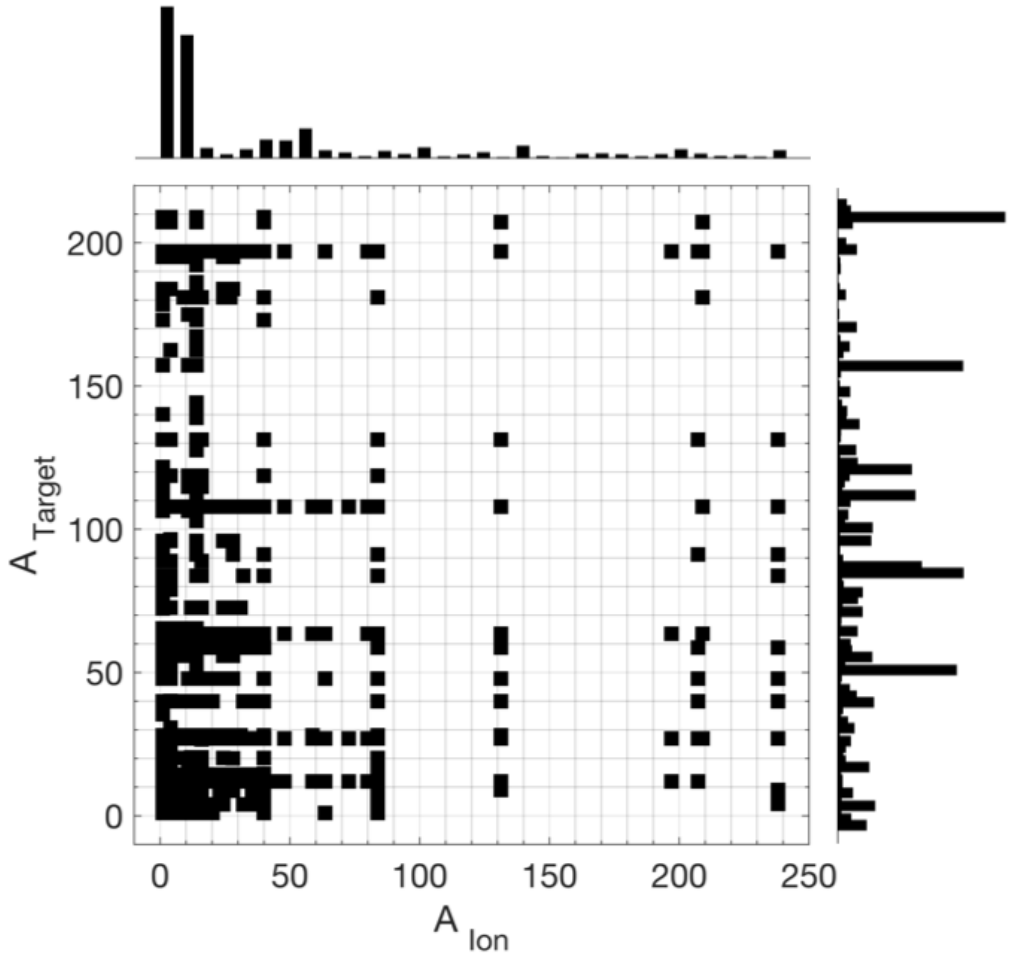

Figure 8.1: Distribution of combinations within the dataset by (relative) atomic mass, one square represents one unique combination out of 522. There are 32 ions along the x-axis and 97 targets on the y-axis. The histograms represent the total number of samples for each ion or target mass, a larger bar indicates more samples at that mass. For clarity, histogram x-axis not to scale.

($A \sim 27$) and silver ($A \sim 108$). The bias of the dataset towards the lighter combinations is unsurprising considering the relative abundance and utility of lighter ions and target materials. On average each combination contains ∼66 observations.

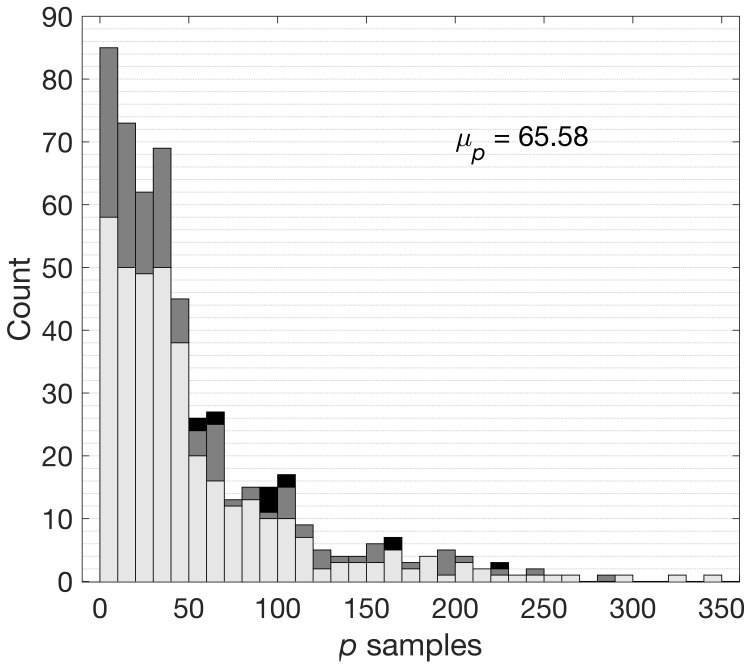

Figure 8.2: Number of samples, p, per combination. Of which solid (light grey), gaseous (dark grey), liquid (black) target materials. Mean number of samples for any single combination is ∼66. For clarity x-axis is truncated – not shown are individual bin counts for 10 combinations ranging up to 1078 samples.

However, the distribution of the number of samples p, figure 8.2, is heavily skewed towards small numbers of observations for each combination. The modal value lies between $0-10$ stopping power observations, likely contributed from a single study and not covering the full energy range. There also exist numerous samples with much greater numbers of measurements, including 10 combinations that are not shown in figure 8.2 with stopping power observations taken across the full energy range totalling between 350 to >1000 samples. 76.6% of the dataset is comprised of solid target materials (light grey bars), with the remaining 21.0% gases (dark grey bars) and 2.4% liquids (black bars).

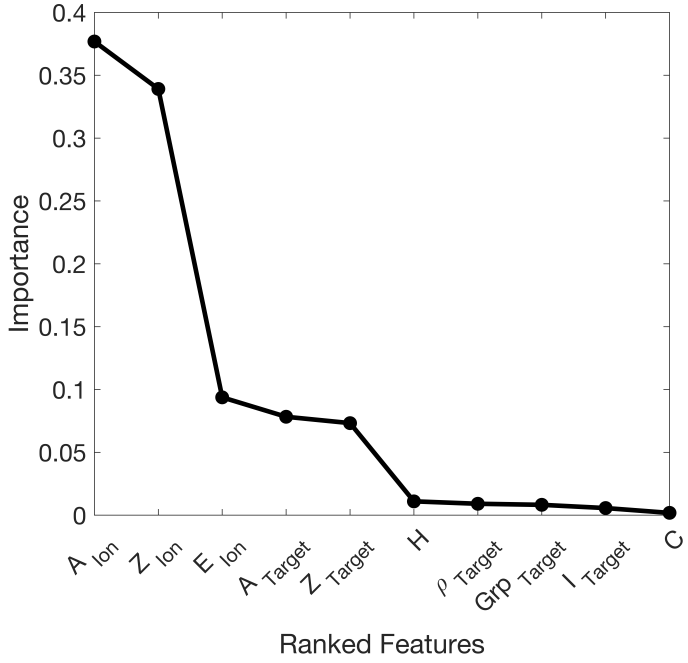

Figure 8.3: The relative importance of features listed for the top ten features: ion atomic mass, A_{ion}; ion atomic number, Z_{ion}; ion energy, E_{ion}; target (relative) atomic mass, A_{target}; target (relative) atomic number, Z_{target}; hydrogen fraction, H; target density, ρ_{target}; target periodic group, Grp_{target}; target mean ionisation energy, I_{target}; carbon fraction, C.

8.3.2 Feature importance

The relative importance of the features is calculated by the mean decrease in impurity (MDI) [291] – defined as the total decrease in node impurity, weighted by the number of samples reaching the node, averaged over all the trees in the forest. MDI gives an understanding of how much each feature influences the successful performance of the model. It allows the most useful features to be selected, and those that give little benefit to be removed from the training data. As a secondary consequence, feature importance may also give interesting insights into real-world, physical, correlations. The feature importance is calculated for each cross-validation and the mean values are taken. Figure 8.3 shows the ranked importance for the top ten features, out of a total of 121. The first five have an overwhelming influence on the model, namely, the (average) atomic numbers and masses of the ion and target, as

well as the ion energy. This is to be expected considering the form of the Bethe stopping power function at higher energies. It is notable that the mass properties of the incident ion are the most significant. Interestingly, the mean ionisation energy and density are much less important – and the physical state of the target material, and whether it is polymeric, are almost insignificant. The fractional target composition, comprising 109 elemental vectors, is also mostly irrelevant. The presence of these features apply individually to each target material – hence they are not key predictors. It should be noted that both hydrogen and carbon score higher than all other elements, which may either signify that the presence of these elements – or their various chemical groups – may more strongly influence the stopping power. More likely is that there is a bias attributed to the model through a higher number of hydrocarbon observations listed in the dataset. This would indeed mean that the model is performing more successfully on these materials but it has no physical correlation to the stopping power. Based upon this evaluation, the final features selected are: the ion energy, atomic mass and atomic number; the target (relative) atomic mass and atomic number and fractional elemental composition.

8.3.3 Performance on training data

The random forest regression model is trained by supervised learning on the full dataset. Each sample is represented by the vector of features described above and mapped to its associated experimental stopping power value. After training, predictions are made for each sample of the dataset to assess how well the model fits to the training data it has seen. The quality of a model can be assessed by comparing the model predictions against the original experimental stopping power values, figure 8.4. Very good correlation is observed, and nearly all points align with the black line that represents a perfect predicted outcome. The calculated value of $R^2 = 0.9989$ indicates an almost perfect fit to the 34,237 samples in the training data across the entire range of stopping powers. The calculated error metrics are displayed in table 8.2.

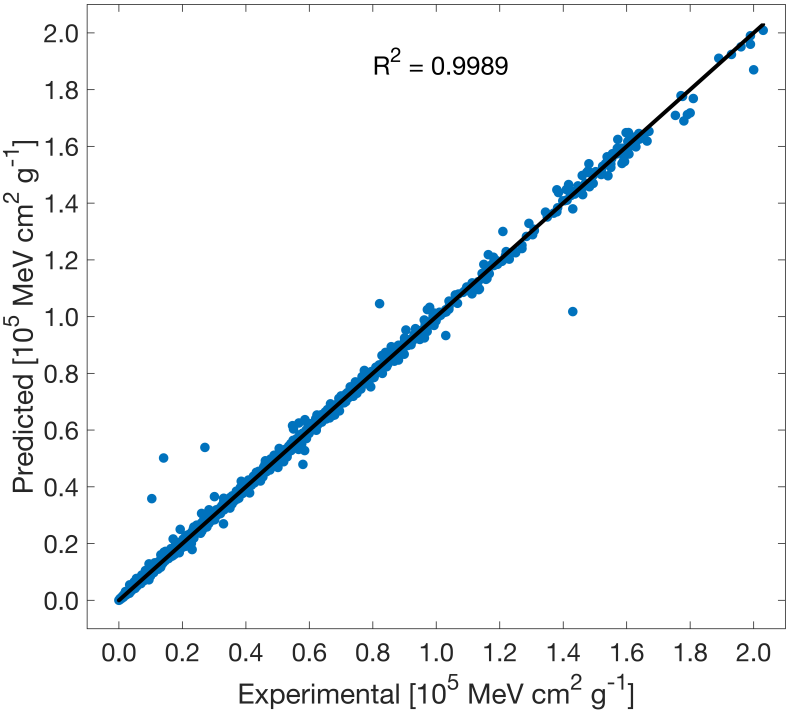

Figure 8.4: Predicted values for all samples plotted against their 'true' experimental values. Predictions are made by model on the training data used to generate it. High R^2 value and small deviations from the 'ideal' model (black line) are observed, indicating that the model fits very well to the dataset.

$\mathbf{R^2}$	**RMSE** [MeV cm^2 g^{-1}]	**MAPE** [MeV cm^2 g^{-1}]	**MAPE** [%]
0.9989	492.7	86.94	2.273

Table 8.2: Error metrics calculated on all samples in dataset, to 4 significant figures.

Errors are also calculated individually for each combination. The frequency distributions of these errors are shown in figure 8.5, along with their mean values. These values are different to those presented in table 8.2 because of their differing methodologies in derivation. Both the dataset as a whole, and the individual combinations, display low RMSE and MAE metrics in relation to the total variation in the stopping power values – from 0 to over 200,000 MeV cm^2 g^{-1}. Additionally MAPE is slightly greater than 2% across the full range of values. It can therefore be assumed that both the quantity of data and the architecture of the model is sufficient to iden-

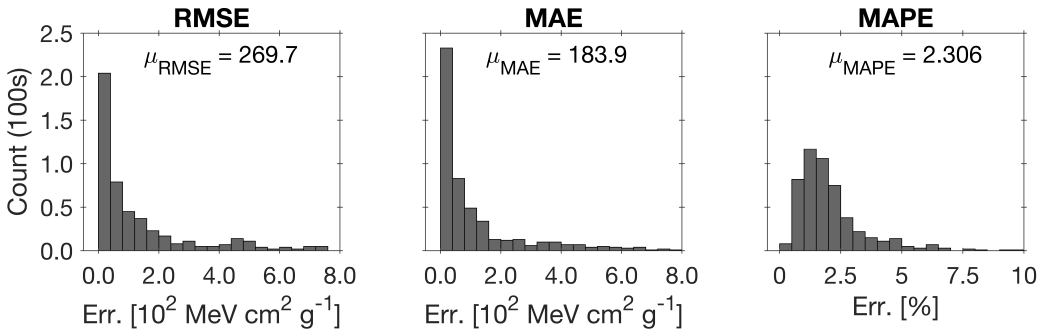

Figure 8.5: Error metrics calculated for each individual combination. Histograms show distribution of error magnitudes across all combinations in the dataset.

tify accurate relationships between the input features and stopping power values. This is indicative of a low bias model that is not underfitting the training data.

8.3.4 Performance on test data

The true test of a model, and key to its ultimate usefulness, is to generate predictions for unseen test data that has not been trained on. This is carried out using LpO-CV for each ion-target combination of p samples. Figure 8.6 plots the predicted values against experimental observations where each combination, in turn, has been held-out for test data. The predictions are therefore 'blind' and rely on the ability of the model to generalise well to new data to achieve good accuracy. Overall, the predictions align with the true experimental values. $R^2 = 0.9316$ suggests that the model is still fitting well to the test data. It is immediately clear that the majority of stopping power values within the dataset are distributed towards the lower end of the range. In this region, representing stopping powers for light ions incident on heavy targets, the model appears to make predictions very near to the 'ideal' values (black line). For higher stopping powers, associated with heavy ions incident on light target materials, the model is unable to make sufficiently accurate predictions and the spread increases proportionally. This is possibly symptomatic of the lesser quantity training data for higher stopping power values. Interestingly, a line of identical predicted values can be resolved at approximately 100,000 MeV cm^2 g^{-1}, suggesting a

possible overfit to a feature in the training data. There are a few additional 'linear' clusters of incorrect predictions that may also be attributed to this.

The R^2 value can be alternatively defined as a measure of the proportion of the variation in the predicted values that can be described by the model [290]. However the utility of a model lies in its overall accuracy and precision – not in how well it explains dataset variation. Hence RMSE, although not a metric for the success of the dataset modelling process itself, is a better indicator of the usefulness of the model. Table 8.3 gives the calculated error metrics on all the predictions as a whole. Given the broad range of stopping powers, up to 200,000 $\mathrm{MeV\,cm^2\,g^{-1}}$, an RMSE = 3,944 $\mathrm{MeV\,cm^2\,g^{-1}}$ is acceptable. The MAE = 814.8 $\mathrm{MeV\,cm^2\,g^{-1}}$ is several times lower and would suggest that the higher RMSE is due to a small number of very large prediction errors – possibly caused by overfitting or by the less accurate high stopping power values. The MAPE could approximately be interpreted as an overall 85% accuracy, with this accuracy expected to be greater for smaller stopping powers.

$\mathbf{R^2}$	**RMSE** [$\mathrm{MeV\,cm^2\,g^{-1}}$]	**MAPE** [$\mathrm{MeV\,cm^2\,g^{-1}}$]	**MAPE** [%]
0.9316	3944	814.8	15.03

Table 8.3: Error metrics calculated on all samples in dataset, to 4 significant figures.

Analysis of the error metrics for individual ion-target combinations can provide greater insight into the limits of the model. Figure 8.7 shows the distribution of errors calculated for each combination, along with the mean values. Only the lower end of the distributions are displayed for clarity, obviating the need to show a long tail of single-count bins. Since the RMSE and MAE scale in proportion to the magnitude of the stopping power, it is expected that the distribution of these errors will be in proportion with the stopping powers in the dataset. Correspondingly, the greatest number of counts is seen in the smallest bin (0-100 $\mathrm{MeV\,cm^2\,g^{-1}}$), and thereafter the majority of combinations have an RMSE and MAE below 1000 $\mathrm{MeV\,cm^2\,g^{-1}}$. The MAPE has a modal value between 4-8%, with a long tail (truncated for clarity)

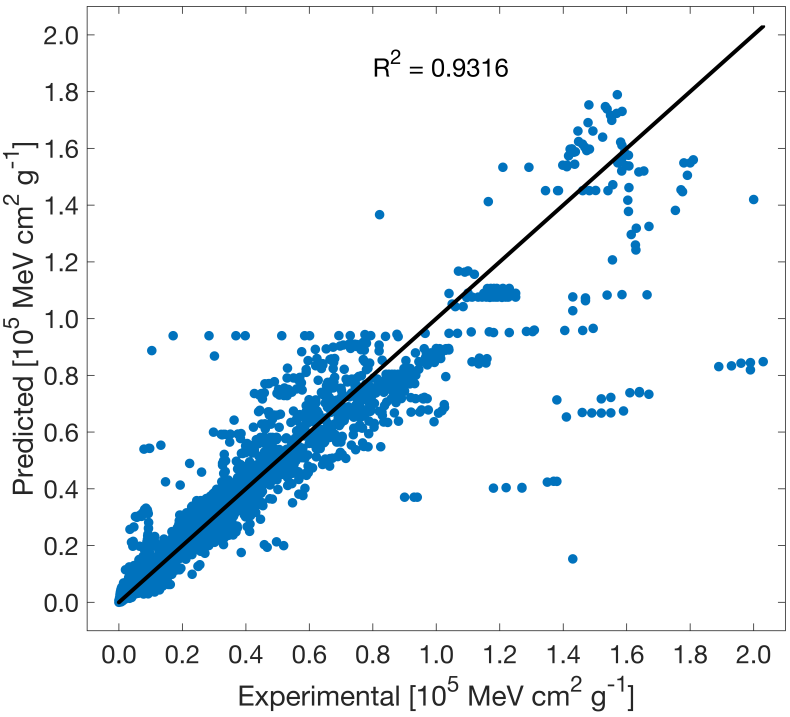

Figure 8.6: Predicted values for all samples plotted against their 'true' experimental values. Predictions are made by model on the unseen test data. An imbalance of data distribution can be observed. Better predictions are made for lower stopping power values, which are better represented in the dataset. Additionally, linear clustering, possibly caused by overfitting, reduces the predictive quality of the model.

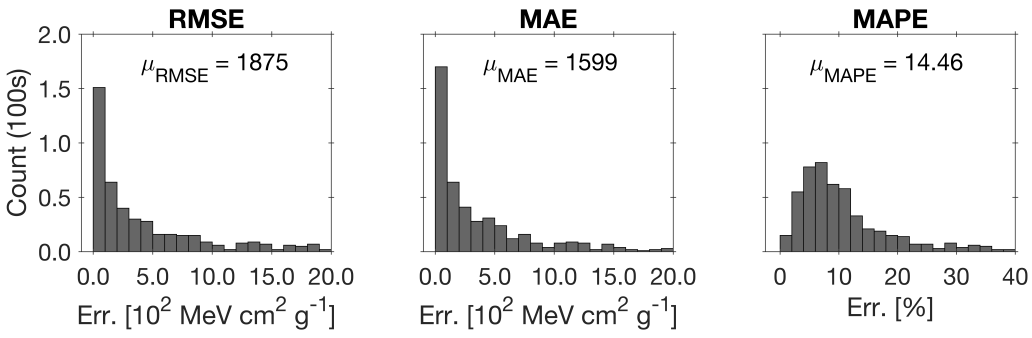

Figure 8.7: Error metrics calculated for each individual combination. Histograms show distribution of error magnitudes across all combinations in the dataset.

consisting of outliers with much higher errors.

It is useful to visualise the source of these outlier values and identify boundaries for which the model performs the most accurately. These boundaries should inform how the model may be improved to generalise better. Figure 8.8 plots the ion and target masses for each combination, A_{Ion} and A_{Target}, respectively, against their RMSE error. Colours represent RMSE errors below 5,000 $\mathrm{MeV\,cm^2\,g^{-1}}$ (green), between 5,000-15,000 $\mathrm{MeV\,cm^2\,g^{-1}}$ (yellow) and above 15,000 $\mathrm{MeV\,cm^2\,g^{-1}}$ (red). Several patterns can be identified. Firstly, the model performs best on the high density of combinations that contain lower-mass ions. This would undoubtedly be a consequence of a greater amount of training data in this regime, although this may perhaps not be the only reason. Secondly, the highest errors occur along the rear, right-hand face of the graph corresponding to light target materials. In particular, hydrogen and helium targets are very poorly predicted, especially at higher ion masses where the stopping powers are larger. However, this is not directly attributable to a lack of data in this region – the dataset consists of 801 observations for a helium target (8th highest target material) and hydrogen 616 (12th highest). Hence the poor generalisability of the model for lighter targets may be due to more complex non-linear relationships that are not present for heavier targets.

The analysis of the model allows two boundary conditions to be proposed: $A_{Ion} < 50$ and $A_{Target} > 4$. These describe the regime in which optimal predictive performance is achieved. Beyond this the model struggles to generalise and produce good predictions, due to a lack of training data, but also possibly as a result of more complex physical relationships in these regions. Table 8.4 shows the result of retraining of the model with various boundary conditions; error metrics are calculated on predictions for all samples. Both the RMSE and MAE are observed to decrease by approximately 75%, which is to be expected considering the reduced number of samples with high stopping powers. The model is, however, observed to improve as a result of the added boundaries both in terms of greater R^2 and lower MAPE. Despite these conditions the dataset still comprises nearly 30,000 samples and therefore remains

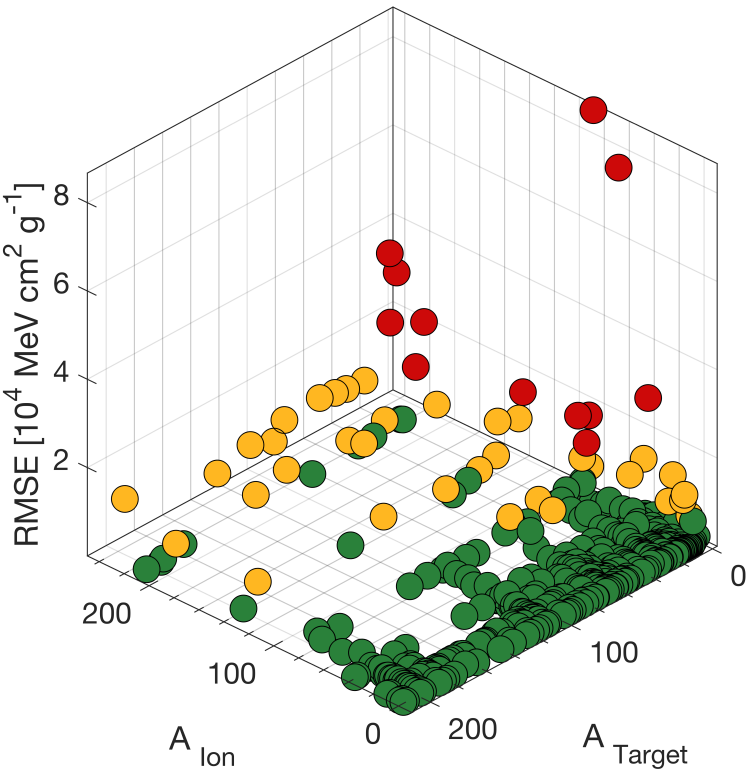

Figure 8.8: The distribution of RMSE with ion and target masses, A_{Ion} and A_{Target} respectively. Higher errors are concentrated along the rear right-hand face of the graph – suggesting that the model does not perform well on very light targets, and heavier incident ions. The largest errors occur for a hydrogen target.

generalised, with the improvements not falsely gained from overfitting to a small subset of the data.

8.3.5 Individual combination examples

The performance of the model is further evaluated on the predicted stopping power functions for each individual combination. A subset of combinations is presented here, describing the general features observed across the full dataset of 522 combinations. In the following figures the predicted stopping power values are plotted in blue, as a function of energy in the range 10^{-3} to 10^{2} MeV. These predictions

Boundary Conditions	Samples	R^2	RMSE	MAE	MAPE
None	34,237	0.9316	3944	814.8	15.03
$A_{Target} > 4$	32,457	0.9627	2817	666.5	11.62
$A_{Ion} < 50$	31,553	0.8920	1523	331.9	14.76
$A_{Target} > 4, A_{Ion} < 50$	29,849	**0.9378**	**1053**	**235.2**	**11.08**

Table 8.4: Error values (evaluated on the whole dataset) are greatly reduced when the model is re-trained and cross-validated with the application of boundary conditions on the training data. Only 14% of samples are lost, suggesting that the error metrics are still representative of a large dataset and well-generalised model.

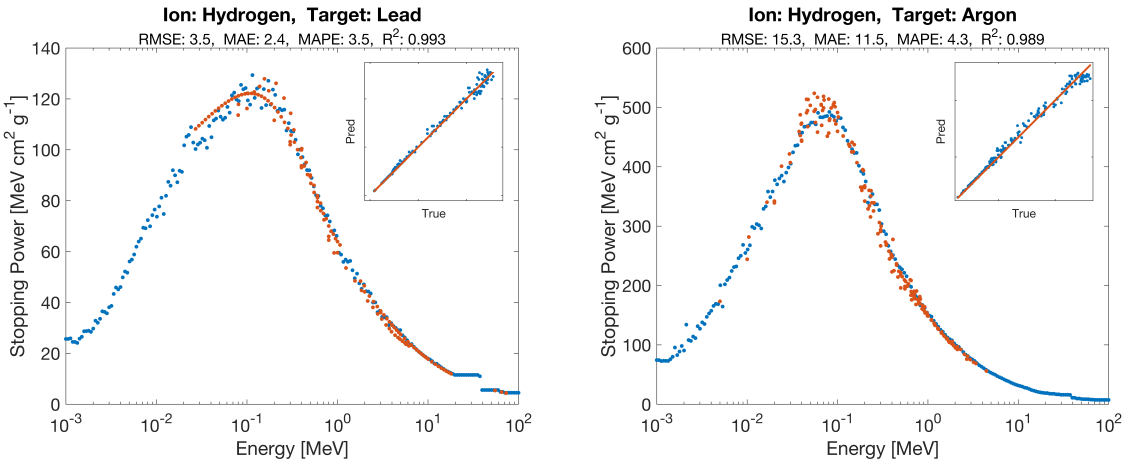

(a) Hydrogen ion on lead target

(b) Hydrogen ion on argon target

Figure 8.9: Stopping power function: experimental observations, y_{true} (red); predictions, y_{pred} (blue).

are generated for 200 energies equally spaced along the logarithmic axis. The experimental data that exists, which doesn't necessarily cover the full energy range, is plotted in red. The predictions are made without the model having 'seen' any of the experimental values and are therefore solely generated by the patterns and relationships determined by the random forest within the remainder of the dataset. As such, the following figures represent the true power of the model to predict the stopping power function across the full energy range, for materials where experimental data is incomplete or does not exist.

Figure 8.9a presents a typical output for a hydrogen ion (proton) incident on a lead target. It can be seen that the model is able to replicate the shape of the stopping power function to a high degree, with minimal discontinuities or noise. There is a discontinuity seen at higher energies, which may be symptomatic of a sparsity of training data in this region. The scatter within the curve is a product of noisy input data and the fact that the model is not overfitting to the training set. The predicted values are seen to align extremely well with the experimental observations and achieve correspondingly low error metrics. The remaining low-energy portion of the curve that is not measured against the experimental values looks like a sensible extrapolation of the curve, and given the low errors on the higher energy data, is most likely an accurate representation of reality. Figure 8.9b shows a typical response for an elemental gas, argon. Similarly, good alignment with experimental values is seen, along with a consistent stopping power function curve – boasting the ability of the model to generalise to gaseous targets.

More complex targets also perform well. Namely, mixtures such as air, figure 8.10a; alloys such as havar, figure 8.10b; polymeric resins such as formvar, figure 8.10c; and compounds such as silicon dioxide, figure 8.10d.

It is interesting to assess the performance of the model on very noisy experimental data, which has been accumulated through many different experiments, such as for iron, figure 8.11a; nickel, figure 8.11b; silicon, figure 8.11c; and zinc, 8.11d. Many of these combinations contain vastly different sets of observations, particularly around the peak of the function. Hence one unavoidable source of error, that cannot be attributed to the quality of the model, is simply disagreement of the predictions against a large number of inconsistent experimental observations. However, it is notable that the blind predictions on these noisy combinations tend to favour a single trend in the experimental data values. This may conversely lend credibility to the favoured set of experimental values, as it would suggest that they are statistically more representative than the others.

The fact that the model may be trained on numerous combinations of highly noisy

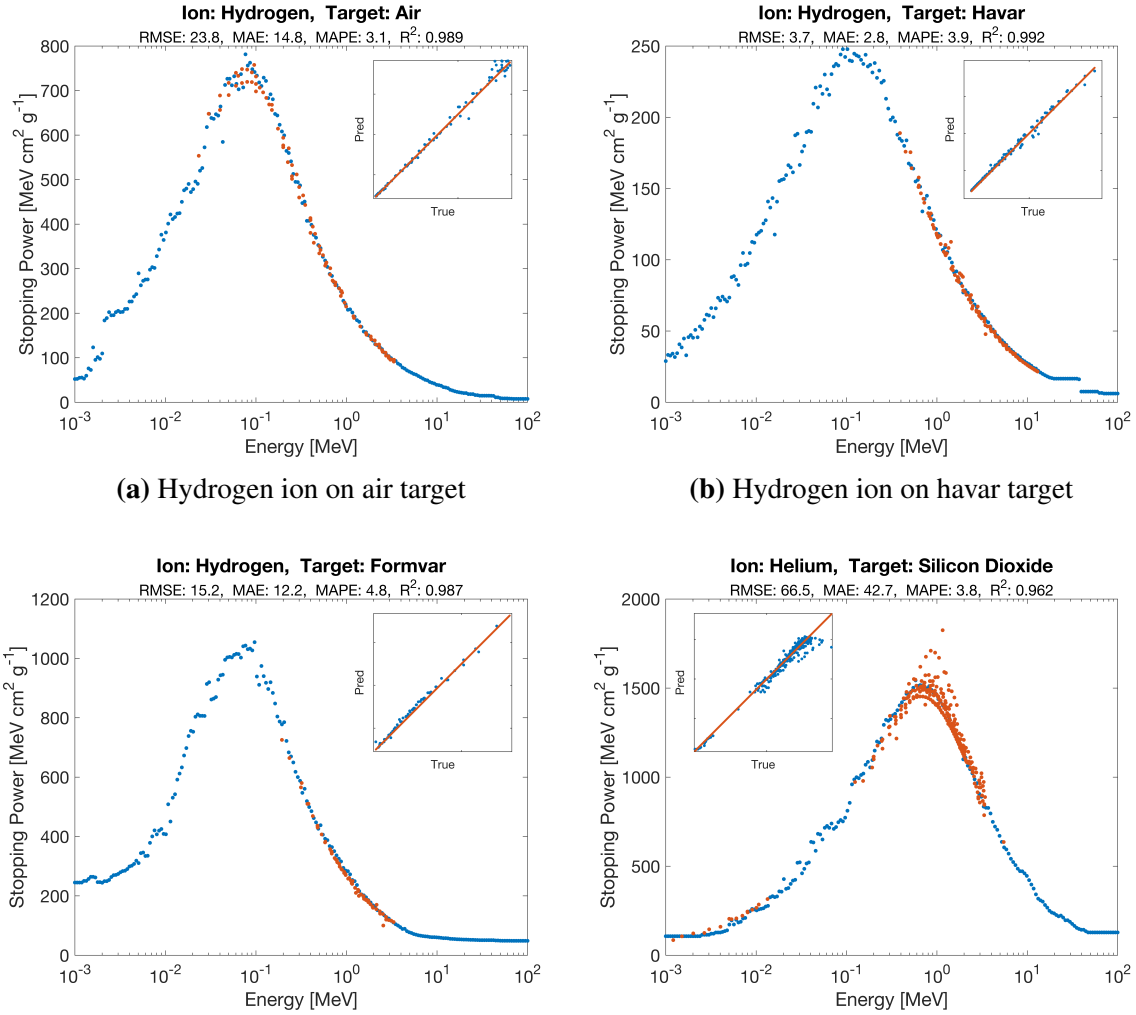

(a) Hydrogen ion on air target

(b) Hydrogen ion on havar target

(c) Hydrogen ion on formvar target

(d) Helium ion on silicon dioxide target

Figure 8.10: Stopping power function for various complex target materials: experimental observations, y_{true} (red); predictions, y_{pred} (blue).

and self-contradictory data, and yet is able to predict clean and continuous stopping power curves is a strong indication that overfitting is not occurring, and that the model is a robust and well generalised. Furthermore, it suggests large potential performance gains if the training data can be cleaned and rationalised.

Predictions generated for heavier ions are presented in figure 8.12. The model is largely able to produce sensible stopping power functions, that agree well with the experimental values. However, the continuity of the curve degrades with increasing ion mass. The thinning-out of experimental observations for higher ion masses

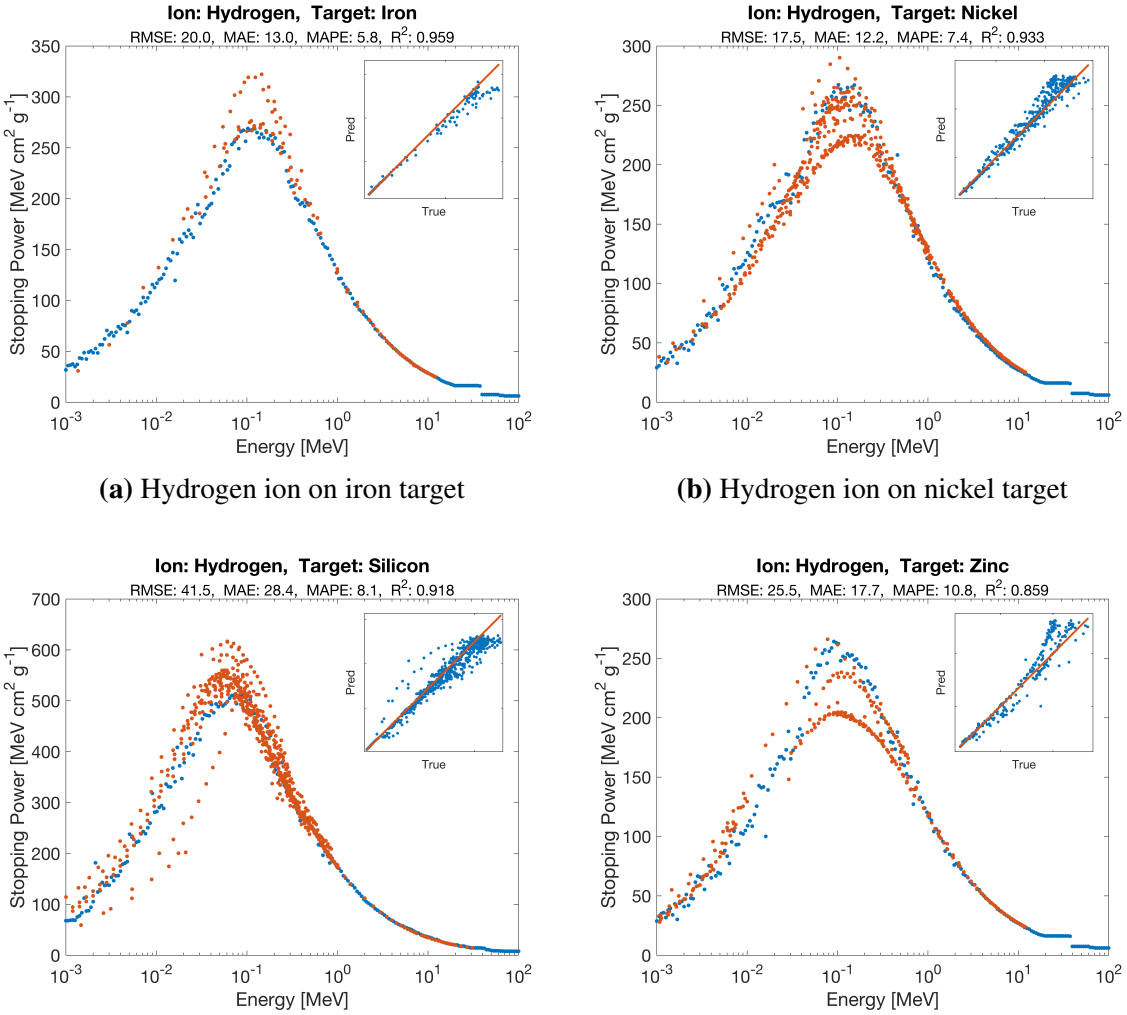

(a) Hydrogen ion on iron target

(b) Hydrogen ion on nickel target

(c) Hydrogen ion on silicon target

(d) Hydrogen ion on zinc target

Figure 8.11: Stopping power function for examples of noisy or incongruous experimental samples: experimental observations, y_{true} (red); predictions, y_{pred} (blue).

is immediately apparent and is an attributable cause for this effect. The poorest congruity is observed in the high energy region; plateaus and discontinuities can be seen, which may be the source of the linear clusters identified in figure 8.6. An upshot is that the high energy regime is well represented analytically by the Bethe equation, so the utility of the model is not compromised significantly, as it's real merit is in achieving accurate low energy predictions. RMSE and MAE are observed to scale approximately in proportion with the magnitude of the stopping power, as expected. Higher ion masses experience greater stopping powers. In

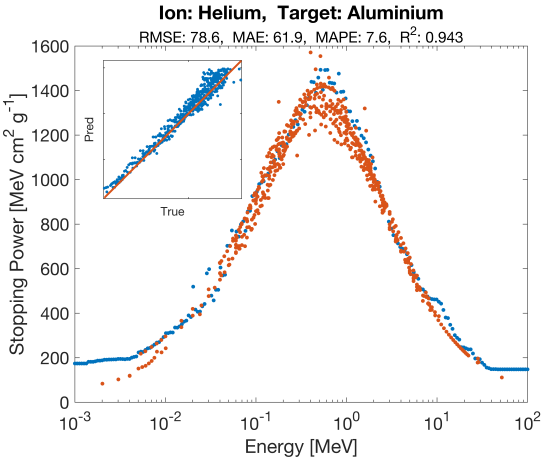

(a) Helium ion on aluminium target

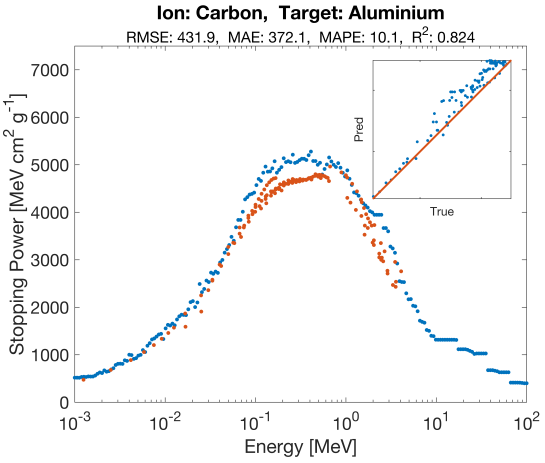

(b) Carbon ion on aluminium target

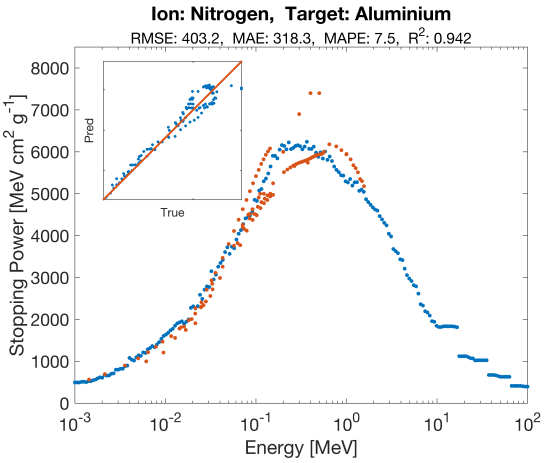

(c) Nitrogen ion on aluminium target

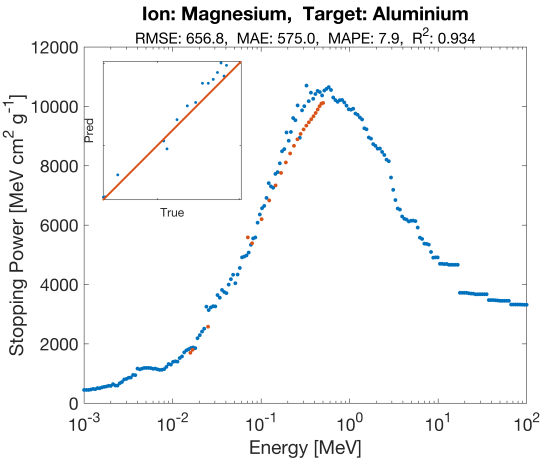

(d) Magnesium ion on aluminium target

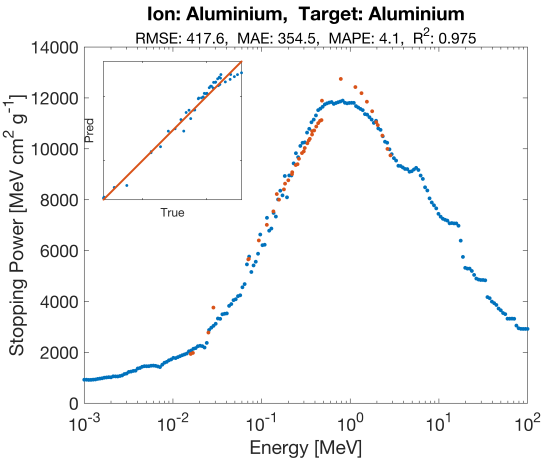

(e) Aluminium ion on aluminium target

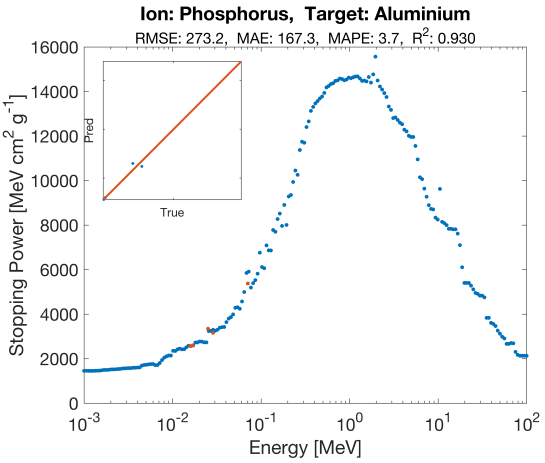

(f) Phosphorus ion on aluminium target

Figure 8.12: Stopping power function for heavier ions on an aluminium target: experimental observations, y_{true} (red); predictions, y_{pred} (blue).

relation to the magnitude these errors be considered relatively small, accounting for between 4-10% of the peak stopping power in figure 8.12.

8.3.6 Prediction of key combinations

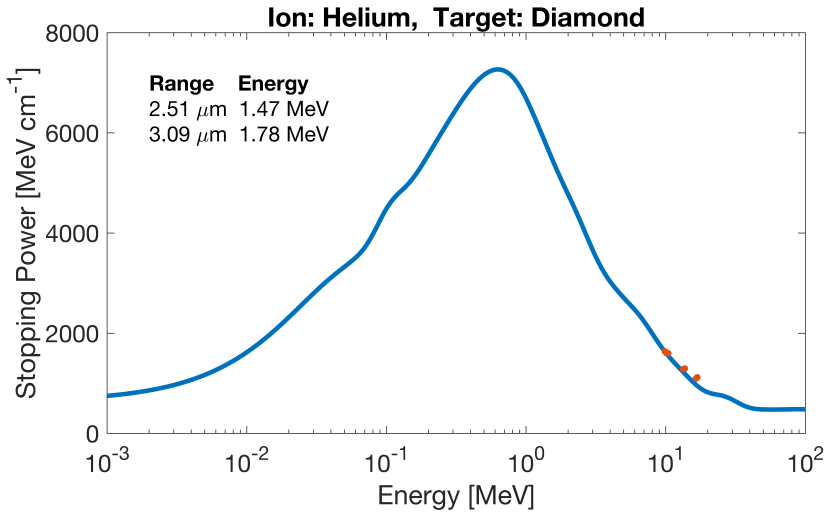

Figure 8.13: Stopping power function for helium ions on a diamond target: experimental observations, y_{true} (red); interpolated prediction curve (blue).

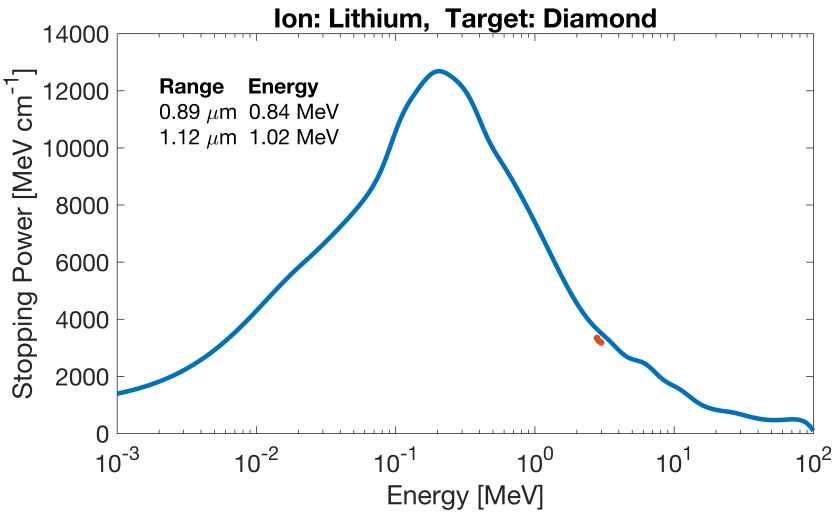

Figure 8.14: Stopping power function for lithium ions on a diamond target: experimental observations, y_{true} (red); interpolated prediction curve (blue).

Aside from its use as a general predictive model, the overarching purpose of the work is to develop more accurate range calculations for the simulation of neutron

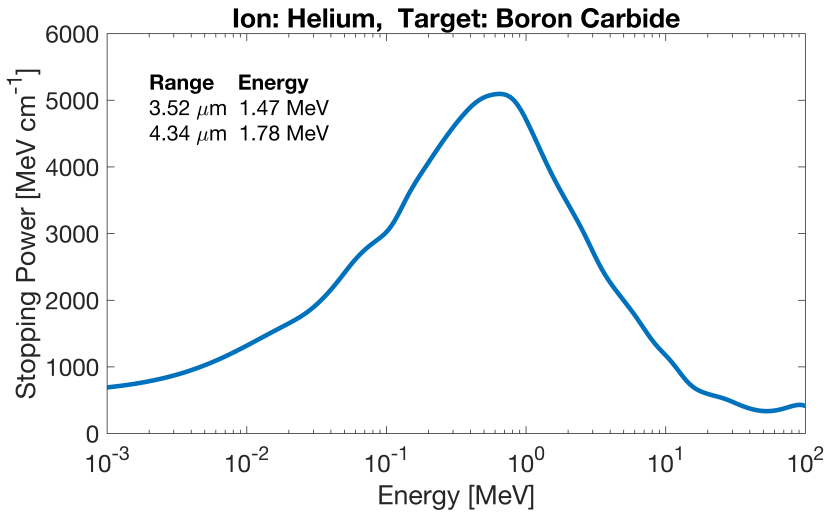

Figure 8.15: Stopping power function for helium ions on a boron carbide target: interpolated prediction curve (blue).

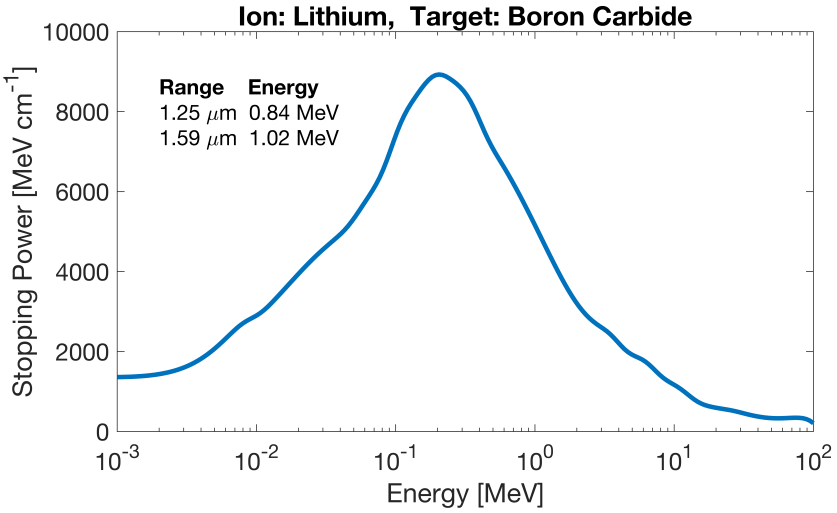

Figure 8.16: Stopping power function for lithium ions on a boron carbide target: interpolated prediction curve (blue).

detectors. For this reason, stopping power functions for certain key combinations are sought. The relevant target materials are boron carbide and diamond; with the ions produced by neutron conversion being helium and lithium. Hence predictions are generated for these combinations, figures 8.13 to 8.16, where the y-axis scale is in units of the stopping power, [$\mathrm{MeV\,cm^{-1}}$] as opposed to the *mass* stopping power, [$\mathrm{MeV\,cm^2\,g^{-1}}$], used previously. The discrete predictions are interpolated to form continuous functions that may be reciprocally integrated to generate range predictions for any ion energy. As an example, inset are the calculated ranges for the initial energies of the ions generated by neutron conversion with ^{10}B. Additionally, the stopping power functions for diamond, figures 8.13 and 8.14, may be compared against the limited amount of experimental data available. A further useful check is to compare the predicted range of a 5.486 MeV helium ion produced by the decay of ^{241}Am. Integration of the stopping power function produces a predicted range of 14.32 μm, which is very similar to the widely quoted value of approximately 14 μm [292].

8.4 Discussion

8.4.1 Model assessment

The initial assessment of any machine learning method should be on the bias and variance of the model. A high bias is consistent with underfitting, in which the model does not present a representative relationship between the input features and the predicted output. This is commonly judged on the performance on the training data, for which large errors would indicate a large bias. The errors on the training set given in table 8.2 would indicate that the bias is relatively low. High variance would suggest the opposite problem – in which the model is overfitting to the data. Low training data errors combined with high errors on test data would indicate poor generalisation and hence a large variance. A random forest model has the benefit of reducing overfitting by design, in that each decision tree is fitted on a different subset of features and samples. Additionally, testing through cross-validation

should provide a comprehensive assessment of the model generalisability. A few artefacts of possible overfitting have been identified in the predictions, but overall the model appears to generate consistent and sensible predictions. The errors in table 8.3 are not unreasonable given other factors involved and would not suggest a substandard level of overfitting or an intolerably high variance. There is also unavoidable amount of scatter within the experimental data – in some cases this is very severe. This means that even a perfect model will encounter a minimum level of error, unless it heavily overfits to the noise.

Given this, the second assessment should be whether the model is fit for purpose. The direct use of the model is to be able to generate a full stopping power function, $S(E)$, for any ion-target combination, without any knowledge of experimental data. Figures 8.9 to 8.12 display this capability is achieved satisfactorily for a wide diversity of ions and targets. A smooth curve fit is produced and is observed to align well with experimental data without appreciably high errors. Predicted values may be generated across the full energy range to form a functional curve from which ion ranges may be calculated. Two boundary conditions have been identified that define ions and targets that the model is better at predicting. These conditions are invariably the result of a lack of experimental training data outside these regimes; however may also point to a wider physical difference in the behaviour of light targets and heavy ions. This would need to be corroborated by further experimental work, and the supplementation of this data to future models.

8.4.2 Comparison to other models

Considering that the work is very novel in its implementation, it is difficult to make a direct comparison with previous work. The method is similar to those used in quantitative structure-property relationship (QSPR) studies, in which machine learning models are used to generate regression or classification predictions of unknown material properties based upon structural and molecular information [293–295]. These tend to be used in chemistry, for example, to predict aqueous solubility [296] or ion-

isation of organic molecules [297]; biology, to predict protein interactions [298]; or medicine, to identify chemical structures that may perform well as drugs [299]. These use cases clearly do not allow quantitative comparison, however the methods used for the model development and validation are very similar and of equally high standard [300–302].

The work may also be compared with the current semi-empirical methods, such as SRIM [303]. The methods of Zeigler et al. differ substantially, but the aim is similar. SRIM appears to use an alternative definition of MAPE to define the accuracy of their model,

$$MAPE_{SRIM} = \frac{100}{n} \sum \left| \frac{y_{true} - y_{pred}}{y_{pred}} \right| \tag{8.13}$$

They publish these accuracy values compared against 25,200 experimental data points, for one of their latest updates SRIM-2010, table 8.5. SRIM attempts to provide the best possible curve fit to experimental data along with interpolation of the curve over energy to provide a full stopping power function. In the case of no pre-existing experimental data, predictions are made by a form of interpolation of the parameters for similar combinations. Because of these fundamental differences in model building and evaluation methodologies, it is unclear whether their error values are assessed based upon parameterised curve-fitting to 'seen' experimental data (the equivalent of making machine learning predictions on the training data) or whether the parameters are evaluated 'blind' by a predictive algorithm (the equivalent of cross-validating predictions on test data) – or even by some combination of the two methods. Hence for comparison, values in table 8.5 are quoted for both training data and the cross-validated test data. It can be seen that the performance of SRIM, as evaluated solely on MAPE, is better than that of the truly blind test predictions of the random forest model. However, it is inferior in comparison to predictions on the training data. Ziegler et. al. state that if erroneous experimental outliers are omitted (those that differ by $> 25\%$) the overall accuracy of their model drops to 4.0%. Similar analysis of the random forest model achieves 6.6%

	SRIM-2010				Random Forest Model (test / train)			
Ions	Samples	Av.	$< 5\%$	$< 10\%$	Samples	Av.	$< 5\%$	$< 10\%$
H	8,300	4.0	74	87	11,380	11.9 / 2.4	44 / 88	67 / 97
He	6,500	3.9	76	89	9,255	9.1 / 2.1	48 / 92	72 / 98
Li	1,400	4.8	72	83	712	24.5 / 2.1	40 / 91	16 / 98
Be - U	9,000	5.8	58	82	12,879	12.4 / 2.0	31 / 92	57 / 98
All	25,200	4.6	69	86	34,237	11.6 / 2.1	40 / 91	64 / 98

Table 8.5: A comparison between the alternative MAPE values published for SRIM-2010 and those derived for the random forest model. Values are calculated for various incident ions: hydrogen, helium, lithium and heavier ions. For each row: 'Av.' = the average MAPE calculated for all samples in that row, '$< 5\%$' = percentage of experimental data within 5 percent of the model values, '$< 10\%$' = percentage of experimental data within 10 percent of the model values.

on the test data and 2.0% on the training data. It should be noted that a further reason that direct comparison is difficult is that any reported statistics will depend on the exact nature of the dataset used – the size, constitution and processing of the set will all cause the models to differ significantly. An interesting, and potentially fruitful investigation would be to adopt the benefits of both models to achieve the best possible predictions. For example, curve fitting may be carried out using the SRIM parameterised formulation, with parameter predictions for new combinations determined by a machine learning method.

8.4.3 Improvements

The current state of the model is such that it remains under-optimised in several aspects. It represents the most pessimistic result achievable by such a method. Primarily, it is disadvantaged by the quality and distribution of the training data. This may ultimately prove to be an impenetrable issue without collection of large amounts of additional experimental data, however it would be expected that substantial improvements may be achieved by simple processing and treatment current dataset. Such treatment may include: balancing of the dataset such that all ions and targets

are represented more equally, training only on combinations that contain experimental data across the full energy range, applying further boundary conditions such as on the state of the target material to produce a more accurate but narrower model. Secondly, the large noise in the experimental data must be addressed. The dataset should ideally be 'cleaned' or otherwise normalised by a method to minimise the scatter and remove outliers – particularly in the case where the experimental data consists of several highly differing stopping power curves. This may be nicely implemented by using the highest accuracy SRIM curves as training data. Finally, the large number of samples discarded in the efficient processing of the original Helmut Paul database should be extracted and added to the dataset, resulting in potentially thousands more observations.

The feature generation process should also be developed to improve the amount of potentially useful information for training. New features could be added that convey more detail on the structure of the target materials, such as molecular fragments, chemical groups or bonding states – which has been shown to improve the performance of SRIM [304].

In terms of the model – it would be expected that there may be algorithms that are better suited to this kind of problem within the multitude of machine learning tools available. Promising candidates would be linear models or neural networks. Further accuracy can be attained with random forest models by optimisation of the model hyperparameters (number of trees, depth, samples at each split, etc.) which can often be determined by an extensive and iterative gridsearch across the parameter space.

8.5 Conclusions

The stopping power of a material upon interaction with an energetic ion is the key measure of how far that ion will travel. The implications of accurate particle range calculations are tremendous, affecting every single application in which particle ra-

diation is used – from nuclear power to medicine. In addition to this, understanding the precise range of neutron products in diamond and boron carbide is crucial for designing the most efficient solid state neutron detectors.

A model has been presented in this work which attempts to overcome current weaknesses in the physical understanding of – as well as the mathematical methods used to interpret – the stopping power at low energies. This is a considerable challenge, however the use of a fundamentally new machine learning methodology has been shown to hold great promise in this field.

A random forest regression algorithm has been trained using over 34,000 experimental measurements, representing the stopping power values for 522 ion-target combinations across the energy range 10^{-3} to 10^{2} MeV, and ion and target atomic masses (A_{Ion} and A_{Target}) 1 to $\sim$ 240. The ultimate aim of the algorithm being the ability to predict the stopping value for any energy, ion and target combination, having seen no pre-existing experimental data. Evaluation is performed using four error metrics (R^2, RMSE, MAE and MAPE) to provide the best understanding of model performance when tested against strict cross-validation criteria.

The resulting model is shown to have minimal bias when evaluating its internal performance, and the errors evaluated on the external 'blind' predictivity of the model concurrently show low levels of overfitting and variance – despite a noisy and unbalanced dataset. Examination of the error distributions suggests better predictions are made for $A_{Ion} < 50$ and $A_{Target} > 4$, which make up nearly 30,000 of the training observations. Hydrogen and helium targets suffer the greatest errors, particularly for heavy ions with large stopping powers, and possibly pointing to more complex non-linear physical relationships in this regime.

The extraordinary power of the model is observed when comparing the predicted stopping power as a function of energy against existing experimental data points. Not only do the predicted curves correspond closely to those of the true values, but the model is able to generalise across target elements, compounds, mixtures, alloys

and polymers; in solid, liquid and gaseous states; for a wide range of ion masses. Although difficult to evaluate fully due to a difference in methods and evaluation benchmarks, the regressive error of the model (2.1%) could be considered nearly half that of the leading interpolant method, SRIM (4.0%); and the fully blind predictions of the model not far behind (6.6%).

The investigation presented in this chapter has clearly shown how the benefits of machine learning methods and big data analysis may begin to provide new and more accurate approaches to decades-old problems in physics.

Chapter 9

Growth and characterisation of thin, boron-doped diamond layers for high-temperature sensor applications

9.1 Introduction

Diamond is special in many ways. No other material possesses such a range of outstanding mechanical characteristics in symphony with such desirable electronic properties. The large breakdown voltage, high carrier mobilities and high thermal conductivity demonstrated in diamond are amongst many that make it an attractive electronic material – particularly for high-power or extreme application devices. A shortcoming arises when looking to exploit diamond as a p- or n- type semiconductor necessary for such devices. The tight carbon bonding and meta-stability of the sp^3 hybridisation state precludes many of the more common semiconductor doping techniques, such as in-diffusion or ion implantation [22]. This restricts most doping processes to the substitutional inclusion of dopants introduced during growth. The list of suitable impurities, given the short diamond lattice constant (3.567 Å [1]), is therefore limited to nitrogen, phosphorus and boron. Nitrogen is a common natural impurity due to its high atmospheric abundance, however it offers a donor level

with an activation energy of approximately 1.7 eV [23]. Similarly, phosphorus has been found to act as a donor activated at 0.5 eV [24]. These deep impurity levels are of little utility to conventional electronic devices and consequently boron, with an acceptor activation energy of 0.37 eV at typical device-purpose concentrations ([B] $< 10^{17}\,\mathrm{cm}^{-3}$), presents itself as the dopant of choice for many applications.

The best electronic characteristics have been obtained using CVD techniques to incorporate boron impurities into the lattice during growth [23, 33, 38]. More recent developments in boron-doped diamond growth have shown hole mobilities as high as $1870\,\mathrm{cm}^2\,\mathrm{V}^{-1}\,\mathrm{s}^{-1}$ [37] at acceptor concentrations of [B] = $10^{16}\,\mathrm{cm}^{-3}$. As described in chapter 2, the activation energy of the boron-induced acceptor states begins to rapidly decline at doping levels above [B] $\sim 10^{18}\,\mathrm{cm}^{-3}$, and becomes vanishingly small above [B] $\sim 10^{20}\,\mathrm{cm}^{-3}$. This is due to the emergence of an impurity band that allows conduction between neighbouring acceptors. The discrete 0.37 eV level degenerates into a broad band of states, gradually reducing the energy gap between the boron state and the diamond valence band edge. This provides a problem for the engineering of devices using boron doped diamond; at modest concentrations, few of the dopant atoms will be thermally activated – at room temperatures the concentration of holes will be less than 1% of the actual boron doping concentration [33]. Whilst higher doping levels obviate this problem, valence band conduction – with high carrier mobility – gives rise to hopping conduction in the impurity band – with low carrier mobility. Not only does this limit the performance levels of any device produced in this way, but the sheer abundance of carriers at this concentration makes the depletion of channels in device structures impossible within any practical voltage window.

This paradox may be somewhat alleviated when operating at higher temperatures, such as those encountered in many harsh sensor environments. Not only can diamond withstand such temperatures for extended periods of time without negative impact, but high performance devices may be made using lower boron concentrations. The challenge currently exists of no commercially-available nor readily

implementable growth recipes for such layers. Consequently, the work presented in this chapter endeavours to investigate and characterise how diamond may be grown with controllable doping concentrations; layer thicknesses; as well as ohmic contacts, to achieve optimal performance in high-temperature sensors.

9.2 Experimental methods

9.2.1 Diamond growth

For the growth of boron-doped diamond layers, intrinsic 5.0 x 5.0 x 0.5 mm^3 electronic grade ([B] $<$ 1 ppb, [N] $<$ 50 ppb) polycrystalline substrates from Element Six are used, polished to a roughness of $R_a < 20$ nm by the supplier. Prior to growth these are treated using an aqueous acid etch solution, to remove any organic contaminants and to oxidise the surface. They are then degreased using acetone, IPA and DI water. The boron-layer growth is carried out in an Astex-AX6500 MWPECVD reactor, with the substrates mounted on a 2 inch flat molybdenum wafer holder.

A recipe is developed and optimised to allow the growth of controllably boron-doped films, building upon the processes described in previous literature – chapter 2 and table 2.5. Unlike for typical heavily-doped growth, to obtain the low doping range required no boron source in the form of trimethylborane (TMB) gas is added into the precursor gas mixture. Instead the dopant is introduced through the residual boron condensates already within the contaminated growth chamber, which is otherwise frequently used with high concentrations of TMB. A large CH_4:CH_4+H_2 gas ratio of 4% is used, along with a forward power of 4 kW in order to enhance the efficiency of impurity incorporation into the diamond lattice. The growth rate is calibrated by an initial extended growth run at a temperature of 1000 °C, as measured using a Williamson dual-wavelength pyrometer, and a process pressure of 80 Torr. Growing for 180 min yields a substrate, sample X, with a layer thickness of 23.9 μm as determined by prior- and post- growth mass measurement on a high-precision microgram scale. Assuming linear growth with time, this would indicate a growth

Sample	CH_4 [sccm]	H_2 [sccm]	TMB [sccm]	Temp. [°C]	Power [W]	Pressure [Torr]	Time [min]
X	40	1000	-	1000	4000	80	180
A	40	1000	-	1000	4000	80	2
B	40	1000	-	935	4000	100	5

Table 9.1: Growth recipes used for growth rate calibration, sample X; thin layer ($\sim$ 265 nm) sample A; and thicker layer ($\sim$ 665 nm) sample B also using a higher growth pressure.

rate of approximately 133 $\mathrm{nm\,min^{-1}}$.

Following this, two samples are grown. Sample A is grown for 2 min using identical parameters to sample X. This is intended to achieve a thin, approximately 265 nm, layer within the low region of boron doping. Sample B is grown for 5 min using identical gas ratios, however with a faster ramp in hydrogen prior to methane injection, and with a 25% greater pressure. This is intended to achieve a layer of approximately 665 nm thickness (although variability in growth rate due to the gas pressure change may be expected) but also possibly with a higher incorporation of boron. The recipes are shown in table 9.1.

After growth, the all samples are subjected to a 6 hour burn in air at 600 °C within a quartz tube oven. At this temperature graphitic (sp^2) surface contamination as a result of the growth is removed. A further aqueous etch completes the removal of graphitic (or other organic) contamination and strongly oxidises the surface.

9.2.2 Metallisation and annealing

Metal contacts are made to samples A and B for the purposes of carrying out electronic characterisation and for device fabrication. A mask is designed to allow photolithographic patterning of a series of concentric annular electrodes. These electrodes are spaced at defined separations to form a series of exposed diamond channels; with leads patterned to 200 x 200 μm contact pads on the lower edge of

the sample for wire-bond packaging. These exposed channels may be further processed for multi-functional chemical sensing (chapter 10). The mask is designed using AutoCAD 2016 and created by patterning chrome on fused silica, with the schematic shown in figure 9.1 and channel dimensions as defined in table 9.2.

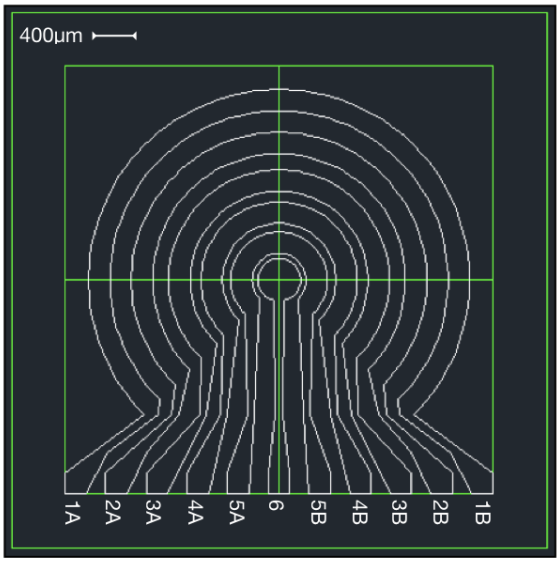

Figure 9.1: Mask design for photolithography designed using AutoCAD 2016. White lines indicate the outline of the chrome features to be patterned onto fused silica glass. Electrodes are numbered 1 to 6 with contact pads A and B for each. Radius of the central circle is 200 µm.

Electrode Pair	Distance [µm]			
	w	$\bar{l}$	r_I	r_O
1A/2A, 1B/2B	200	7664	1380	1580
2A/3A, 2B/3B	150	5722	1030	1180
3A/4A, 3B/4B	100	4040	730	830
4A/5A, 4B/5B	80	2534	450	530
5A/6, 5B/6	50	1160	200	250

Table 9.2: Channel dimensions defined by the metallisation mask: width, w, average length, $\bar{l}$, inner radius r_I, outer radius, r_O. All distance quantities relate to the non-metallised diamond channels between the electrodes.

Prior to metallisation, the boron-doped diamond surfaces are oxygen terminated

to ensure complete oxidation of the surface and to suppress any hydrogen surface conductivity. This is carried out using a UV photochemical process in which the samples are exposed to ozone for 1 hour at 200 °C and 50 mBar. The sample is mounted on a ceramic heater in a custom-built chamber, which is flushed with oxygen 5 times prior to processing. The sample is then heated for 30 min, achieving a continuous oxygen flow before starting the UV ozone generator.

Photolithography is used to pattern the contact areas, for which an optimised recipe was developed and is as described below:

1. Submerse in a 'Piranha' etchant solution (3 parts concentrated H_2SO_4 and 1 part 30% H_2O_2) for 20 min, followed by a standard degrease and dry with a high-flow N_2 gun to clean surface of organic contaminants.

2. Mount onto spin coater using a small vacuum chuck capable of holding a 5 x 5 mm sample.

3. Drop coat sample with LOR-10B photoresist. Ramp for 2 sec up to 500 rpm, hold for 10 sec, ramp to 4000 rpm for 2 sec, hold for 30 sec, ramp down to 0 rpm for 2 sec.

4. Soft-bake sample on covered hotplate at 190 °C for 10 min.

5. Mount onto spin coater. Drop coat with S1818 photoresist. Ramp for 2 sec up to 500 rpm, hold for 10 sec, ramp to 4000 rpm for 2 sec, hold for 30 sec, ramp down to 0 rpm for 2 sec.

6. Soft-bake sample on covered hotplate at 115 °C for 1 min.

7. Mount on vacuum chuck in Karl Suss MJB3 Mask Aligner. Align sample to mask features, figure 9.1. Make soft contact between sample and mask. Expose to UV light (intensity 20.3 $\mathrm{mW\,cm^{-2}}$) for 2.4 sec.

8. Develop in MF-26A developer for 60 sec. Immediately rinse in de-ionised water and dry with N_2 gun.

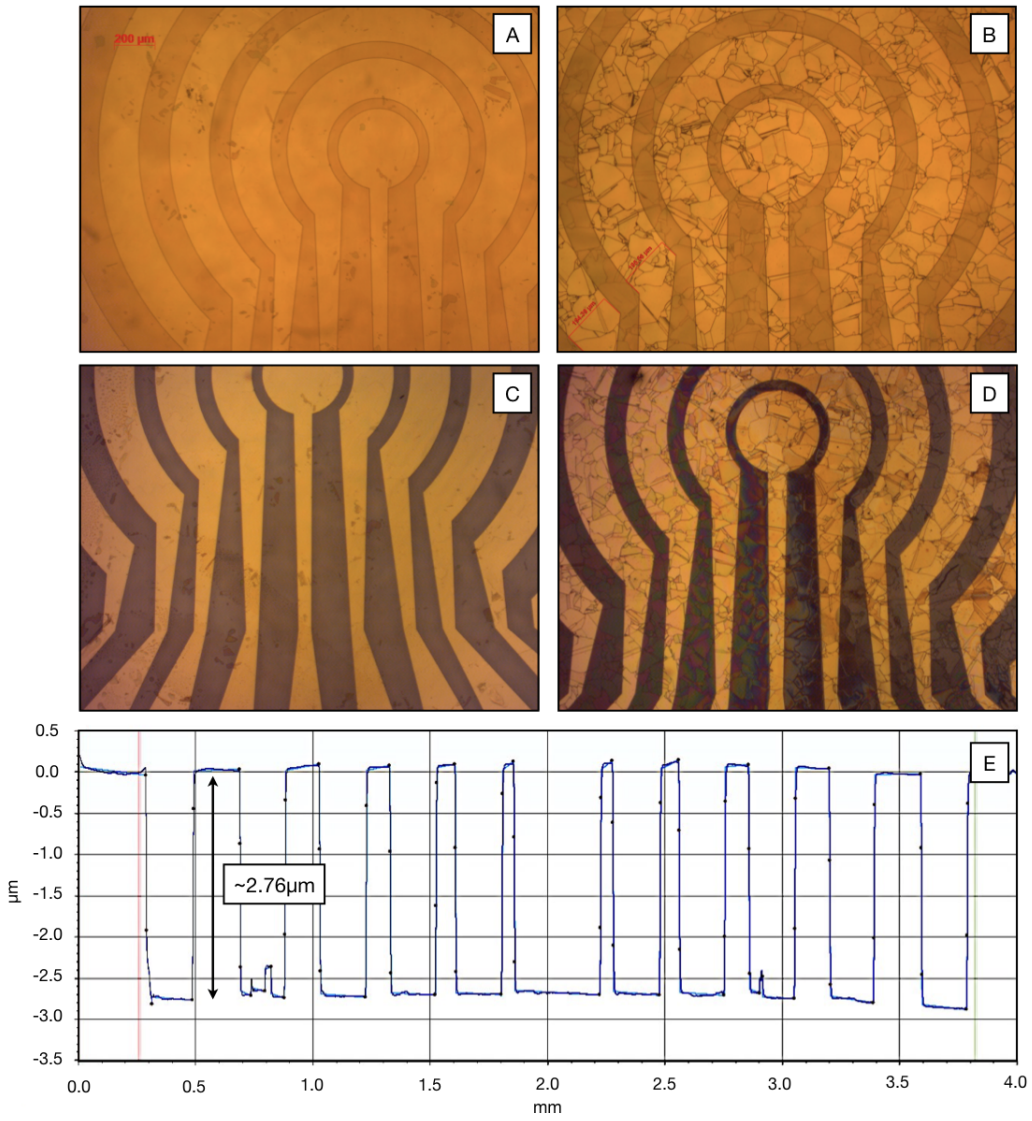

Figure 9.2: Microscope images of features after photoresist spin-coating, exposure and development (a) sample A and (b) sample B. Metallised contact pattern after lift-off, (c) sample A and (d) sample B. (e) Dektak profile of developed photoresist features on sample A, average step height is 2.76 µm. For scale, the radius of the central circle is 200 µm.

Anneal step	Temp. [K]	Time [min]	Ramp time [min]	Pressure [mBar]
0	300	-	-	-
1	470	60	15	5.1×10^{-6}
2	670	60	15	5.6×10^{-6}
3	870	60	20	4.8×10^{-6}
4	1070	60	55	8.4×10^{-6}

Table 9.3: Anneal parameters for samples A and B. Annealing is carried out at a series of increasing temperatures from stages 0 to 4, with electronic characterisation made after each stage to measure the onset of carbide formation and low-resistance contacts.

The resulting features are measured using a Dektak profliometer over 10 scans, and optical microscope to gauge successful implementation of the recipe prior to metal deposition. Figure 9.2(a), (b), (e) show defined features, with a consistent average step height of 2.76 μm. This indicates successful spin coating of the two-layer photoresist (LOR-10B, $\sim$ 1.0 μm + S1818, $\sim$ 1.8 μm); that a homogenous layer is achieved; that the UV exposure results in sharp features with minimal undercutting; and also, that the features are developed without residual photoresist left on the exposed diamond surface.

To achieve ohmic electronic contact to the diamond surface a tri-layer metal stack is deposited using an Edwards A500-FL500 electron beam evaporator. A 40 nm titanium layer is initially deposited as the carbide-forming layer, above this a 15 nm platinum layer is designed to avoid diffusion of titanium ions, and a capping layer of 100 nm gold for robust electronic contact using probes or bond wires. Lift-off of the photoresist is then carried out by submersion in 1165 resist remover for 60 sec, followed by immediate submersion in DI water and drying with N_2 gun.

The metallised samples are annealed to promote the formation of a titanium-carbide interface layer. Annealing is carried out at a series of increasing temperatures, table 9.3, with electronic measurements taken in between processes to characterise the

onset of carbide formation and low contact resistance. Each anneal is conducted in a custom vacuum chamber, which is pumped down using both rotary and turbo pumps to achieve a base pressure of approximately 10^{-7} mBar. For the lower temperature anneals (470 K, 670 K), the samples are placed centrally on a 20 x 20 mm ceramic heater, and once under vacuum, the voltage on a Tenma 72-2550 programmable DC power supply is slowly ramped over 15 min from 0 V to 18.5 V and 39.0 V, respectively. The temperature is measured through a thermocouple integrated into the heater. After the 60 min annealing time the temperature is similarly ramped down over 15 min and allowed to cool fully before venting the system. For the higher temperature anneals, a 2 inch Ceramisis heater is used with a Ceramisis Power Cube power supply and controller, and molybdenum-sheathed type-C thermocouple for temperature measurement. The procedure is similar to the low temperature process, but with longer ramp times to avoid excessive heater outgassing and thermal shock to the sample.

9.2.3 Electronic characterisation

Current-voltage (I-V) and contact resistance measurements are made using an Everbeing EB-6 DC probe station. Samples are placed upon an adjustable X-Y stage and held in place using double-sided Kapton tape. 20 μm diameter tungsten probes are moved with X-Y-Z micropositioner manipulators with sub-micron precision to contact the 200 x 200 μm metal contact pads along the lower edge of the samples. Using a microscope these probes can be carefully positioned such that they make precise contact without causing damage to the metallisation or the probes themselves. The probe station sits upon a vibration-isolated table to prevent mechanical agitation of the probes from external sources; it also is enclosed within a dark shielding cabinet to minimise external electromagnetic interference.

A Keithley 4200 semiconductor characterisation system, capable of 100 fA resolution, is connected to the probes by tri-axial shielded connectors via a feedthrough in the cabinet. Current measurements are made for a voltage sweep between -5 to 5 V

for each channel by contacting the appropriate electrode pair, as defined in table 9.2, and after each anneal stage as defined in table 9.3. All measurements are conducted in air and at room temperature (approximately 300 K).

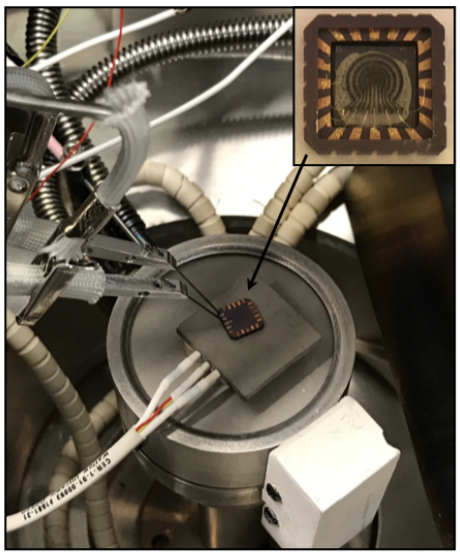

Figure 9.3: Impedance spectroscopy experimental setup; inset: sample mounted and wire-bonded into ceramic package.

Samples are then mounted using silver epoxy into leadless ceramic packages for further electronic characterisation. 25 µm diameter wire-bonds are formed between the sample contact pads and peripheral package contact pads using a Kuilicke & Soffa 4523 gold wedge bonder, see inset figure 9.3.

Packaged samples are placed face-down on a 2.5 cm square ceramic heater with built-in thermocouple, within in a custom-built steel vacuum chamber. Suspended probes allow electronic contact directly to the pads on the rear of the ceramic package, figure 9.3. All wires are sheathed in fibreglass and passed through a chamber feedthrough. The probes are connected to a Solartron 1260 Impedance System with Solartron 1296 Dielectric Interface (allowing impedance measurements in the range 1 - 10^{14} Ω, 10^{-2} - 10^{7} Hz) via coaxial connectors. The ceramic heater is powered by a Tenma 72-2550 programmable DC supply, with the thermocouple readout through a custom Arduino interface. This allows full remote computer automation of tem-

perature control and impedance measurements. Prior to measurements, the chamber is pumped down using rotary and vacuum pump stages to achieve a base pressure of approximately 3×10^{-7} mBar. On the connected PC, SMaRT impedance spectroscopy software in conjunction with a custom Python script is used to program and log a repeated experimental sequence that consists of initiating a voltage set point on the DC power supply, a subsequent temperature ramp by the heater, a delay to achieve sufficient temperature stabilisation and finally an impedance measurement across a specified frequency range.

Measurements are taken at a series of temperatures between 300K - 700 K, with the temperature gradient permitted to stabilise for approximately 15 min after each ramp. For sample A, a large AC input voltage of 2.0 V is applied (in order to stimulate a measurable signal) and the phase and magnitude of the resulting current is measured at frequencies between 5×10^{-2} - 10^{7} Hz; in the case of sample B an AC voltage of 0.1 V is applied and the current measured at frequencies between 10^{-1} - 10^{7} Hz. The temperature ramp and measurements are performed three times for each sample to rule out irreversible thermally-induced changes that may influence the results.

9.3 Results and discussion

9.3.1 I-V characterisation

The current-voltage characteristics of samples A and B are measured to provide a first-order characterisation of the electronic properties of the metallised samples. The voltage sweeps in figure 9.4, show the change in electronic properties for sample A as annealing temperature is increased. For the as-deposited metal contacts, and for subsequent low temperature anneals (470 K, 670 K) the current flow is very small across the voltage window, indicating a highly resistive contact. The linearity of the I-V relationship suggests a resistive, non-ohmic contact even after annealing at 670 K for 60 min; albeit an improvement on the as-deposited contact.

At higher annealing temperatures, the current flow through the channel increases substantially – as does the linearity of the I-V relationship indicating the onset of ohmic-type properties with higher annealing temperatures.

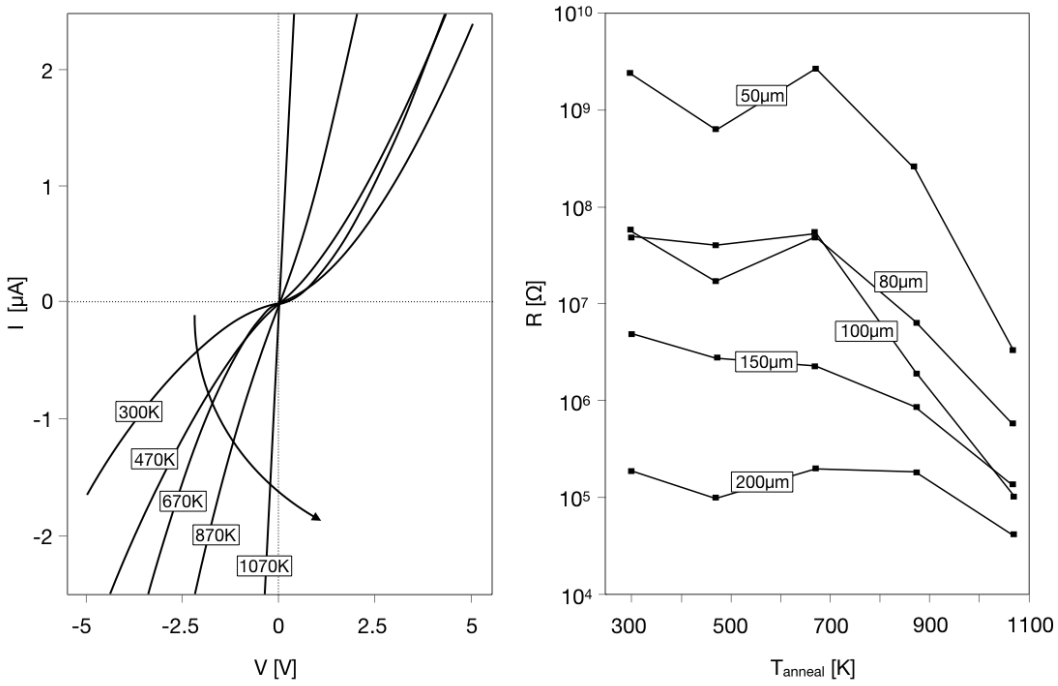

Figure 9.4: Sample A: left, current-voltage plot for a single channel for each anneal temperature (300 - 1070 K); right, mean resistance as a function of anneal temperature for each channel width (50 - 200 µm).

Similarly, the mean channel resistance of sample A is seen to fall significantly as the annealing temperature is increased over 670 K; for the most resistive channels the mean resistance is more than 700 times less after annealing. A significant relationship is observed between measured resistance and channel dimensions. The geometry of the test pattern means that the narrower channels have larger measured resistances since their channel length (eg. w 50 x l 1160 µm) is much smaller than for the wider channels (eg. w 200 x l 7764 µm).

In the case of sample B the as-deposited contacts, and the contacts after all subsequent anneals, have a perfect linear I-V correlation as shown in figure 9.5. The effect of low temperature annealing appears to have a negligible impact on the mean

channel resistances, with current flow in the order of mA across the voltage window. There is, however, significant deviation from this after the final 1070 K anneal as the resistance of all channels is observed to increase by nearly a factor of four.

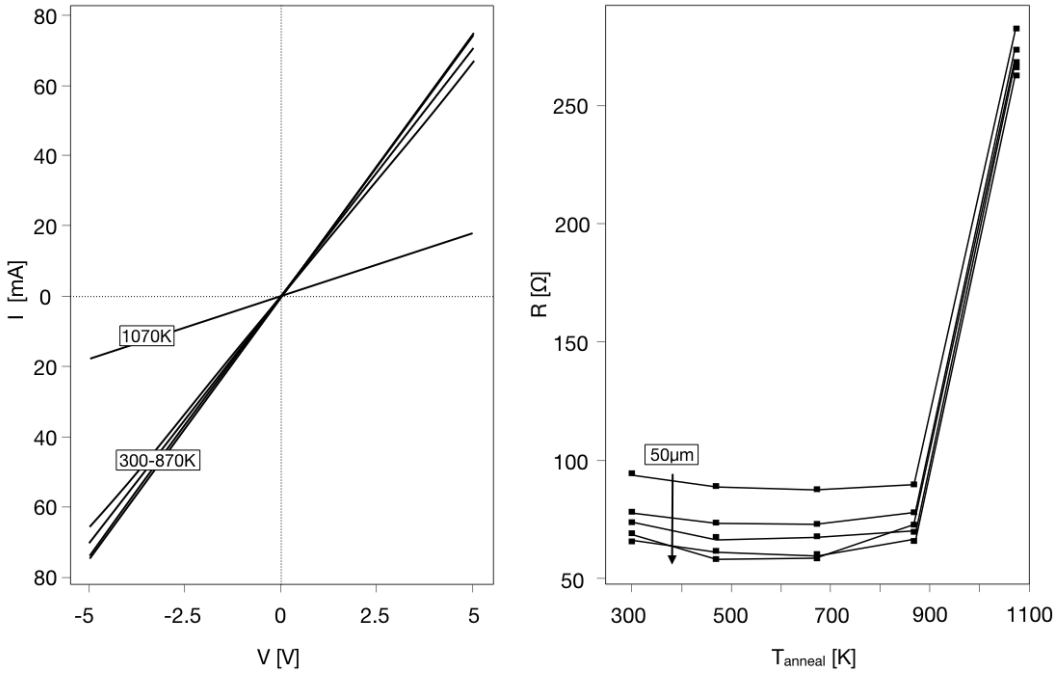

Figure 9.5: Sample B: left, current-voltage plot for a single channel for each anneal temperature (300 - 1070 K); right, mean resistance as a function of anneal temperature for each channel width (50 - 200 µm).

The properties of sample B are unusual for a number of reasons. The as-deposited metal contacts are expected to show non-ohmic, rectifying, properties due to the inherent potential barrier at the metal-semiconductor junction. Thermal annealing, and the formation of a metal-carbide layer under the contact should reduce the measured resistance, as observed for sample A. However the resistance increase upon high temperature (1070 K) annealing indicates a change in the semiconductor state or else a degradation of the contact properties.

9.3.2 Circular transmission line measurements

Two valuable parameters to extract are the specific contact resistances of the metallisation on samples A and B and the diamond sheet resistances, as functions of anneal temperature. Following the derivation of Reeves [231] for circular transmission line measurement described in chapter 6, one arrives at the relationship $\phi(\alpha) = \chi$, equation (6.3). Both $\phi(\alpha)$, equation (6.4), and χ, equation (6.5), are plotted numerically using the contact radii (in [cm]): $r_0 = 0.02$, $r_1' = 1.25r_0$, $r_1 = 2.25r_0$, $r_2' = 2.65r_0$, $r_2 = 3.65r_0$ and the values R_1, R_2 and R_{end} obtained experimentally, such as in figure 9.6 for sample B. The point of intersection of the functions gives the value of α at which equation (6.3) is true, allowing $\theta(\alpha)$ to be found and thus the specific contact resistance to be obtained using equations (6.6) and (6.7); as well as the sheet resistance.

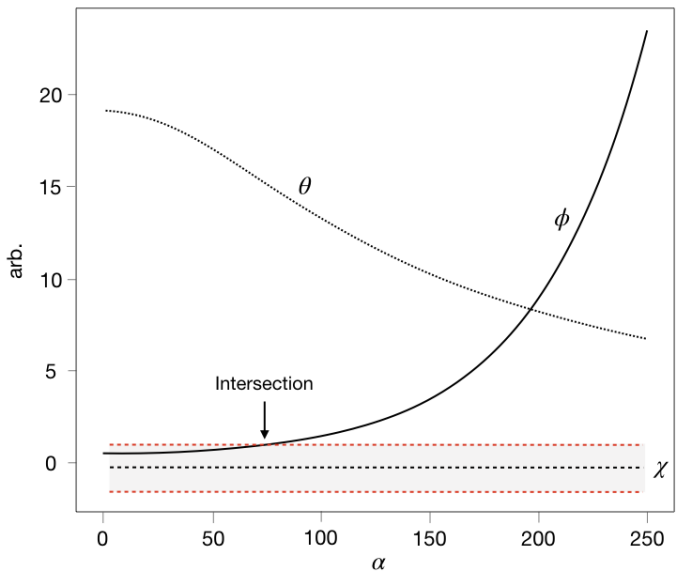

Figure 9.6: Sample B: $\phi(\alpha)$ (given by equation (6.4)) and $\theta(\alpha)$ (given by equation (6.7)) plotted numerically against α; and χ (given by equation (6.5)) plotted using experimental values after annealing at 870 K. The red dotted lines give the upper and lower experimental error boundaries within which a solution (labelled 'intersection') to equation (6.3) may lie. The y-axis is the magnitude of the individual quantities in arbitrary units.

For the samples A and B the CTLM derivation by Reeves does not strictly apply,

and for certain experimental measurement values there is no real solution to equation (6.3), i.e. $\phi(\alpha = 0) > \chi$, meaning that a specific contact resistance cannot be derived. This inconsistency can be attributed to the atypical contact patterns, which differ quite significantly from the ideal circular ring contacts in figure 6.5. Similar limitations with the Reeves CTLM have been previously investigated by Xu et. al [305], where it is shown that unreliable measurements of the contact end resistance (R_{end}) can introduce large errors into the solution for specific contact resistance – even for ideal contact patterns. They note, as do others [306,307], that due to the sensitivity of the model in some cases a real solution is not obtainable at all. For the Reeves model to remain applicable in this instance, and to avoid an intractable derivation for the unconventional contact pattern, a method by which errors in the measured resistances R_1, R_2, R_{end} owing to the incongruous experimental setup is used. These errors are accounted for and mathematically propagated through to the solution for α.

$$\delta\chi = \sqrt{\left(\frac{\partial\chi}{\partial R_1}\delta R_1\right)^2 + \left(\frac{\partial\chi}{\partial R_2}\delta R_2\right)^2 + \left(\frac{\partial\chi}{\partial R_{end}}\delta R_{end}\right)^2} \tag{9.1}$$

For a function $\chi(R_1, R_2, R_{end})$ the propagated errors can be described by equation (9.1), where δR_1, δR_2 and δR_{end} are the absolute experimental errors in the measured resistances. As a consequence of equation (6.3), it can be asserted that $\delta\phi = \delta\chi$ and hence the total error for the point of intersection between functions ϕ and χ is equivalent to $2\delta\chi$. By assuming an experimental error of 25% applicable to the measured resistance values, which may be loosely justified as a consequence of the non-ideal contact area occurring within one quarter of the circular pattern, an upper and lower boundary: $\chi - 2\delta\chi \leq \chi_S \leq \chi + 2\delta\chi$ is obtained within which a real solution can lie, highlighted in figure 9.6.

These boundaries give a range to the possible real values of α, which can then be used to calculate a mean value for the specific contact resistance, ρ_C, and diamond

sheet resistance. The results are plotted for samples A and B in figures 9.7 and 9.8, respectively, as functions of anneal temperature in Kelvin. It should be noted that although this method allows some of the limitations concerning the sensitivity of the Reeves CTLM to be overcome, it represents an imperfect analytical model for the measuring the specific contact resistance of the unconventional contact pattern, and as such there are unquantifiable uncertainties attached to the values extracted.

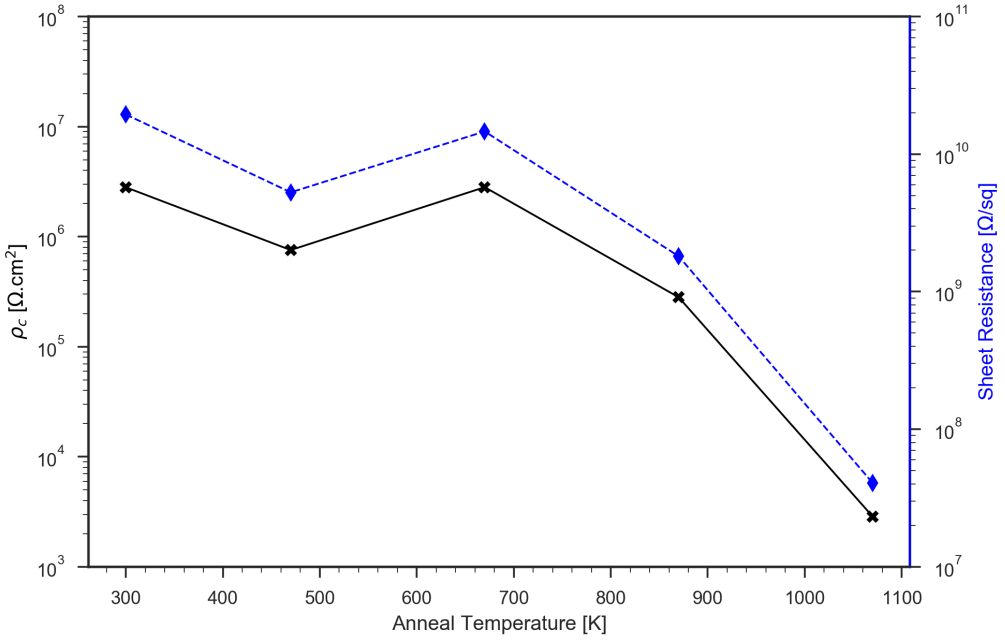

Figure 9.7: Sample A: the mean specific contact resistance, ρ_C (black line) and sheet resistance (blue line) as derived by CTLM, as a function of anneal temperature.

In the case of sample A, the specific contact resistance is observed to decrease by several orders of magnitude, from $\rho_C = 2.81 \times 10^6\,\Omega\text{cm}^2$ as deposited to $\rho_C = 2.87 \times 10^3\,\Omega\text{cm}^2$ when annealed. The most significant reduction in contact resistance is achieved at temperatures beyond 670 K, which is to be expected for a contact metal such as Ti; previous literature suggests carbide formation most readily occurs in the range 670 - 770 K [53–57]. Importantly, despite annealing, the contact resistance remains large which suggests that it is limited by the conductive properties of the diamond layer. Assuming sufficient evolution of the titanium-carbide

interface layer upon anneal, Fermi level pinning at the oxygenated surface should establish a Schottky barrier height of approximately 0.5 eV. The contact resistance would therefore remain dependent on the charge transport mechanisms across this barrier which are dictated by the acceptor dopant concentration. The fact that the specific contact resistance for sample A is of the order $\rho_C \sim 10^3\,\Omega\mathrm{cm}^2$ implies a very low boron concentration and hence highly temperature dependent thermionic emission into the metal contact. The sheet resistance is seen to fall in accordance with the contact resistance, from which an approximate sample resistivity of $\rho \sim 10^3\,\Omega\mathrm{cm}$ can then be deduced using the estimated thickness of the doped layer, $\sim$ 265 nm. Previous investigations [23, 32] imply that a room temperature resistivity of this magnitude is consistent with a doping concentration in the range [B] $\sim 10^{17}$ - $10^{18}\,\mathrm{cm}^{-3}$, where valence band conduction is the dominant hole transport mechanism in diamond.

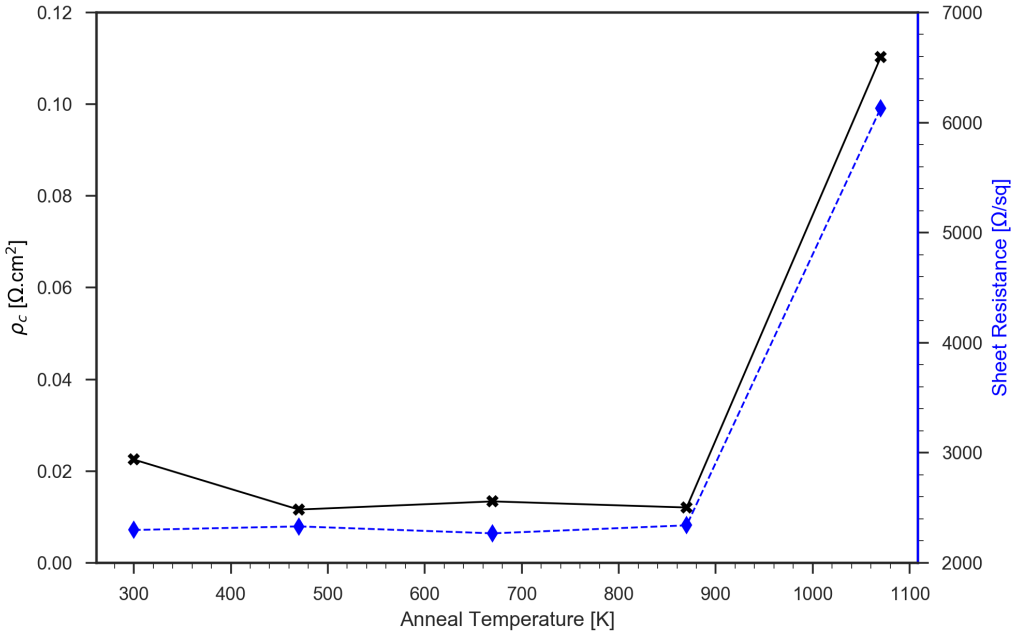

Figure 9.8: Sample B: the mean specific contact resistance, ρ_C (black line) and sheet resistance (blue line) as derived by CTLM, as a function of anneal temperature.

In comparison, sample B exhibits a much lower contact resistance – of the order ρ_C

Sample A	ρ_C [$\Omega\,\mathrm{cm}^2$]	R_{sh} [$\Omega\,\mathrm{sq}^{-1}$]	ρ [$\Omega\,\mathrm{cm}$]
As-deposited	2.81×10^6	1.94×10^{10}	5.14×10^5
Post anneal	2.87×10^3	4.07×10^7	1.08×10^3
Sample B			
As-deposited	2.25×10^{-2}	2.30×10^3	1.53×10^{-1}
Post anneal	1.10×10^{-1}	6.13×10^3	4.08×10^{-1}

Table 9.4: Specific contact resistance, sheet resistance and resistivity for samples A and B, measured for metal contacts as-deposited and after annealing.

$\sim 10^{-2}\,\Omega\,\mathrm{cm}^2$. This observation would indeed correspond to a much higher boron concentration than present in sample A; the magnitude of the contact resistance and sample resistivity (assumed layer thickness of 665 nm) suggest that this may be as high as [B] $\sim 10^{20}\,\mathrm{cm}^{-3}$. A boron concentration of this level would imply two things: firstly, that the acceptor density is great enough for hopping conduction to occur at room temperature, explaining the low resistivity of sample B; and secondly, that the dominant transport mechanism at the contact is likely due to field emission (FE).

This may be one reason that annealing has little effect on the specific contact resistance. In the FE transport regime, the contact resistance is strongly determined by the acceptor concentration over other factors such as barrier height and temperature. There may also be some degree of ohmic interface formation immediately upon the titanium deposition if the diamond surface is damaged during or after growth [58] that would exclude the need for thermally-induced carbide defect formation.

Kawarada [49] proposes that surface oxidation treatments may not be sufficient to remove hydrogen termination at the grain boundaries and hence could offer a low-resistance conduction path – an increase in the sample resistivity at high annealing temperatures could therefore be an indication of the thermal dehydrogenation of these paths. It has also been suggested [57, 59] that at high temperatures or for extended annealing times, the defect sublayer created by titanium carbide formation

may reach a maximum density and begin to outdiffuse – hence causing an increase in contact resistance. This may explain the degradation of the contact properties observed at high annealing temperatures, figure 9.8.

9.3.3 Impedance spectroscopy

Impedance spectroscopy (IS) is carried out to resolve the various frequency-dependent contributions to the sample impedances. The IS data for sample A are shown in figure 9.9, along with the Cole-Cole representation in figure 9.10. Several significant features are observed as the temperature is increased. At low temperatures (< 400 K), the characteristics are that of a near-infinitely resistive dielectric – behaviour similar to that of an open circuit. The impedance magnitudes, particularly at low frequencies are very large – of the order of 10^{11} - $10^{12}\,\Omega$ at 295 K. This room temperature behaviour is indicative of a material with very few activated carriers available to fulfil a conduction path between the electrodes. As temperatures are increased, the magnitude of the real and imaginary impedances decrease by several orders of magnitude, eventually to around 10^{8} - $10^{9}\,\Omega$, at nearly 700 K. In the region beyond 436 K, the low-frequency imaginary component tends to zero and the familiar complex semi-circle emerges. The dramatic decrease in impedance implies the thermal activation of carriers from a deep acceptor level in the doped diamond.

Furthermore, the existence of a single resolvable complex semi-circle indicates one dominant conduction path between the electrodes. At higher temperatures (> 463 K), an additional component is observed at low frequencies, deviating from the response of an ideal dielectric. A loop with positive imaginary impedance may suggest a pseudo-capacitance developed by a thermally-induced change occurring to the diamond surface or electrodes. However the appearance of this feature over multiple temperature ramps suggests that it is reversible, and the measurements under high vacuum with an oxygenated diamond surface should rule out any change in surface termination during heating. Hence this feature may point to an inductive

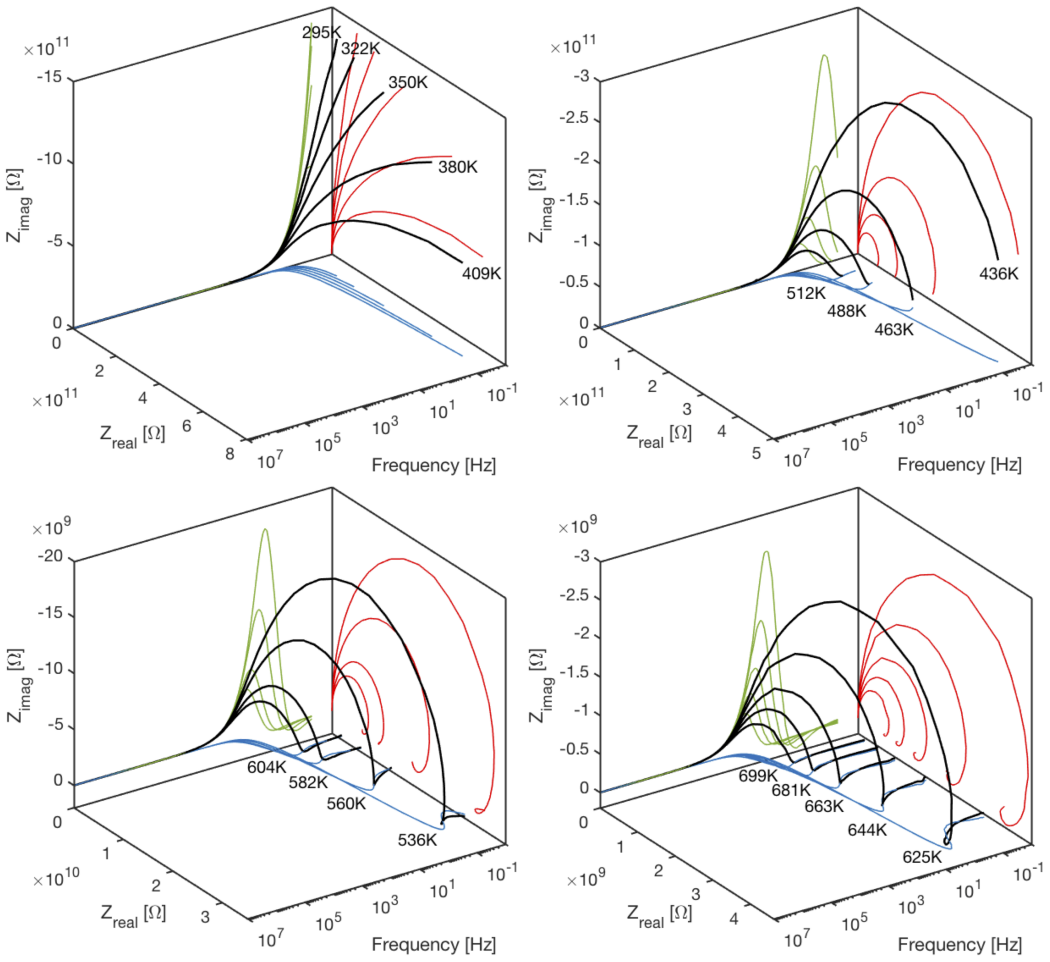

Figure 9.9: Sample A: A 3-dimensional plot of IS data along frequency, real and imaginary impedance axes, taken at increasing temperatures between 295 - 699 K (left-right, top-bottom). Projections: Cole-Cole plot (red), real Bode plot (blue), imaginary Bode plot (green).

contribution to conduction through the material or at the contacts.

The Bode projection, figure 9.11, shows the change in impedance magnitude with frequency. As the frequency tends to infinity the impedance magnitude decreases logarithmically, invariable of temperature. As the AC frequency approaches that of DC (0 Hz), the plot highlights the logarithmic decrease in impedance magnitude with increasing temperature. Additionally, the natural logarithm of impedance may be plotted against reciprocal temperature on an Arrhenius plot, figure 9.12. The carrier activation energy can be calculated by the gradient of this line as given by

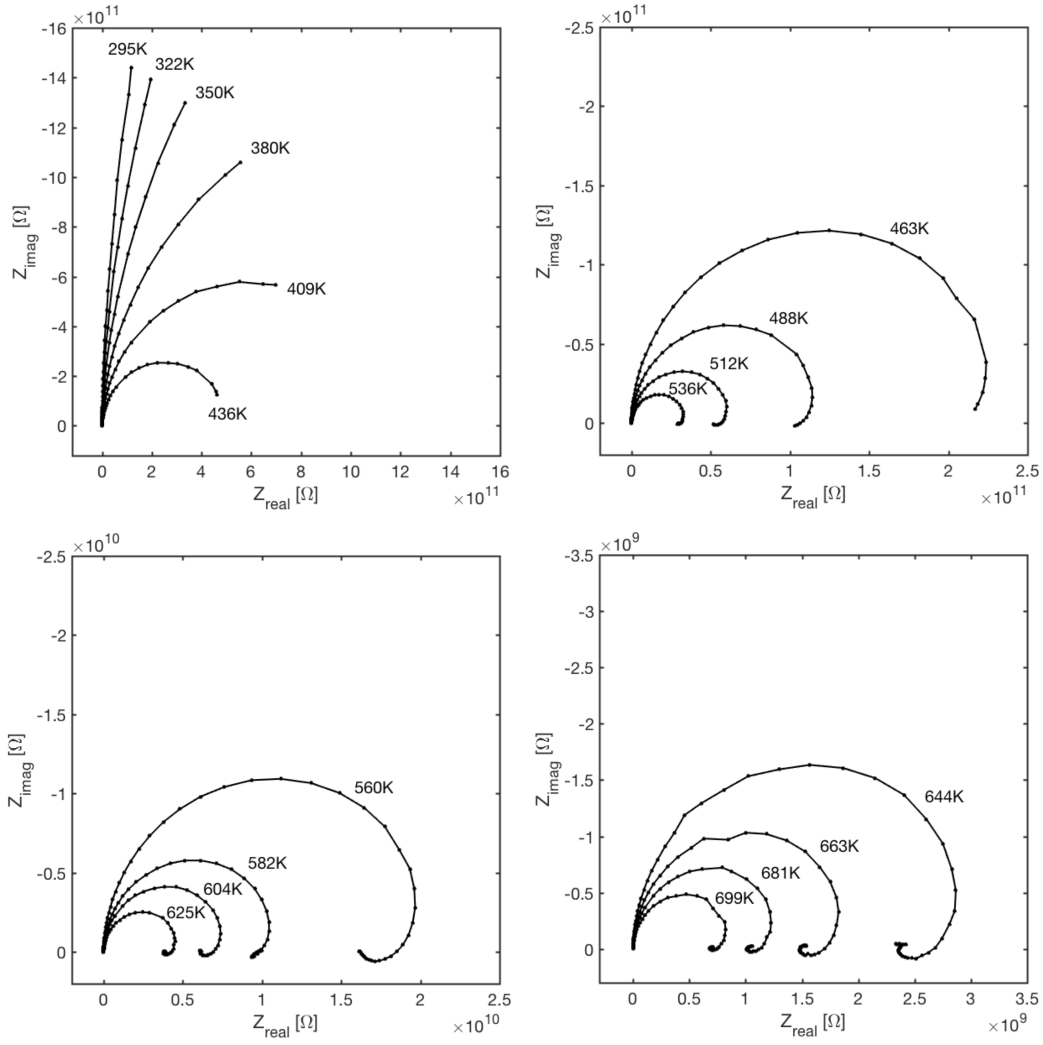

Figure 9.10: Sample A: Cole-Cole plots for IS measurements taken at increasing temperatures between 295 - 699 K (left-right, top-bottom). A characteristic semicircle can be seen at higher temperatures, indicative of a thermally activated material.

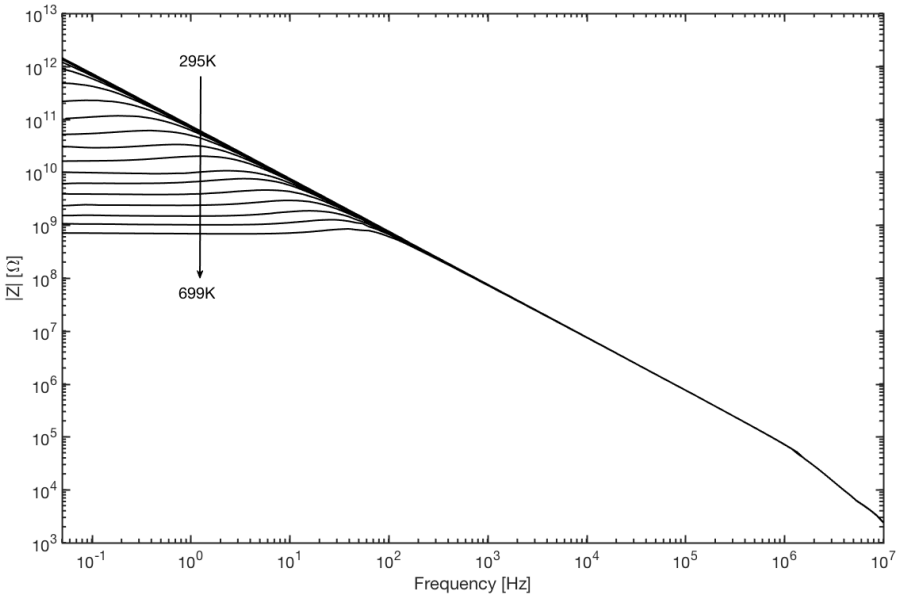

Figure 9.11: Sample A: Bode plot, showing the change in impedance magnitude $|Z|$ with frequency. The effect of temperature is clear at low frequencies where the impedance magnitude decreases logarithmically.

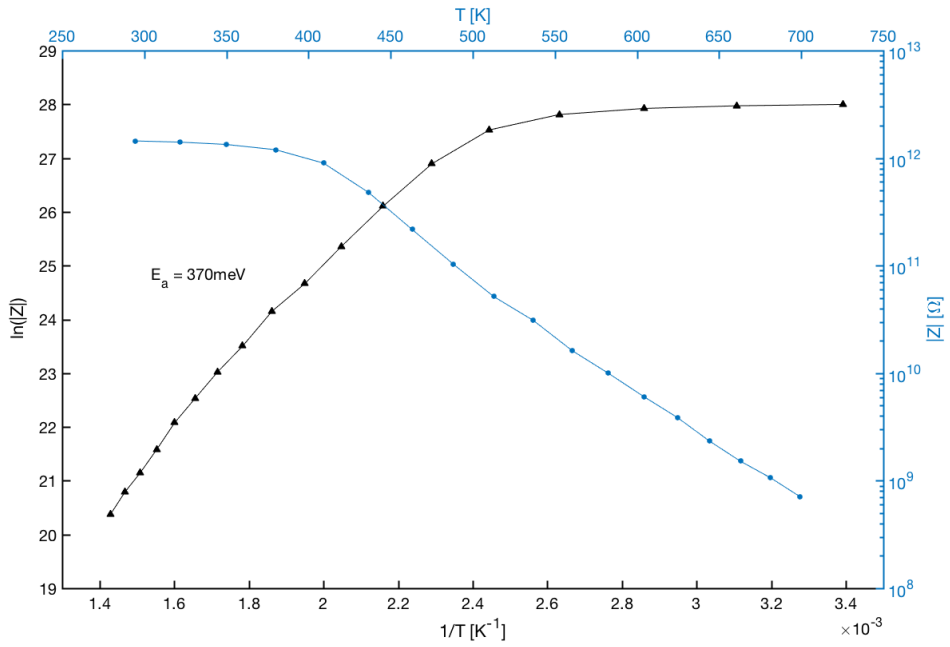

Figure 9.12: Sample A: Arrhenius plot (black line, primary axes), showing the natural logarithm of the impedance against reciprocal temperature; also shown is the change in impedance magnitude $|Z|$ against temperature T (blue line, secondary axes). An activation energy of $E_A = 370$ meV may be extracted.

equation (9.2), where k_B is the Boltzmann constant in units of $\mathrm{eV\,K^{-1}}$.

$$E_A = k_B \frac{\partial \ln(Z)}{\partial\left(\frac{1}{T}\right)} \tag{9.2}$$

In the case of sample A, the gradient given by a linear fit through all points in the measured temperature range yields an activation energy of E_A = 370 meV. This corresponds to the deepest boron activation energy for a doping concentration [B] $\sim$ $10^{17}\,\mathrm{cm^{-3}}$. This low dopant concentration would corroborate the high contact resistance and sample resistivity measured, as well as the near-dielectric behaviour seen in the Cole-Cole representations. It is possible to resolve a knee in the Arrhenius plot at 420 K which may suggest two different activation energies – E_A = 749 meV and E_A = 21 meV. The former value is significantly larger than any boron-induced state – which may by elimination imply nitrogen activation; the latter value may be a shallow boron state. However, the existence of two carrier activation energies is unlikely given the single conduction path observed in figure 9.10 and experimentally measured values pointing to carrier transport in the valence band regime. The knee may instead be a result of the resistive contacts. As measured by the CTLM method, the specific contact resistance for sample A is very high at room temperature and the dominant current transport regime at the metal-diamond interface is thermionic emission. This process is highly temperature dependent, and as such the contact resistance may be the dominant contribution to impedance at low temperatures – becoming negligible for higher temperatures.

The impedance spectroscopy data in figure 9.13, and Cole-Cole representation in figure 9.14 show significantly differing characteristics for sample B. The most notable of which is the lack of a discernible complex semi-circle in the negative y-axis. Any measured system that comprises electrodes in contact with a material inevitably contains a geometrical capacitance, as well as a parallel bulk resistance – so an RC equivalent circuit should always be present. However if the RC product is very small, the characteristic circular arc may not be resolvable within the measured temperature range [229].

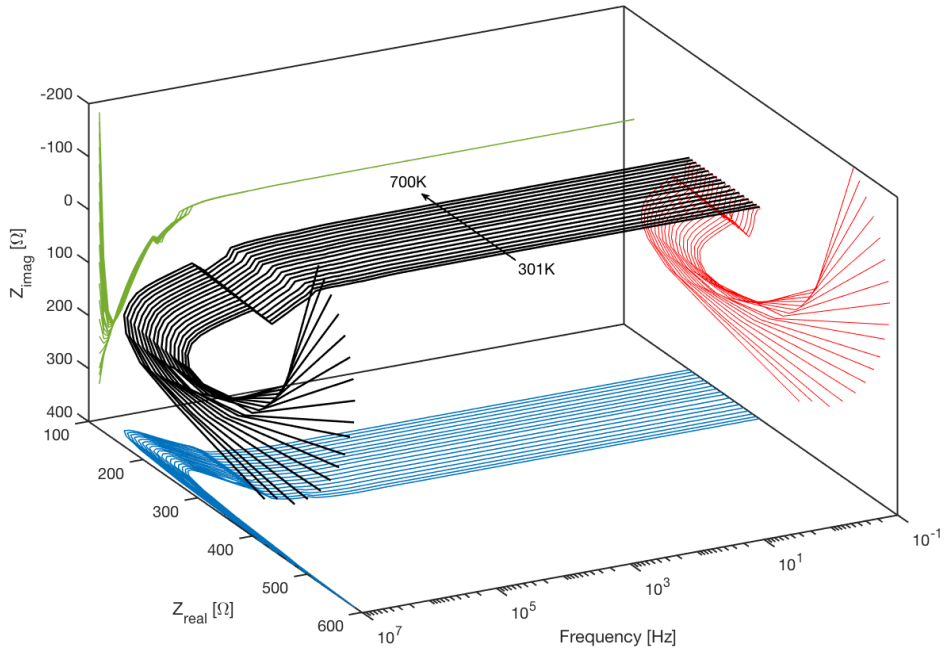

Figure 9.13: Sample B: A 3-dimensional plot of IS data along frequency, real impedance and imaginary impedance axes. Projections: Cole-Cole plot (red), real Bode plot (blue), imaginary Bode plot (green).

At room temperature (301 K) a small negative imaginary impedance can be observed for high frequencies, which decreases with increasing temperature. It is therefore possible that measurements conducted below room temperature may yield more familiar behaviour as the hole density decreases. The fact that the magnitudes of the real and imaginary impedance values are relatively very small – smaller by several orders of magnitude when compared with sample A – also suggest that sample B has properties akin to that of a highly doped metallic conductor with a very low impedance. Consequently, the data points in the Cole-Cole representation may therefore be explained by dominant high frequency inductive effects rather than dielectric material properties.

This is highlighted in the impedance Bode projection, figure 9.15, which shows little frequency dependence below 10^5 Hz, whereas above this the impedance fluctuates and nearly doubles. This change can be attributed to the 'skin effect' – in which the majority of the current density exists within the skin depth of the material due to

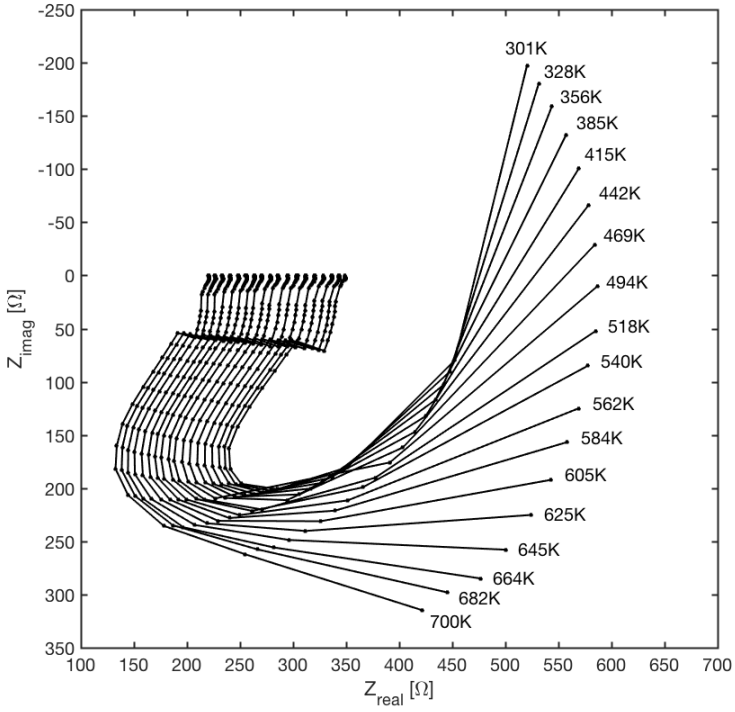

Figure 9.14: Sample B: Cole-Cole plot taken at increasing temperatures between 295 - 699 K. The lack of a complex semi-circle is clear, and is most likely not resolvable within the measured temperature range. Instead there may be a dominant high frequency inductive component.

the inductive effect of AC fields. At high frequencies, the skin depth becomes very narrow causing a consequential increase in resistance.

The Arrhenius plot, figure 9.16, yields an activation energy of $E_A = 21$ meV using the gradient given by a linear fit through all points in the measured temperature range. This shallow boron activation state suggests a high doping concentration, of at least [B] $\sim 10^{20}\,\mathrm{cm}^{-3}$, and dominant hopping conduction – correlating the low contact resistances and sample resistivity measured, as well as the impedance data above. As with sample A, two activation energies may be weakly resolved – with a knee at 415 K – $E_A = 60$ meV and $E_A = 7$ meV, possibly corresponding to two unique conduction mechanisms. This might suggest conduction paths through the grain boundaries, and the grain interiors of the highly polycrystalline diamond layer.

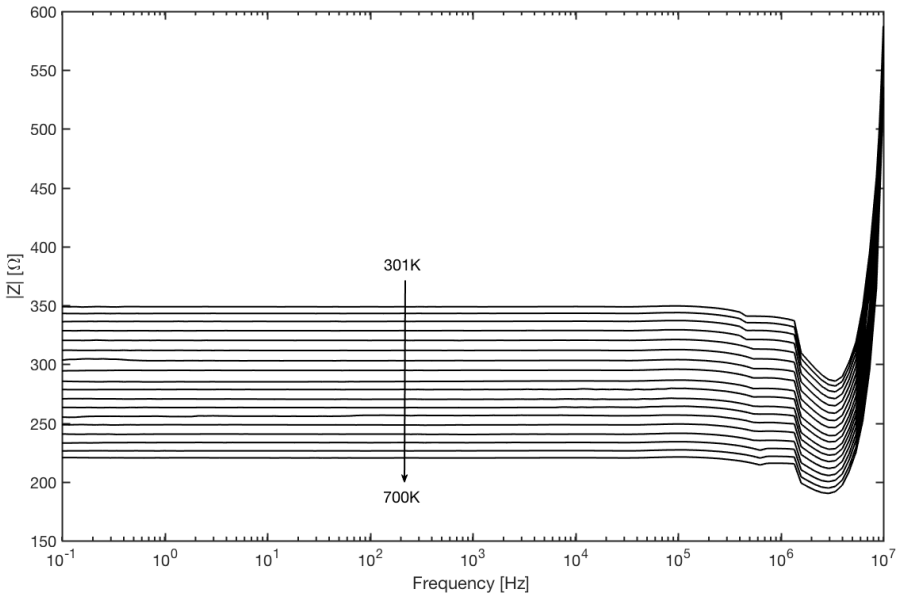

Figure 9.15: Sample B: Bode plot showing the change in impedance magnitude $|Z|$ with frequency. Very little frequency dependence can be observed below 10^5 Hz; the high frequency impedance increase could be attributed to the 'skin effect'.

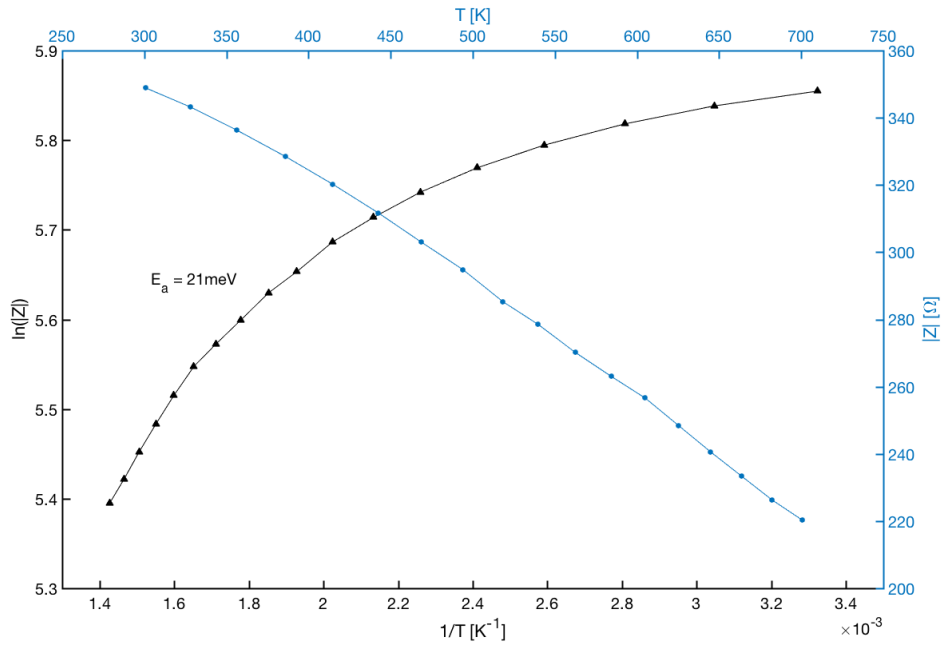

Figure 9.16: Sample B: Arrhenius plot (black line, primary axes), showing the natural logarithm of the impedance against reciprocal temperature; also shown is the change in impedance magnitude $|Z|$ against temperature T (blue line, secondary axes). An activation energy of $E_A = 21$ meV may be extracted.

9.4 Conclusions

Boron-doped diamond layers were grown onto polycrystalline intrinsic substrates using a 4 kW MWPECVD reactor. A process was developed to achieve controllable layer thicknesses, with dopants conservatively introduced through the residual boron chamber contamination. Two final samples were grown: sample A, a layer approximately 265 nm thick, which was grown with a 4% CH_4 concentration at a temperature of 1000 °C and pressure of 80 Torr; and sample B, a layer approximately 665 nm thick, which was grown in identical conditions but at a temperature of 935 °C and higher pressure of 100 Torr. These were subjected to a photochemical ozone treatment and acid etch to oxygenate the surface, and subsequently metallised using lift-off photolithography to pattern electrodes onto the layers. Room temperature electronic characterisation was performed consecutively throughout a multiple step annealing treatment at increasing temperatures, and temperature-variable impedance spectroscopy was then carried out when fully annealed.

Sample A exhibits electronic properties that are evident of a low boron doping concentration, in the region [B] $\sim 10^{17}$ - $10^{18}\,cm^{-3}$. The activation energy of 0.37 eV extracted from the Arrhenius plot, suggests that at room temperature the dominant carrier transport mechanism is valence band conduction – which yields a very resistive layer and little carrier activation. This is reflected in the measured sample resistivity, extracted by use of a modified circular transmission line model. Annealing at temperatures greater than 670 K is shown to be effective in reducing the specific contact resistance by several orders of magnitude, as a titanium-carbide defect layer is formed at the interface. However, despite this, the specific contact resistance remains relatively large and the I-V contact properties lack perfect ohmicity – observations that further support the low acceptor concentration. It is therefore proposed that thermionic emission over the Schottky barrier is the dominant interface process and contributes to the highly temperature-dependent electronic properties of the sample. On the other hand, sample B demonstrates properties that would indicate a much higher boron doping concentration, approximately [B] $\sim 10^{20}\,cm^{-3}$. Near-

metallic behaviour is evident in the low sample resistivity and impedance spectra; and the Arrhenius plot yields an activation energy of 0.02 eV. This implies that the boron concentration is high enough to facilitate dominant hopping conduction between impurity sites. Another consequence of this very conductive layer is the small specific contact resistance and the ohmic I-V relationship. The contact properties appear to be largely independent of annealing treatments, which suggest that the acceptor density is great enough to cause field emission carrier transport at the metal-diamond interface, even as-deposited.

Large differences in samples A and B are evident from the electronic characterisation carried out in this chapter. Eliminating their complementary characteristics in terms of intrinsic diamond substrate used and growth parameters, it is clear that these differences arise from either the process pressure during growth or the layer thickness – a function of growth time. Thickness would not be expected to be a limiting factor, particularly at magnitudes > 100 nm, at which the layer can be assumed to be a bulk conductor. However an increase in process pressure does point to an improvement in the efficiency of boron impurity inclusion – as alluded to in previous studies [35, 39, 40]. Further work to determine the effect of growth pressure on the electronic properties of doped polycrystalline diamond layers is required, particularly to facilitate even finer control over device properties. The experimental methods would also be improved by using a contact pattern more applicable to the CTLM, as would secondary-ion mass spectrometry (SIMS) characterisation layers to further verify the acceptor concentrations and layer thicknesses.

Crucially, however, the work presented in this chapter has fulfilled the aim of developing a MWPECVD growth process which may be directly linked to the electronic properties of the layers that are grown. The future fabrication of ion-sensitive field effect transistors (ISFETs) for use at high temperatures will benefit greatly from controllable, thin and low-doped layers that show activated valence band conduction above room temperature. Additionally, the development of electrochemical dissolved oxygen (DO) sensors will benefit from a highly doped electrode material

with metallic properties. Consequently, samples A and B will be used for further sensor fabrication in chapter 10.

Chapter 10

Diamond pH and dissolved oxygen sensors for extreme environments

10.1 Introduction

The need for the accurate monitoring of water quality occurs across a wide range of public sector, environmental, industrial and military applications [151–154], constituting a fast-growing multi-billion pound market [155–157]. The harsh nature of some of these fluid systems limits the use of many conventional sensing technologies. High temperatures and pressures may be encountered, along with damaging levels of radiation and a chemically aggressive environment. This means that the sensors that currently exist are incompatible, or suffer from severely reduced operational lifetimes, poor stability and may be practically cumbersome. The additional complexity associated with access to these systems in the case of offline analysis compounds the problem with issues of operator safety and financial cost. Due to its radiation hardness, high chemical inertness and mechanical resilience, diamond therefore presents itself as a material suitable for prolonged exposure to these conditions. As described in greater detail in chapter 2, diamond can also be boron-doped to form a p-type semiconductor with unique properties that facilitate unparalleled electronic and electrochemical performance.

Two metrics that are key indicators of water quality are pH and dissolved oxygen (DO) concentration. Conventionally, pH has been measured by sensing the potential formed across an interface as a result of an imbalance in ion concentrations [159]. Potentiometric sensors, such as the glass electrode (GE) [158] leverage this principle to measure pH between an electrode that is designed to be selective to H^+ ions and a constant-potential reference electrode. The fragility, instability and relative bulkiness of these early devices has driven research into other methods such as optical [160] or conductimetric [161] pH sensors, although the greatest advantages can be found using solid-state solutions. Pioneered in the early 1970s [163], these are based upon MOSFET devices, however differ by the fact that the gate metal is removed and instead contacted by the solution to be measured. The source and drain contacts are encapsulated and a reference electrode maintains the gate potential. Site-binding of protons at amphoteric surface groups results in a surface potential that can be observed as a modulation of the current passing through the channel of the device, proportional to the pH of the solution.

Dissolved oxygen concentration may also be measured in a number of ways depending on the application. Technologies that currently exist include optical techniques [187]; paramagnetic sensing [188]; tunable laser diode (TDL) spectroscopy [190, 191]; and many more [192, 193]. In addition, DO is commonly measured by the electrochemical reduction current of dissolved oxygen at an electrode such as Pt [194]. By careful design, and accounting for diffusion, this current is linearly correlated to the oxygen concentration in solution.

The methodologies of pH measurement using ISFETs and amperometric DO sensing may be transferred to diamond in order to benefit from its unique advantages. Previous studies on diamond have shown pH sensitivities approaching, or even exceeding [167] that of the theoretical Nernst limit of 59.2 mV/pH [168]. Devices have been successfully fabricated using FET structures with hydrogen transfer-doped [165–167, 169–176], as well as boron-doped [177–181] channels. Hydrogen channel devices are subject to disputed theories [176] over the mechanism by which

current modulation is achieved, but consensus points to the requirement for the co-presence of oxygen moieties on the surface [167]. These devices show high sensitivities but are disadvantaged by the chemical instability of the C-H bond. Boron channel ISFETs have greater lifetimes and stability [179], although present devices rely on delta-doping for sufficient channel modulation at room temperature, which is very hard to achieve. Concurrently, electrochemical oxygen reduction on diamond has been investigated comprehensively [207–213], motivated as a result of the wide electrochemical window, chemical stability and low background currents shown by diamond. Boron-doped diamond has subsequently been shown [214] to operate as an optimal electrode for DO sensing, where reduction occurs stably via a four-electron pathway and the measured current is a linear function of concentration.

Despite the wealth of research presenting the principles for, and great advantages of, diamond pH and DO sensing, there has been little progress on practical implementation to meet the pressing need for resilient water quality sensors. A number of challenges have yet to be overcome:

- Primarily, diamond sensors need to be made for the realistic operating environments within which they are expected to perform. For example, in the primary cooling circuit of a PWR water enters the bottom of the nuclear reactor core at $\sim$ 290 °C and is heated to $\sim$ 330 °C by the time it emerges, at the same time pressures over 160 bar are maintained in order to keep it in the liquid phase [308]. Under these conditions, the semiconducting properties of diamond are vastly different to those at room temperature and sensors need to be re-designed accordingly.

- Due to the physical inaccessibility of these applications, and the sizeable costs associated with the present measurement techniques to be replaced, any novel technology is required to provide a complete solution to the needs of the operator. By definition, this requires sensors to be fully integrated and multi-functional in detecting all key metrics associated with the environment. This

requires intelligent sensor design, to achieve a 'lab-on-a-chip' functionality.

- Finally, the resilient benefits of diamond may not be exploited if the point of weakness lies elsewhere. Hence careful consideration must be made of the packaging and deployment of such a diamond sensor.

The work presented in this chapter seeks to address these needs. The initial prototyping for the first fully-integrated and multi-functional diamond sensor directly deployable into harsh environments is presented. A novel sensor design is described that allows compact sensing of key metrics on multiple channels. Ultimately, this design will allow the measurement of pH, DO, temperature and conductivity of any fluid – however, the measurement of pH and DO present the greatest technical challenges and are explored further. The sensors are processed for both pH measurement using an ISFET structure, and amperometric DO electrodes. In the absence of access to a PWR or similar test facility, proof of principle is shown in a custom test and calibration cell. The ISFET is shown to operate as an effective hydrogen channel device at room temperature, with the expected onset of low boron-doped microchannel conduction at higher temperatures. The DO sensor shows linear reduction of oxygen with increasing concentration at micrometer-scale electrodes. Finally, methods by which these sensors may be packaged to allow deployment in a real application environment over an extended lifetime are subject to future work discussed in chapter 11.

10.2 Device design

In order to perform multi-functional sensing tasks, a device is required that consists of several individually addressable channels in a compact format. These channels need to accommodate for the requirements of each sensing technique on the device, namely:

- pH sensor (3 electrodes): ISFET devices require contacts to both source and drain electrodes. Additionally, a gate electrode is also required to contact the

solution directly – which may be fulfilled by a Pt [173] or Ag/AgCl [167] reference electrode.

- DO sensor (2 electrodes): amperometric reduction is ideally carried out using a 3-electrode electrochemical setup, where electrical connection is made to the working electrode, as well as a counter and reference electrodes. However it is suggested [202] that if the currents are limited to being sufficiently small (μA to pA) the reference electrode remains ideally polarised and allows the use of two-electrode configurations.

- Conductivity sensor (3 electrodes): the conductivity of a solution may be deduced by circular transmission line measurements (CTLM, presented in chapter 9), allowing the resistance of the electrodes and semiconductor to be accounted for and an accurate value extracted.

- Temperature sensor (n/a): temperature should be sensed by a separate (non-diamond) component, so that thermal effects can be accounted for independent of the system. This component may exist on the dry side of the sensor and benefit from responsive readings due to the high thermal conductivity of diamond.

Integrating these sensors into a single lab-on-chip necessitates the use of a total of 8 electrodes, two of which act as reference electrodes. This redundancy allows the total number to be reduced to 6 if the sensing is duty-cycled at an appropriate frequency – meaning that the reference electrodes can be shared, as well as the working electrode and inner conductivity ring. Additionally, the overall layout of the electrodes is defined by the use of concentric circular transmission lines for conductivity sensing. By making each contact a concentric ring, not only can CTLM measurements be conveniently made, but chip real-estate is maximised by sensor tessellation, and measurements may benefit from symmetrical electric fields across the device.

The size of each sensor also requires consideration. Review of previous litera-

ture would suggest that ISFETs perform well at channel lengths of the order of 60 µm [178] to 500 µm [179] and gate widths of several mm. Whereas for oxygen reduction, the use of low micron-scale electrodes is highly beneficial. Mass transport rates to the electrode are increased due to non-planar diffusion, the double-layer capacitance is reduced as a result of the smaller surface area, and leakage currents are minimised [309]. Further to this, smaller electrodes have the direct effect of producing smaller reduction currents, allowing a two electrode arrangement to be used [202]. Consequently, the working electrode of the DO sensor should be designed to be as small as possible and occupy the most central concentric electrode. Finally, as per the requirements of the CLTM – the three conductivity rings must be spaced at differing separations.

The layer thicknesses and doping levels in the diamond must additionally be tailored to the sensitive operation of each device at high temperatures. The growth of layers with controlled thickness and dopant concentration, [B], are presented in chapter 9. For maximum ISFET sensitivity, the channel should ideally be able to be fully depleted within the gate potential window, ΔV_G^{max}, which for high-quality single crystal has been determined to be ~ 3.5 V [203]. Lower quality polycrystalline films that contain graphitic inclusions see a reduced window of about 2.7 V [310]. The maximum channel thickness t_{max} for full depletion is given by equation (10.1) [177], where $\varepsilon_s = 5.5$ is the dielectric constant of diamond, $\varepsilon_0 = 8.85 \times 10^{-12}\,\mathrm{F\,m^{-1}}$ is the vacuum permittivity and N_A is the doping concentration in the channel.

$$t_{max} = \sqrt{\frac{2\varepsilon_s\varepsilon_0\Delta V_G^{max}}{qN_A}} \tag{10.1}$$

The optimal layer is therefore between 130 - 40 nm thick, for a doping concentration of 10^{17} - $10^{18}\,\mathrm{cm^{-3}}$. The case for the electrochemical oxygen sensor is more trivial. An effective working electrode requires metallic properties to facilitate optimal electron exchange. Hence diamond should be degenerately doped to a boron concentration of $\sim 10^{20}\,\mathrm{cm^{-3}}$.

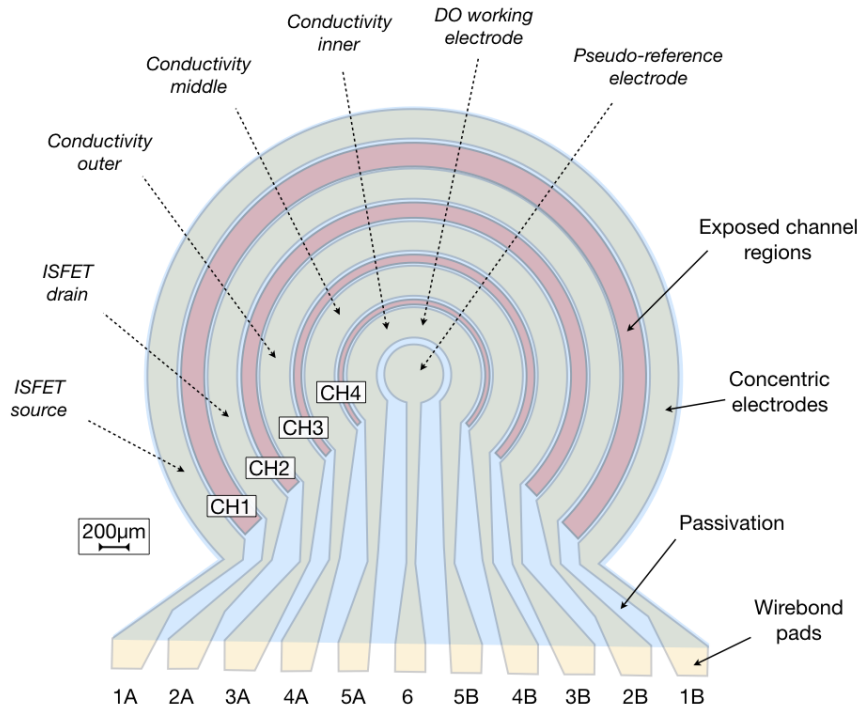

Figure 10.1: Schematic presenting the prototype devices developed. Six concentric electrodes are formed, leaving four channels exposed with dimensions optimised for the specific sensor types. The electrodes break out into square wire-bond pads along the lower edge of the device; and are passivated to electrically isolate them from the solution. Dotted arrows show the proposed sensor layout for the final integrated device.

Development of the final integrated device will require a series of selective growth and etch steps to achieve the correct sensor layout. In addition to this, a method by which a reference – or pseudo-reference – electrode may be integrated into the device must be explored; as well as a suitable means of contacting the sensor electrodes from the dry face of the sensor. These advances are the subject of concurrent ongoing and future work, and will be highlighted in chapter 11. For the purposes of the initial prototype studies presented here, two separate sensors are developed. One consisting of a thin layer of lightly boron-doped material for the operation of a diamond ISFET; the other consisting of heavily doped diamond for an amperometric DO sensor. Both these devices are developed using an iteration of the novel lab-on-chip layout, figure 10.1. This design consists of six concentric circular electrodes,

forming four channels with dimensions (listed in table 9.2) suited for the operation of the sensors described. These electrodes are passivated to electrically isolate the contacts from the solution, leaving the channels exposed. To avoid contacting through the device, the electrodes break out into a series of square pads along the lower edge of the device to allow wire-bonding into a package.

10.3 Experimental methods

10.3.1 Initial processing

For the devices investigated in this chapter, two polycrystalline diamond substrates are supplied by Element Six. As described at length in chapter 9, these substrates are subjected to CVD growth of boron-doped diamond layers where the recipes are listed in table 9.1. By electronic characterisation it is determined that one sample (device A) has a 265 nm thick layer doped with [B] $\sim 10^{17}$ - 10^{18} cm^{-3} and the second (device B) has a 665 nm thick layer doped with [B] $\sim 10^{20}$ cm^{-3}. With some growth optimisation still to do, these are considered close to being optimal for ISFET and amperometric DO sensing at $\sim$ 640 K, respectively. An air burn in a quartz oven, followed by a UV photochemical process are used to oxygen terminate the surface of the samples. Metal electrodes consisting of Ti/Pt/Au are then deposited by a lift-off photolithography process and electron-beam evaporation. These are finally annealed to reduce the contact resistance with the diamond.

10.3.2 Surface treatment

As a consequence of this initial processing and as corroborated by the electronic characterisation, both devices A and B are expected to be left with a homogenous oxygen surface termination. In order to demonstrate ISFET behaviour at room temperature, device A is treated to induce hydrogen surface conductivity. This may be achieved by exposure to a pure hydrogen plasma within a diamond growth chamber. At favourable temperature and microwave power, oxygen is removed from the

surface and replaced by hydrogen due to the high reactivity of atomic hydrogen.

Device A is mounted onto a water-cooled stage within a SEKI Technotron AX5010 reactor. The chamber is evacuated by rotary and turbo pumps to achieve a base pressure of 2×10^{-5} Torr. The cooling achieves an initial stable sample temperature of approximately 12 °C. Hydrogen gas is injected into the chamber at a rate of 200 sccm maintained by MKS mass flow controllers, increasing the pressure to 40 Torr. In order to achieve partial hydrogenation whilst maintaining a certain density of oxygen surface moieties (required for hydrogen ISFET operation [167]) the treatment is relatively mild. Hence the power of the 2.45 GHz magnetron is ramped quickly to 1 kW in order to ignite the plasma and achieve the desired process temperature in the shortest possible time. Once the sample has reached 275 °C (90 sec), as measured by a Williamson dual-wavelength pyrometer, it is maintained for 30 sec. The magnetron power is then immediately ramped back down to quench the plasma. The device is cooled in a hydrogen atmosphere for 45 min before removing from the chamber.

10.3.3 SU-8 passivation

For lab-based characterisation of these sensors a passivation is required that is chemically and physically robust for an extended period of time. A suitable material for this purpose, and used extensively for MEMS and lab-on-chip systems [311–313], is SU-8 epoxy-based photoresist.

SU-8 can be patterned by standard photolithography processes to form highly cross-linked and resistant features, however the deposition of effective layers is somewhat elusive – the main problems being delamination caused by poor adhesion and achieving a homogenous and well cross-linked film. Exhaustive (> 100 iteration) recipe development was conducted to mitigate for these problems when depositing SU-8 on diamond and gold.

Initial trials using SU-8 2025 proved to be unsuccessful due to delamination of the

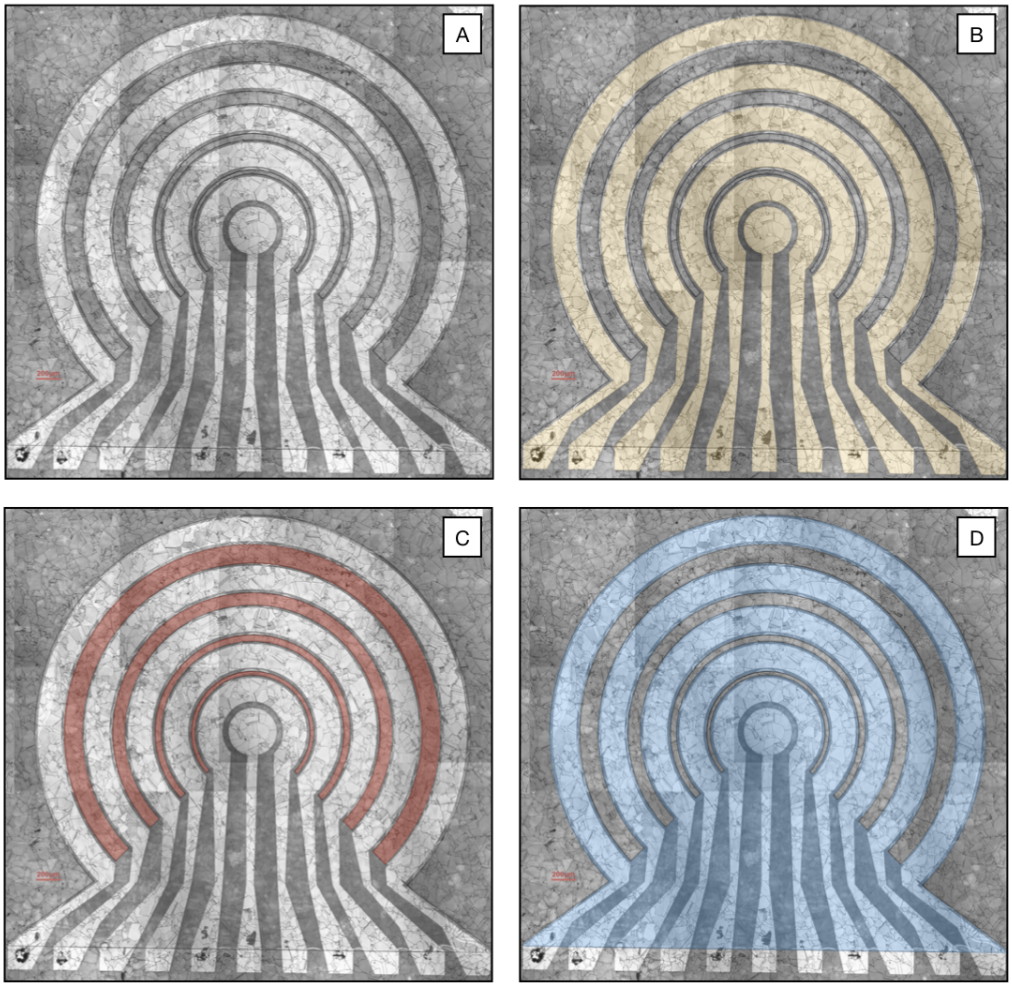

Figure 10.2: A composite image of device B after passivation, produced by optical microscope at 10 times magnification: A) final device; B) Ti/Pt/Au concentric electrodes highlighted; C) exposed channel regions highlighted; D) SU-8 3025 passivation highlighted.

films. Instead, subsequent tests using SU-8 3025 supplied by MicroChem, which promises better adhesive properties, showed improved results. The following final recipe highlights key methods refined for successful deposition:

1. Clean sample with standard degrease process and dry with a high-flow N_2 gun to clear surface of contaminants, followed by thorough dehydration bake for 20 min at 115 °C.

2. Mount onto spin coater using a small vacuum chuck capable of holding a 5 x 5 mm sample.

3. Drop coat sample with an excess quantity of SU-8 3025 photoresist. Ramp for 2 sec to 500 rpm, hold for 2 sec, ramp to 9000 rpm for 4 sec, hold for 45 sec, ramp down to 0 rpm for 2 sec. The high rotational speed is required to achieve a thin, homogenous layer with a minimal edge-bead.

4. Soft-bake sample on covered hotplate at 60 °C for 1 min, then on a hotplate at 95 °C for 9 min. This extended, two-stage bake is crucial for minimising stress in the film.

5. Mount on vacuum chuck in Karl Suss MJB3 Mask Aligner. Align sample to mask features. Make soft contact between sample and mask. Expose to UV light (intensity 20.3 $\mathrm{mW\,cm^{-2}}$) for 11.4 sec. Over-exposure in this instance is required to evolve sufficient strong acid in the exposed areas of the SU-8, which is a negative photoresist. Adverse effects of over-exposure are mitigated by the relatively large feature size.

6. Post-exposure bake on covered hotplate at 60 °C for 1 min, then on a hotplate at 95 °C for 4.5 min. This step must be carefully controlled to ensure complete cross-linking, which occurs via a thermally driven, acid-catalysed reaction.

7. Develop in EC solvent for 5 min. Rinse immediately in IPA for 2 min, deionised water for 2 min, followed by N_2 gun to dry. The developing step needs to remove all photoresist remaining in the channel regions to avoid impeding

sensor performance. EC solvent was used instead of acetone developer, which was observed to leave a surface residue that is difficult to remove without aggressive sonication.

8. Hard bake the developed features on a covered hotplate. Ramp from ambient temperature to 150 °C over 10 min, hold for 10 min and leave to cool in air. After this, the SU-8 features should be resistant to high temperatures, chemical corrosion and limited amounts of physical attack. Lifetime tests were performed to ensure the resist was unchanged after submersion for 48 hours in acetone, pH buffer, as well as after light scratching with a needle.

The SU-8 is patterned using a CAD-designed mask, produced by a similar process used for the lift-off metallisation mask, figure 9.1. The above recipe results in consistent, high aspect-ratio features with a step height of 11 μm as measured by Dektak profilometer over 10 scans. Mapped optical microscope images are taken at 10 times magnification and digitally stitched together to form a composite image of the sample after deposition of the passivation layer. The various features of device B are highlighted in figure 10.2.

10.3.4 Packaging and PCB mounting

The processed devices are mounted into ceramic leadless chip carriers (LCC), supplied by Spectrum Semiconductor Materials Inc., using silver epoxy paste cured at 100 °C for 15 min. 25 μm diameter gold wire-bonds are made between the bond pads on the device and those in the LCCs using a Kuilicke & Soffa 4523 gold wedge bonder, heated at 120 °C to promote adhesion of the bonds. The wire-bond map is shown in figure 10.3 along with the colours of the leads eventually emerging from the breakout board.

A custom printed circuit board (PCB) was designed for the purpose of providing shielded breakout connections from the LCC to the characterisation equipment, figure 10.4. The design was produced using OrCAD PCB design software, consisting

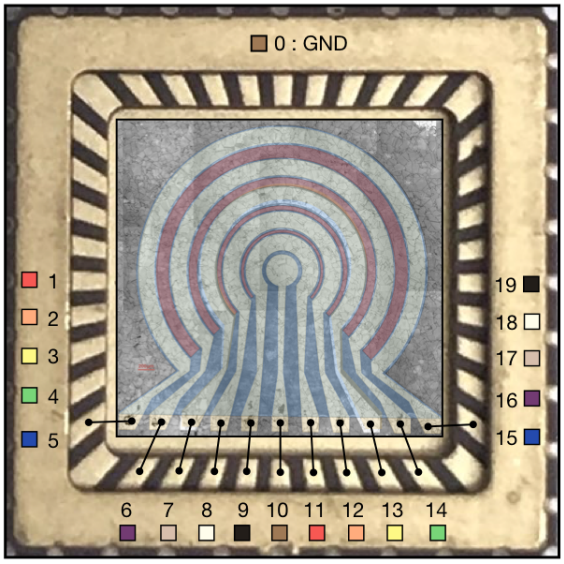

Figure 10.3: Map showing the position of gold wire-bonds made from the electrode pads on the sensors to those on the ceramic chip carrier. Colours and numbers represent the addresses of each connection emerging from the breakout board.

of top and bottom copper track and drill hole plots. The final boards were laser etched from 1.6 mm thick FR-4 sheets, using a LPKF ProtoLaser U3 laser prototyping system. The LCCs are soldered at the upper end of the board, with screw holes for precise mounting in the test cell; tracks feed out to a 20-way connector that allows an addressable, coloured ribbon cable to be attached. All the tracks are shielded by a ground plane on the reverse side of the PCB.

10.3.5 Test and calibration cell

The measurement of a liquid presents several practical challenges in order to contact the sensitive channel regions and maintain electrical isolation of the connections. Previous studies of ISFET devices have relied on very crude solutions such as epoxy encapsulation to achieve this [178]. Alternatively, the manufacture of bespoke components could be outsourced to a supplier at considerable expense. Instead an effective and modular experimental setup is developed to solve these issues, figure 10.5. The system consists of a main glass vessel which can be filled with the

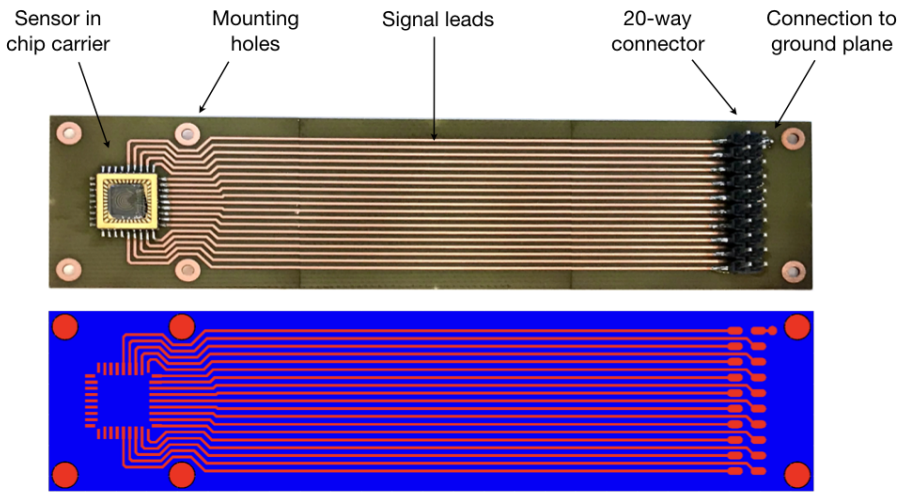

Figure 10.4: Top, photograph of PCB used for breakout connections and test cell mounting. Devices are wirebonded into LCCs, which are subsequently soldered to the copper tracks on the PCB. These feed down to a 20-way connector to interface with characterisation equipment. All tracks are shielded by a ground plane on the reverse side. Screw holes are positioned for precise alignment in test cell. Bottom, Gerber files produced in OrCAD PCB design software.

test solution. A lid fits on top of the vessel with entry points for a Pt counter electrode and Ag/AgCl reference electrode, supplied by Metrohm; as well as a gas feed that terminates in a sparger to ensure greater gas contact area, reducing the time required to dissolve the gas into the solution. The lower face of the vessel is clamped to a spacer plate using a collar; a large nitrile o-ring ensures a good seal. The spacer plate is interchangeable and has one or two precision milled and countersunk holes depending on whether pH or DO is being sensed respectively. These holes allow the channel rings of the diamond sensors to be exposed to the solution, as well as an optical oxygen sensor for calibration of DO measurements. Small nitrile o-rings are attached to the lower face of the spacer plate to ensure a water tight seal is made with the sensors. The PCB containing the diamond sensor is attached to a mount plate using M2 screws and tapped holes to ensure secure and accurate alignment; the optical fibre tip for the DO sensor is clamped into the mount plate. Great care is taken to ensure the sensors are perfectly level and no leak occurs. Finally, the whole cell is supported by four threaded stainless steel rods and, once assembled,

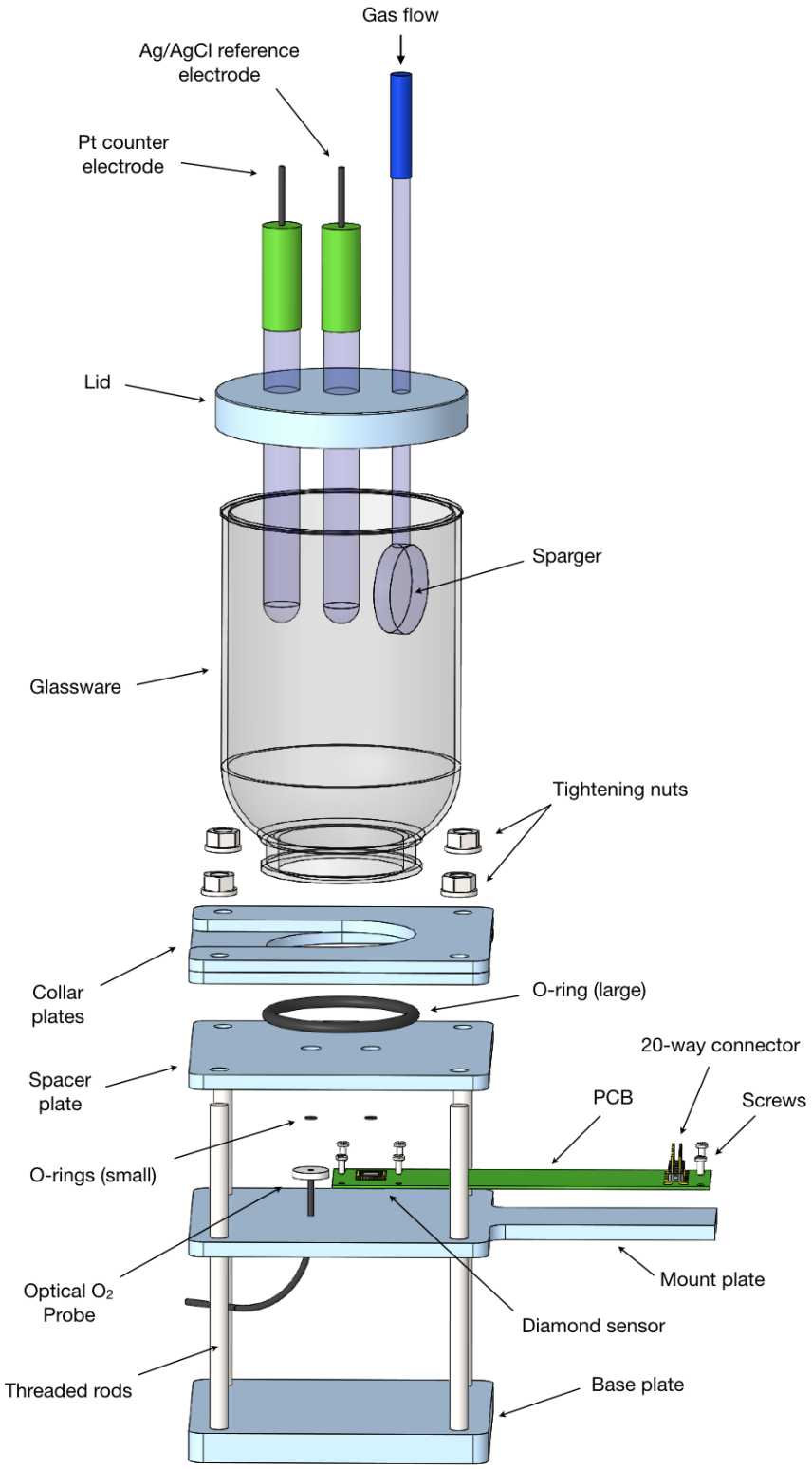

Figure 10.5: An exploded CAD schematic of the test cell. A Pt counter and Ag/AgCl reference electrode are inserted into the glass cell through the lid, alongside the gas flow tube terminating in a sparger. The collar plates and tightening nuts clamp the glassware in place above the large o-ring and spacer plate. Below this are two smaller o-rings which sit atop the diamond sensor (wirebonded into a breakout PCB) and fibre-optic oxygen sensor. The sensors are aligned and attached to the mount plate.

is clamped together using wingnuts. Springs allow gradual tightening whilst ensuring full alignment of the components. The lid, collar, spacer, sensor mount and base plates are all constructed from PTFE due to its superior chemical inertness and thermal properties. The shapes are designed using AutoCAD Fusion 360 and laser cut from sheets using a Universal Laser Systems PLS6.150D. Images of the test cell in use for both pH and DO sensing are shown in figure 10.6.

10.3.6 pH measurements

To make measurements on the ISFET sensor, the PCB is mounted and the test cell is clamped to achieve a water tight seal. A standard rinse process is defined for rinsing the sensor in both DI water and pH buffers: soak in excess solution, remove solution by pipette and any remaining residue by gentle dabbing with a lint-free cleanroom wipe followed by N_2 gun to dry. Prior to all measurements, the sensor is rinsed three times in DI water to clean the sensor.

Output characteristics are defined as a voltage sweep of the drain-source voltage V_{DS} at a constant gate-source voltage V_{GS}. Transfer characteristics are defined as a voltage sweep of the gate-source voltage V_{GS} at a constant drain-source voltage V_{DS}. In both instances the channel current I_{DS} is measured. Leakage characteristics are measured as a voltage sweep of the gate-source voltage V_{GS} whilst measuring the gate-source current I_{GS}. These measurements are taken using a custom Matlab script to control two Keithley 2400 source meters over a GPIB interface.

The first experiment consists of measuring the FET characteristics of the device in a constant pH 7 buffer solution. After the initial rinse in DI water, the sensor is rinsed twice in pH 7 buffer before finally being soaked in the buffer for measurements. A Metrohm Pt wire electrode is used as the gate electrode. To emulate the layout of the eventual integrated sensing device, measurements are made using the outer two rings of the device, electrodes 1A and 2A (CH1) in figure 10.1. The current is stabilised at V_{DS} = -0.6 V for 60 sec prior to each measurement. Output characteristics are taken between V_{DS} = -0.6 V to 0 V and repeated for a fixed V_{GS} stepped between

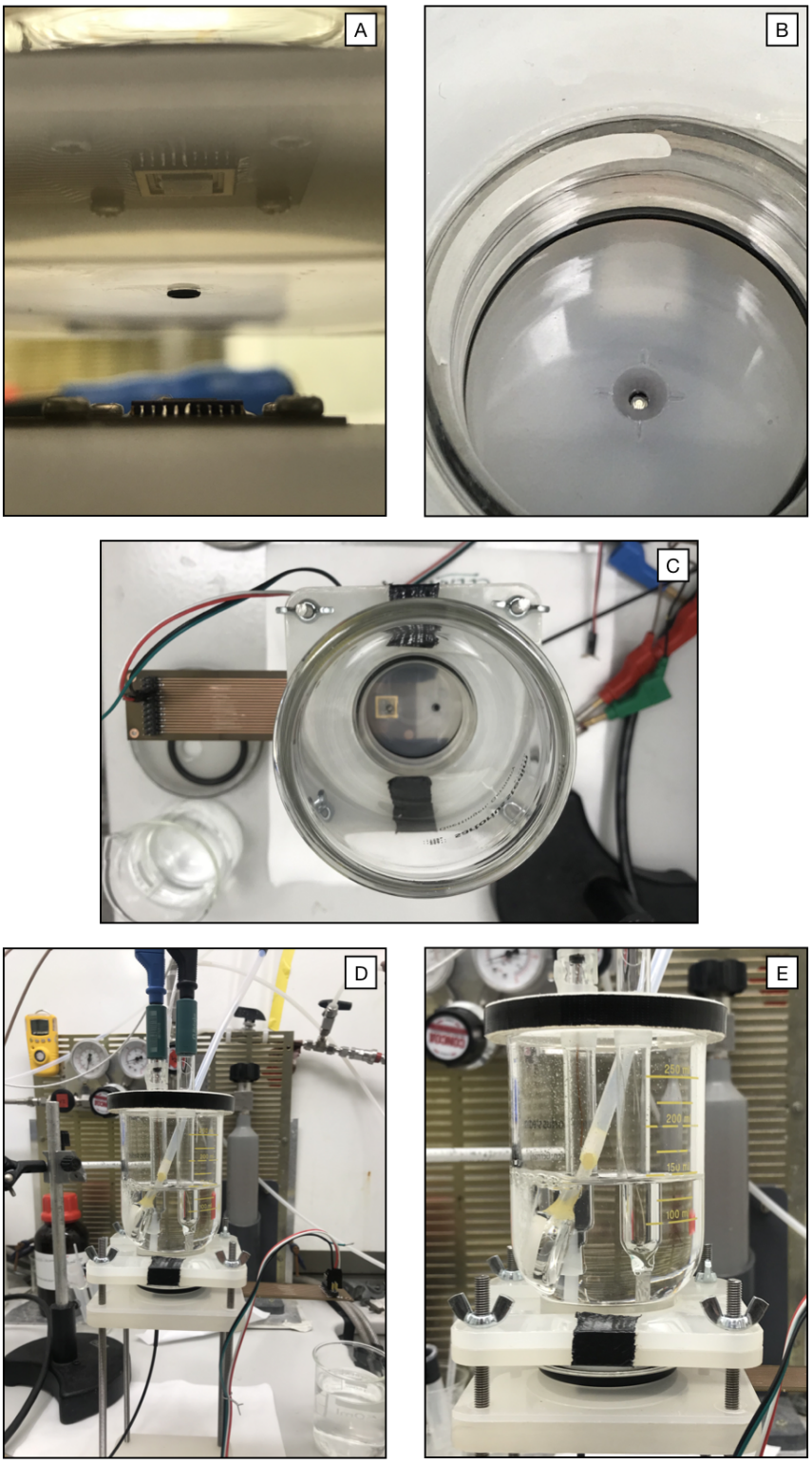

Figure 10.6: Images of the test cell in use: A) the small o-ring centred above the sensor (seen in reflection); B) exposed area of ISFET sensor seen from above; C) exposed area of DO sensor mounted to PCB, left, and fibre optic O_2 sensor, right, seen from above; D) side view of test cell during DO measurements, the Ag/AgCl reference and Pt counter electrodes as well as the gas sparger are mounted through the top of the cell, and optical fibre for O_2 calibration sensor can be seen below; E) side view of test cell, close-up.

-0.6 V and 0.6 V. Similarly, transfer characteristics are taken between V_{GS} = -0.6 V to 0.6 V and repeated for a fixed V_{DS} stepped between -0.6 V and -0.1 V. The leakage current I_{GS} is measured between V_{GS} = -1.0 V to 1.0 V at a fixed V_{DS} = 0 V.

The second experiment consists of measuring the transfer characteristics of the FET in different pH solutions. For this purpose, a series of pH buffers supplied by Sigma Aldrich are used (pH 2, 5, 7, 9, 10 and 12). The sensor is rinsed in the relevant buffer solution before being soaked for measurements. The current is stabilised at V_{DS} = -0.5 V for 60 sec, followed by measuring the transfer characteristics between V_{GS} = -0.5 V to 0.2 V at a fixed V_{DS} = -0.5 V. After each measurement, the sensor is rinsed three times with DI water.

Finally, the temporal pH response is tested. V_{GS} and V_{DS} are both held at -0.5 V, whilst I_{DS} is sampled every 0.1 sec. The pH buffers are manually cycled, without rinsing, between pH 2 and 12.

10.3.7 DO concentration measurements

To make measurements on the DO sensor, the PCB is mounted along with the fibre-optical oxygen probe (which measures DO based upon a luminescence-quenching mechanism that occurs on the probe surface). The test cell is clamped to achieve a water tight seal. The optical oxygen probe is connected to a FireStingGO_2 oxygen meter which measures the temperature-, pressure- and relative humidity-compensated oxygen concentration ([$\mathrm{mg\,L^{-1}}$]) in the solution, set to sample every 1 sec. A Pt wire counter electrode and Ag/AgCl reference electrode (supplied by Metrohm) are used. These, along with the diamond sensor output, are connected to a Metrohm AutoLab PGSTAT 204 potentiostat. The PGSTAT 204 is interfaced to a PC by USB where measurements are executed using NOVA Advanced Electrochemical software. Additionally a custom Python script is used to precisely time-stamp the sensor measurements to correlate against the output of the FireStingGO_2 oxygen meter.

The cell is filled with water. Various ratios of oxygen and nitrogen may be flowed into the solution through the sparger, controlled by MKS Instruments mass-flow controllers. Initially, the solution is purged with pure N_2 flowed at 40 sccm for 30 min to achieve 0% O_2 saturation. This allows calibration of the FireStingGO_2 oxygen meter and measurements to be started from a consistent baseline. The experiment proceeds by application of a -0.8 V measurement potential (vs. the reference electrode) to the diamond sensor for 50 sec, whilst measuring the reduction current. A reconditioning procedure, which has been shown to improve the stable performance of DO sensors [202], is then applied – consisting of a 3 sec potential step at +0.2 V. This measurement is repeated 5 times. The gas ratios are then changed in order to flow O_2 into the water and allowed to stabilise for 10 min. The experiment is repeated multiple times for increasing O_2 flows.

10.4 Results

10.4.1 Device A: ISFET characteristics

The output and transfer characteristics for device A are shown in figure 10.7. The effect of hydrogen surface termination is immediately clear upon comparison with the results presented in figure 9.4. The mean resistance of the channel is seen to have dropped from $\sim 10^6\,\Omega$ to $\sim 10^2\,\Omega$ due to the presence of a transfer doped surface channel with high carrier density. Moreover, the shape of the I-V curve is linear as opposed to rectifying. These linear output characteristics show no pinch-off within the range of applied gate potentials, however the current is modulated. More positive gate voltages are observed to deplete the channel and reduce the current, as would be expected from p-type conduction. Full depletion is not achieved, resulting in an always-on device. A threshold voltage of V_T = 0.95 V may be calculated by extrapolation of the transfer curves.

Analysis of the gate leakage, figure 10.8, shows very small currents of up to 38 nA in the operational range of the device (V_{GS} = 0 to -0.6 V). For one thing, this suggests

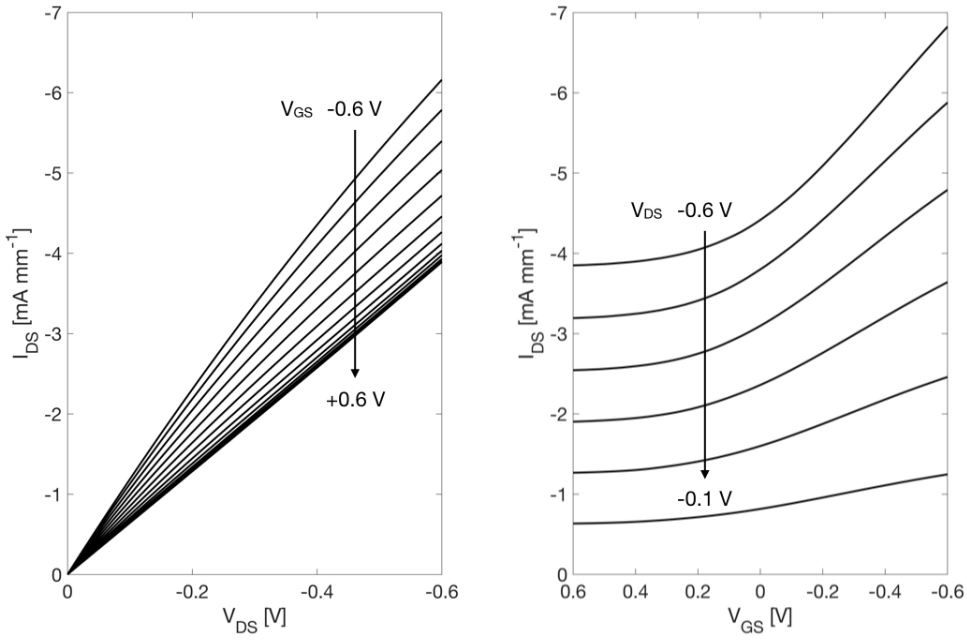

Figure 10.7: Left, output characteristics, and right, transfer characteristics for device A in pH 7 buffer solution. More positive gate voltages reduce the drain-source current, indicating depletion of the p-type channel. A threshold voltage of V_T = 0.95 V may be calculated.

successful passivation of the contact electrodes, as well as minimal charge transfer across the electrolyte-diamond interface or tunnelling across the depletion layer. At larger positive and negative biases the current increases exponentially, which is an indicator of possible hydrogen or oxygen evolution. These Faradic currents are most likely caused by hydrolysis at non-sp^3 carbon (which has a smaller electrochemical window) present at the grain boundaries of the polycrystalline diamond. The fact that the current passes zero at approximately -0.54 V would indicate a bias as a result of device asymmetry. This is unsurprising considering the concentric geometry of the device leads to a considerably larger source than drain contact.

10.4.2 Device A: pH sensitivity

The transfer characteristics of device A are measured for a range of pH buffers, figure 10.9. A shift in the drain-source current can be seen as the pH is changed

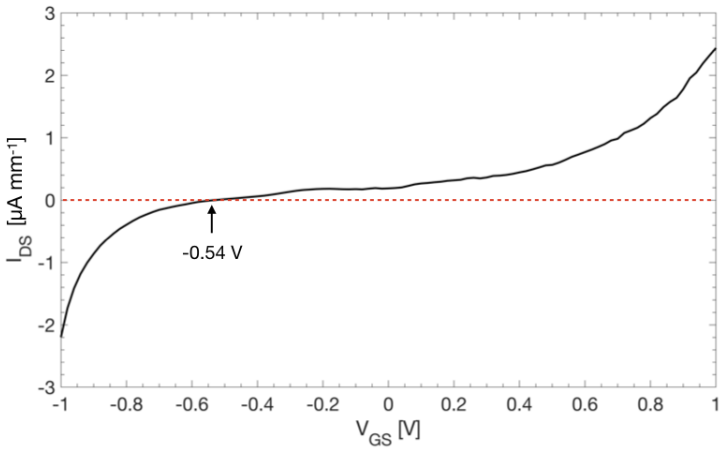

Figure 10.8: The gate leakage current of device A, taken whilst the gate potential is swept and the channel is maintained at 0 V. A maximum leakage current of 38 nA is observed in the operational region of the device. Larger exponential currents are generated outside window this due to hydrolysis at non-diamond carbon most likely present at the polycrystalline grain boundaries.

whilst maintaining a drain-source voltage of -0.5 V. Lower pH values are observed to produce higher channel currents. The sensitivity of an ISFET is usually presented in terms of a change in gate potential equivalent to a change of pH, therefore the change in gate voltage required to maintain a constant current across the range of pH is plotted alongside. Error bars represent a variance of $V_{GS} \pm 0.03$ V to account for gate voltage drift between measurements, whilst the pH buffers are considered to have an error of $\pm$ 0.3 pH due to thermal fluctuations in the laboratory, as well as the variable degradation of the buffers having been in storage for a substantial period of time. A linear regression fit through these points shows a sensor response of -29.2 $\pm$ 1.3 mV/pH.

It is interesting to observe the temporal response of the sensor to a change in pH. Figure 10.10 shows the change in channel current as buffers are manually cycled between pH 12 and 2 over the course of approximately 8 min, whilst V_{GS} and V_{DS} are maintained at -0.5 V. A noticeable step change is seen; as expected, a lower pH results in higher channel currents. Between steps an unstable current is recorded for a few seconds as the previous buffer solution is removed from the sensor, it is

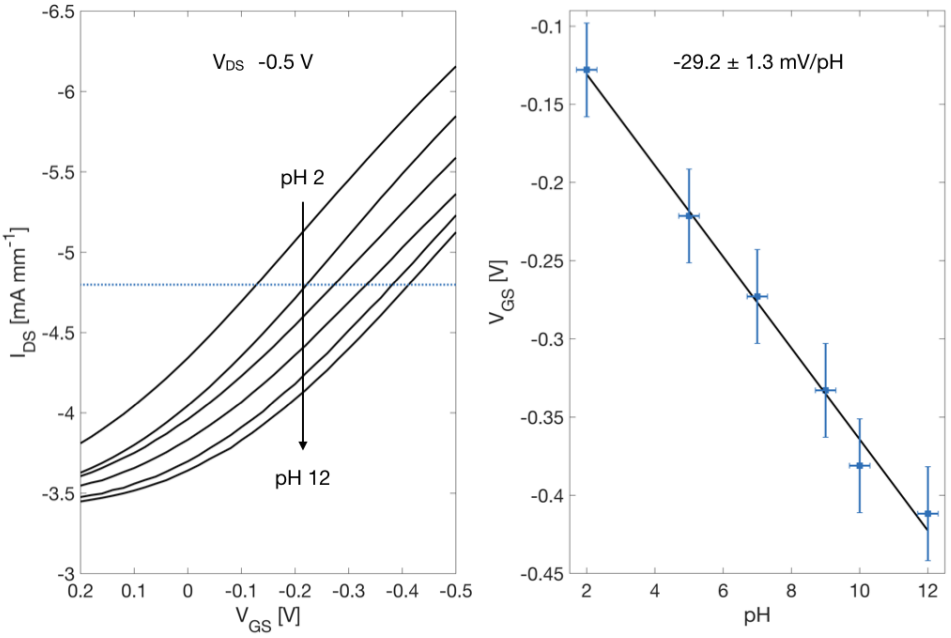

Figure 10.9: Left, the transfer characteristics for device A taken for a range of pH. The channel current is observed to decrease for higher values of pH. Right, the change in gate potential required to maintain a constant current (indicated by blue dotted line in the transfer characteristics) for each pH. A linear fit gives an approximate sensitivity of -29.2 $\pm$ 1.3 mV/pH. Error bars are estimated to be $\pm$ 0.03 V and $\pm$ 0.3 pH.

exposed to air, and the new buffer added. This is unavoidable noise due to the particular experimental setup. The repeatability of measurements is very good. Peak current is seen to drift approximately 1.1% for pH 12 and 0.8% for pH 2 over the duration of the experiment. In each instance the current is recorded as it stabilises from being changed. There is a fast impulse ($\sim$ 3 sec) as the new buffer is dropped onto the sensor and displaces the air on the surface. This is followed by a downward stabilisation of the current, which is more pronounced for lower pH. A total change in signal of 13.6% is observed.

10.4.3 Device B: DO sensitivity

Real-time sensing of DO *in situ* requires the continual reduction of oxygen at the working electrode. In order to avoid a degradation in performance due to effects

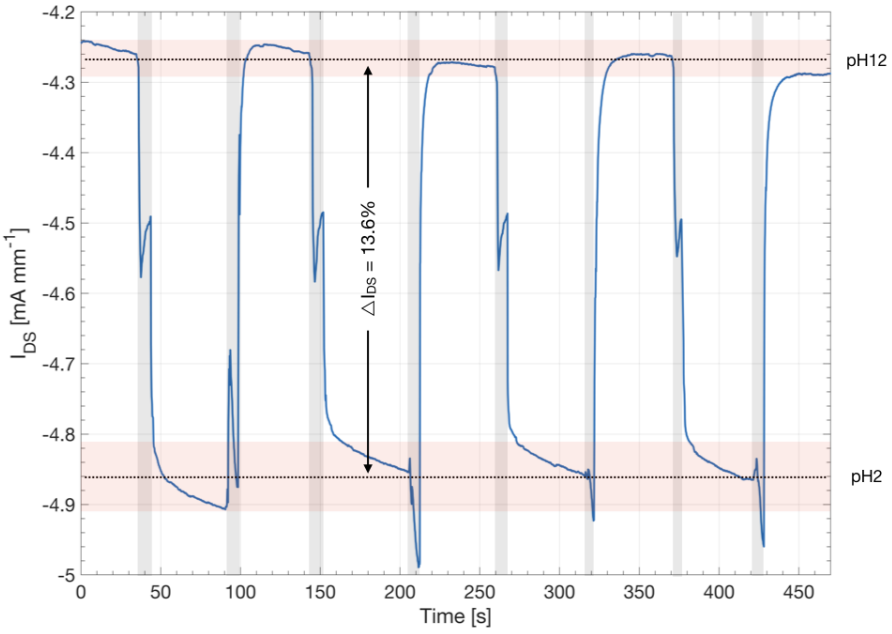

Figure 10.10: The temporal response of device A, sampled every 0.1 s as buffer solutions are cycled between pH 2 and 12. A repeatable step signal change of approximately 13.6% I_{DS} can be seen, as well as a relatively fast response. Noisy currents are observed during manual buffer changeover, highlighted in grey. The drift in current for each pH is highlighted in red.

such as electroplating, electrochemical reconditioning of the sensor should ideally be performed regularly. These operational conditions are emulated in the laboratory test cell using device B by measuring the reduction current as DO content is modulated over an extended period of time. A continuous square potential waveform is applied for the duration of the experiment consisting of a 50 sec step at -0.8 V, followed by a 3 sec step at +0.2 V to recondition the electrode. Figure 10.11 shows a snapshot of the current response as the waveform is applied. At this point in the experiment the O_2:N_2 flow ratio has been changed and the DO concentration of the solution allowed to stabilise for 10 min to a value of 2.72 $\mathrm{mg\,L^{-1}}$. A stable and repeatable response is observed during each step, where an inflection in the current is seen whilst the positive potential step is applied, followed by a fast recovery back to the constant reduction current.

This regular temporal pattern is observed consistently throughout the measurement

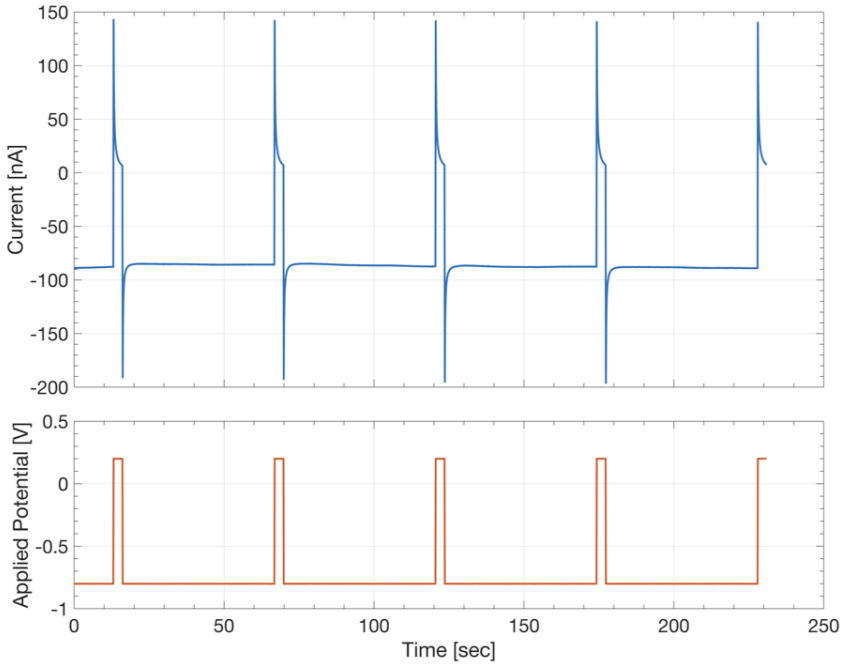

Figure 10.11: The current response of device B at a stable oxygen concentration of 2.72 $\mathrm{mg\,L^{-1}}$. A potential step waveform is applied throughout the experiment consisting of -0.8 V measuring 50 sec period, followed by a +0.2 V sensor reconditioning pulse for 3 sec. A repeatable and consistent reduction current is observed for each pulse.

as the DO concentration of the solution is incrementally increased and allowed to stabilise each time. To determine the calibrated DO response of the sensor, the limiting current, I_{lim}, is defined as the final current value of the series of measuring pulses before the gas ratios are changed. This value is plotted against dissolved oxygen concentration C_{O_2} in units of $\mathrm{mg\,L^{-}}1$, figure 10.12.

The plots presented in figure 10.12 are known as the 'calibration curve' of device B. This is the quantifiable sensor response, in this instance current values (black), for change in DO concentration. The left plot presents the sensor response for a wide range of C_{O_2} from approximately 2 - 35 $\mathrm{mg\,L^{-1}}$; equivalent to $\sim$ 4 - 76 % O_2 or 22 - 380 % air saturation at 20 °C and 1013 mbar. The right plot shows a narrow range from approximately 2 - 10 $\mathrm{mg\,L^{-1}}$; equivalent to $\sim$ 4 - 21 % O_2 or 22 - 110 % air saturation. The blue dotted line in each instance highlights 100% air saturation

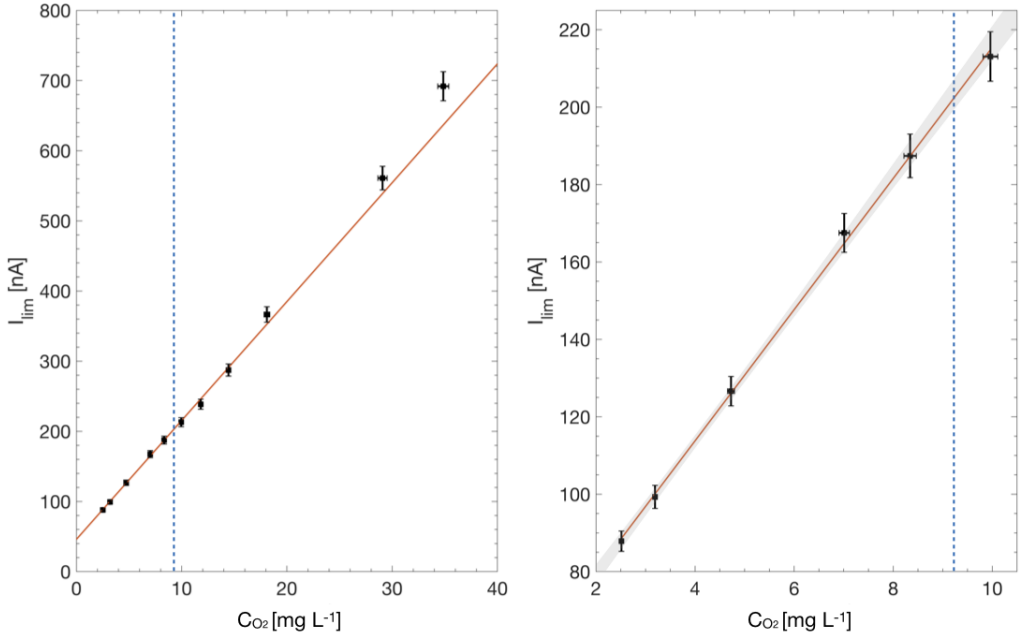

Figure 10.12: The calibration curve for device B, showing the limiting current I_{lim} sensitivity as a function of increasing DO concentration C_{O_2}. Left, results for a wide range of DO values up to 35 mg L^{-1} (or 380% air saturation, where 100% is indicated by the blue dotted line). A deviation from linearity is observed for concentrations above $\sim$ 17 mg L^{-1}. Right, results for the low DO range measurements, through which a linear regressive fit is made (red line). The light grey region indicates the possible envelope of fits if error bars are taken into account.

(9.1 mg L^{-1}). The 3% error bars for I_{lim} are derived from a long-term stability test (presented below) of the current about its mean, with generous allowance made for fluctuations in background current which will dominate particularly at small DO values. The 1.5% error bars for C_{O_2} are equivalent to the lowest specified accuracy of the optical oxygen probe, which performs better at lower DO concentrations.

The sensor response is seen to be highly linear ($R^2 > 0.999$) in the low C_{O_2} range ($\sim$ 0 - 17 mg L^{-1}) with slight positive deviations when the solution is more than three times air saturated. A linear regression fit (red line) through the first six measured points shown in the right hand plot gives a slope, or sensitivity, of $s = 16.95$ nA mg^{-1} L, with a standard deviation of $\sigma_s = 0.26$; and intercept of $i = 46.01$ nA with $\sigma_i = 1.69$. The limit of detection (LOD), being the lowest concentration of

O_2 that can be detected but not quantified, may be defined as $3\sigma_i/s$ [314] and gives a value of 0.299 $\mathrm{mg\,L^{-1}}$, or approximately 300 ppb (parts per billion). The limit of quantification (LOQ), being the lowest concentration which may be quantitatively determined is $10\sigma_i/s$ and gives a value of 0.997 $\mathrm{mg\,L^{-1}}$, or approximately 1 ppm (parts per million). If error bars in x and y are taken into account, the envelope of possible regression fits (shown in grey) may be estimated by a Monte Carlo method [315], giving a best-fit slope of 17.15 ± 0.76 $\mathrm{nA\,mg^{-1}\,L}$ and intercept of 44.92 ± 3.86 nA. The non-zero intercept indicates the presence of a background current which may be caused by imperfect deoxygenation of the solution, impurities in the solution, or unwanted electronic artefacts generated by the AutoLab potentiostat. The most likely cause, possibly in addition to these factors, is the generation of Faradic currents from hydrolysis at the diamond gain boundaries. Corroborating this, the magnitude of the intercept leakage current (at the applied potential of -0.8V) is remarkably similar to that seen for the ISFET device figure 10.8.

10.4.4 Device B: Stability measurements

To investigate the temporal variability of the reduction current, and to assess the possible error in the limiting current values, a current stability experiment was conducted. The gas flow ratio was adjusted and allowed to stabilise to achieve 17.35 ± 0.29 $\mathrm{mg\,L^{-1}}$ throughout the duration of the measurement. This value was chosen as it lies on the limit of the linear detection range of the device. The reduction current was logged, using the standard measuring/reconditioning pulse sequence, for 60 min. Current during the reconditioning stages was not recorded. Figure 10.13 presents the percentage fluctuation of the reduction current against its mean value, normalised against the variability in oxygen concentration as recorded by the optical sensor. Over 70 measurement and reduction cycles occur during the measurement period and the normalised deviation range is approximately $\pm$ 0.65 %, representing remarkable stability in the medium term. An overall linearly increasing trend can be seen, which could be quantified as a potential drift rate of $\sim$ +1% per hour.

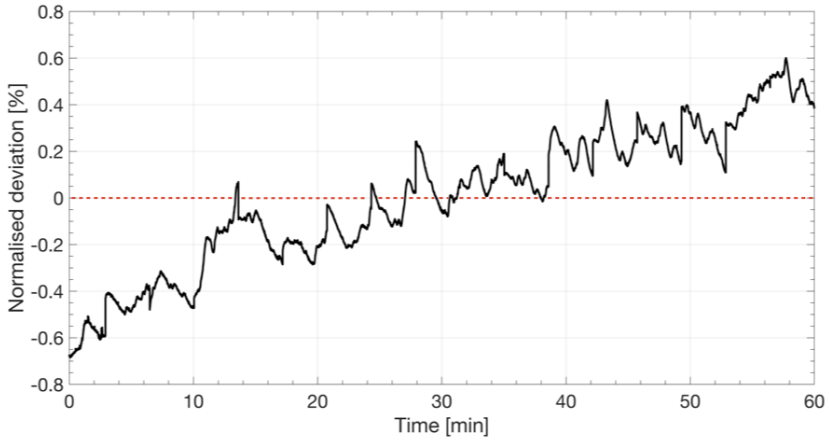

Figure 10.13: The stability for device B over a 60 min extended measurement, plotted as the percentage deviation of the reduction current from its mean value. This value is normalised against fluctuations in the oxygen concentration, maintained at 17.35 ± 0.29 mgL^{-1} throughout the duration of the measurement.

10.4.5 Device B: Chronoamperometric interpretation

Chronoamperometry can be performed in order to deduce the apparent number of electrons involved in the oxygen reduction reaction, n_{app}. This is a technique that involves recording the current as a function of time over a potential step such as to measure the onset of mass-transfer limited reduction as determined by the Cottrell equation (10.2), where F is the Faraday constant, A is the surface area of the electrode, D_{O_2} is the diffusion coefficient of oxygen, and C_{O_2} is the DO concentration. The repetitive pulse sequence shown in figure 10.11 is typical of the type of chronoamperometric experiment conducted and it is explored if the recorded current may be interpreted using equation (10.2) to deduce n_{app}. The method relies on plotting the current values recorded as the potential is stepped from +0.2 V to -0.8 V against $t^{-1/2}$, figure 10.14, from which the gradient of the linear fit is taken to calculate n_{app}.

$$I(t) = \frac{n_{app} F A D_{O_2}^{1/2} C_{O_2}}{\pi^{1/2} t^{1/2}} \tag{10.2}$$

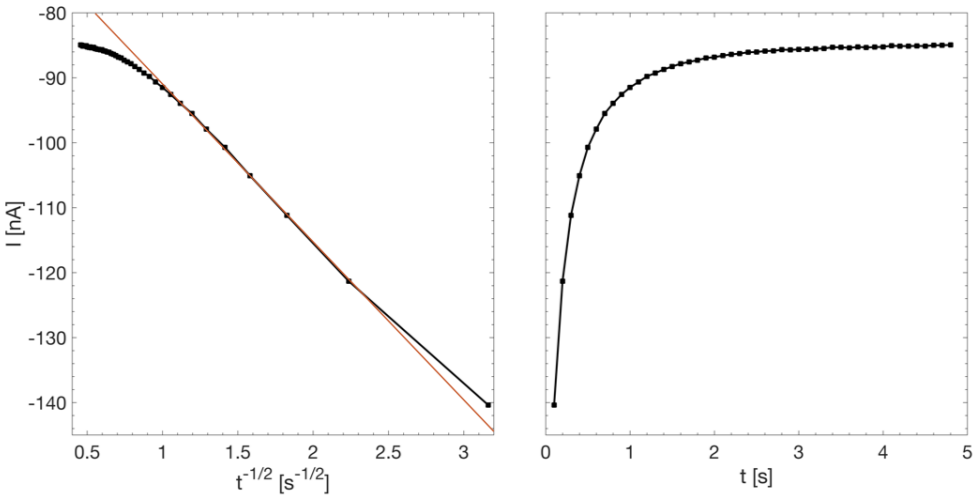

Figure 10.14: Chronoamperometric curves for device B. The reduction current is plotted as the potential is stepped from +0.2 V to -0.8 V. Left, against time t; right, against $t^{-1/2}$. Oxygen concentration is stabilised at 2.52 mgL^{-1}. Red line indicates a linear regressive fit, which allows the apparent number of reduction electrons n_{app} to be calculated.

Using values of $A = 1.56 \times 10^{-6} \pm 7.8 \times 10^{-8}\,\mathrm{m}^2$ and $D_{O_2} = 2.28 \times 10^{-5}\,\mathrm{cm}^2\,\mathrm{s}^{-1}$ [198], the calculation results in a value of $n_{app} = 1.14$, which is several times lower than the value that would be expected from the four-electron reduction reaction equations (4.6a) and (4.6b). Whilst this is not impossible, it is seen that the magnitude of the gradient is highly dependent on the data points taken at the smallest time values ($di/dt \propto t^{-3/2}$), hence the sampling rate of 10 sec^{-1} is most likely insufficient to provide a reasonable fit without incurring very large errors on the value of n_{app}. An alternative method is to deduce n_{app} from the equation for the limiting current, equation (4.7), and using the sensitivity as given by figure 10.12. In this instance a more reasonable value of $n_{app} = 3.95 \pm 0.21$ is obtained; where the error is calculated by propagation of the respective uncertainties.

10.5 Discussion

In the absence of suitable test facilities, device A was fabricated using a hydrogen-induced surface channel to allow room temperature ISFET characteristics to be de-

duced. At higher temperatures, it is expected that this surface termination should degrade, whilst the carriers in the boron-doped channel will become activated. The device will transition from performing as a room-temperature transfer-doped channel ISFET to a robust boron-channel device.

For the experiments presented in this chapter, device A is seen to behave as an always-on linear regime FET within the gate potential range (limited by the electrochemical window of diamond). Saturation of the output characteristics is not observed due to the high sheet charge density induced by the hydrogen termination, and the nature of the channel depletion with positive gate voltages confirms that the carriers are p-type. No saturation of the transfer characteristics is observed at negative potentials, which has been reported in other devices [177] and would be indicative of a dominant and detrimental leakage current. Instead, the low leakage current of device A represents effective contact passivation and low quantities of sp^2 carbon inclusions. In fact, the magnitude of the gate leakage is comparable to that of other high-quality single crystal devices [178]. The effect of device asymmetry due to the concentric contact pattern is observed in a shift of the zero-point current, but as long as the leakage remains low this should not present a problem for device performance.

A linear dependency of the transfer characteristics is measured across a range of pH buffers. The sensitivity, s, of device A is represented as a -29.2 $\pm$ 1.3 mV/pH shift in the gate voltage to maintain equilibrium as the solution pH is altered. The negative sign of this shift is similar to that observed by other studies that use a Pt gate electrode [174, 175]. In this instance a Pt electrode is used deliberately in an attempt to move towards a more robust lab-on-chip solution that does not rely on a fragile Ag/AgCl reference. It is shown that in these cases the compensating pH dependency of the Pt electrode itself, calculated as s_{ref} = -59 mV/pH, must be taken into account [176]. This means that the real sensitivity of the diamond surface should be corrected to $s_{diam} = s - s_{ref} =$ +29.8 $\pm$ 1.3 mV/pH. This value is similar to, or in some cases better than those achieved for boron doped devices, 27

- 36 mV/pH [178,180,181]; hydrogen-terminated devices using Ag/AgCl reference electrodes 15 - 30 mV/pH [169, 170, 172, 176]; and many times improved on the corrected values of $\sim$ 5 mV/pH for hydrogen devices using Pt electrodes [174,175]. The fact that only a mild hydrogen treatment is performed on device A adds merit to the assumption that there is a minimum presence of oxygen moieties remaining on the surface. This would support the model proposed by Garrido et al. [167] of lateral modulation of the transfer doped channel by oxygen site-binding. The supra-Nernstian response of 72 mV/pH seen in those studies may be achieved on device A by tuning the surface treatment to favour a more O-terminated surface.

The linear regression of the ISFET response achieves a fit of $R^2 > 0.992$, which indicates a very strong relationship. Any deviation from perfect linearity may be accounted for the in the size of the error bars of the measured values. Alternatively, it has been suggested [173] that it could also be attributed to a channel mobility reduction due to the scattering of holes by the ions in the electrolyte.

The temporal response of the sensor over repeated cycles in pH shows good repeatability, with a consistent step change as the buffer solutions are changed between pH 2 and 12. There is a noticeable stabilisation in the channel current after each step, which may be indicative of equilibration of the surface potential over a certain timescale. It is interesting to note that the current decay is greater for smaller pH values. The variation of current stabilisation with time for different pH values and gate potentials might yield interesting insight into the surface chemistry taking place, and should be investigated further. Additionally, the method should be improved to reduce the disruptive manual changeover of solutions and to better resolve the sensor response time – perhaps by titration of universal buffer solution.

Device B differs from device A by the higher concentration of boron in the doped layer. This makes it suitable as a diamond working electrode in amperometric oxygen reduction. The highly linear response in the region between 0 - 17 $\mathrm{mg\,L^{-1}}$ represents excellent performance in the range for the low DO environments in which the final sensor is expected to operate, with only a minor deviation to this response

for higher concentrations. Additionally, the small reduction currents $\sim$ 100 nA should allow a two electrode set up to be used [202], simplifying the integrated device design.

The sensitivity of the device is calculated to be 16.95 $\pm$ 0.26 nA mg^{-1} L, with a background current of 49 nA and a limit of detection of approximately 300 ppb. This would suggest a seven-fold increase in sensitivity over some of the best non-diamond sensors [202] – which use optimised Pt microdisc electrodes to achieve sensitivities between 0.31 - 2.31 nA mg^{-1} L. On the other hand, the greatly reduced surface area of the microdiscs offer a lower background current and hence a better LOD (30 - 260 ppb) than device A. In direct comparison to other boron-doped diamond sensors [214], a similar background current is seen – again, likely due to sp^2 inclusions – and slightly improved sensitivity, $\sim$ 23 nA mg^{-1} L, but notably a much better LOD of 1 ppb is claimed. This improvement is attributable to the use of Pt nanoparticles which act to electrocatalytically enhance the reduction of oxygen – and points to a potential route for improving the performance of device B. However, it remains to be seen how the harsh application environment within which the final integrated sensor will operate might affect the stability of such surface, with a strong preference to avoid the use of nanoparticles. An alternatively more robust solution should be explored in future studies, which is LOD enhancement by micro-electrode patterning on the diamond surface to enhance the rate of diffusion.

The medium-term stability of the device is observed to be remarkably good, which shows that the reconditioning procedure is effective even after nearly 70 cycles. The overall positive linear trend might suggest that there is a mechanism for increasing activity at the electrode over time. This is contrary to what would be expected considering that platinum electrodes are known to lose their activity over prolonged periods [201]. It may be that the reconditioning pulses are responsible for electrochemically cleaning the diamond surface of pre-existing contamination. This would cause increased activity initially, but eventually the drift should level out. If this is indeed happening, it would point to the necessity for an extended pre-conditioning

step before the start of any measurement to remove residual contamination. However without further experiment it is difficult to attribute this as a significant trend. To gain deeper insight, as well as to best emulate real-world conditions, stability should ideally be measured over several days.

Finally, an attempt to extract the apparent number of electrons involved in the reduction reaction by chronoamperometric analysis suffered large errors as a result of insufficient sampling frequency around the potential step. A dedicated experiment using equipment capable of much higher current recording rates would be needed to achieve suitable accuracy for this method. Instead, a value of n_{app} = 3.95, with a small and quantifiable error of $\pm$ 0.2, is found by analysis of the limiting current value. This is very close to the four-electron reduction reaction considered to occur at a Pt electrode [316] and that observed by Hutton et. al [214] indicating the reaction pathways described by equations (4.6a) and (4.6b) may be involved. However the electron-transfer kinetics on diamond remain complex, with factors such as pH [207], quality of the material [317] and the rate of mass transport [318] that may affect n_{app}.

10.6 Conclusions

A need has been identified for robust multi-functional water sensors that are capable of operating in extreme environments. The extraordinary properties of diamond offer a promising route to meet this need, however minimal work has been carried out on its practical implementation. In this chapter, a novel device design has been proposed that will allow sensing of multiple key metrics in harsh conditions. The design consists of a compact lab-on-chip format made up of concentric circular electrodes that will eventually allow pH, dissolved oxygen (DO) concentration and conductivity to be measured on a single device. These electrodes are configured such that common functions may be shared; space on the chip is maximised; and the dimensions of each sensor are optimal for their performance.

Following this initial design, measurements on two prototype devices are presented: device A, a pH-sensitive field effect transistor; and device B, an amperometric DO sensor. These are based upon polycrystalline CVD diamond substrates – which will allow cost effective scaling of the technology – with boron-doped layers specific to their sensing functions. In the absence of a high-temperature test installation, device A is hydrogen terminated to achieve a transfer-doped channel at room temperature. Measurements are carried out using test equipment that has been designed and produced specifically for the purpose of characterising these sensors, along with future prototypes.

Device A shows modulation of the channel by an applied gate potential in solution, indicating linear p-type FET characteristics with low leakage current. Under change of pH a shift in the transfer characteristics is measured, translating into a linear sensitivity of 29.8 ± 1.3 mV/pH – once the compensating effect of the Pt gate electrode has been taken into account. The temporal response over repeated pH cycles is shown to be stable and repeatable. In many cases, this device performance is superior to current devices, and may be improved further by tuning the surface treatment. It is expected that device A will exhibit ISFET behaviour at high temperatures (> 600 K), even with degradation of the hydrogen surface termination, as the boron-doped channel is activated.

Device B shows a substantial linear change in reduction current with DO concentration. The sensitivity of the device is 16.95 ± 0.26 nA mg^{-1} L, displaying a major sensitivity improvement over non-diamond devices and comparable with that of boron-doped diamond that has been electrocatalytically enhanced with Pt nanoparticles. The limit of detection of 300 ppb may be improved by promoting greater oxygen diffusion through patterning of diamond micro-electrodes. The stability of device B is notable over the medium term, likely benefited by the regular electrochemical reconditioning. Longer term stability tests will be conducted in future work to simulate real world conditions and to investigate any sources of systematic drift.

Through these initial experiments it has therefore been shown that high-performance diamond pH and DO sensors may be produced on polycrystalline diamond, using a novel sensor design that paves the way for fully integrated sensing solutions in extreme environments.

Chapter 11

Conclusions

11.1 Summary of findings

In this thesis, the application of diamond as a sensor for extreme environments is investigated. Stated from the outset is the fact that diamond is unique in its collection of unrivalled mechanical, electronic and electrochemical properties. Through the investigations presented in this work these properties are brought to the foreground to demonstrate how previously intractable problems may be solved by the research and development of diamond-based devices.

In chapter 7 the optimal performance of diamond devices for thermal neutron detection are evaluated in detail. Neutron detectors currently suffer from low total efficiency, as well as bulkiness and poor resilience in their demanding operational environments. Diamond, in combination with a high cross-section neutron absorber such as boron carbide, has shown great promise in the drive to solve these problems. However its potential remains unfulfilled in want of a greater understanding of how the geometry and material properties may be optimised. A computational model has been written using Monte Carlo methods to allow diamond detector structures to be built, tested and optimised to further this understanding, and to provide a route to achieving maximum efficiency. Results have been generated for three distinct planar diamond/boron carbide device structures: an 'indirect' conversion layer, a tri-layer

sandwich detector, as well a 'direct' structure constituting a p-type diamond/n-type semiconducting boron carbide diode. The characteristic spectra of each device are simulated, for the first time including the effect of statistical charge carrier generation, recombination and trapping; as well as electronic noise. Significant advances include linking the material properties (including the carrier mobility-lifetime products) of diamond and boron carbide to their charge collection efficiency (CCE) and the consequent impact on detector performance in terms of spectral resolution and total efficiency; decomposing and quantifying the sources of spectral broadening; and aggregating the physical effects to perform complete geometrical and material optimisation. The outcome is a model that gives several important and detailed recommendations for realising the upper bounds of solid state neutron detection using diamond.

Chapter 8 aims to solve an interrelated computational problem, with much wider implications within physics itself. That is, the calculation of ion stopping powers in the low-energy regime – outside the applicability of the Bethe equation. Current approaches are based on empirical corrections and/or fitted interpolants, which suffer a degree of error and, importantly, do not generalise well to ions and targets that lack experimental data. A new technique has been put forward in this chapter that leverages recent developments in machine learning, allowing the use of existing datasets to train a statistical model with the purpose of generating new predicted outputs. A dataset consisting of over 34,000 experimental stopping power measurements is used to train a supervised decision tree ensemble. The model has then been evaluated using R^2, RMSE, MAE and MAPE metrics to provide a comprehensive overview of performance – both on its internal regressive performance, and crucially, its external predictivity. Exhaustive cross-validation is performed on the dataset to achieve the most rigorous predictive assessment possible. Exploratory data analysis and feature importance results are also presented. Overall, the model is shown to be particularly capable of producing predictions with low bias and minimal overfitting. Stopping power curves, plotted against incident ion energy, are generated for a wide variety of elements and compounds including solids, liq-

uids and gases; as well as alloys, mixtures and polymers – for ions up to Z = 92. This includes results for diamond and boron carbide, used in chapter 7. Despite the model never having 'seen' any prior data points, the predictions fit the experimental data extraordinarily well. Although hard to gauge given the difference in methods and evaluation metrics, comparisons show that the regressive error of the model (2.1%) could be considered nearly twice as good as that of the leading semi-empirical method, SRIM-2010 (4.0%) [303]; with the fully 'blind' predictions not far behind (6.6%). The model therefore paves the way for exciting new approaches to traditional physics problems using 'big data' and artificial intelligence.

Chapter 9 describes the growth and characterisation of boron-doped diamond layers on polycrystalline diamond, with properties suitable for making high-temperature devices. Having built on the wealth of prior research into doped diamond – but distinct lack of commercially-available or readily implementable growth processes – a recipe for controlled p-type doping has been developed, using only the residual boron content of the growth chamber as opposed to conventional boron sources. The layers are characterised using a modified circular transmission line measurement (CTLM) technique and impedance spectroscopy (IS) up to temperatures $>$ 700 K. Additionally, the effect of annealing temperature on carbide formation and contact resistance has been explored in order to optimise the metal/diamond interface properties. Two samples are presented, doped using different growth duration and pressure, that, given the electronic characterisation are considered to be highly suited for sensor fabrication and performance at high temperatures. The first is shown to have a layer $\sim$ 265 nm thick with boron doping concentration in the region of [B] $\sim$ 10^{17} - 10^{18} cm^{-3}, with an activation energy of 0.37 eV. The second achieves a layer $\sim$ 665 nm thick with a doping concentration [B] $\sim$ 10^{20} cm^{-3} and activation energy of 0.02 eV.

Finally, chapter 10 seeks to address the pressing need for multi-functional sensors that can perform for extended periods of time in extreme fluid environments. Up until now there has been limited work to advance the principles of diamond sens-

ing beyond fundamental research; the chapter therefore begins by outlining how new diamond device structures can be made that will allow the direct application of resilient diamond lab-on-chip technology. This design has then been used to inform the fabrication of prototype devices that are capable of sensing pH, using an ISFET structure; and dissolved oxygen (DO) concentration, using amperometric measurements. The ISFET employs a surface transfer-doped channel showing linear p-type FET behaviour at room temperature, with the anticipated onset of boron-doped channel characteristics at high temperatures. A pH sensitivity of 29.8 $\pm$ 1.3 mV/pH has been measured, as well as a stable and repeatable response to pH over time. The DO sensor also shows excellent stability over time, along with a linear sensitivity of 16.95 $\pm$ 0.26 nA mg^{-1} L and a 300 ppb limit of detection. All measurements have been made using a cell that has been designed to facilitate the test and calibration of these prototype sensors. The experiments show that high-performance pH and DO sensors on polycrystalline diamond can be made, using a design that breaks new ground in fully integrated sensing solutions for extreme environments.

As a whole, the work presented in this thesis has constituted several important steps forward in realising the performance offered by diamond in both solid-state neutron detection and water quality sensing. These promising investigations have stimulated several currently on-going and future studies that aim to either improve on the methodology used, or to build on the successful outcomes.

11.2 Future work

11.2.1 Diamond diode structures for highly efficient neutron detection

The foundations established in chapters 3 and 7, suggest that it should be feasible to fabricate an innovative direct conversion neutron detector using diamond. The objective is to produce a diode device, consisting of an n-type boron carbide, p-type

diamond heterojunction. This device will benefit from the robust and radiation-hard nature of diamond, along with its excellent electronic properties. Using the optimisation algorithms presented in chapter 7, the precise device geometry can be tailored to produce a detector that has unparalleled total efficiency.

Experimental work to achieve this goal has progressed alongside that presented formally in this thesis, and the brief background to which is outlined in appendix A. The primary task is to develop an effective deposition method of high quality semiconducting boron carbide on diamond. In initial experiments, thin films have been prepared by molecular adsorption of ortho- and meta-carborane onto a substrate, with decomposition into semiconducting boron carbide induced by UV or electron-beam radiation. For the purposes of process engineering and characterisation of the films, the substrates used are n-type (5.4 Ωcm) and p-type (14 Ωcm) $< 100 >$ diced silicon wafers. Whilst the properties of these substrates differ substantially from diamond, they allow for frequent and iterative deposition runs in order to develop suitable growth parameters and process conditions. They also permit direct comparison with the results of Robertson et al. [253, 319] presented in appendix A.

Various PVD methods have been explored to date. Thermogravimetric analysis (TGA), figure 11.1, has indicated a solid-vapour phase transition for both meta- and ortho-carboranes that is complete at approximately 180 °C, 1 atm. Consequently, a deposition process based upon the Lely method, which is used for the growth of SiC crystals [320–322], has been developed and tested successfully (subject to further refinement). This simple method relies on the sublimation of the source material by heating, diffusive transport to the substrate in the gas phase and deposition of the species on the surface of the substrate, which may or may not be seeded.

A simple growth setup has been designed and built, figure 11.2, consisting of a heated aluminium growth vessel with the solid source material at the bottom and the silicon substrate at the top, cooled by a heatsink. The substrate and source temperatures need to be carefully selected to control the vapour-phase content and growth quality. As does the source-substrate distance and the mass of source mate-

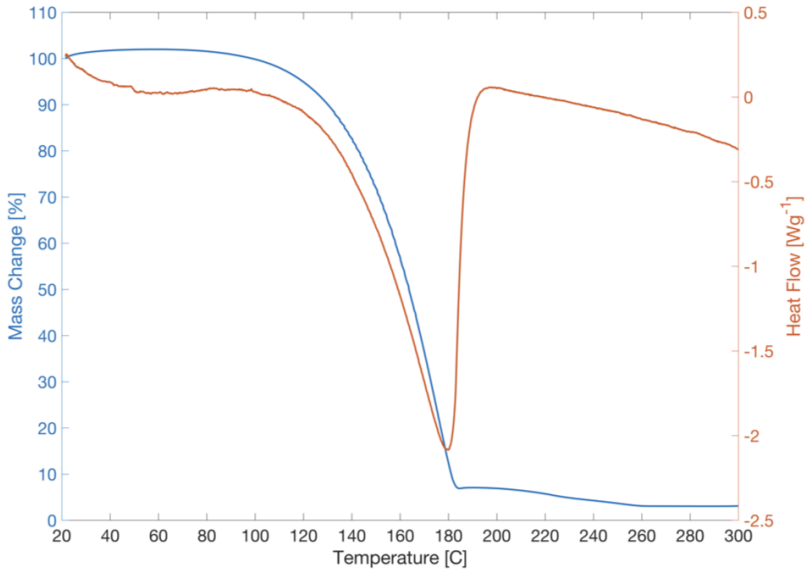

Figure 11.1: Thermogravimetric analysis (TGA) of meta-carborane source material. The mass of the sample (blue) and heat flow (red) is measured over time as the temperature is increased, showing a phase change in the range 100 to 180 °C.

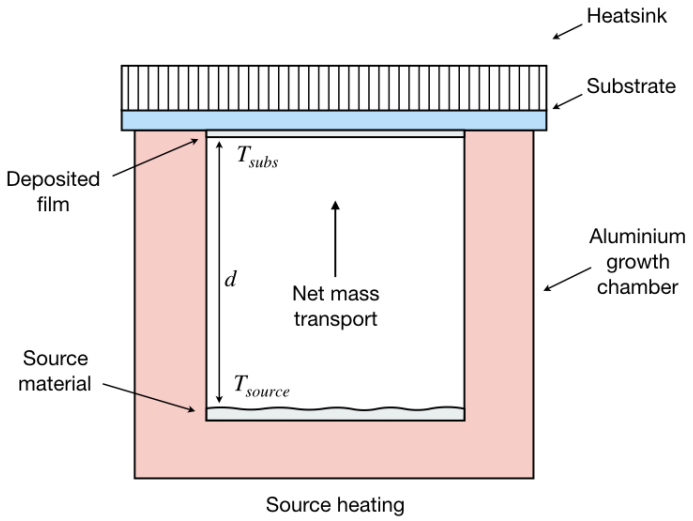

Figure 11.2: A schematic of carborane film deposition geometry. The source material is sublimated by heating the aluminium growth chamber, transported to the substrate in the gas phase and deposited on the surface. A temperature gradient is maintained by use of a heatsink.

rial. Diffusion-limited growth rate has been shown to be approximately proportional to $\Delta T/Pd$; where ΔT is the temperature gradient, d is the source-substrate separation distance and P is the growth pressure [323]. Homogeneous carborane films such as those shown in figure 11.3 have been grown at ambient pressure using 5 mg source material, heated at 200 °C for 30 min, with a separation distance of 2.5 mm. Ultraviolet light in the wavelength range 160 – 300 nm from a Heraeus Noblelight D200 lamp is used to induce the necessary B-H bond scission and molecular cross-linking to form semiconducting boron carbide.

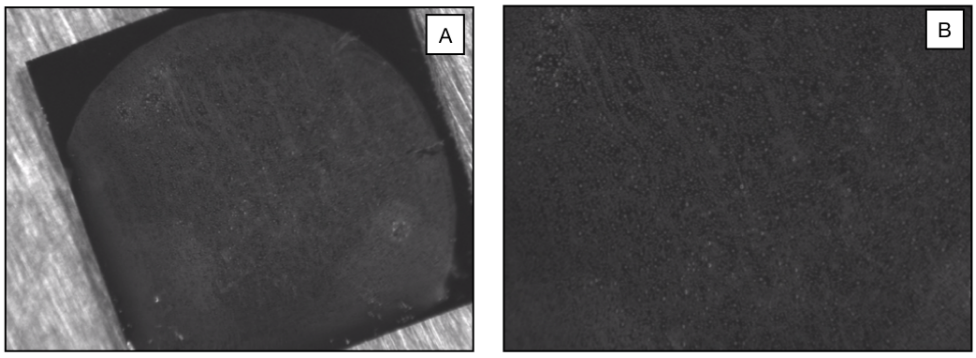

Figure 11.3: An example of meta-carborane film growth on a p-type silicon substrate. Microscope images: a) 1 x, b) 5 x optical zoom.

Further to the work already carried out there are several important studies to be completed. In the first instance the remaining parameter space of growth conditions needs to be explored in greater detail, alongside relevant characterisation metrics. Film quality (homogeneity, pinhole density, crystal size, grain boundaries, etc.) should be established by inspection using scanning electron microscopy (SEM), from which the process should be adjusted accordingly. A reliable growth rate needs to be established for the optimised process, with film thickness measured using a method such as Dektak profilometry. Additionally, the process of UV – or even electron-beam – induced carborane film decomposition should be investigated. Relevant characterisation to determine the chemical state change as a consequence of successful decomposition would likely be x-ray photoelectron spectroscopy (XPS) and Raman spectroscopy, as shown by Pasquale et al. [324].

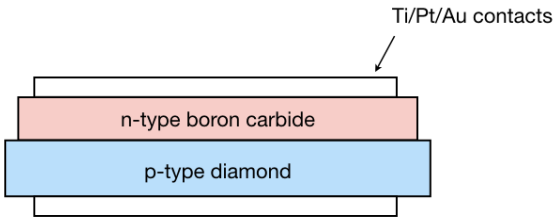

Figure 11.4: Schematic of a proposed heterojunction diode neutron detector, consisting of a planar n-type boron carbide/p-type diamond geometry where layer thicknesses and material properties are optimised according to the Monte Carlo simulations in chapter 7.

Based on the successful outcomes of controllable film deposition and decomposition, electronic characterisation should be made. Crucially, for the optimisation model in chapter 7 to be most effective, carrier properties will need to be determined using Hall effect measurements. Simple p-n junction diodes will be produced on the silicon substrates and ohmic contacts (Ti/Pt/Au) deposited using photolithography to pattern a planar device. Fabrication and characterisation of silicon-based diodes should be succeeded by transfer of the deposition process to diamond substrates, which may require further optimisation. Diamond-based diodes should then be fabricated using a similar processing and characterisation method for comparison, figure 11.4. The result of this work will be a novel diode structure based upon a semiconducting boron carbide/diamond p-n junction, which should function as a highly efficient and robust thermal neutron detector.

11.2.2 A multi-functional diamond sensor system for extreme environments

In many industrial applications the detailed analysis of a fluid is only possible by manually siphoning off a sample and transferring it to a laboratory. This procedure is not only time consuming for the specialist operator, but requires spatially cumbersome laboratory equipment, provides very low sampling frequency, and exposes both the operator and the environment outside of the closed system to the risk of

dangerous contamination. The work presented in chapters 9 and 10, has been the result of great interest from BAE Systems Maritime Ltd. to develop a new water quality sensing solution to overcome these problems.

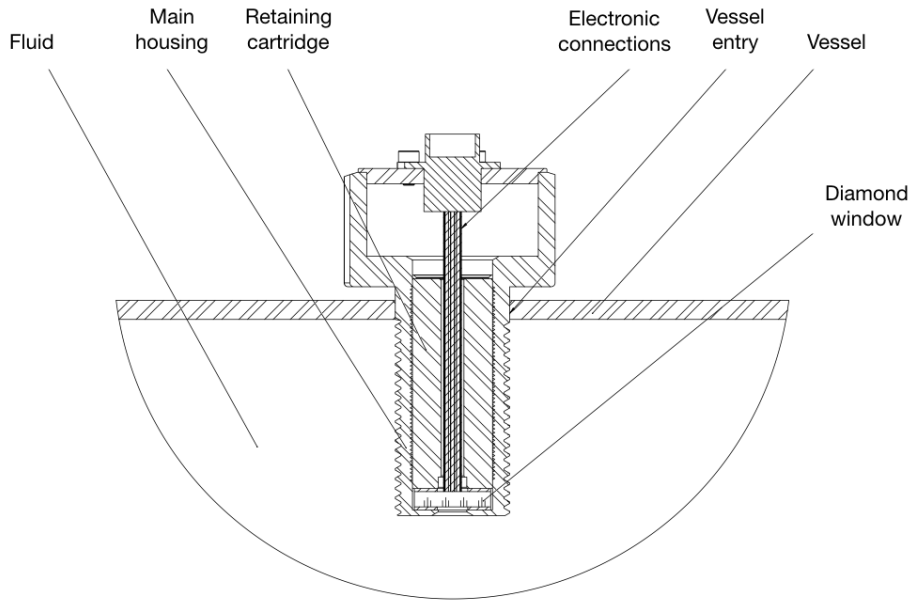

Figure 11.5: A CAD design schematic for the proposed packaging of diamond sensors to be deployed in extreme environments.

The eventual aim of the pioneering sensor design discussed in chapter 10 will be to provide a comprehensive solution for in-line, real time monitoring and analysis of liquids within extremely challenging environments. The device will give accurate measurements of pH, dissolved oxygen, temperature and conductivity, in hot, corrosive and radioactive environments whilst acting as a robust pressure boundary against the fluid. This will enable complete monitoring of a system, giving unprecedented levels of real time information during its operational lifetime and potentially saving millions of pounds in overheads and downtime.

During the final stages this PhD studentship, a successful proposal was co-authored[†] for a research contract from BAE Systems Maritime Ltd., lasting for 24 months and with a value of over £842,000. The commencement of this exciting project in

[†]Along with the author, co-contributors to this project are: R. B. Jackman, R. J. Moors, A. C. Pakpour-Tabrizi, J. O. Welch.

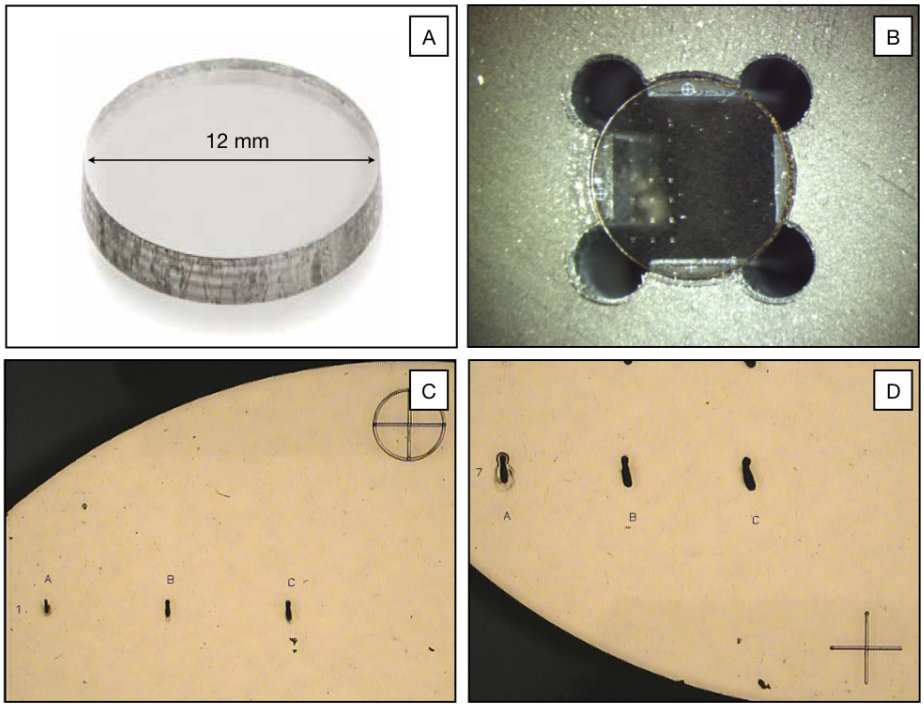

Figure 11.6: Images presenting the initial trials of making electrical contact through diamond windows using graphitic microchannels (GMCs): a) blank diamond window, as procured, b) top view of iterative GMC tests on diamond window, c) & d) microscope images of the diamond surface showing GMCs produced after a series of different laser exposures, including etched crosses 300 µm in diameter.

December 2018 will now allow the realisation of the next stage in development of the sensors established in chapters 9 and 10.

Progress on the initial workpackages is underway, as a joint effort by the co-authors of the proposal. Work to date has consisted of refining the final packaging design, which will allow the diamond sensor to interface with the fluid at high temperature and pressure (and is the subject of the patent no. PCT/GB2017/050580), figure 11.5. This consists of a housing which may be inserted directly into a vessel containing the fluid, with the concentric sensor elements exposed. It has also constituted procuring large diameter polycrystalline diamond windows, which will be processed to form the multi-functional lab-on-chip concept previously discussed. Initial trials of a conductive back-contacting method using graphitic micro-channels

(GMCs) [325, 326] have also been performed, figure 11.6. This method relies on the laser-induced graphitisation of diamond along a precise track to create low-resistance electronic channels in three-dimensions.

The project will be completed in December 2020.

Appendix A

Semiconducting boron carbide for neutron detectors

Boron carbides are a group of boron-carbon compounds. Most commonly referred to is boron carbide (B-C) with the approximate chemical formula B_4C, which is an extremely hard ($>$ 30 MPa Vickers hardness) ceramic material known for its use in tank armour and bulletproof vests. In the nuclear industry B_4C is used in control rods and shielding due to the highly neutron absorbing properties attributed by the large boron concentration. The crystal structure is complex – hence the approximate chemical formula – formed of twelve-atom icosahedral clusters (3D polyhedral solids formed of 20 faces and 12 vertices) in a rhombohedral lattice unit, joined by three-atom chains [327]. Carbon atoms may exist in these inter-icosahedral chains, in combinations such as C-B-C or C-C-C, or alternatively substitute boron atoms within the icosahedra themselves. Boron carbide is therefore considered a family of compounds, varying in composition from the 'ideal' chemical formula – occasionally written as $B_{12}C_3$. Some of these compounds may be carbon-rich ([C] 20 at.%), with the incorporation of carbon atoms into the boron icosahedra; or boron-rich ([C] 8.8 at.%), having a carbon atom deficiency. The most commonly accepted structural model for B_4C boron carbide is composed of $B_{11}C$ icosahedra linked by C-B-C chains. Figure A.1 shows ^{12}B icosahedra linked by C-B-C chains giving an approximate chemical formula of $B_{6.5}C$.

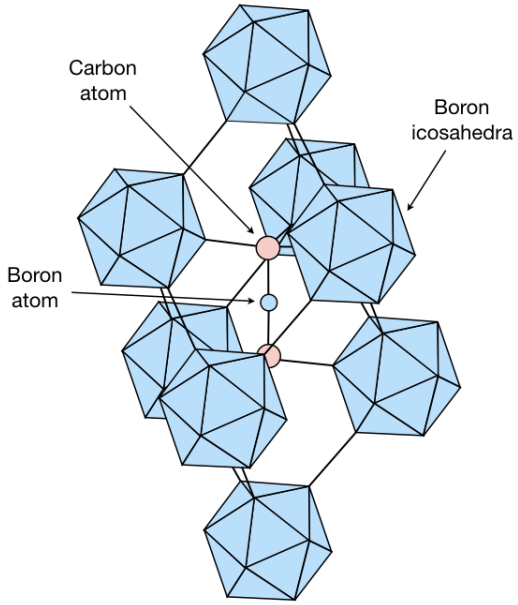

Figure A.1: Unit cell of $B_{6.5}C$ boron carbide – blue indicates boron icosahedra and boron atoms, red indicates carbon atoms (adapted from [327]).

Importantly, boron carbide provides a route to producing boron-rich semiconducting films, with properties such as bandgap, conductivity and n- or p-type 'doping' polarity dependent on its composition and deposition method. Micro- and nanocrystalline films have been deposited from numerous source materials; such as by Ar sputtering a boron carbide (B_4C) target [328–330]; or by CVD with diborane (B_2H_6) [331], boron trichloride (BCl_3) [332] or nido-pentaborane (B_5H_8) precursors [333–335], with the addition of methane gas (CH_4). This has been extensively reviewed by Sezer and Brand [336]. More recently, successful work has focused on using single-precursor cage molecules known as carboranes for semiconducting film growth.

Carboranes are a family of cluster compounds, formed of boron, carbon and hydrogen. They are a subset of heteroboranes, compounds of the chemical formula B_xH_y in which one or more of the constituent atoms is replaced by another element. These compounds are polyhedral in structure, of which most interesting are the highly stable icosahedra which form the building blocks of rhombohedral boron carbide. Carboranes may be further classified by the number of vertices missing from a com-

Isomer ($C_2B_{10}H_{12}$)	Skeletal formula
1,2-closo-dicarbadodecarborane (ortho-)	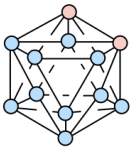
1,7-closo-dicarbadodecarborane (meta-)	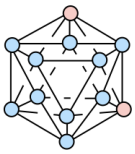
1,12-closo-dicarbadodecarborane (para-)	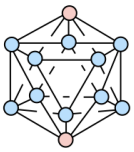

Table A.1: Ortho-, meta- and para- carborane isomers along with their skeletal formulae.

plete polyhedron: closo- (zero), nido- (one), arachno- (two), etc. The most commonly studied carboranes are the icosahedral closo-dicarbadodecarboranes, with a chemical formula $C_2B_{10}H_{12}$. These occur in the form one of three isomers, differing in the location of the carbon atoms within the icosahedral frame. These are 1,2-, 1,7- and 1,12- closo-dicarbadodecarborane also known as ortho-, meta- and para-carborane, table A.1.

Early work by Robertson et al. [337–339] showed the possibility of depositing semiconducting B_5C films from ortho-carborane as a single source precursor using synchrotron radiation induced CVD (SRCVD). They highlight the significance of the ability to form rectifying diodes using the all-boron carbide films on n-type silicon. Further work on the deposition of ortho-carborane was carried out, with greater focus on using PECVD with a 13.56 MHz RF plasma to deposit and characterise films for rectifying diodes on n-type Si, aluminium [340] and SiC substrates [256]. Strong evidence of p-type conductivity inherent to the boron carbide films was shown in these cases, with the electronic properties of the material largely independent of substrate type or crystal grain size.

Models [341,342] would suggest a nearly identical electronic structure between the

carborane isomers, with similar energetic positions of the HOMO and LUMO band edges. However experimental photoemission and inverse photoemission analysis of adsorbed molecular films of ortho- and meta- carborane shows an unexpected shift of these edges with respect to the Fermi level, independent of the metal adsorption surface. It is found [255, 343] that the LUMO for meta-carborane is significantly closer to the Fermi level than the equivalent for ortho-carborane. Suggesting that not only can semiconducting films be deposited from carborane precursors, but different isomers may yield polytypes of boron carbide that are either n-type (for meta-carborane precursors) or p-type (for ortho-carborane precursors) without the need for transition metal doping. It has also been shown that para-carborane forms a unique boron carbide polytype with a different band-gap and conductivity [344].

These semiconducting n- or p-type B-C films can be formed by the dehydrogenation of the source carboranes whilst in the gas phase by an RF plasma (PECVD). Other gas-phase deposition techniques exist, Ghosh et al. [254] use pulsed DC PECVD; Shin et al. [345] describe the deposition of carborane onto silicon substrates using a deuterium glow discharge pulsed DC method. Chaudhari et al. [346] demonstrate the use of hot wire CVD (HWCVD) to deposit films (0.2 μm thick) onto n-type crystalline silicon (c-Si) by thermal decomposition of an o-carborane precursor in Ar carrier gas. Alternatively, adsorbed molecular carborane films may be formed by vapour deposition. Decomposition to semiconducting B-C can then be performed by synchrotron white light, electron bombardment or UV radiation [255, 324, 343, 347, 348].

In light of these studies it is demonstrated how a 'direct' heterojunction diode for neutron detection [253, 319] may be formed by PECVD deposition of approx. 300 nm p-type B-C from ortho-carborane onto sputter-cleaned n-type Si substrates. Neutron detection is made under a maximum radiative flux of $1.5 \times 10^{11}\,\mathrm{cm}^{-2}\,\mathrm{s}^{-1}$ at a reverse bias of -18 V. The anticipated band gap of 0.5 - 1 eV [333] in the boron carbide layer is responsible for the measured $\sim 2 \times 10^5$ electron-hole pairs generated per neutron. Low efficiency is observed, which is attributed primarily to the

under-optimised geometry allowing these ions to escape without depositing all their kinetic energy; and the low isotopic proportion of ^{10}B (19.8%, non-enriched) in the ortho-carborane precursor. The authors suggest that efficiency in such a device can be expected to exceed 80% with a 50 - 100 μm thick ^{10}B enriched boron carbide layer.

Appendix B

Corrections to the Bethe equation for electronic stopping power

B.1 Barkas correction

The Barkas correction accounts for distant interactions and implies a charge dependence on stopping power. Negatively charged particles are observed to travel further than positively charged particles of equal mass and velocity [349]. The exact form of the correction is non-conclusive and varies amongst calculations, however the first theory was developed by Ashley et al. [273, 274] and can be written,

$$L_1(\beta) = \frac{\sqrt{2}F_{ARB}}{Z^{1/2}x^{3/2}}\left(\frac{b}{x^{1/2}}\right) \tag{B.1}$$

where,

$$x = \frac{1}{Z}\left(\frac{\beta}{\alpha}\right)^2 \tag{B.2}$$

and the parameters b and F_{ARB} are tabulated values, where b is a scaled minimum impact parameter with a value between 1 and 2.

B.2 Bloch correction

The Bloch correction can be written,

$$z^2 L_2(\beta) = -y^2 \sum_{n=1}^{\infty} \left[n\left(n^2 + y^2\right) \right]^{-1} \tag{B.3}$$

where

$$y = \frac{z\alpha}{\beta} \tag{B.4}$$

and α is the fine structure constant.

B.3 Shell correction

Bethe's equation makes assumptions based upon the first-order Born approximation. Importantly, that the velocity of the incident ion is much greater than the velocities of the atomic electrons of the medium it is traversing. In fact, at lower ion energies (velocities) the electronic contributions to the stopping power begin to diminish – initially that of the K-shell electrons; and for even lower energies, also the L-shell and higher electron shells.

The shell correction can be deduced using multiple methods. ICRU Report No. 49 [272] describes the evaluation of the shell correction as a sum of the corrections for each shell and sub-shell. Inner shells are approximated using hydrogenic wave functions, with the outer shells assumed to have a dependence on the inner shell corrections. Scale factors are introduced and adjusted to bring the stopping power into agreement with experimental values. Parameterised fitting formulas such as those published by Ziegler [304] include the shell correction as part of the semi-empirical approach to stopping power calculation.

B.4 Density-effect correction

The density-effect correction accounts for the polarisation of the target as the particle traverses, resulting in a reduction in stopping power. It is calculated using the dielectric response function of the material, for which there exist simplified models to evaluate the correction for any material based upon physical properties and the binding energies of electrons in each atomic shell. This correction is only significant for particles with high energy; at lower energies the correction to the stopping power is negligible.

References

[1] H. Pierson, *Handbook of Carbon, Graphite, Diamond and Fullerenes: Properties, Processing and Applications*. William Andrew Publishing/Noyes, 1993.

[2] H. Liu and D. Dandy, *Diamond Chemical Vapor Deposition - Nucleation and Early Growth Stages*. William Andrew Publishing/Noyes, 1995.

[3] J. Zazula, "LHC Project Note 78/97," tech. rep., 2007.

[4] H. Davy, "Some Experiments on the Combustion of the Diamond and Other Carbonaceous Substances," *Philosophical Transactions of the Royal Society of London*, vol. 104, pp. 557–570, 1814.

[5] H. Liander and E. Lundblad, "Artificial diamonds," *Asea Journal*, vol. 28, no. 5-6, pp. 97–98, 1955.

[6] F. P. Bundy, H. T. Hall, H. M. Strong, and R. H. Wentorf, "Man-made diamonds," *Nature*, vol. 176, no. 4471, pp. 51–55, 1955.

[7] J. Angus, Y. Wang, and M. Sunkara, "Metastable growth of diamond and diamond-like phases," *Annu. Rev. Mater. Sci.*, vol. 21, pp. 221–248, 1991.

[8] M. Naamoun, A. Tallaire, F. Silva, J. Achard, P. Doppelt, and A. Gicquel, "Etch-pit formation mechanism induced on HPHT and CVD diamond single crystals by H2/O2 plasma etching treatment," *Physica Status Solidi (A) Applications and Materials Science*, vol. 209, no. 9, pp. 1715–1720, 2012.

[9] W. G. Eversole, "Synthesis of Diamond," 1962.

[10] B. V. Derjaguin and D. B. Fedoseev, "The Synthesis of Diamond at Low Pressure," *Scientific American*, vol. 233, no. 5, pp. 102–109, 1975.

[11] B. V. Spitsyn, L. L. Bouilov, and B. V. Derjaguin, "Vapor growth of diamond on diamond and other surfaces," *Journal of Crystal Growth*, vol. 52, pp. 219–226, 1981.

[12] J. C. Angus, H. A. Will, and W. S. Stanko, "Growth of diamond seed crystal by vapor deposition," *Journal of Applied Physics*, vol. 39, no. 6, pp. 2915–2922, 1968.

[13] S. Matsumoto, Y. Sato, M. Kamo, and N. Setaka, "Vapor Deposition of Diamond Particles from Methane," *Japanese Journal of Applied Physics*, vol. 21, no. 4, pp. L183–L185, 1982.

[14] M. Kamo, Y. Sato, S. Matsumoto, and N. Setaka, "Diamond synthesis from gas phase in microwave plasma," *Journal of Crystal Growth*, vol. 62, no. 3, pp. 642–644, 1983.

[15] S. Matsumoto, Y. Sato, M. Tsutsumi, and N. Setaka, "Growth of diamond particles from methane-hydrogen gas," *Journal of Materials Science*, vol. 17, no. 11, pp. 3106–3112, 1982.

[16] K. Ohtsuka, K. Suzuki, A. Sawabe, and T. Inuzuka, "Epitaxial Growth of Diamond on Iridium," *Japanese Journal of Applied Physics*, vol. 35, p. L1072, 1996.

[17] D. K. Reinhard, T. A. Grotjohn, M. Becker, M. K. Yaran, T. Schuelke, and J. Asmussen, "Fabrication and properties of ultrananо, nano, and microcrystalline diamond membranes and sheets," *Journal of Vacuum Science & Technology B: Microelectronics and Nanometer Structures*, vol. 22, no. 6, p. 2811, 2004.

[18] R. S. Sussmann, *CVD Diamond for Electronic Devices and Sensors*. Wiley, 2009.

[19] T. Teraji, "Chemical vapor deposition of homoepitaxial diamond films," *Physica Status Solidi (A)*, vol. 203, no. 13, pp. 3324–3357, 2006.

[20] J. Pernot, P. N. Volpe, F. Omnès, P. Muret, V. Mortet, K. Haenen, and T. Teraji, "Hall hole mobility in boron-doped homoepitaxial diamond," *Physical Review B - Condensed Matter and Materials Physics*, vol. 81, no. 20, pp. 1–7, 2010.

[21] J. Isberg, J. Hammersberg, E. Johansson, D. J. Twitchen, and A. J. Whitehead, "High carrier mobility in single-crystal plasma-deposited diamond," *Science*, vol. 297, pp. 1670–1673, 2002.

[22] R. Kalish, "Ion-implantation in diamond and diamond films: doping, damage effects and their applications," *Applied Surface Science*, vol. 117-118, pp. 558–569, 1997.

[23] T. H. Borst and O. Weis, "Boron-Doped Homoepitaxial Diamond Layers: Fabrication, Characterization, and Electronic Applications," *Physica Status Solidi (a)*, vol. 154, no. 1, pp. 423–444, 1996.

[24] R. Kalish, "The search for donors in diamond," *Diamond and Related Materials*, vol. 10, no. 9-10, pp. 1749–1755, 2001.

[25] S. Koizumi, "Growth and characterization of phosphorus doped n-type diamond thin films," *Physica Status Solidi (A) Applied Research*, vol. 172, no. 1, pp. 71–78, 1999.

[26] S. Koizumi, T. Teraji, and H. Kanda, "Phosphorus-doped chemical vapor deposition of diamond," *Diamond and Related Materials*, vol. 9, no. 3-6, pp. 935–940, 2000.

[27] K. Haenen, "Temperature dependent spectroscopic study of the electronic structure of phosphorus in n-type CVD diamond films," *Diamond and Related Materials*, vol. 9, no. 3-6, pp. 952–955, 2000.

[28] M. Nesladek, "Conventional n-type doping in diamond: State of the art and recent progress," *Semiconductor Science and Technology*, vol. 20, no. 2, pp. 19–27, 2005.

[29] M. A. Pinault-Thaury, T. Tillocher, D. Kobor, N. Habka, F. Jomard, J. Chevallier, and J. Barjon, "Phosphorus donor incorporation in (1 0 0) homoepitaxial diamond: Role of the lateral growth," *Journal of Crystal Growth*, vol. 335, no. 1, pp. 31–36, 2011.

[30] S. Yamasaki, E. Gheeraert, and Y. Koide, "Doping and interface of homoepitaxial diamond for electronic applications," *MRS Bulletin*, vol. 39, no. 6, pp. 499–503, 2014.

[31] L. G. Wang and A. Zunger, "Phosphorus and sulphur doping of diamond," *Physical Review B*, vol. 66, no. 16, p. 161202, 2002.

[32] J.-P. Lagrange, A. Deneuville, and E. Gheeraert, "Activation energy in low compensated homoepitaxial boron-doped diamond films," *Diamond and Related Materials*, vol. 7, no. 9, pp. 1390–1393, 1998.

[33] K. Nishimura, K. Das, and J. T. Glass, "Material and electrical characterization of polycrystalline boron-doped diamond films grown by microwave plasma chemical vapor deposition," *Journal of Applied Physics*, vol. 69, no. 5, pp. 3142–3148, 1991.

[34] A. T. Collins, A. W. S. Williams, and E. C. Lightowlers, "Impurity conduction in synthetic semiconducting diamond," *J. Phys. C: Solid St. Phys.*, vol. 3, pp. 1727–1735, 1970.

[35] V. Mortet, M. Daenen, T. Teraji, A. Lazea, V. Vorlicek, J. D'Haen, K. Hae-

nen, and M. D'Olieslaeger, "Characterization of boron doped diamond epilayers grown in a NIRIM type reactor," *Diamond and Related Materials*, vol. 17, no. 7-10, pp. 1330–1334, 2008.

[36] M. Werner, R. Locher, W. Kohly, D. Holmes, S. Klose, and H. Fecht, "The diamond Irvin curve," *Diamond and Related Materials*, vol. 6, no. 2-4, pp. 308–313, 1997.

[37] P.-N. Volpe, J. Pernot, P. Muret, and F. Omnès, "High hole mobility in boron doped diamond for power device applications," *Applied Physics Letters*, vol. 94, no. 9, p. 092102, 2009.

[38] H. Okushi, "High quality homoepitaxial CVD diamond for electronic devices," *Diamond and Related Materials*, vol. 10, no. 3-7, pp. 281–288, 2001.

[39] S. G. Ri, H. Kato, M. Ogura, H. Watanabe, T. Makino, S. Yamasaki, and H. Okushi, "Electrical and optical characterization of boron-doped (111) homoepitaxial diamond films," *Diamond and Related Materials*, vol. 14, no. 11-12, pp. 1964–1968, 2005.

[40] T. Teraji, H. Wada, M. Yamamoto, K. Arima, and T. Ito, "Highly efficient doping of boron into high-quality homoepitaxial diamond films," *Diamond and Related Materials*, vol. 15, no. 4-8, pp. 602–606, 2006.

[41] N. Fujimori, H. Nakahata, and T. Imai, "Properties of boron-doped epitaxial diamond films," *Japanese Journal of Applied Physics*, vol. 29, no. 5, pp. 824–827, 1990.

[42] M. I. Landstrass and K. V. Ravi, "Hydrogen passivation of electrically active defects in diamond," *Applied Physics Letters*, vol. 55, no. 14, pp. 1391–1393, 1989.

[43] S. Ri, Y. Akiba, H. Yoichi, K. Tateki, and I. Masamori, "Formation mechanism of p-type surface conductive layer on deposited diamond films,"

Japanese Journal of Applied Physics, vol. 34, no. 10, pp. 5550–5555, 1995.

[44] W. Chen, D. Qi, X. Gao, and A. T. S. Wee, "Surface transfer doping of semiconductors," *Progress in Surface Science*, vol. 84, no. 9-10, pp. 279–321, 2009.

[45] K. Das, V. Venkatesan, K. Miyata, D. L. Dreifus, and J. T. Glass, "A review of the electrical characteristics of metal contacts on diamond," *Thin Solid films*, vol. 212, pp. 19–24, 1992.

[46] S. Grot, G. S. Gildenblat, C. W. Hatfield, C. Wronski, A. R. Badzian, T. Badzian, and R. Messier, "The effect of surface treatment on the electrical properties of metal contacts to boron-doped homoepitaxial diamond film," *IEEE Electron Device Letters*, vol. 11, no. 2, pp. 100–102, 1990.

[47] G. Kawaguchi, J. Nakanishi, A. Otsuki, T. Oku, and M. Murakami, "Dependence of contact resistance on metal electronegativity for B-doped diamond films," *Journal of Applied Physics*, vol. 75, no. 10, pp. 5165–5170, 1994.

[48] Y. Mori, H. Kawarada, and A. Hiraki, "Properties of metal / diamond interfaces and effects of oxygen adsorbed onto diamond surface," *Applied Physics Letters*, vol. 58, no. 9, pp. 940–941, 1991.

[49] H. Kawarada, "Hydrogen-terminated diamond surfaces and interfaces," *Surface Science Reports*, vol. 26, pp. 205–259, 1996.

[50] X. Liu, B. Yang, Y. Jia, and Y. Li, "Electrical characteristics of metal contacts to boron-doped polycrystalline semiconducting diamond thin films," *Chinese Phys. Letts*, vol. 13, no. 7, pp. 541–544, 1996.

[51] C. A. Hewett, M. J. Taylor, J. R. Zeidler, and M. W. Geis, "Specific contact resistance measurements of ohmic contacts to semiconducting diamond," *Journal of Applied Physics*, vol. 77, no. 2, pp. 755–760, 1995.

[52] M. Werner, R. Job, A. Denisenko, A. Zaitsev, W. Fahrner, C. Johnston, P. Chalker, and I. Buckley-Golder, "How to fabricate low-resistance metal-diamond contacts," *Diamond and Related Materials*, vol. 5, pp. 723–727, 1998.

[53] J. Nakanishi, A. Otsuki, T. Oku, O. Ishiwata, and M. Murakami, "Formation of ohmic contacts to p-type diamond using carbide forming metals," *Journal of Applied Physics*, vol. 76, no. 4, pp. 2293–2298, 1994.

[54] M. Yokoba, Y. Koide, A. Otsuki, F. Ako, T. Oku, and M. Murakami, "Carrier transport mechanism of Ohmic contact to p-type diamond," *Journal of Applied Physics*, vol. 81, no. 10, p. 6815, 1997.

[55] Y. Koide, "Metal-diamond semiconductor interface and photodiode application," *Applied Surface Science*, vol. 254, no. 19, pp. 6268–6272, 2008.

[56] Y. Chen, M. Ogura, S. Yamasaki, and H. Okushi, "Investigation of specific contact resistance of ohmic contacts to B-doped homoepitaxial diamond using transmission line model," *Diamond and Related Materials*, vol. 13, pp. 2121–2124, 2004.

[57] T. Tachibana and J. T. Glass, "Correlation of interface chemistry to electrical properties of metal contacts on diamond," *Materials Science*, vol. 2, no. 5-7, pp. 963–969, 1993.

[58] T. Tachibana, B. E. Williams, and J. T. Glass, "Correlation of the electrical properties of metal contacts on diamond films with the chemical nature of the metal-diamond interface," *Physical Review B*, vol. 45, pp. 11975–11981, 5 1992.

[59] K. L. Moazed, J. R. Zeidler, and M. J. Taylor, "A thermally activated solid state reaction process for fabricating ohmic contacts to semiconducting diamond," *Journal of Applied Physics*, vol. 68, no. 5, pp. 2246–2254, 1990.

[60] C. Y. Chang, Y. K. Fang, and S. M. Sze, "Specific contact resistance of metal-semiconductor barriers," *Solid State Electronics*, vol. 14, no. 7, pp. 541–550, 1971.

[61] G. P. Carver, J. J. Kopanski, D. B. Novotny, and R. A. Forman, "Specific Contact Resistivity of Metal-Semiconductor Contacts - A New, Accurate Method Linked to Spreading Resistance," *IEEE Transactions on Electron Devices*, vol. 35, no. 4, pp. 489–497, 1988.

[62] Industry Arc, "Neutron Detection Market," tech. rep., 2018.

[63] A. J. Peurrung, "Recent developments in neutron detection," *Nuclear Instruments and Methods in Physics Research Section A: Accelerators, Spectrometers, Detectors and Associated Equipment*, vol. 443, no. 2-3, p. 16, 1999.

[64] A. Oed, "Detectors for thermal neutrons," *Nuclear Instruments and Methods in Physics Research Section A: Accelerators, Spectrometers, Detectors and Associated Equipment*, vol. 525, no. 1-2, pp. 62–68, 2004.

[65] S. Mukhopadhyay, "Solid State Neutron Detector - A Review of Status," tech. rep., National Security Technologies, LLC (United States), 2010.

[66] A. P. Simpson, S. Jones, M. J. Clapham, and S. A. McElhaney, "A review of neutron detection technology alternatives to helium-3 for safeguards applications," in *INMM 52nd Annual Meeting*, 2011.

[67] T. Shimaoka, J. H. Kaneko, Y. Sato, M. Tsubota, H. Shimmyo, A. Chayahara, H. Watanabe, H. Umezawa, and Y. Mokuno, "Fano factor evaluation of diamond detectors for alpha particles," *Physica Status Solidi (A) Applications and Materials Science*, vol. 213, no. 10, pp. 2629–2633, 2016.

[68] H. Pernegger, S. Roe, P. Weilhammer, V. Eremin, H. Frais-Kölbl, E. Griesmayer, H. Kagan, S. Schnetzer, R. Stone, W. Trischuk, D. Twitchen, and A. Whitehead, "Charge-carrier properties in synthetic single-crystal diamond

measured with the transient-current technique," *Journal of Applied Physics*, vol. 97, no. 7, pp. 1–9, 2005.

[69] A. N. Caruso, "The physics of solid-state neutron detector materials and geometries," *Journal of physics. Condensed matter : an Institute of Physics journal*, vol. 22, no. 44, p. 443201, 2010.

[70] V. Andreev, A. Vassiljev, E. Ivanov, D. Ilyin, A. Krivshich, and A. Serebrov, "Ultracold neutron detector for neutron lifetime measurements," *Nuclear Instruments and Methods in Physics Research Section A: Accelerators, Spectrometers, Detectors and Associated Equipment*, vol. 845, pp. 548–551, 2 2017.

[71] P. Rinard, "Neutron interactions with matter," tech. rep., Los Alamos National Lab, New Mexico, 1991.

[72] N. Soppera, M. Bossant, and E. Dupont, "JANIS 4: An Improved Version of the NEA Java-based Nuclear Data Information System," *Nuclear Data Sheets*, vol. 120, pp. 294–296, 6 2014.

[73] C. Petrillo, F. Sacchetti, O. Toker, and N. J. Rhodes, "Solid state neutron detectors," *Nuclear Instruments and Methods in Physics Research, Section A: Accelerators, Spectrometers, Detectors and Associated Equipment*, vol. 378, no. 3, pp. 541–551, 1996.

[74] R. D. Mckeag and R. B. Jackman, "Diamond UV photodetectors : sensitivity and speed for visible blind applications," *Diamond and Related Materials*, vol. 7, 1998.

[75] L. Barberini, S. Cadeddu, and M. Caria, "A new material for imaging in the UV: CVD Diamond," *Nuclear Instruments and Methods in Physics Research Section A: Accelerators, Spectrometers, Detectors and Associated Equipment*, vol. 460, no. 1, pp. 127–137, 2001.

[76] A. Balducci, M. Marinelli, E. Milani, M. E. Morgada, A. Tucciarone, G. Verona-Rinati, M. Angelone, and M. Pillon, "Extreme ultraviolet single-crystal diamond detectors by chemical vapor deposition," *Applied Physics Letters*, vol. 86, no. 19, p. 193509, 2005.

[77] A. Mainwood, "Recent developments of diamond detectors for particles and UV radiation," *Semiconductor science and technology*, vol. 15, no. 9, p. R55, 2000.

[78] A. Kaiser, D. Kueck, P. Benkart, A. Munding, G. M. Prinz, A. Heittmann, H. Huebner, R. Sauer, and E. Kohn, "Concept for diamond 3-D integrated UV sensor," *Diamond and related materials*, vol. 15, no. 11-12, pp. 1967–1971, 2006.

[79] Y. Koide, M. Liao, and J. Alvarez, "Thermally stable solar-blind diamond UV photodetector," *Diamond and related materials*, vol. 15, no. 11-12, pp. 1962–1966, 2006.

[80] A. T. Collins, "Detectors for UV and Far UV Radiation," *CVD Diamond for Electronic Devices and Sensors*, pp. 163–183, 2009.

[81] M. J. Guerrero, D. Tromson, M. Rebisz, C. Mer, B. Bazin, and P. Bergonzo, "Requirements for synthetic diamond devices for radiotherapy dosimetry applications," *Diamond and related materials*, vol. 13, no. 11-12, pp. 2046–2051, 2004.

[82] G. A. P. Cirrone, G. Cuttone, L. Rafaele, M. G. Sabini, C. De Angelis, S. Onori, M. Pacilio, M. Bucciolini, M. Bruzzi, and S. Sciortino, "Natural and CVD type diamond detectors as dosimeters in hadrontherapy applications," *Nuclear Physics B-Proceedings Supplements*, vol. 125, pp. 179–183, 2003.

[83] Y. Garino, A. Lo Giudice, C. Manfredotti, M. Marinelli, E. Milani, A. Tucciarone, and G. Verona-Rinati, "Performances of homoepitaxial single crys-

tal diamond in diagnostic x-ray dosimetry," *Applied physics letters*, vol. 88, no. 15, p. 151901, 2006.

[84] M. Di Fraia, A. De Sio, M. Antonelli, R. Nesti, D. Panella, R. H. Menk, G. Cautero, M. Coreno, D. Catone, N. Zema, and others, "Fast beam monitor diamond-based devices for VUV and X-ray synchrotron radiation applications," *Journal of Synchrotron Radiation*, vol. 26, no. 2, 2019.

[85] E. Griesmayer, P. Kavrigin, C. Weiss, and S. Kalbfleisch, "Applications of single-crystal CVD diamond XBPM detectors with nanometre x-ray beams," in *AIP Conference Proceedings*, vol. 2054, p. 60052, AIP Publishing, 2019.

[86] C. Bloomer, G. Rehm, P. Salter, and M. Newton, "A single crystal CVD diamond x-ray beam diagnostic with embedded graphitic wire electrodes," in *AIP Conference Proceedings*, vol. 2054, p. 60058, AIP Publishing, 2019.

[87] J. Livingstone, A. W. Stevenson, D. J. Butler, D. Häusermann, and J.-F. Adam, "Characterization of a synthetic single crystal diamond detector for dosimetry in spatially fractionated synchrotron x-ray fields," *Medical physics*, vol. 43, no. 7, pp. 4283–4293, 2016.

[88] T. Zhou, W. Ding, M. Gaowei, G. De Geronimo, J. Bohon, J. Smedley, and E. Muller, "Pixelated transmission-mode diamond X-ray detector," *Journal of synchrotron radiation*, vol. 22, no. 6, pp. 1396–1402, 2015.

[89] L. Wang, J. Liu, R. Xu, H. Peng, W. Shi, and Y. Xia, "A nanocrystalline CVD diamond film as an x-ray radiation detector," *Semiconductor science and technology*, vol. 22, no. 2, p. 128, 2006.

[90] L. Y. Liu, X. P. Ouyang, L. Lei, L. Wang, Z.-b. Zhang, H.-b. Pan, and X.-p. Zhang, "CVD diamond film detector for X-ray detection," *Atomic Energy Science and Technology*, vol. 43, no. 4, pp. 377–380, 2009.

[91] F. Li, L. Hou, C. Su, G. Yang, and S. Liu, "CVD diamond based soft X-ray

detector with fast response," *High Power Laser and Particle Beams*, vol. 22, no. 6, pp. 1404–1406, 2010.

[92] C. Bloomer, "The Use of Single-crystal CVD Diamond as a Position Sensitive X-ray Detector," 2016.

[93] J. A. Dueñas, J. de la Torre Pérez, A. Martín Sánchez, and I. Martel, "Diamond detector for alpha-particle spectrometry," *Applied Radiation and Isotopes*, vol. 90, pp. 177–180, 2014.

[94] F. Schirru, D. Chokheli, and M. Kiš, "Thin single crystal diamond detectors for alpha particle detection," *Diamond and Related Materials*, vol. 49, pp. 96–102, 10 2014.

[95] P. Bergonzo, F. Foulon, R. Marshall, C. Jany, A. Brambilla, R. McKeag, and R. Jackman, "Thin film diamond alpha detectors for dosimetry applications," *Diamond and Related Materials*, vol. 8, pp. 952–955, 1999.

[96] M. Pomorski, B. Caylar, and P. Bergonzo, "Super-thin single crystal diamond membrane radiation detectors," *Applied Physics Letters*, vol. 103, no. 11, p. 112106, 2013.

[97] P. Bergonzo, F. Foulon, A. Brambilla, D. Tromson, C. Jany, and S. Haan, "Corrosion hard CVD diamond alpha particle detectors for nuclear liquid source monitoring," *Diamond and Related Materials*, vol. 9, pp. 1003–1007, 2000.

[98] L. Lei, X. Ouyang, N. Cao, X. Zhang, L. Wang, and Y. Zhong, "Charge collection efficiency of chemical vapor deposition diamond film detector to alpha-particles," *High Power Laser and Particle Beams*, vol. 21, no. 7, pp. 1083–1087, 2009.

[99] Q. Su, Y. Xia, L. Wang, J. Liu, J. Ruan, and W. Shi, "Electrical properties of CVD diamond detector and detection for alpha particle," *Modern Physics*

Letters A, vol. 20, no. 38, pp. 2949–2956, 2005.

[100] S. G. Wang, Q. Zhang, S. F. Yoon, and J. Ahn, "CVD Diamond Thin Films for Alpha Particle Detector Application," *MRS Online Proceedings Library Archive*, vol. 692, 2001.

[101] H. Johnson, A. Zaniewski, J. Holmes, R. Alarcon, M. Benipal, F. Koeck, H. Surdi, and R. Nemanich, "PIN Diamond Diode Detectors for Alpha Radiation," *Bulletin of the American Physical Society*, 2018.

[102] A. Kumar and A. Topkar, "Alpha particle response study of polycrstalline diamond radiation detector," in *AIP Conference Proceedings*, vol. 1731, p. 60001, AIP Publishing, 2016.

[103] G. Bei-Bei, W. Lin-Jun, Z. Ming-Long, and X. Yi-Ben, "Investigation of chemical-vapour-deposition diamond alpha-particle detectors," *Chinese Physics Letters*, vol. 21, no. 10, p. 2051, 2004.

[104] W. Lin-Jun, L. J.-M. S. Qing-Fen, and S. W.-M. X. Yi-Ben, "Electrical properties of alpha-particle detectors based on CVD diamond films," *Acta Physica Sinica*, vol. 5, 2006.

[105] C. Mer, D. Tromson, J. De Sanoit, M. Pomorski, and P. Bergonzo, "Diamond detectors for alpha monitoring in corrosive media for nuclear waste activity monitoring," in *2009 1st International Conference on Advancements in Nuclear Instrumentation, Measurement Methods and their Applications*, pp. 1–4, IEEE, 2009.

[106] I. Wodniak, K. Drozdowicz, J. Dankowski, B. Gabańska, A. Igielski, A. Kurowski, B. Marczewska, T. Nowak, and U. Woźnicka, "CVD diamond detectors for fast alpha particles escaping from the tokamak DT plasma," *Nukleonika*, vol. 56, pp. 143–147, 2011.

[107] P. J. Sellin and M. B. H. Breese, "Spectroscopic response of coplanar di-

amond alpha particle detectors," *IEEE Transactions on Nuclear Science*, vol. 48, no. 6, pp. 2307–2312, 2001.

[108] Z. Minglong, X. Yiben, W. Linjun, S. Hujiang, and G. Beibei, "Performance of CVD diamond alpha particle detectors," *Solid state communications*, vol. 130, no. 8, pp. 551–555, 2004.

[109] S. F. Kozlov, E. A. Konorova, M. I. Krapivin, V. A. Nadein, and V. G. Yudina, "Usage of diamond detectors as immersed alpha-counters," *IEEE Transactions on nuclear science*, vol. 24, no. 1, pp. 242–243, 1977.

[110] E.-K. Souw and R. J. Meilunas, "Response of CVD diamond detectors to alpha radiation," *Nuclear Instruments and Methods in Physics Research Section A: Accelerators, Spectrometers, Detectors and Associated Equipment*, vol. 400, no. 1, pp. 69–86, 1997.

[111] P. Bergonzo, F. Foulon, R. D. Marshall, C. Jany, A. Brambilla, R. D. McKeag, and R. B. Jackman, "High collection efficiency CVD diamond alpha detectors," *IEEE Transactions on Nuclear Science*, vol. 45, no. 3, pp. 370–373, 1998.

[112] B. Caylar, M. Pomorski, J. Alvarez, J.-P. Kleider, A. Oh, T. Wengler, and P. Bergonzo, "Novel 3D micro-structuring of diamond for radiation detector applications: enhanced performances evaluated under particle and photon beams," in *Diamond 2011*, 2011.

[113] V. N. Amosov, N. B. Rodionov, V. A. Dravin, K. K. Artemev, and S. A. Mechchaninov, "Testing the prototype diamond detector for the ITER neutral-particle spectrometer," *Instruments and Experimental Techniques*, vol. 60, no. 1, pp. 122–125, 2017.

[114] D. Meier, "Diamond as a particle detector," *Italian Phys. Soc. Proc.*, vol. 52, p. 105, 1996.

[115] M. Mathes, M. Cristinziani, H. Kagan, S. Smith, W. Trischuk, J. Velthuis, and N. Wermes, "Characterization of a single crystal diamond pixel detector in a high energy particle beam," *Journal of Instrumentation*, vol. 3, no. 12, p. P12002, 2008.

[116] T. Behnke, A. Oh, A. Wagner, W. Zeuner, A. Bluhm, C. P. Klages, M. Paul, and L. Schäfer, "Development of diamond films for particle detector applications," *Diamond and Related Materials*, vol. 7, no. 10, pp. 1553–1557, 1998.

[117] H. Frais-Kolbl, E. Griesmayer, H. Kagan, and H. Pernegger, "A fast low-noise charged-particle CVD diamond detector," *IEEE Transactions on nuclear science*, vol. 51, no. 6, pp. 3833–3837, 2004.

[118] M. Marinelli, E. Milani, A. Paoletti, A. Tucciarone, G. Verona-Rinati, G. Luce, S. Albergo, V. Bellini, V. Campagna, C. Marchetta, and others, "Use of high-sensitivity diamond detectors in DC mode for detailed beam-profile measurements in particle accelerators," *Diamond and related materials*, vol. 10, no. 3-7, pp. 706–709, 2001.

[119] J. Morse, M. Salomé, E. Berdermann, M. Pomorski, W. Cunningham, and J. Grant, "Single crystal CVD diamond as an X-ray beam monitor," *Diamond and related materials*, vol. 16, no. 4-7, pp. 1049–1052, 2007.

[120] P. Bergonzo, F. Foulon, A. Brambilla, D. Tromson, C. Mer, B. Guizard, and S. Haan, "Diamond detectors for alpha monitoring in corrosive media for nuclear fuel assembly reprocessing," *MRS Online Proceedings Library Archive*, vol. 608, 1999.

[121] M. Pomorski, E. Berdermann, M. Ciobanu, a. Martemyianov, P. Moritz, M. Rebisz, and B. Marczewska, "Characterisation of single crystal CVD diamond particle detectors for hadron physics experiments," *Physica Status Solidi (a)*, vol. 202, pp. 2199–2205, 9 2005.

[122] C. Mer, M. Pomorski, P. Bergonzo, D. Tromson, M. Rebisz, T. Domenech, F. Foulon, M. Nesladek, O. A. Williams, and R. B. Jackman, "An insight into neutron detection from polycrystalline CVD diamond films," *Diamond and Related Materials*, vol. 13, pp. 791–795, 2004.

[123] P. Lebedev, "Neutron spectrometery by diamond detector for nuclear radiation," *IEEE Transactions on Nuclear Sciencea*, vol. 22, pp. 171–172, 1975.

[124] M. Pillon, M. Angelone, and A. V. Krasilniko, "14 MeV neutron spectra measurements with 4% energy resolution using a type IIa diamond detector," *Radiation Protection Dosimetry*, vol. 66, no. 1-4, pp. 371–374, 1996.

[125] A. Pietropaolo, C. Andreani, M. Rebai, L. Giacomelli, G. Gorini, E. Perelli Cippo, M. Tardocchi, A. Fazzi, G. Verona Rinati, C. Verona, M. Marinelli, E. Milani, C. D. Frost, and E. M. Schooneveld, "Single-crystal diamond detector for time-resolved measurements of a pulsed fast-neutron beam," *EPL (Europhysics Letters)*, vol. 92, no. 6, 2010.

[126] L. Y. Liu, X. P. Ouyang, Z. B. Zhang, J. F. Zhang, X. P. Zhang, Y. H. Zhong, and W. Wang, "Polycrystalline chemical-vapor-deposited diamond for fast and ultra-fast neutron detection," *Science China Technological Sciences*, vol. 55, no. 9, pp. 2640–2645, 2012.

[127] A. Oh, M. Moll, A. Wagner, and W. Zeuner, "Neutron irradiation studies with detector grade CVD diamond," *Diamond and Related Materials*, vol. 9, no. 11, pp. 1897–1903, 2000.

[128] M. Angelone, M. Marinelli, E. Milani, G. Pucella, M. Pillon, A. Tucciarone, and G. Verona-Rinati, "Neutron detection and dosimetry using polycrystalline CVD diamond detectors with high collection efficiency," *Radiation Protection Dosimetry*, vol. 120, no. 1-4, pp. 345–348, 2006.

[129] G. J. Schmid, J. a. Koch, R. a. Lerche, and M. J. Moran, "A neutron sensor based on single crystal CVD diamond," *Nuclear Instruments and Methods*

in Physics Research, Section A: Accelerators, Spectrometers, Detectors and Associated Equipment, vol. 527, no. 3, pp. 554–561, 2004.

[130] R. Cardarelli, M. Angelone, A. Milocco, F. Andreoli, and M. Pillon, "Development of an high resolution neutron spectroscopy system using a diamond detector and a remote digital acquisition methodology," *Fusion Engineering and Design*, vol. 89, no. 9-10, pp. 2184–2188, 2014.

[131] M. Angelone, N. Fonnesu, M. Pillon, G. Prestopino, F. Sarto, E. Milani, M. Marinelli, C. Verona, and G. Verona-Rinati, "Spectrometric performances of monocrystalline artificial diamond detectors operated at high temperature," *IEEE Transactions on Nuclear Science*, vol. 59, no. 5 PART 3, pp. 2416–2423, 2012.

[132] F. Belli, M. Rebai, A. Murari, G. Grosso, P. Calvani, A. Muraro, M. Nocente, G. Gorini, D. M. Trucchi, S. Popovichev, J. Figueiredo, M. Girolami, L. Giacomelli, M. Tardocchi, and D. Rigamonti, "First neutron spectroscopy measurements with a pixelated diamond detector at JET," *Review of Scientific Instruments*, vol. 87, no. 11, p. 11D833, 2016.

[133] C. Cazzaniga, M. Tardocchi, M. Rebai, G. Grosso, M. Girolami, G. Croci, P. Calvani, D. Trucchi, G. Gorini, and E. P. Cippo, "Pixelated Single-crystal Diamond Detector for fast neutron measurements," *Journal of Instrumentation*, vol. 10, no. 03, pp. C03016–C03016, 2015.

[134] M. Angelone, M. Pillon, L. Bertalot, F. Orsitto, M. Marinelli, E. Milani, G. Pucella, A. Tucciarone, G. Verona-Rinati, S. Popovichev, and A. Murari, "Time dependent 14 MeV neutrons measurement using a polycrystalline chemical vapor deposited diamond detector at the JET tokamak," *Review of Scientific Instruments*, vol. 76, no. 1, 2005.

[135] C. Cazzaniga, E. Andersson Sundén, F. Binda, G. Croci, G. Ericsson, L. Giacomelli, G. Gorini, E. Griesmayer, G. Grosso, G. Kaveney, M. Nocente,

E. Perelli Cippo, M. Rebai, B. Syme, and M. Tardocchi, "Single crystal diamond detector measurements of deuterium-deuterium and deuterium- tritium neutrons in Joint European Torus fusion plasmas," *Review of Scientific Instruments*, vol. 85, no. 043506, 2014.

[136] N. Izumi, J. A. Koch, V. Y. Glebov, M. J. Moran, R. E. Turner, T. W. Phillips, G. J. Schmid, C. Stoeckl, T. C. Sangster, R. L. Griffith, and R. A. Lerche, "CVD diamond as a high bandwidth neutron detector for inertial confinement fusion diagnostics," *Review of Scientific Instruments*, vol. 74, no. 3, pp. 1828–1831, 2003.

[137] M. Rebai, C. Andreani, A. Fazzi, C. D. Frost, L. Giacomelli, G. Gorini, E. Milani, E. Perelli Cippo, A. Pietropaolo, G. Prestopino, E. Schooneveld, M. Tardocchi, C. Verona, and G. Verona Rinati, "Fission diamond detector tests at the ISIS spallation neutron source," *Nuclear Physics B - Proceedings Supplements*, vol. 215, no. 1, pp. 313–315, 2011.

[138] A. Kumar and A. Topkar, "A Study of the Fast Neutron Response of a Single-Crystal Diamond Detector at High Temperatures," *IEEE Transactions on Nuclear Science*, vol. 65, no. 1, pp. 630–635, 2018.

[139] O. Philip, F. Gicquel, V. Ernst, and Z. Zhou, "Development and Test of a Diamond-Based Fast Neutron Detector for 200 °c Operation," *IEEE Transactions on Nuclear Science*, vol. 64, no. 10, pp. 2683–2689, 2017.

[140] S. Almaviva, M. Marinelli, E. Milani, G. Prestopino, A. Tucciarone, C. Verona, G. Verona-Rinati, M. Angelone, D. Lattanzi, M. Pillon, R. M. Montereali, and M. A. Vincenti, "Thermal and fast neutron detection in chemical vapor deposition single-crystal diamond detectors," *Journal of Applied Physics*, vol. 103, no. 5, 2008.

[141] M. Marinelli, E. Milani, G. Prestopino, M. Scoccia, A. Tucciarone, G. Verona-Rinati, M. Angelone, M. Pillon, and D. Lattanzi, "High perfor-

mance 6LiF -diamond thermal neutron detectors," *Applied Physics Letters*, vol. 89, no. 14, pp. 10–13, 2006.

[142] M. Angelone, M. Pillon, G. Prestopino, M. Marinelli, E. Milani, C. Verona, G. Verona-Rinati, G. Aielli, R. Cardarelli, R. Santonico, R. Bedogni, and A. Esposito, "Thermal and fast neutron dosimetry using artificial single crystal diamond detectors," *Radiation Measurements*, vol. 46, no. 12, pp. 1686–1689, 2011.

[143] A. Pietropaolo, G. Verona Rinati, C. Verona, E. M. Schooneveld, M. Angelone, and M. Pillon, "A single-crystal diamond-based thermal neutron beam monitor for instruments at pulsed neutron sources," *Nuclear Instruments and Methods in Physics Research, Section A: Accelerators, Spectrometers, Detectors and Associated Equipment*, vol. 610, no. 3, pp. 677–681, 2009.

[144] P. Finocchiaro, E. Griesmayer, A. Pappalardo, C. Weiss, E. Jericha, and P. Kavrigin, "Pulse-shape analysis for gamma background rejection in thermal neutron radiation using CVD diamond detectors," *Nuclear Instruments and Methods in Physics Research Section A: Accelerators, Spectrometers, Detectors and Associated Equipment*, vol. 795, pp. 88–91, 2015.

[145] M. Angelone, D. Lattanzi, M. Pillon, M. Marinelli, E. Milani, A. Tucciarone, G. Verona-Rinati, S. Popovichev, R. M. Montereali, M. A. Vincenti, and A. Murari, "Development of single crystal diamond neutron detectors and test at JET tokamak," *Nuclear Instruments and Methods in Physics Research, Section A: Accelerators, Spectrometers, Detectors and Associated Equipment*, vol. 595, no. 3, pp. 616–622, 2008.

[146] D. Lattanzi, M. Angelone, M. Pillon, S. Almaviva, M. Marinelli, E. Milani, G. Prestopino, A. Tucciarone, C. Verona, G. Verona-Rinati, S. Popovichev, R. M. Montereali, M. A. Vincenti, and A. Murari, "Single crystal CVD dia-

monds as neutron detectors at JET," *Fusion Engineering and Design*, vol. 84, no. 7-11, pp. 1156–1159, 2009.

[147] S. Almaviva, G. Prestopino, G. Verona-Rinati, A. Tucciarone, M. Marinelli, E. Milani, C. Verona, M. Angelone, and M. Pillon, "Thermal neutron dosimeter by synthetic single crystal diamond devices," *Applied Radiation and Isotopes*, vol. 67, no. 7-8, pp. S183–S185, 2009.

[148] S. Almaviva, M. Marinelli, E. Milani, G. Prestopino, A. Tucciarone, C. Verona, G. Verona-Rinati, M. Angelone, and M. Pillon, "Improved performance in synthetic diamond neutron detectors: Application to boron neutron capture therapy," *Nuclear Instruments and Methods in Physics Research, Section A: Accelerators, Spectrometers, Detectors and Associated Equipment*, vol. 612, no. 3, pp. 580–582, 2010.

[149] C. Weiss, G. Badurek, E. Berthoumieux, M. Calviani, E. Chiaveri, D. Dobos, E. Griesmayer, C. Guerrero, and V. Vlachoudis, "A CVD diamond detector for (n, α) cross-section measurements," *Proceedings of Science*, vol. 6, no. 15, pp. 1–8, 2011.

[150] P. G. Nedosekin, V. A. Dravin, E. M. Tyurin, V. G. Ral'chenko, V. A. Kolyubin, K. N. Zyablyuk, R. A. Khmel'nitskii, V. N. Pashentsev, A. P. Bol'shakov, and S. A. Afanas'ev, "Slow-neutron detector based on thin CVD diamond film," *Russian Engineering Research*, vol. 37, no. 4, pp. 354–358, 2017.

[151] "Water Security Initiative: Interim Guidance on Planning for Contamination Warning System Deployment, EPA 817-R-07-002," tech. rep., Environmental Protection Agency, USA, 2007.

[152] YSI Inc., "Applications." https://www.ysi.com/applications [Accessed: 3rd March 2019].

[153] SUEZ Water Technologies and Solutions, "Industry Applications." https://www.suezwatertechnologies.com/industries [Accessed: 3rd March

2019].

[154] Envitech Ltd., "Applications." http://envitech.co.uk/environmental-applications/ [Accessed: 3rd March 2019].

[155] Technavio, "Global Water Quality Sensor Market 2018-2022," tech. rep., 2018.

[156] S. Chavan, "Water Quality Monitoring Systems Market by Component (pH Sensors, DO Sensors, Temperature Sensors, Turbidity Sensors, and Others) and Application (Utilities, Industrial, Commercial, and Residential): Global Opportunity Analysis and Industry Forecast, 2018," tech. rep., Allied Market Research, 2018.

[157] Transparency Market Research, "Water Quality Sensor Market - Global Industry Analysis, Size, Share, Growth, Trends and Forecast 2016 - 2024," tech. rep., 2016.

[158] A. A. Belyustin, "The centenary of glass electrode: From Max Cremer to F. G. K. Baucke," *Journal of Solid State Electrochemistry*, vol. 15, no. 1, pp. 47–65, 2011.

[159] P. Bergveld, "ISFET , Theory and Practice," in *IEEE Sensor Conference Toronto*, no. October, pp. 1–26, 2003.

[160] D. Wencel, T. Abel, and C. McDonagh, "Optical chemical pH sensors," *Analytical Chemistry*, vol. 86, no. 1, pp. 15–29, 2014.

[161] A. Arshak, E. I. Gill, K. Arshak, O. Korostynska, and C. Cunniffe, "Drop-coated polyaniline composite conductimetric pH sensors," in *ISSE 2007 - 30th International Spring Seminar on Electronics Technology 2007; Conference Proceedings: Emerging Technologies for Electronics Packaging*, pp. 213–218, 2007.

[162] O. Korostynska, K. Arshak, E. Gill, and A. Arshak, "Review Paper: Materials and Techniques for In Vivo pH Monitoring," *IEEE Sensors*, vol. 8, no. 1, pp. 20–28, 2008.

[163] P. Bergveld, "Short Communications: Development of an Ion-Sensitive Solid-State Device for Neurophysiological Measurements," *IEEE Transactions on Biomedical Engineering*, vol. BME-17, no. 1, pp. 70–71, 1970.

[164] N. I. M. Noh, K. A. Yusof, M. Zolkapli, A. Z. Abdullah, W. F. H. Abdullah, and S. H. Herman, "Effect of channel width-to-length ratio on isothermal point of MOSFET-ISFET structure," in *Proceedings - RSM 2013: 2013 IEEE Regional Symposium on Micro and Nano Electronics*, pp. 130–133, 2013.

[165] A. Denisenko, A. Aleksov, and E. Kohn, "pH sensing by surface-doped diamond effect of the diamond surface termination," *Diamond and Related Materials*, vol. 10, no. 3-7, pp. 667–672, 2001.

[166] H. Kawarada, Y. Araki, T. Sakai, T. Ogawa, and H. Umezawa, "Electrolyte-Solution-Gate FETs Using Diamond Surface for Biocompatible Ion Sensors," *Physica Status Solidi (A) Applied Research*, vol. 185, no. 1, pp. 79–83, 2001.

[167] J. A. Garrido, A. Härtl, S. Kuch, M. Stutzmann, O. A. Williams, and R. B. Jackmann, "pH sensors based on hydrogenated diamond surfaces," *Applied Physics Letters*, vol. 86, no. 073504, 2005.

[168] W. M. Siu and R. S. C. Cobbold, "Basic Properties of the Electrolyte-SiO2-Si-System," *IEEE Transactions on Electron Devices*, vol. ED 26, no. 1, pp. 1805–1815, 1979.

[169] P. Christiaens, M. H. Abouzar, A. Poghossian, T. Wagner, N. Bijnens, O. A. Williams, M. Daenen, K. Haenen, O. Douhéret, J. D'Haen, Z. Mekhalif, M. J. Schöning, and P. Wagner, "PH sensitivity of nanocrystalline diamond films,"

Physica Status Solidi (A) Applications and Materials Science, vol. 204, no. 9, pp. 2925–2930, 2007.

[170] R. K. Ahmad, A. C. Parada, N. Tumilty, and R. B. Jackman, "Nanodiamond-gated diamond field-effect transistor for chemical sensing using hydrogen-induced transfer doping for channel formation," *Applied Physics Letters*, vol. 97, no. 20, 2010.

[171] T. Sakai, K.-S. Song, H. Kanazawa, Y. Nakamura, H. Umezawa, M. Tachiki, and H. Kawarada, "Ozone-treated channel diamond field-effect transistors," *Diamond and Related Materials*, vol. 12, pp. 1873–1876, 2003.

[172] K. S. Song, Y. Nakamura, Y. Sasaki, M. Degawa, J. H. Yang, and H. Kawarada, "pH-sensitive diamond field-effect transistors (FETs) with directly aminated channel surface," *Analytica Chimica Acta*, vol. 573-574, pp. 3–8, 2006.

[173] C. E. Nebel, H. Kato, B. Rezek, D. Shin, D. Takeuchi, H. Watanabe, and T. Yamamoto, "Electrochemical properties of undoped hydrogen terminated CVD diamond," *Diamond and Related Materials*, vol. 15, no. 2-3, pp. 264–268, 2006.

[174] B. Rezek, H. Watanabe, D. Shin, T. Yamamoto, and C. E. Nebel, "Ion-sensitive field effect transistor on hydrogenated diamond," *Diamond and Related Materials*, vol. 15, no. 4-8, pp. 673–677, 2006.

[175] B. Rezek, D. Shin, H. Watanabe, and C. E. Nebel, "Intrinsic hydrogen-terminated diamond as ion-sensitive field effect transistor," *Sensors and Actuators, B: Chemical*, vol. 122, no. 2, pp. 596–599, 2007.

[176] M. Dankerl, A. Reitinger, M. Stutzmann, and J. A. Garrido, "Resolving the controversy on the pH sensitivity of diamond surfaces," *Physica Status Solidi - Rapid Research Letters*, vol. 2, no. 1, pp. 31–33, 2008.

[177] A. Denisenko, G. Jamornmarn, H. El-Hajj, and E. Kohn, "pH sensor on O-terminated diamond using boron-doped channel," *Diamond and Related Materials*, vol. 16, pp. 905–910, 2007.

[178] R. Edgington, A. R. Ruslinda, S. Sato, Y. Ishiyama, K. Tsuge, T. Ono, H. Kawarada, and R. B. Jackman, "Boron δ-doped (111) diamond solution gate field effect transistors," *Biosensors and Bioelectronics*, vol. 33, no. 1, pp. 152–157, 2012.

[179] M. Dipalo, C. Pietzka, A. Denisenko, H. El-Hajj, and E. Kohn, "O-terminated nano-diamond ISFET for applications in harsh environment," *Diamond and Related Materials*, vol. 17, pp. 1241–1247, 2008.

[180] Y. Shintani, S. Ibori, K. Igarashi, T. Naramura, M. Inaba, and H. Kawarada, "Polycrystalline boron-doped diamond with an oxygen-terminated surface channel as an electrolyte-solution-gate field-effect transistor for pH sensing," *Electrochimica Acta*, vol. 212, pp. 10–15, 2016.

[181] Y. Shintani, M. Kobayashi, and H. Kawarada, "An all-solid-state pH sensor employing fluorine-terminated polycrystalline boron-doped diamond as a pH-insensitive solution-gate field-effect transistor," *Sensors*, vol. 17, no. 5, 2017.

[182] N. Mitani and Y. Einaga, "The simple voltammetric analysis of acids using highly boron-doped diamond macroelectrodes and microelectrodes," *Journal of Electroanalytical Chemistry*, vol. 626, no. 1-2, pp. 156–160, 2009.

[183] S. Fierro, N. Mitani, C. Comninellis, and Y. Einaga, "pH sensing using boron doped diamond electrodes.," *Physical Chemistry Chemical Physics*, vol. 13, pp. 16795–16799, 2011.

[184] S. Fierro, R. Seishima, O. Nagano, H. Saya, and Y. Einaga, "In vivo pH monitoring using boron doped diamond microelectrode and silver needles:

Application to stomach disorder diagnosis," *Scientific Reports*, vol. 3, pp. 1–4, 2013.

[185] E. L. Silva, A. C. Bastos, M. A. Neto, R. F. Silva, M. G. Ferreira, M. L. Zheludkevich, and F. J. Oliveira, "Novel diamond microelectrode for pH sensing," *Electrochemistry Communications*, vol. 40, pp. 31–34, 2014.

[186] T. L. Read, S. J. Cobb, and J. V. Macpherson, "An sp2 Patterned Boron Doped Diamond Electrode for the Simultaneous Detection of Dissolved Oxygen and pH," *ACS Sensors*, p. acssensors.9b00137, 2019.

[187] C.-s. Chu, Y.-l. Lo, and T.-w. Sung, "Photonic Sensors Review on Recent Developments of Fluorescent Oxygen and Carbon Dioxide Optical Fiber Sensors," *Photonic Sensors*, vol. 1, no. 3, pp. 234–250, 2011.

[188] A. C. Manning, R. F. Keeling, P. Severinghaus, and L. Jolla, "Precise atmospheric oxygen measurements with a paramagnetic oxygen analyzer several repeated measurements interval various aspects of the global The analyzer was used to measure atmospheric period strongly changes sources to define," *Global Biogeochemical Cycles*, vol. 13, no. 4, pp. 1107–1115, 1999.

[189] W. C. Maskell and B. C. H. Steele, "Solid state potentiometric oxygen gas sensors," *Journal of Applied Electrochemistry*, vol. 16, pp. 475–489, 1986.

[190] M. C. Laderer, M. B. Frish, R. T. Wainner, B. D. Green, M. C. Laderer, and J. Stafford-Evans, "Progress in reducing size and cost of trace gas analyzers based on tunable diode laser absorption spectroscopy," in *Proceedings of SPIE 5586, Advanced Environmental, Chemical, and Biological Sensing Technologies II*, 2014.

[191] W. A. V. Drasek, O. Charon, K. Mulderink, D. M. Sonnenfroh, and M. G. Allen, "Multifunctional industrial combustion process monitoring with tunable diode lasers," in *Proceedings of SPIE 4201, Optical Methods for Industrial Processes*, 2001.

[192] R. Ramamoorthy, P. K. Dutta, and S. A. Akbar, "Oxygen sensors : Materials , methods , designs," *Journal of Materials Science*, vol. 38, no. 21, pp. 4271–4282, 2003.

[193] P. Shuk and R. Jantz, "Oxygen Gas Sensing Technologies : A Comprehensive Review," in *2015 9th International Conference on Sensing Technology (ICST)*, pp. 12–17, IEEE, 2015.

[194] L. C. Clark, R. Wolf, D. Granger, and Z. Taylor, "Continuous Recording of Blood Oxygen Tensions by Polarography," *Journal of Applied Physiology*, vol. 6, no. 3, pp. 189–193, 1953.

[195] A. Damjanovic and V. Brusic, "Electrode Kinetics of Oxygen Reduction on Oxide-free Platinum Electrodes," *Electrochimica Acta*, vol. 12, pp. 615–628, 1967.

[196] H. Wroblowa and G. Razumney, "Electroreduction of Oxygen," *Journal of Electroanalytical Chemistry*, vol. 69, pp. 195–201, 1976.

[197] E. Yeager, "Dioxygen Electrocatalysis: Mechanisms in Relation to Catalyst Structure," *Journal of Molecular Catalysis*, vol. 38, pp. 5–25, 1986.

[198] D. Pletcher and S. Sotiropoulos, "A study of cathodic oxygen reduction at platinum using microelectrodes," *Journal of Electroanalytical Chemistry*, vol. 356, pp. 109–119, 1993.

[199] R. Knake, P. Jacquinot, A. W. Hodgson, and P. C. Hauser, "Amperometric sensing in the gas-phase," *Analytica Chimica Acta*, vol. 549, no. 1-2, pp. 1–9, 2005.

[200] Alliance Technical Sales, "A Guide to Oxygen Measurement: Theory and Practice of Oxygen Applications," tech. rep., 2016.

[201] D. Pletcher and S. Sotiropoulos, "Towards a microelectrode sensor for the determination of oxygen in waters," *Analytica Chimica Acta*, vol. 322, no. 2

JAN, pp. 83–90, 1996.

[202] M. Sosna, G. Denuault, R. W. Pascal, R. D. Prien, and M. Mowlem, "Development of a reliable microelectrode dissolved oxygen sensor," *Sensors and Actuators, B: Chemical*, vol. 123, no. 1, pp. 344–351, 2007.

[203] G. M. Swain, A. B. Anderson, and J. C. Angus, "Applications of Diamond Thin Films in Electrochemistry," *MRS Bulletin*, vol. 23, no. 9, p. 56, 1998.

[204] M. Panizza and G. Cerisola, "Application of diamond electrodes to electrochemical processes," *Electrochimica Acta*, vol. 51, pp. 191–199, 2005.

[205] N. Yang, J. S. Foord, and X. Jiang, "Diamond Electrochemistry at the Nanoscale : A Review," *Carbon*, vol. 99, p. 90, 2016.

[206] G. M. Swain and R. Ramesham, "The electrochemical activity of boron-doped polycrystalline diamond thin film electrodes," *Analytical Chemistry*, vol. 65, pp. 345–351, 2 1993.

[207] T. Yano, D. Tryk, K. Hashimoto, and A. Fujishima, "Electrochemical Behavior of Highly Conductive Boron-Doped Diamond Electrodes for Oxygen Reduction in Alkaline Solution," *J. Electrochem. Soc.*, vol. 145, no. 6, pp. 1870–1876, 1998.

[208] K. Stolarczyk, E. Nazaruk, J. Rogalski, and R. Bilewicz, "Mediatorless catalytic oxygen reduction at boron-doped diamond electrodes," *Electrochemistry Communications*, vol. 9, no. 1, pp. 115–118, 2007.

[209] A. Kapałka, G. Fóti, and C. Comninellis, "Investigations of electrochemical oxygen transfer reaction on boron-doped diamond electrodes," *Electrochimica Acta*, vol. 53, no. 4, pp. 1954–1961, 2007.

[210] V. S. Dilimon, N. S. Venkata Narayanan, and S. Sampath, "Electrochemical reduction of oxygen on gold and boron-doped diamond electrodes in am-

bient temperature, molten acetamide-urea-ammonium nitrate eutectic melt," *Electrochimica Acta*, vol. 55, no. 20, pp. 5930–5937, 2010.

[211] Y. Zhang, S. Asahina, S. Yoshihara, and T. Shirakashi, "Oxygen reduction on Au nanoparticle deposited boron-doped diamond films," *Electrochimica Acta*, vol. 48, pp. 741–747, 2003.

[212] Y. Zhang, V. Suryanarayanan, I. Nakazawa, S. Yoshihara, and T. Shirakashi, "Electrochemical behavior of Au nanoparticle deposited on as-grown and O-terminated diamond electrodes for oxygen reduction in alkaline solution," *Electrochimica Acta*, vol. 49, no. 28, pp. 5235–5240, 2004.

[213] I. Yagi, T. Ishida, and K. Uosaki, "Electrocatalytic reduction of oxygen to water at Au nanoclusters vacuum-evaporated on boron-doped diamond in acidic solution," *Electrochemistry Communications*, vol. 6, no. 8, pp. 773–779, 2004.

[214] L. Hutton, M. E. Newton, P. R. Unwin, and J. V. Macpherson, "Amperometric oxygen sensor based on a platinum nanoparticle-modified polycrystalline boron doped diamond disk electrode.," *Analytical chemistry*, vol. 81, no. 3, pp. 1023–32, 2009.

[215] V. C. Müller and N. Bostrom, "Future progress in artificial intelligence: A survey of expert opinion," in *Fundamental Issues of Artificial Intelligence*, Berlin: Springer, 2014.

[216] N. Bostrom, "How Long Before Superintelligence?," *Int. Jour. of Future Studies*, vol. 2, 1998.

[217] J. Barrat, *Our Final Invention*. Thomas Dunne Books, 2013.

[218] D. Hill, "7 Key Factors Driving the Artificial Intelligence Revolution." https://singularityhub.com/2016/08/29/7-factors-driving-the-artificial-intelligence-revolution/ [Accessed: 22/02/2018].

[219] P. Lops, M. de Gemmis, and G. Semeraro, "Content-based Recommender Systems: State of the Art and Trends," in *Recommender Systems Handbook*, Boston, MA: Springer, 2011.

[220] A. Esteva, B. Kuprel, R. A. Novoa, J. Ko, S. M. Swetter, H. M. Blau, and S. Thrun, "Dermatologist-level classification of skin cancer with deep neural networks," *Nature*, vol. 542, no. 7639, pp. 115–118, 2017.

[221] S. Shen, H. Jiang, and T. Zhang, "Stock market forecasting using machine learning algorithms," tech. rep., Department of Electrical Engineering, Stanford University, 2012.

[222] A. Müller and S. Guido, *Introduction to Machine Learning with Python*. O'Reilly Media, Inc., 2016.

[223] E. Alpaydin, *Introduction to Machine Learning*. The MIT Press, 3rd ed., 2014.

[224] L. Breiman, "Random forests," *Machine Learning*, vol. 45, no. 1, pp. 5–32, 2001.

[225] T. Ho, "Random Decision Forests," in *3rd International Conference on Document Analysis and Recognition*, (Montreal, Canada), pp. 278–282, 1995.

[226] M. Werner and R. Locher, "Growth and application of undoped and doped diamond films," *Rep. Prog. Phys.*, vol. 61, pp. 1665–1710, 1998.

[227] P. W. May, "Diamond thin films: a 21st-century material," *Phil. Trans. R. Soc. Lond. A*, vol. 358, pp. 473–495, 2000.

[228] Jatosado, "Electron-beam evaporation, Power Point, CC BY-SA 3.0." https://commons.wikimedia.org/w/index.php?curid=20296340itle [Accessed: 22/01/2018].

[229] E. Barsoukov and J. R. Macdonald, *Impedance Spectroscopy: Theory, Experiment, and Applications*. Wiley, 2nd ed., 2005.

[230] R. Edgington, *Diamond at the brain-machine interface*. PhD thesis, University College London, University of London, 2012.

[231] G. Reeves, "Specific contact resistance using a circular transmission line model," *Solid-State Electronics*, vol. 23, no. 5, pp. 487–490, 1980.

[232] H. H. Berger, "Models for contacts to planar devices," *Solid State Electronics*, vol. 15, no. 2, pp. 145–158, 1972.

[233] Geant4 Collaboration, "Geant4 Installation Guide: Building and Installing Geant4 for Users and Developers," 2015.

[234] C. J. Werner, "MCNP6.2 Release Notes, LA-UR-18-20808," tech. rep., Los Alamos National Laboratory, 2018.

[235] R. C. Alig, S. Bloom, and C. W. Struck, "Scattering by ionization and phonon emission in semiconductors," *Phys. Rev. B*, vol. 22, no. 12, pp. 5565–5582, 1980.

[236] M. Pomorski, E. Berdermann, A. Caragheorgheopol, M. Ciobanu, M. Kiš, A. Martemiyanov, C. Nebel, and P. Moritz, "Development of single-crystal CVD-diamond detectors for spectroscopy and timing," *Physica Status Solidi (A) Applications and Materials Science*, vol. 203, no. 12, pp. 3152–3160, 2006.

[237] U. Fano, "Ionization Yield of Radiations. II. The Fluctuations of the Number of Ions," *Phys. Rev.*, vol. 72, no. 26, 1947.

[238] C. Grupen, *Particle Detectors: Cambridge Monographs on Particle Physics, Nuclear Physics and Cosmology*. Cambridge University Press, 1996.

[239] H. Spieler, "Signal formation and acquisition," in *Semiconductor Detector Systems*, Oxford University Press, 2005.

[240] K. Hecht, "Zum Mechanismus des lichtelektrischen Primarstromes in isolierenden Kristallen," *Zeitschrift fur Physik*, vol. 77, no. 3-4, pp. 235–245, 1932.

[241] C. L. Lingren and J. F. Butler, "Evaluating the Performance of Semicondiuctor Radiation Detectors Through Static Charge Analysis," *IEEE Transactions on Nuclear Science*, vol. 45, no. 3, pp. 1723–1725, 1998.

[242] J. Isberg, J. Hammersberg, H. Bernhoff, D. J. Twitchen, and A. J. Whitehead, "Charge collection distance measurements in single and polycrystalline CVD diamond," *Diamond and Related Materials*, vol. 13, no. 4-8, pp. 872–875, 2004.

[243] H. Spieler, "Electronic noise," in *Semiconductor Detector Systems*, Oxford University Press, 2005.

[244] A. Tarun, S. Lee, C. Yap, K. Finkelstein, and D. Misra, "Impact of impurities and crystal defects on the performance of CVD diamond detectors," *Diamond and Related Materials*, pp. 6–11, 2015.

[245] C. J. H. Wort and R. S. Balmer, "Diamond as an electronic material," *Materials Today*, vol. 11, no. 1-2, pp. 22–28, 2008.

[246] AZO Materials, "Boron Carbide (B4C) - Properties and Information about Boron Carbide." https://www.azom.com/properties.aspx?ArticleID=75 [Accessed: 15/11/2018].

[247] J. Hammersberg, J. Isberg, E. Johansson, T. Lundström, O. Hjortstam, and H. Bernhoff, "Injection dependent long carrier lifetimes in high quality CVD diamond," *Diamond and Related Materials*, vol. 10, no. 3-7, pp. 574–579, 2001.

[248] M. A. Plano, M. I. Landstrass, L. S. Pan, S. Han, D. R. Kania, S. McWilliams, and J. W. Ager, "Polycrystalline CVD diamond films with high electrical mobility," *Science*, vol. 260, no. 5112, pp. 1310–1312, 1993.

[249] S. Han and R. S. Wagner, "Grain boundary effects on carrier transport in undoped polycrystalline chemical-vapor-deposited diamond," *Applied Physics Letters*, vol. 68, no. 21, pp. 3016–3018, 1996.

[250] H. Yoneda, K. I. Ueda, Y. Aikawa, K. Baba, and N. Shohata, "The grain size dependence of the mobility and lifetime in chemical vapor deposited diamond photoconductive switches," *Journal of Applied Physics*, vol. 83, no. 3, pp. 1730–1733, 1998.

[251] A. Owens, *Compound Semiconductor Radiation Detectors*. Taylor & Francis, 2016.

[252] C. Lundstedt, A. Harken, E. Day, B. W. Robertson, and S. Adenwalla, "Modeling solid-state boron carbide low energy neutron detectors," *Nuclear Instruments and Methods in Physics Research, Section A: Accelerators, Spectrometers, Detectors and Associated Equipment*, vol. 562, no. 1, pp. 380–388, 2006.

[253] B. W. Robertson, S. Adenwalla, A. Harken, P. Welsch, J. I. Brand, P. A. Dowben, and J. P. Claassen, "A class of boron-rich solid-state neutron detectors," *Applied Physics Letters*, vol. 80, no. 19, pp. 3644–3646, 2002.

[254] S. Ghosh, P. Mishra, C. Srivastava, R. Choudhary, and A. Bidaye, "Synthesis and characterization of semiconducting BC films for neutron sensors by pulse DC plasma CVD," in *AIP Conf. Proc.*, vol. 1451, pp. 118–120, 2012.

[255] A. N. Caruso, R. B. Billa, S. Balaz, J. I. Brand, and P. A. Dowben, "The heteroisomeric diode," *Journal of Physics: Condensed Matter*, vol. 16, pp. L139–L146, 2004.

[256] S. Adenwalla, P. Welsch, A. Harken, J. I. Brand, A. Sezer, and B. W. Robertson, "Boron carbide/n-silicon carbide heterojunction diodes," *Applied Physics Letters*, vol. 79, no. 26, pp. 4357–4359, 2001.

[257] E. Day, M. J. Diaz, and S. Adenwalla, "Effect of bias on neutron detection in thin semiconducting boron carbide films," *Journal of Physics D: Applied Physics*, vol. 39, no. 14, p. 2920, 2006.

[258] R. Trammell and F. J. Walter, "The effects of carrier trapping in semiconductor gamma-ray spectrometers," *Nuclear Instruments and Methods*, vol. 76, no. 2, pp. 317–321, 1969.

[259] A. Owens, "Spectral degradation effects in an 86 cm3 Ge(HP) detector," *Nuclear Instruments and Methods in Physics Research Section A: Accelerators, Spectrometers, Detectors and Associated Equipment*, vol. 238, pp. 473–478, 8 1985.

[260] A. Kozorezov, J. Wigmore, A. Owens, R. den Hartog, A. Peacock, and H. A Al-Jawhari, "Resolution degradation of semiconductor detectors due to carrier trapping," *Nuclear Instruments and Methods in Physics Research Section A: Accelerators, Spectrometers, Detectors and Associated Equipment*, vol. 546, pp. 209–212, 7 2005.

[261] J. Iwanczyk, W. Schnepple, and M. Masterson, "The effect of charge trapping on the spectrometric performance of HgI2 gamma-ray detectors," *Nuclear Instruments and Methods in Physics Research Section A: Accelerators, Spectrometers, Detectors and Associated Equipment*, vol. 322, pp. 421–426, 11 1992.

[262] A. Owens, "Semiconductor materials and radiation detection," *Journal of Synchrotron Radiation*, vol. 13, no. 2, pp. 143–150, 2006.

[263] N. Hong, J. Mullins, K. Foreman, and S. Adenwalla, "Boron carbide based solid state neutron detectors: The effects of bias and time constant on de-

tection efficiency," *Journal of Physics D: Applied Physics*, vol. 43, no. 27, 2010.

[264] M. Paquette, G. Bhattarai, and A. Caruso, "Understanding the Electronic Structure of the a-B5C:Hx-to-Metal Interface," tech. rep., University of Missouri, Kansas City, 2016.

[265] J. C. Lund and F. Olschner, "Simulation of Charge Transport in Semiconductor Radiation Detectors," *Nuclear Instruments and Methods in Physics Research Section A*, vol. 288, pp. 31–34, 1990.

[266] K. Shah, J. Lund, and F. Olschner, "Charge collection efficiency in a semiconductor radiation detector with a non-constant electric field," *IEEE Transactions on Nuclear Science*, vol. 37, no. 2, pp. 183–186, 1990.

[267] D. S. McGregor and J. K. Shultis, "Spectral identification of thin-film-coated and solid-form semiconductor neutron detectors," *Nuclear Instruments and Methods in Physics Research, Section A: Accelerators, Spectrometers, Detectors and Associated Equipment*, vol. 517, no. 1-3, pp. 180–188, 2004.

[268] S. Agostinelli, J. Allison, K. Amako, J. Apostolakis, H. Araujo, P. Arce, and others, "Geant4—a simulation toolkit," *Nuclear Instruments and Methods in Physics Research Section A: Accelerators, Spectrometers, Detectors and Associated Equipment*, vol. 506, pp. 250–303, 7 2003.

[269] A. D. Harken and B. W. Robertson, "Comparative modelling of performance limits of solid-state neutron detectors based on planar B-rich capture layers," *Journal of Physics D: Applied Physics*, vol. 39, no. 23, pp. 4961–4968, 2006.

[270] S. M. Seltzer, J. M. Fernandez-Verea, P. Andreo, P. M. Bergstrom Jr, D. T. Burns, I. Krajcar Bronic, C. K. Ross, and F. Salvat, "ICRU Report No. 90: Key Data for Ionizing-Radiation Dosimetry: Measurement Standards and Applications," Tech. Rep. 1, International Comission on Radiation Units and Measurements (ICRU), 2014.

[271] H. A. Bethe, "Zur Theorie des Durchgangs schneller Korpuskularstrahlen durch Materie," *Ann. d. Physik*, vol. 5, p. 325, 1930.

[272] M. J. Berger, M. Inokuti, H. H. Andersen, H. Bichsel, D. Powers, S. M. Seltzer, D. Thwaites, and D. E. Watt, "ICRU Report No. 49: Stopping Powers and Ranges for Protons and Alpha Particles," tech. rep., International Comission on Radiation Units and Measurements (ICRU), 1992.

[273] J. C. Ashley, R. H. Ritchie, and W. Brandt, "Z3 effect in the stopping power of matter for charged particles," *Phys. Rev. B*, vol. 5, p. 2393, 1972.

[274] J. C. Ashley, R. H. Ritchie, and W. Brandt, "Z3 dependent stopping power and range contributions," *Phys. Rev. A*, vol. 8, p. 2402, 1973.

[275] F. Bloch, "Zur Bremsung rasch bewegter Teilchen beim Durchgang durch die Materie," *Ann. Phys.*, vol. 16, p. 285, 1933.

[276] H. Bichsel, "Stopping Power of Fast Charged Particles in Heavy Elements, National Institute of Standards and Technology (Report NIST IR-4550)," tech. rep., National Institute of Standards and Technology, Report NIST IR-4550, 1991.

[277] R. M. Sternheimer, S. M. Seltzer, and M. Berger, "Density effect for the ionization loss of charged particles," *Phys. Rev. B*, vol. 26, p. 6067, 1982.

[278] R. M. Sternheimer, "The density effect for the ionization loss in various materials," *Phys. Rev.*, vol. 88, p. 851, 1952.

[279] C. Varelas and J. Biersack, "Reflection of energetic particles from atomic or ionic chains in single crystals," *Nucl. Instr. Meth.*, vol. 79, no. 2, p. 213, 1970.

[280] H. H. Andersen and J. F. Ziegler, "Hydrogen: Stopping Powers and Ranges in All Elements," in *The Stopping and Ranges of Ions in Matter (Vol. 3)*, Pergamon Press, Elmsford, New York, 1977.

[281] W. Donahue, W. D. Newhauser, and J. F. Ziegler, "Analytical model for ion stopping power and range in the therapeutic energy interval for beams of hydrogen and heavier ions," *Physics in Medicine and Biology*, vol. 61, no. 17, pp. 6570–6584, 2016.

[282] J. F. Ziegler, "Helium: Stopping Powers and Ranges in all Elemental Matter," in *The Stopping and Ranges of Ions in Matter (Vol. 4)*, Pergamon Press, Elmsford, New York, 1977.

[283] D. Watt, *Stopping Cross Sections, Mass Stopping Powers and Ranges in 30 Elements for Alpha Particles (1 keV to 100 MeV)*. PhD thesis, University of St. Andrews, Scotland, 1988.

[284] D. Powers, "Stopping Cross Sections and Ranges for Alpha Particles in Matter (Report prepared for the ICRU Stopping Power Committee)," tech. rep., Department of Physics, Baylor University, Waco, Texas, 1978.

[285] W. Neuwirth and G. Both, "Aggregates of atoms and their stopping cross sections," *Nuclear Inst. and Methods in Physics Research, B*, vol. 12, no. 1, pp. 67–72, 1985.

[286] H. Paul, "Stopping Power of Matter for Ions: Graphs, Data, Comments and Programs." https://www-nds.iaea.org/stopping/ [Accessed: 05/09/2018].

[287] L. Buitinck, G. Louppe, M. Blondel, F. Pedregosa, A. Mueller, O. Grisel, V. Niculae, P. Prettenhofer, A. Gramfort, J. Grobler, R. Layton, J. Vanderplas, A. Joly, B. Holt, and G. Varoquaux, "API design for machine learning software: experiences from the scikit-learn project," tech. rep., 2013.

[288] F. Pedregosa, G. Varoquaux, A. Gramfort, V. Michel, B. Thirion, O. Grisel, M. Blondel, P. Prettenhofer, R. Weiss, V. Dubourg, J. Vanderplas, A. Passos, and others, "Scikit-learn: Machine Learning in Python," *Journal of Machine Learning Research*, vol. 12, pp. 2825–2830, 2012.

[289] "Scikit-learn User Guide: 1.11. Ensemble Methods." http://scikit-learn.org/stable/modules/ensemble.html#forest [Accessed: 27/02/2018].

[290] D. L. Alexander, A. Tropsha, and D. A. Winkler, "Beware of R2: Simple, Unambiguous Assessment of the Prediction Accuracy of QSAR and QSPR Models," *Journal of Chemical Information and Modeling*, vol. 55, no. 7, pp. 1316–1322, 2015.

[291] L. Breiman, J. Friedman, R. Olshen, and C. Stone, *Classification and Regression Trees*. Chapman and Hall, 1984.

[292] M. Tsubota, J. H. Kaneko, D. Miyazaki, T. Shimaoka, K. Ueno, T. Tadokoro, A. Chayahara, H. Watanabe, Y. Kato, S.-i. Shikata, and H. Kuwabara, "High-temperature characteristics of charge collection efficiency using single CVD diamond detectors," *Nuclear Instruments and Methods in Physics Research Section A: Accelerators, Spectrometers, Detectors and Associated Equipment*, vol. 789, pp. 50–56, 2015.

[293] C. Nantasenamat, C. Isarankura-Na-Ayudhya, T. Naenna, and V. Prachayasittikul, "A practical overview of quantitative structure-activity relationship," *Excli - Experimental and Clinical Sciences*, vol. 8, pp. 74–88, 2009.

[294] P. Liu and W. Long, "Current mathematical methods used in QSAR/QSPR studies," *International Journal of Molecular Sciences*, vol. 10, no. 5, pp. 1978–1998, 2009.

[295] K. Roy, S. Kar, and R. Das, "What is QSAR? Definitions and Formulism," in *A primer on QSAR/QSPR modeling: Fundamental Concepts*, pp. 2–6, New York, NY: Sprinter-Verlag Inc., 2015.

[296] D. S. Palmer, N. M. O'Boyle, R. C. Glen, and J. B. O. Mitchell, "Random Forest Models To Predict Aqueous Solubility," *Journal of Chemical Information and Modeling*, vol. 47, no. 1, pp. 150–158, 2007.

[297] R. Fraczkiewicz, "In Silico Prediction of Ionization," *Comprehensive Medicinal Chemistry II*, vol. 5, pp. 603–626, 2007.

[298] E. Freyhult, K. Andersson, and M. Gustafsson, "Structural Modeling Extends QSAR Analysis of Antibody-Lysozyme Interactions to 3D-QSAR," *Biophysical Journal*, vol. 84, no. 4, pp. 2264–2272, 2003.

[299] C. Nantasenamat, I. Chartchalerm, and V. Prachayasittikul, "Advances in computational methods to predict the biological activity of compounds," *Expert Opinon on Drug Discovery*, vol. 5, no. 7, 2010.

[300] P. Gramatica, "Principles of QSAR models validation: Internal and external," *QSAR and Combinatorial Science*, vol. 26, no. 5, pp. 694–701, 2007.

[301] A. Tropsha, "Best practices for QSAR model development, validation, and exploitation," *Molecular Informatics*, vol. 29, no. 6-7, pp. 476–488, 2010.

[302] A. Tropsha, P. Gramatica, and V. K. Gombar, "The Importance of Being Earnest: Validation is the Absolute Essential for Successful Application and Interpretation of QSPR Models," *Molecular Informatics*, vol. 22, no. 1, pp. 69–77, 2003.

[303] J. F. Ziegler, J. P. Biersack, and U. Littmark, "The Stopping and Range of Ions in Solids," in *The Stopping and Ranges of Ions in Matter (Vol. 1)*, Pergamon Press, Elmsford, New York, 1985.

[304] J. F. Ziegler and J. M. Manoyan, "The stopping of ions in compounds," *Nuclear Inst. and Methods in Physics Research, B*, vol. 35, no. 3-4, pp. 215–228, 1988.

[305] C. Xu, J. Wang, M. Wang, H. Jin, Y. Hao, and C. P. Wen, "Reeves's circular transmission line model and its scope of application to extract specific contact resistance," *Solid-State Electronics*, vol. 50, no. 5, pp. 843–847, 2006.

[306] J. Kriz, K. Gottfried, C. Kaufmann, and T. Gebner, "Determination of ohmic contacts to n-type 6H- and polycrystalline 3C-SiC using circular transmission line structures," *Diamond and Related Materials*, vol. 7, pp. 77–80, 1998.

[307] S. Xue, Y. Han, Z. Wu, and Y. Luo, "Measurement of specific contact resistivity of ohmic contact on p-GaN," *Chin. J. Semicond.*, vol. 25, no. 5, pp. 965–969, 2005.

[308] G. Meyer and E. Stokke, "Description of Sizewell B Nuclear Power Plant," tech. rep., Institutt for energiteknikk (IFE) OECD Halden Reactor Project Halden, Norway, 1997.

[309] B. R. Scharifker, "Microelectrode Techniques in Electrochemistry," in *Modern Aspects of Electrochemistry* (J. O. Bockris, B. E. Conway, and R. E. White, eds.), pp. 467–519, Boston, MA: Springer US, 1992.

[310] H. B. Martin, "Hydrogen and Oxygen Evolution on Boron-Doped Diamond Electrodes," *Journal of the Electrochemical Society*, vol. 143, no. 6, pp. 133–136, 1996.

[311] P. Abgrall, V. Conedera, H. Camon, A.-m. Gue, and N.-t. Nguyen, "SU-8 as a structural material for labs-on-chips and microelectromechanical systems," *Electrophoresis*, vol. 28, pp. 4539–4551, 2007.

[312] E. H. Conradie and D. F. Moore, "SU-8 thick photoresist processing as a functional material for MEMS applications," *Journal of Micromechanics and Microengineering*, vol. 12, pp. 368–374, 2002.

[313] H. Lorenz, M. Despont, N. Fahrni, N. LaBianca, P. Renaud, and P. Vettiger, "SU-8 : a low-cost negative resist for MEMS," *Journal of Micromechanics and Microengineering*, vol. 7, pp. 121–124, 1997.

[314] A. Shrivastava and V. Gupta, "Methods for the determination of limit of de-

tection and limit of quantitation of the analytical methods," *Chronicles of Young Scientists*, vol. 2, no. 1, p. 21, 2011.

[315] J. Browaeys and T. Beau, "Linear fit with both uncertainties in x and in y," 2017.

[316] E. Yeager, "Electrocatalysts for O2 reduction," *Electrochimica Acta*, vol. 29, no. 11, pp. 1527–1537, 1984.

[317] R. Bogdanowicz, J. Czupryniak, M. Gnyba, J. Ryl, T. Ossowski, M. Sobaszek, E. M. Siedlecka, and K. Darowicki, "Amperometric sensing of chemical oxygen demand at glassy carbon and silicon electrodes modified with boron-doped diamond," *Sensors and Actuators, B: Chemical*, vol. 189, pp. 30–36, 2013.

[318] D. Pletcher and S. Sotiropoulos, "Cathodic Reduction of Oxygen in Water and Media of Low Ionic-Strength," *Journal of the Chemical Society-Faraday Transactions*, vol. 91, no. 3, pp. 457–462, 1995.

[319] B. W. Robertson, S. Adenwalla, A. Harken, P. Welsch, J. I. Brand, J. P. Claassen, N. M. Boag, and P. A. Dowben, "Semiconducting boron-rich neutron detectors," in *Proceedings of SPIE*, vol. 4785, pp. 226–233, 2002.

[320] S. Y. Karpov, Y. N. Makarov, E. N. Mokhov, M. G. Ramm, M. S. Ramm, A. D. Roenkov, R. A. Talalaev, and Y. A. Vodakov, "Analysis of silicon carbide growth by sublimation sandwich method," *Journal of crystal growth*, vol. 173, pp. 408–416, 1997.

[321] A. S. Segal, A. N. Vorob'ev, S. Y. Karpov, E. N. Mokhov, M. G. Ramm, M. S. Ramm, A. D. Roenkov, Y. A. Vodakov, and Y. N. Makarov, "Growth of silicon carbide by sublimation sandwich method in the atmosphere of inert gas," *Journal of Crystal Growth*, vol. 208, no. 1, pp. 431–441, 2000.

[322] E. Mokhov, A. Roenkov, and A. Segal, "SiC Sublimation Growth at Small

Spacing between Source and Seed," *Materials Science Forum*, vol. 740-742, pp. 69–72, 2013.

[323] T. Kimoto, "Bulk and epitaxial growth of silicon carbide," *Progress in Crystal Growth and Characterization of Materials*, vol. 62, no. 2, pp. 329–351, 2016.

[324] F. L. Pasquale and J. A. Kelber, "Site-specific electron-induced cross-linking of ortho-carborane to form semiconducting boron carbide," *Applied Surface Science*, vol. 258, no. 7, pp. 2639–2642, 2012.

[325] T. V. Kononenko, M. S. Komlenok, V. P. Pashinin, S. M. Pimenov, V. I. Konov, M. Neff, V. Romano, and W. Lüthy, "Femtosecond laser microstructuring in the bulk of diamond," *Diamond and Related Materials*, vol. 18, no. 2-3, pp. 196–199, 2009.

[326] F. Picollo, D. Gatto Monticone, P. Olivero, B. a. Fairchild, S. Rubanov, S. Prawer, and E. Vittone, "Fabrication and electrical characterization of three-dimensional graphitic microchannels in single crystal diamond," *New Journal of Physics*, vol. 14, 2012.

[327] F. Thevenot, "Boron carbide - A comprehensive review," *Journal of the European Ceramic Society*, vol. 6, no. 4, pp. 205–225, 1990.

[328] M. A. McKernan, "Magnetron sputter deposition of boron and boron carbide," *Surface and Coatings Technology*, vol. 49, no. 1-3, pp. 411–415, 1991.

[329] L. G. Jacobsohn, R. K. Schulze, M. E. H. Maia Da Costa, and M. Nastasi, "X-ray photoelectron spectroscopy investigation of boron carbide films deposited by sputtering," *Surface Science*, vol. 572, no. 2-3, pp. 418–424, 2004.

[330] E. Pascual, E. Martinez, J. Esteve, and A. Lousa, "Boron carbide thin films deposited by tuned-substrate RF magnetron sputtering," *Diamond and Related Materials*, vol. 8, pp. 402–405, 1999.

[331] L. Dimmey, H. Park, P. Jones, and F. Cocks, "The optical band gap of hydrogenated amorphous boron thin films : the effect of substrate temperature," *Journal of Electronic Materials*, vol. 10, no. 1, pp. 111–117, 1981.

[332] M. Olsson, S. Söderberg, B. Stridh, U. Jansson, and J. O. Carlsson, "Chemical vapour deposition of boron carbides II: Morphology and microstructure," *Thin Solid Films*, vol. 172, no. 1, pp. 95–109, 1989.

[333] S. Lee, J. Mazurowski, G. Ramseyer, and P. A. Dowben, "Characterization of boron carbide thin films fabricated by plasma enhanced chemical vapor deposition from boranes," *Journal of Applied Physics*, vol. 72, no. 10, pp. 4925–4933, 1992.

[334] Sunwoo Lee and P. A. Dowben, "The Properties of Boron Carbide/Silicon Heterojunction Diodes Fabricated by Plasma-Enhanced Chemical Vapor Deposition," *Appl. Phys. A*, vol. 58, no. 3, pp. 223–227, 1994.

[335] S. Lee, T. Ton, D. Zych, and P. A. Dowben, "Conductance in Microcrystalline BxCx/Si Heterojunction Diodes," in *MRS Proceedings*, vol. 283, p. 483, Cambridge University Press, 1992.

[336] A. O. Sezer and J. Brand, "Chemical vapor deposition of boron carbide," *Materials Science and Engineering: B*, vol. 79, no. 3, pp. 191–202, 2001.

[337] D. Byun, S.-d. D. S.-D. Hwang, P. A. Dowben, F. K. Perkins, F. Filips, N. J. Ianno, F. Kieth Perkins, F. Filips, N. J. Ianno, F. K. Perkins, F. Filips, and N. J. Ianno, "Heterojunction fabrication by selective area chemical vapor deposition induced by synchrotron radiation," *Applied Physics Letters*, vol. 64, no. 15, pp. 1968–1970, 1994.

[338] D. Byun, B. R. Spady, N. J. Ianno, and P. A. Dowben, "Comparison of different chemical vapor deposition methodologies for the fabrication of heterojunction boron-carbide diodes," *Nanostructured Materials*, vol. 5, no. 4, pp. 465–471, 1995.

[339] J. M. Carpinelli, E. W. Plummer, D. Byun, and P. A. Dowben, "Scanning tunneling microscopy study of intermediates in the dissociative adsorption of closo-1,2-dicarbadodecaborane on Si(111)," *Journal of Vacuum Science & Technology B: Microelectronics and Nanometer Structures*, vol. 13, no. 3, pp. 1203–1206, 1995.

[340] S.-d. Hwang, D. Byun, N. J. Ianno, and P. A. Dowben, "Fabrication of boron-carbide / boron heterojunction devices," *Applied Physics Letters*, vol. 68, no. 11, pp. 1495–1498, 1996.

[341] K. Aflatooni, G. A. Gallup, and P. D. Burrow, "Temporary Anion States of closo-Carboranes and Diethyl Carborane," *The Journal of Physical Chemistry A*, vol. 106, pp. 4703–4708, 5 2002.

[342] A. Salam, M. Deleuze, and J. Francois, "Computational study of the structural and vibrational properties of ten and twelve vertex closo-carboranes," *Chemical Physics*, vol. 286, no. 1, pp. 45–61, 2003.

[343] A. N. Caruso, L. Bernard, B. Xu, and P. A. Dowben, "Comparison of adsorbed orthocarborane and metacarborane on metal surfaces," *J. Phys. Chem. B*, vol. 107, no. 36, pp. 9620–9623, 2003.

[344] P. Lunca-Popa, J. I. Brand, S. Balaz, L. G. Rosa, N. M. Boag, M. Bai, B. W. Robertson, and P. A. Dowben, "Evidence for multiple polytypes of semiconducting boron carbide (C2B10) from electronic structure," *J. Phys. D: Appl. Phys*, vol. 38, pp. 1248–1252, 2005.

[345] H. Shin, E. Kim, S. Y. Lee, S.-H. Lee, S.-J. Park, K.-S. Chung, S.-H. Hong, and J. Kim, "Studies on formation of carborane film prepared by using a deuterium glow discharge method," *Journal of Nanoscience and Nanotechnology*, vol. 13, no. 11, pp. 7444–7447, 2013.

[346] P. Chaudhari, A. Singh, A. Topkar, and R. Dusane, "Hot wire chemical vapor deposited boron carbide thin film/crystalline silicon diode for neutron

detection application," *Solid-State Electronics*, vol. 78, pp. 156–158, 2012.

[347] H. Zeng, D. Byun, J. Zhang, G. Vidali, M. Onellion, and P. A. Dowben, "Adsorption and bonding of molecular icosahedra on Cu(100)," *Surface Science*, vol. 313, no. 3, pp. 239–250, 1994.

[348] K. Park, M. R. Pederson, L. L. Boyer, W. N. Mei, R. F. Sabirianov, X. C. Zeng, S. Bulusu, S. Curran, J. Dewald, E. Day, S. Adenwalla, M. J. Diaz, L. G. Rosa, S. Balaz, and P. A. Dowben, "Electronic structure and vibrational spectra of C2B10-based clusters and films," *Physical Review B*, vol. 73, no. 035109, 2006.

[349] H. Bichsel, "Barkas effect and effective charge in the theory of stopping power," *Phys. Rev. A*, vol. 41, p. 3642, 1990.